UNIVERSITÉ DE SHERBROOKE

Faculté de génie
Département de génie civil

MÉTHODES D'ANALYSE D'IMAGES POUR L'ÉVALUATION DE LA DÉGRADATION DES STRUCTURES EN BÉTON

(Transform- and Statistical-based Image Analysis for Assessment of Deterioration in Concrete Infrastructure)

Thèse de doctorat
Spécialité : génie civil

Jury:

Patrice Rivard	Directeur de recherche
Dong Chen He	Codirecteur de recherche
Gérard Ballivy	Rapporteur
Marie-Flavie Auclair-Fortier	Examinateur
Kaveh Saleh	Examinateur

Shahid KABIR

Sherbrooke (Québec), Canada Juillet 2008

Your file Votre référence
ISBN: 978-0-494-42626-5
Our file Notre référence
ISBN: 978-0-494-42626-5

Résumé

La connaissance de l'état des infrastructures civiles requiert l'élaboration et l'optimisation de méthodes alternatives d'évaluation de la détérioration de surface afin d'obtenir de l'information précise et quantitative complémentaire aux inspections visuelles. À cet effet, les méthodes reposant sur la prise d'images numériques montrent un grand potentiel et sont de plus en plus employées pour évaluer l'état du béton. Ces méthodes, telles la thermographie infrarouge, les images en tons de gris et les images en couleur, offrent des rendements intéressant en termes de coût-efficacité et sont relativement faciles à utiliser. Il y a néanmoins un besoin énorme pour le développement et l'optimisation de techniques efficaces d'analyse d'images afin d'extraire l'information pertinente relative à l'endommagement du béton à partir d'images brutes.

Dans ce contexte, cette recherche propose l'utilisation de l'analyse statistique texturale de matrice de cooccurrence en tons de gris (GLCM) en combinaison avec l'analyse par l'ondelette de Haar afin d'améliorer la détection des défauts recherchés. Deux classificateurs d'éléments de détérioration sont proposés; le réseau supervisé de neurones artificiels par perceptron multicouche et une classification non supervisée, le *K-means clustering*. Ces techniques ont été appliquées à des images thermographiques, couleur et en tons de gris prises à partir de spécimens de laboratoire et de terrain montrant différents niveaux de détérioration du béton. D'autres traitements ont été réalisés sur des images provenant de sondes de diagraphie acoustiques et optiques (imagerie en trou de forage), impliquant des techniques additionnelles de filtrages.

Les résultats montrent que l'approche hybride d'analyse textural est efficace pour la discrimination des types de défauts recherchés. Ils indiquent également que les filtres passe-bas et les filtres spatiaux médians sont mieux adaptés que les operateurs de type *edge-detector* ou gradient de Laplace; cependant, les approches par analyse texturale ont surpassé toutes les autres techniques. La classification des défauts par réseau de neurones artificiels s'est avérée supérieur à celle par *K-means*. En ce qui concerne l'imagerie, la thermographie a produit des résultats plus précis que la couleur et les tons de gris. Parmi les paramètres quantifiés sur les images, on note la surface totale dégradée, la longueur et l'ouverture des fissures. Ces paramètres ont bien corrélé l'endommagement évalué par d'autres méthodes, comme la mesure de l'expansion du béton ou les vitesses d'ondes ultrasonores.

Transform- and Statistical-based Image Analysis for Assessment of Deterioration in Concrete Infrastructure

Shahid Kabir (2008)
Ph.D. Thesis in Civil Engineering
Department of Civil Engineering, University of Sherbrooke

Abstract

The evaluation of the condition of infrastructure requires the development and optimization of alternative inspection methods for assessing surface deterioration in order to obtain accurate and quantitative information to supplement visual inspections. To this end, non-destructive methods that produce image data show great potential and are increasingly being used in concrete applications. These methods, based on IR thermography and greyscale and colour imaging, are generally cost and time effective and are relatively easy to employ. There is, however, a need for efficient image analysis techniques to extract relevant damage information from the imagery. In this context, this research proposes the use of grey level co-occurrence matrix statistical texture analysis in combination with Haar's wavelet analysis for improved defect detection. Two classifiers are proposed, the supervised multi-layer perceptron artificial neural network and the unsupervised *K*-means clustering approach, for evaluation of their effectiveness in characterizing the deterioration from the imagery. These techniques are applied to thermographic, colour and greyscale imagery of laboratory specimens and field samples exhibiting different levels of concrete deterioration. Further experiments are conducted on borehole acoustic imagery involving the additional techniques of spatial filters and edge-detectors in an effort to determine their efficiency in detecting concrete damage.

The results demonstrate that the hybrid texture approach is quite effective for defect discrimination. They also indicate that the lowpass and median spatial filters performed better than the gradient-based and Laplacian edge-detectors; however, the texture approaches outperformed all of the other techniques. The artificial neural network was found to provide better classification accuracies compared with the *K*-means algorithm. Concerning the imagery, the thermography produced more accurate results than the colour and greyscale imagery. The information derived from the imagery consists of total surface damage; for map-crack imagery, the total length of cracks and range of crack width openings were also computed. The damage quantities obtained for the laboratory specimens show good correlation with test measurements recorded for the specimens, such as expansion and impact-echo velocities.

Executive Summary

Imaging techniques for non-destructive testing are increasingly being employed for evaluating the condition of and assessing damage in concrete infrastructure. These methods can provide objective, quantitative information while reducing the time and cost involved, thus complementing inspections based on conventional visual approaches. However, in order to extract accurate data from the images, efficient image analysis methods need to be developed. This study proposes the application of a hybrid scheme based on Haar's discrete wavelet transform and statistical texture analysis using first-order statistics and second-order grey-level co-occurrence matrix (GLCM) approaches in order to extract deterioration features from the concrete imagery. Also employed, are an artificial neural network (ANN) supervised classifier, and the unsupervised *K*-means clustering technique, in order to evaluate their effectiveness in characterizing the deterioration and deriving damage information, such as the total amount of surface damage.

These methods are applied to thermographic, colour and greyscale imagery of concrete blocks that were exposed outdoors to the elements, and concrete slabs that were kept in the laboratory in controlled environments; all specimens exhibit various levels of damage due to the alkali-aggregate reaction. Imagery of field samples were also employed, which consist of concrete components from various bridges located in the cities of Montreal and Sherbrooke, Quebec. In addition, borehole acoustic imagery obtained from a concrete lock was analyzed using the same techniques, as well as various spatial filters and edge-detection operators, with a view to assessing the efficiency of the different approaches.

Experiments are conducted using imagery processed with texture analysis methods alone, as well as with images processed with the combined approach of the wavelet transform and texture analysis, in an effort to determine the contribution of the wavelet approach to the detection of concrete damage. The impact of first-order information is studied through classifications involving only second-order data, as well as a combination of first- and second-order data. Classifications for the imagery are also carried out on three different datasets: a spatial dataset consisting of only textural information, a spectral dataset containing only the unprocessed image

samples, and a combination dataset of both spatial and spectral data. This is done in order to determine the impact of the textural and spectral data in characterizing concrete damage.

The results of the experiments show that the hybrid approach of texture analysis and the wavelet transform is more effective than the texture analysis method alone. Also, the addition of the first-order texture data improved classification accuracies compared with classifications using only second-order texture information. Furthermore, the combined datasets achieved higher overall classification accuracies than the purely spectral and spatial datasets, indicating the positive contribution of the texture and spectral information in the analysis of concrete imagery. Among the spatial filters and edge-detection algorithms, the spatial and median filters performed better than all of the other techniques, and the gradient-based methods were more effective than the Laplacian; however, the texture approaches produced overall better results. Concerning the different classifiers, the supervised ANN classifier provided better classifications than the unsupervised *K*-means clustering algorithm. In terms of imagery, the results show that the infrared thermography produced more accurate results compared with the colour and greyscale images; however, the greyscale imagery is more computationally-effective.

The classifications using the ANN classifier and the combination datasets were used to quantify damage in the concrete. The resulting damage quantities obtained for the laboratory specimens through the image analysis approach presented in this study show good correlation with test measurements recorded for the specimens, such as expansion measurements and impact-echo velocities. In the case of images manifesting cracking, the total length of cracks, and range of crack widths were also calculated.

This research indicates the validity of the hybrid approach of texture analysis described in this thesis for application to the evaluation of concrete infrastructure through non-destructive testing imaging. Future studies can focus on the incorporation of this image analysis model as a damage assessment component of an automated monitoring system for concrete infrastructure, which could be employed to classify a collection of concrete images according to the level of damage. Since the imaging and inspection data can be stored in a digital format, a history of inspection results can be examined and compared in order to quantitatively establish changes that occur with time.

ACKNOWLEDGMENTS

I would like to gratefully acknowledge the valuable assistance and advice provided for this research project and in the writing of this thesis by my director Dr. Patrice Rivard, as well as the support, confidence and encouragement shown by my co-directors Dr. Dong-Chen He and Dr. Gérard Ballivy.

I would also like to thank Dr. Benoit Fournier from CANMET for allowing the use of the CANMET concrete specimens. This project was supported by a grant from the Fonds québécois de recherche sur la nature et les technologies (FQRNT). Special thanks to "Groupe de recherche sur l'auscultation et l'instrumentation (GRAI)" for supplying the image data as well as the laboratory and in-situ data.

I greatly appreciate the helpful discussions and suggestions, as well as the aid of various professors, colleagues and personnel at GRAI of the University of Sherbrooke.

Table of Contents

Preface

Part I Theoretical Framework

CHAPTER 1: Introduction

Part II Review of Image Analysis and Concrete Infrastructure

CHAPTER 2: Imaging for Concrete Infrastructure

CHAPTER 4: Results and Discussion

List of Figures

List of Tables

List of Peer-reviewed Publications in Journals and International Conferences Pertaining to this Thesis

List of Journal Publications

Kabir, S., Rivard, P. and Ballivy, G. (2008) *Neural Network-Based Damage Classification in Bridge Infrastructure using Texture Analysis,* Canadian Journal of Civil Engineering, vol. 35, no. 3, pp. 258–267.

Kabir, S. and Rivard, P. (2007) *Classification of Crack-Damage in Bridges based on Grey Level Co-occurrence Matrix using Haar's Discrete Wavelet Transform*, Computers & Concrete International Journal, vol. 4, no. 3, pp. 243-257.

Kabir, S., Rivard, P. and Ballivy, G. (2006) *Detection of AAR Deterioration Patterns in Concrete using Wavelets for Multiscale Texture Analysis*, Durability of Concrete, ACI Special Publication, vol. 234, p.127-146.

Kabir, S., Rivard, P. and He, D-C. (2007) *Acoustic Borehole Imaging for Inspection of Concrete Dam,* International Journal of Advances in Civil Engineering (Submitted in April, 2008).

List of Conference Proceedings

Kabir, S. (2008) *Image Processing in Concrete Applications: Review and Prospective*, 2nd International Structural Specialty Conference on Partnership for Innovation: Instrumentation and Monitoring of Structures, CSCE Annual Conference, Quebec City, Accepted for CSCE Conference, June 10-13, 2008.

Kabir, S. and Rivard, P. (2008) *Optical Borehole Acoustic Imagery for Structural Damage Analysis*, 2nd International Structural Specialty Conference on Partnership for Innovation: Instrumentation and Monitoring of Structures, CSCE Annual Conference, Quebec City, Accepted for CSCE Conference, June 10-13, 2008.

Kabir, S. and Rivard, P. (2008) *Statistical- and Transform-based Methods for Recognition and Quantitative Analysis of Deterioration in Concrete Infrastructure*, 12th International Conference

on Computing and Decision Making in Civil and Building Engineering, Structural Damage-assessment, Beijing, ICCCBE, October 15-17, 2008.

Kabir, S. and Rivard, P. (2006) *Analysis of Surface-Damage through Concrete Imaging,* Proceedings of 2nd International RILEM Symposium on Advances in Concrete through Science and Engineering, Quebec City, Sep 11-13, 2006.

Kabir, S., Rivard, P., Ballivy, G. and He, D-C. (2006) *Textural Analysis for Crack-Detection Using Infrared Thermography, Visual Colour, and Greyscale Concrete Imagery*, Proceedings of 11th International Conference on Computing and Decision Making in Civil and Building Engineering on Structural Damage-assessment, Montreal, June 14-16, 2006, pp. 3296-3305.

Kabir, S., He, D-C. and Rivard, P. (2006) *Urban Classification of High Resolution IKONOS Imagery using Texture*, Proceedings of 11th International Conference on Computing and Decision Making in Civil and Building Engineering on IT in Urban Planning, Montreal, June 14-16, 2006, pp. 326-335.

Kabir, S. and Rivard, P. (2009) *A Mathematical Model for Structural Damage Assessment based on Hybrid methods using Statistical and Signal Processing*, Third International Conference on Modeling, Simulation and Applied Optimization (ICMSAO'09), American University of Sharjah (AUS), Sharjah, United Arab Emirates January 20-22, 2009 (Submitted in April 2008).

Kabir, S., Rivard, P. and Ballivy, G. (2009) *Content-based Damage Retrieval Method using Colour Histograms, Texture Measures, and Local Features for Concrete NDT Imagery*, 7th International Symposium on Non Destructive Testing in Civil Engineering (NDT-CE' 09), Nantes (France), June 30th - July 3rd, 2009 (accepted)

Part I

Theoretical Framework

CHAPTER 1

Introduction

1.1 NDT Imaging for Concrete Deterioration

The durability of concrete has increasingly become the focal point of research in the concrete community throughout the world. How to make durable concrete, and what maintenance procedures must be implemented to extend the service life of concrete, are regularly discussed at concrete related meetings, seminars, workshops, as well as major international conferences (Rhim, 2001). This is due to the fact that deterioration in concrete severely affects the service life, safety and maintenance costs of concrete structures.

In order to rehabilitate damaged concrete infrastructure, or even to determine whether the concrete is worthy of repair, it is often necessary to carry out a systematic evaluation of the state of the concrete prior to specifying any kind of repair procedure. Concrete distress may be detected at an early stage, before the functionality of a structure is seriously damaged. At any age, the quality of a structure, in the sense of integrity and potential durability, is almost totally dependent on the quality of construction. Assessment of the condition of the concrete structure should, therefore, be carried out at as early as possible, preferably immediately following construction.

The deteriorating condition of concrete infrastructure and the prohibitive costs required for upgrading them require the development of innovative and effective decision support tools. Such tools will enable predictions about the condition and future performance of concrete structures and the allocation of limited funds for optimized maintenance that yields improved reliability and minimum life cycle costs. Furthermore, improved control on the variability between predicted and actual repair quantities would tend to reduce the long-term unit price of repair work as contractors adapt to less instances of work shortfalls.

There is a growing need for precise and reliable methods that use non-destructive testing (NDT) techniques to assess the deterioration in concrete structures and the extent of associated damage. Current use and development of monitoring methods and imaging techniques employing NDT is limited due to the unavailability of enough experimental data and field applications. The lack of this type of research is largely due to the fact that traditionally civil engineering has shown little interest in these techniques mainly because of insufficient knowledge of the available methods, as well as technical limitations and their related high costs. Over the years, though, many technological obstacles, such as computer efficiency, infrared camera resolution, equipment transportability, as well as the price of equipment, have been greatly reduced. The development of NDT imaging methods is very promising because it also provides a better understanding of the physio-chemical phenomena that interact within the concrete.

Certain imaging methods have proven to be very efficient in collecting concrete data. However; acquiring data is only the first step in assessing and evaluating concrete deterioration. This data has to be processed and interpreted in order to present the information in a more meaningful and useful format. If efficient and accurate imaging techniques can be developed, this approach can be a highly potential source of reliable information concerning the actual condition of concrete, which can be used to predict the safety and serviceability of concrete structures.

1.2 Research Overview

This thesis is broadly divided into three sections. Part I consists of an introduction to the need of NDT imaging for concrete infrastructure; it also consists of the theoretical framework of the research, which includes an elaboration of the problems related to concrete deterioration, and the evaluation of concrete structures. In addition, this section includes the hypothesis and objectives formulated to overcome the specific challenges associated with concrete assessment, which are enumerated in this study.

Part II of the thesis deals with a review of image analysis techniques; it presents some fundamental concepts specifically about texture analysis, signal processing, edge-detection, and classification approaches, along with details as to how these techniques function. The second part also discusses the mechanisms and their effects of the major concrete deterioration factors of

the alkali-aggregate reaction, steel corrosion, freeze-thaw cycles, and erosion, as well as non-destructive testing methods that employ concrete imaging.

Part III of this thesis is composed of *a* description of the study area, laboratory specimens and field samples employed, and the different types of data, including acoustic, thermographic, greyscale, and colour imagery, used in this research. Also included in this section, is the methodology steps employed in the experimental stage of this research: signal processing through the Haar's wavelet transform, texture analysis using the first-order statistical technique and the second-order grey level cooccurrence matrix (GLCM), spatial filters based on various approaches, and classifications based on the artificial neural network (ANN), and *K*-means clustering techniques. Finally, chapter four presents the results and discussion, and chapter five provides the conclusions and recommendations of this thesis.

1.3 Research Significance

Surface damage, such as cracks, in images are usually treated as objects, and are thus quantified through techniques that first segment the objects from the background to extract shape or object features, and then classify the images based on those features. However, in their study on the classification of pits and cracks in corrosion images, Livens et al. (1996) found that segmentation approaches worked well on individual images, but proved unsatisfactory when applied to a large set of samples due to the variability in the background. So they adopted a method based on analysis of the textured appearance of the pits and cracks in the images, which was successfully employed to discriminate between the two types of damage. The present research aims at finding a new application for texture methods in the analysis of concrete damage from NDT imagery. Different types of concrete damage each have a specific texture typical of the type of deterioration, which should permit their discrimination through texture analysis methods.

There are few studies that have applied image processing techniques, such as texture analysis, to extract textural features in order to obtain concrete deterioration information from optical imagery and there have so far been even fewer efforts to combine two approaches, such as statistical methods and signal processing methods. Since, there are no obvious quantitative measures to characterize texture, texture analysis can prove to be quite difficult to implement.

Nevertheless, a good understanding or a more satisfactory interpretation of an image should include the description of both spectral and textural aspects of the image (He and Wang, 1991); thus, the door for research in computer vision remains wide open. Consequently, texture analysis techniques, usually used in the field of medical imagery and remote sensing, can find new and original applications in civil engineering.

The use of image processing methods on NDT imagery for the extraction of concrete deterioration information can be compared with visual inspection approaches that were traditionally employed to evaluate the condition of a concrete structure in service. Contrary to visual inspections, which, in most cases, remain qualitative, the proposed methods employ classification techniques, which present the greater advantage of providing quantitative information due to their capacity to analyze images, pixel by pixel, based on their numerical properties. Also, acquiring most of the types of NDT imagery employed in this research is not relatively costly, time consuming, or a disruption to traffic, thus allowing for more frequent monitoring, which is another important factor in effective bridge maintenance (Abudayyeh et al., 2004). As a result, the information obtained from the approaches described in this study can be used to supplement visual inspections. The quantitative nature of this data and its regular collection can promote the establishment of deterioration criteria through the determination of correlation between deterioration factors and damage within concrete. Furthermore, these techniques present the potential to be incorporated into an automated monitoring system for concrete infrastructure. Up to now, automated recognition of deterioration modes in concrete from monitoring data has been the object of very few research projects. In this context, this study constitutes an important contribution to a better understanding of automated image analysis, and how such tools can be used to assist inspectors in the assessment of the condition of concrete structures in order to provide more reliable concrete monitoring and decision making.

1.4 Theoretical Framework

1.4.1 Problematic

Concrete researchers are constantly developing innovative methods for condition assessment, performance prediction, and maintenance management for the cost-effective rehabilitation of

aging and deteriorating concrete structures, which are major components of urban infrastructure systems. The research undertaken covers different types of concrete structures; however, its main thrust is on concrete bridge systems, which constitute a critical link in the urban transportation network.

Concrete bridge deck deterioration is a significant problem that must be addressed to preserve highway infrastructure investments in bridges around the world (Scott et al., 2003). According to the Institute for Research in Construction (IRC, 2003), chloride-induced corrosion is the major cause of bridge deterioration in Canada and elsewhere. Along with being exposed to severe environments, concrete structures in Canada are also subject to increasing mechanical loading, and the majority are approaching the end of their service lives. These problems, combined with design and construction deficiencies, inadequate protection, and lack of systematic approaches to inspection and maintenance, have led to structural deterioration resulting in loss of serviceability and functionality, and a reduction in safety.

It is estimated that over 40% of all bridges in Canada are older than 35 years (IRC, 2003) and in need of maintenance, rehabilitation or replacement, the backlog for which is estimated at about ten billion dollars (IRC, 2003). Consequently, a primary challenge facing our local, provincial and federal governments is effective allocation of limited funding for the maintenance and repair of transportation assets.

One of the most pressing problems facing bridge management is the lack of accuracy and the variability between traditional deck deterioration estimates and the actual quantities of repair work required on a given bridge. Conventional evaluation methods for concrete structures, are mainly based on visual inspections, where trained inspectors examine the various components of a structure using non-destructive testing techniques, such as visual observation of cracks, efflorescence, and staining of the deck underside and curbs, to evaluate the condition of the components, and give them a ranking (Washer, 1998). This type of evaluation is subjective in nature and strongly depends on the experience and skill of the inspectors (Abdel-Qader, 2003); the lack of objective and quantitative information can produce significant differences between the estimated and the actual condition of a structure, and the amount of repair work needed. Although visual inspection may be effective in many cases, it is costly, time-consuming, and

often a disruption to traffic. Also, none of these methods have demonstrated the ability to predict deck deterioration problems six to eight years in advance, the desired time period for project planning (U.S. Department of Transportation, 2003).

Non-destructive testing (NDT) of materials is the characterization, discrimination and prediction of material defects non-destructively (Chen, 1998). This is a desirable approach because it does not change or destroy the usefulness of the material, which is essential for applications to bridge deck and highway infrastructure inspections. Compared to metal, however, NDT of concrete is a relatively immature discipline. One reason for this is that concrete itself has a very heterogeneous nature; in addition to this, concrete is often reinforced with steel rebar. These factors make detection of defects difficult to separate from naturally occurring, and generally safe, inclusions. Furthermore, universal failure criteria do not exist for concrete structures. As a result, there is a need for the study of correlation between deterioration factors and damage within concrete in order to establish such criteria, as well as for the development of more reliable NDT techniques for concrete structures (Chong et al., 1990).

After the arrival of digital signal processing, pattern recognition techniques have been increasingly used in NDT problems. In general, the goals of pattern recognition and signal processing in NDT are to improve inspection reliability, to improve damage detection and characterization, to automate inspection tasks, and to generate information about the material properties in order to assess the remaining life of a structure (Chen, 1998). These methods of inspection, which generate waveform or image data, have several advantages, the most important being that the extent of deterioration can be detected, characterized and measured more accurately.

Interpreting image data of concrete, however, is a very challenging task, since concrete is highly heterogeneous. Concrete is generally produced in the field with limited quality control. Grain size distribution is highly variable and properties of the constituent material are greatly varied making it difficult to obtain accurate images. Other sources of difficulties in interpreting images of concrete structures include the generally complex physical geometry, existence of inclusions, restricted accessibility to the object, and the problems related to the sensitivity of the method used to the heterogeneities in concrete.

1.4.2 Hypotheses

Several hypotheses were formulated in order to address the problems elaborated in this thesis. The research conducted within the scope of this thesis is founded on the following hypotheses:

- Detection of deterioration and its extent from concrete imagery can be achieved through statistical texture analysis;
- Detection of defects based on statistical texture analysis can be enhanced through the use of the wavelet transform, which allows for a multiresolution analysis, where the low scales show the coarse details and the higher scales show the finer details of the image;
- Discrimination of concrete damage can be enhanced by employing both first- and second-order texture information;
- Combination of spectral and spatial information can provide better characterization of concrete deterioration compared to spectral or spatial data alone.

1.4.3 Objectives

The following objectives were developed to support the hypotheses formulated for this study; further justification for these can be found throughout the methodology in chapter 3.

1.4.3.1 Global Objectives

- Optimization of image processing techniques in order to extract quantitative deterioration information from concrete images obtained using various NDT imaging methods;
- Establishment of correlation between the level of damage in the concrete and the information obtained from processing of the NDT data.

1.4.3.2 Specific Objectives

- Application of the multi-resolution analysis using Haar's wavelet transform on different types of NDT image data of concrete in order to analyse textures contained in the images at different scales;

- Extraction of first- and second-order texture information from the images using the texture analysis methods of first-order statistics and second-order grey level co-occurrence matrix (GLCM) approaches in order to optimize textural discrimination;

- Establishment of optimum texture features for different types of concrete damage;

- Combination of spatial and spectral data in the classification process in order to improve accuracy;

- Detection of damage from acoustic concrete images using spatial filters and edge-detection operators in order to evaluate the different filters for their efficiency in distinguishing crack damage compared with the transform- and statistical-based methods;

- Characterization of different types of concrete deterioration through the supervised classification technique of artificial neural networks, as well as the unsupervised *K*-means classifier in order to evaluate the effectiveness of each classification method in discriminating concrete damage;

- Evaluation of the efficiency of the various types of NDT imaging methods of thermographic, colour, and greyscale imagery, in detecting different types of concrete deterioration.

- Establishment of correlation between damage quantities obtained from processing of the concrete imagery and test measurements recorded for the laboratory specimens.

Part II

Review of Image Analysis and Concrete Infrastructure

CHAPTER 2

Imaging for Concrete Infrastructure

2.1 Texture Analysis

Texture is described by the spatial distribution of the local tonal variations in a scene and can be found in abundance in the visual world, at all scales of perception. As soon as there is enough detail in an adequate visual angle, a texture becomes distinguishable. Figure 2.1 presents some examples of visual textures (Brodatz, 1966).

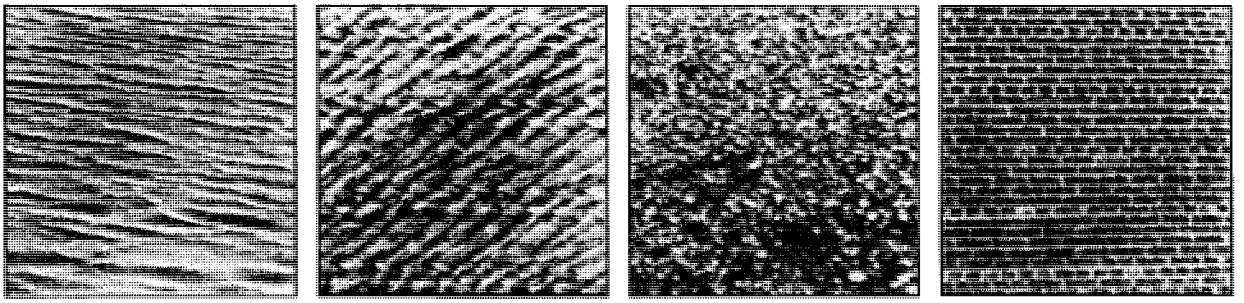

(a) Waves in water **(b) Straw mat** **(c) Gravel** **(d) Brick wall**

Figure 2.1: Examples of Different Types of Textures

Humans have a powerful innate ability to recognize textural differences. Although the complex neural and psychological processes by which this is accomplished have so far evaded detailed scientific explanation (Hay and Niemann, 1996), studies concerning texture perception by the human visual system have provided useful insights into the importance of textural information, as well as the complex nature of texture discrimination. Studies conducted by Julesz (1962) found that humans perceive textures using a low-level mechanism that performs an analysis of second-order statistics of intensities in texture fields, based on his hypothesis that textures with identical second-order statistics are not preattentively distinguishable, such as the texture pair in

Figure 2.2(a). Later on though, Julesz found a few counterexamples to his theory; he discovered a set of textures with equal second-order statistics, which are preattentively discriminable based on perceived local geometrical features, as seen in Figure 2.2(b) (Julesz et al., 1973).

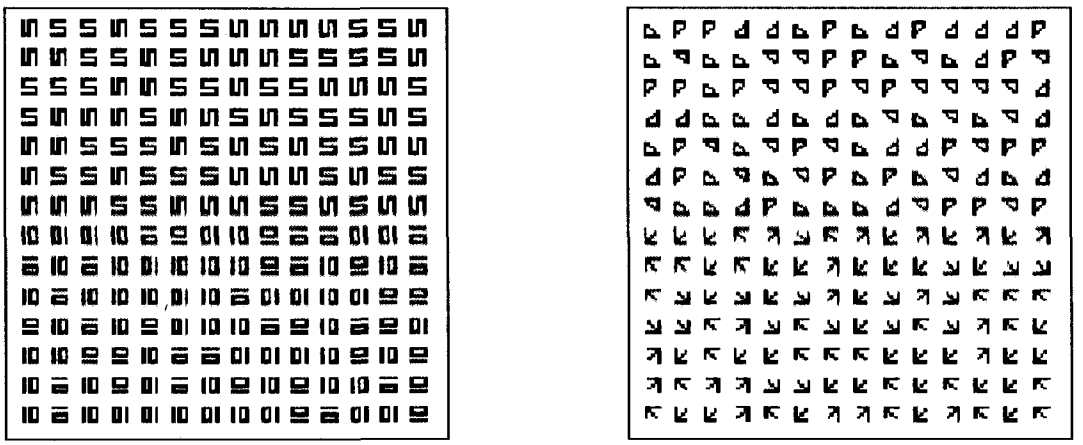

(a) (b)

Figure 2.2: Texture Pairs with Equal Second-order Statistics.

These notions are very significant in the study of texture analysis, which deals with various techniques for modeling textures and extracting texture features that can then be applied to such tasks as, classification, segmentation, texture synthesis and shape extraction. The concepts of human texture perception are meaningful to other fields as well, such as image processing and pattern recognition, which attempt to solve problems involving visual data through the use of texture (Tomita and Tsuji, 1990). Pattern recognition is a very common method used in discriminating objects. In order to recognize different types of objects in the visual world, we can use the texture of an object that has its own specific visual pattern as an indication. According to Pickett (1970), the basic requirement for an optical pattern to be seen, as texture, is that there be a large number of elements (spatial variations in intensity or wavelength), each to some degree visible and on the whole, densely and evenly arrayed over the field of view.

2.1.1 Image Texture

Texture is an important aspect for the analysis of many types of images. Texture analysis is a major technique used in image processing and pattern recognition, mainly because of the fact

that it can provide information about the arrangement and spatial properties of image fundamental elements. Such texture information is complementary to multispectral analysis and is sometimes the only way in which a digital image can be characterized (He and Wang, 1991).

In fact, Haralick et al. (1973) demonstrated this concept through their study, which showed that spectral classification precisions of an image could be increased with the integration of textural data. This conclusion caused texture analysis to become an extremely interesting field of research, especially for applications in remote sensing. Since texture plays a key role in all types of images, from remotely sensed, biomedical, and microscopic images to printed documents, texture analysis has a very wide range of practical applications that are useful to a variety of domains, from mature fields, such as remote sensing (Shaban and Dikshit, 2001) to more recent disciplines, such as medical imaging (Zizzari et al. 2001), document processing (Jain and Bhattacharjee, 1992) and automated inspection (Li et al., 2001).

There is no straight forward definition for texture. One definition taken from literature on image processing is as follows (Coggins, 1982): An image texture is described by the number and types of its (tonal) primitives and the spatial organization or layout of its (tonal) primitives... A fundamental characteristic of texture: it cannot be analyzed without a frame of reference of tonal primitives being stated or implied. For any smooth grey-tone surface, there exists a scale such that when the surface is examined, it has no texture. Then as resolution increases, it takes on a fine texture and then a coarse texture (Haralick, 1979).

For applications in image processing, texture is generally described as the group of relationships between grey levels of neighbouring pixels that contribute to the overall appearance and visual characteristics of an image. This description takes into account the forms and periodicities contained in the image; however, it does not provide a rigorous mathematical description for texture with which a quantitative evaluation of textures present in natural images can be made. With this in mind, Haralick et al. (1973) proposed the texture definition that images are represented by the spatial distribution of objects of a specific size and having reflectance or emmitance characteristics. The spatial organization and the relationships between these objects correspond to the spatial distribution of grey levels in the image. Thus, texture can be considered as the pattern of the spatial distribution of grey levels.

One important factor that is usually overlooked in the definition of texture is the scale of observation, or resolution, at which the texture is viewed. This is significant because texture is a complex multiscale phenomenon (Ahearn, 1988); it has a recursive nature. A primitive at one scale may contain a micro-texture composed of primitives defined at a smaller scale. For example, consider the texture represented in a brick wall (Tuceryan and Jain, 1998). When viewed at a low resolution, the texture of the wall is perceived as formed by primitives, which are the bricks, as seen in Figure 2.3(a). When viewed at a higher resolution, texture is perceived as the details present in the surface of each individual brick, as seen in Figure 2.3(b).

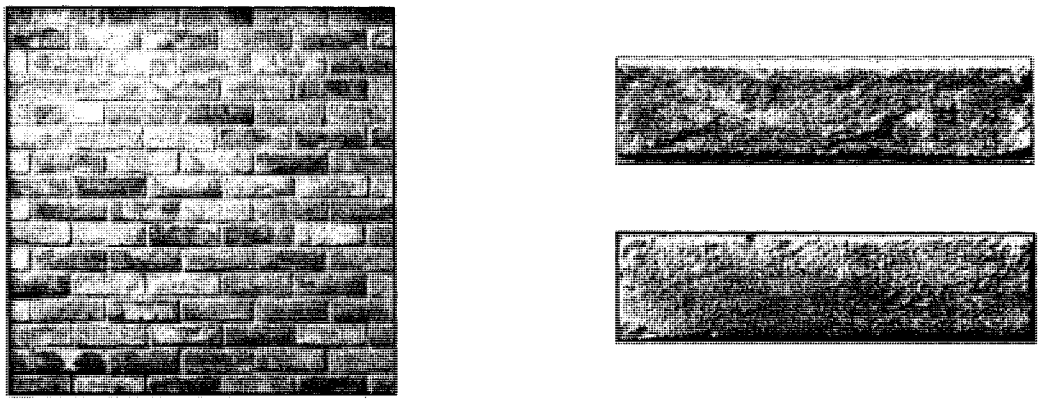

(a) Low resolution **(b) High resolution**

Figure 2.3: Textures at Different Scales in a Brick Wall

2.1.2 Statistical Texture Approaches

Texture analysis techniques can generally be divided into two broad categories: structural methods and statistical methods (Haralick, 1979; Sali and Wolfson, 1992). Structural methods of texture analysis consider texture to be composed of texture primitives that are arranged according to a specific placement rule. Different types of primitives, their orientation and shape, along with other properties are considered to determine the appearance of texture. This type of analysis includes the extraction of texture primitives in the image, shape analysis of the texture primitives, and estimation of the placement rule of the texture primitives. Structural texture analysis approaches can derive much more detailed textural information and are generally used for the analysis of coarse macro-textures (Tomita and Tsuji, 1990).

Statistical texture methods analyze the spatial distribution of grey values by computing local features at each point in the image, and deriving a set of statistics from the distributions of the local features. Depending on the number of pixels defining the local feature, statistical methods can be further classified into first-order (one pixel), second-order (two pixels) and higher-order (three or more pixels) statistics. The basic difference is that first-order statistics estimate properties, such as average and variance, of individual pixel values, while ignoring the spatial interaction between image pixels, whereas second- and higher-order statistics estimate properties of two or more pixel values occurring at specific locations relative to each other. Various texture features can then be extracted from these statistics. This type of analysis is usually employed for fine micro-textures (Tomita and Tsuji, 1990).

2.1.2.1 First-order Statistics

First-order statistics can be computed from a probability function, known as a histogram, which measures the probability of a pixel with a certain grey value occurring in an image. Figure 2.4(a) presents an image and Figure 2.4(b) provides its corresponding histogram.

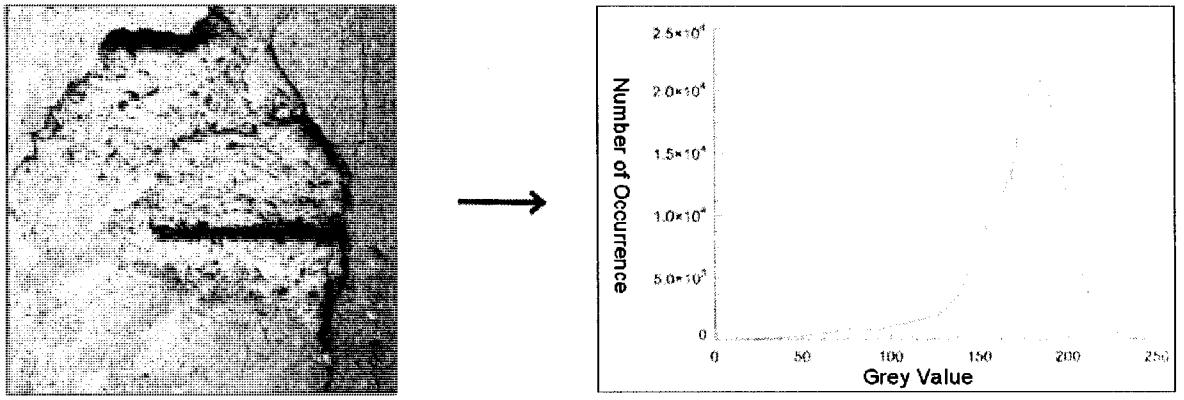

(a) Image Data **(b) Histogram**

Figure 2.4: Histogram of Corrosion Image

A class of texture measures can be derived from first-order statistics of primitives or local features of a texture pattern. The simplest primitives, called pixels, may be used; however, moments (means, variances, etc) of pixel intensity distributions convey only crude textural information. More meaningful textural information can be captured from a structural description

of the texture pattern. The texture is considered as being composed of more complex local features (such as edges, lines, blobs, relative intensity extrema, regions of uniform intensity, etc.), each having particular attributes (orientation, size, contrast, area, etc.). First-order statistics of these attributes may be used to characterize the texture.

2.1.2.2 Second-order Statistics

A second-order histogram is an array that is formed based on the probabilities that pairs of pixels, separated by a certain distance and a specific direction, will have co-occurring grey levels. This array, or second-order histogram, is also known as the grey level co-occurrence matrix (GLCM). Use of co-occurrence matrices for the extraction of textural information from an image is based on the hypothesis that image texture can be defined by the spatial relationships between pixel grey levels of the image (Haralick, 1979). Since the co-occurrence matrix expresses the two-dimensional distribution of pairs of grey-level occurrences, it can be considered a summary of the spatial and spectral frequencies of the image.

Let f be a rectangular, discrete image containing a finite number of grey levels; f is defined over the domain:

$$D = \{(i, j) : i \in [0, n_i), j \in [0, n_j), i, j \in I\} \tag{2.1}$$

by the relation:

$$f = \{((i, j), k) : (i, j) \in D, k = f(i, j), k \in [0, n_g), k \in I\} \tag{2.2}$$

where I denotes the set of integers, n_i and n_j are the horizontal and vertical dimensions of f, and n_g is the number of grey levels in f.

The grey level co-occurrence matrix (GLCM), G, is a square matrix of dimension n_g and is a function of both the image, f, and a displacement vector, d:

$$d = \{ [i, j] : (| i | , | j |) \in D, \| [i, j] \| > 0 \} \quad (2.3)$$

in the image plane (i, j), which constitutes the second-order spatial relation:

$$G (f, d) = [g_{ij} (f, d)] \quad (2.4)$$

Each element g_{ij} of the matrix represents an estimate of the probability that two pixels separated by d have grey levels i and j.

2.2 Signal Processing

Signal processing deals with the analysis, interpretation and manipulation of signals, which are streams of information that represent some particular type of data. Signal processing is one of the most powerful technologies to shape science and engineering in the twenty-first century, in a broad range of fields, such as communications, and imaging, to name a few (Smith, 1998). In digital signal processing, engineers usually study digital signals in one of the following domains: time domain for one-dimensional signals, spatial domain for multidimensional signals, frequency domain, autocorrelation domain, and wavelet domain.

The transform of a signal is just another form of representing the signal. The wavelet transform provides a time-frequency representation of a signal. While the Fourier transform uses waves to analyze signals, the wavelet transform uses wavelets of finite energy. A wave is an oscillating function of time or space and is periodic (Figure 2.5(a)). In contrast, wavelets are localized waves (Figure 2.5(b)); they have their energy concentrated in time or space and are suited to the analysis of transient signals.

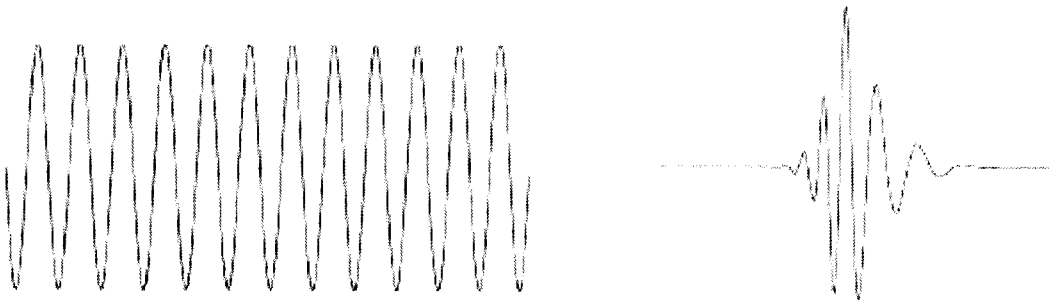

(a) Wave **(b) Wavelet**

Figure 2.5 Examples of a Wave and a Wavelet

2.2.1 Wavelet Transforms

Recent psycho-visual studies indicate that the human visual system processes images in a multi-scale manner (Daugman, 1990). In the past, one difficulty of texture analysis was the lack of adequate tools to characterize different scales of texture effectively (Zhu and Yang, 1998). Developments in multi-resolution analysis techniques, such as Gabor and Haar transforms, Gaussian and Laplacian pyramids, have helped to overcome this difficulty. In the last decade, the wavelet theory in particular, became a mathematical framework that provides a more formal, solid and unified approach to multi-resolution representations (Scheunders et al., 1997). This was achieved through the work of Mallat (1989), who established the connection between wavelets and the multi-resolution theory.

One of the standard approaches in the field of analysis is to break up a complicated phenomenon into many simpler pieces to be studied individually. Earlier methods of analysis relied mostly on Fourier transform techniques, but due to their lack of localization in the time domain, and their limited resolutions, these were not found useful for applications that require time information. Figure 2.6 shows the Fourier transform of a signal.

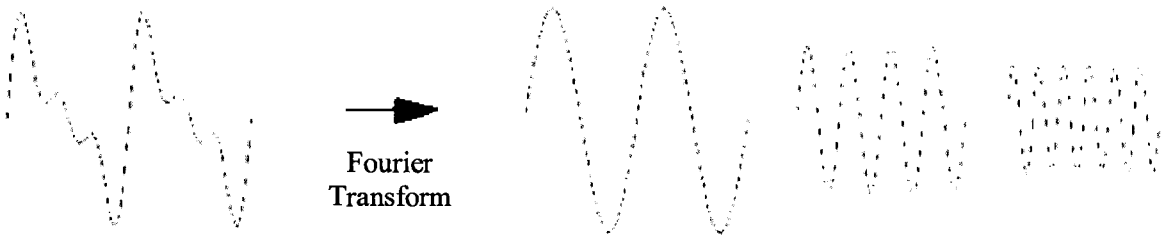

Figure 2.6: Fourier Transform

The wavelet transform is one of the most recent solutions to overcome the drawbacks of the Fourier transform, as well as those of multi-resolution representations. Although the theory behind wavelets has been around for several decades, it was not until the early 1980s, when Strömberg (1981) discovered the first orthogonal wavelets that researchers began to understand the potential of this powerful technique (Jawerth and Sweldens, 1994). The wavelet transform was inspired by the idea that the scale of the basis functions could be varied instead of their frequency: a subtle yet powerful modification. Instead of representing a function as a sum of weighted delta functions, as in the time domain, or as a sum of weighted sinusoids, as in the frequency domain, the function is represented as a sum of time-shifted and scaled representations of some arbitrary function, otherwise known as the mother wavelet (Perkins and Fricke, 2000).

In wavelet analysis, the use of a fully scalable modulated window solves the problem of time resolution. The window is shifted along the signal and for every position the spectrum is calculated. The wavelet transform first compares the entire function to the wavelet, and then compares smaller pieces of the function to the wavelet. This process is completed on successively smaller and smaller scales. This forms a representation of the original function as a sum of wavelets of various scales and positions in time, achieving a balance between locality in time and locality in frequency or scale. The result of the wavelet transform is a collection of time-frequency representations of the signal, all with different resolutions, as demonstrated in (Figure 2.7). This collection of representations provides for a multiresolution analysis.

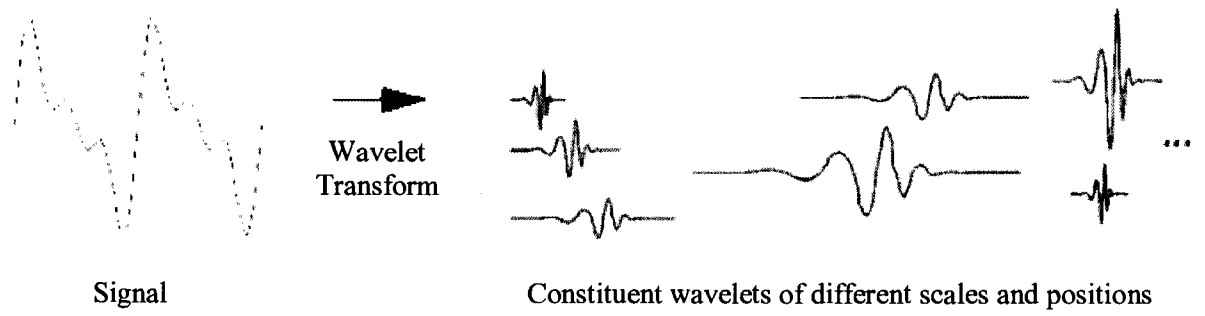

Figure 2.7: Wavelet Transform

The continuous wavelet transform is provided by the equation:

$$X_{WT}(\tau, s) = \frac{1}{\sqrt{|s|}} \int x(t) \cdot \psi^* \left(\frac{t-\tau}{s} \right) dt \qquad (2.5)$$

where $x(t)$ is the signal to be analyzed, and $\psi(t)$ is the mother wavelet or the basis function.

The mother wavelet used to generate all the basis functions is designed based on some desired characteristics associated with that function. The translation parameter τ relates to the location of the wavelet function as it is shifted through the signal. Thus, it corresponds to the time information in the wavelet transform. The scale parameter s is defined as |1/frequency| and corresponds to frequency information. Scaling either dilates (expands) or compresses a signal. Large scales (low frequencies) dilate the signal and provide detailed information hidden in the signal, while small scales (high frequencies) compress the signal and provide global information about the signal. As a result, the wavelet transform simply performs the convolution operation of the signal and the basis function.

2.2.1.1 Haar's Wavelet

A Hungarian mathematician by the name of Alfred Haar (1910) discovered the first wavelet with orthogonal properties in 1910. In recent years the Haar theory has been improved and applied to various fields in engineering and science (Hsiao, 2004). The Haar wavelet is simply a step

function (Figure 2.8); nevertheless, it forms an orthonormal wavelet basis, and due to its simplicity and place in history, it has become the standard example used in introducing wavelets.

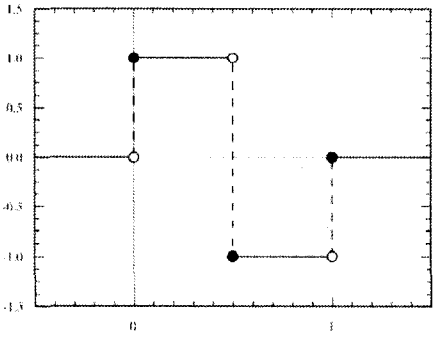

Figure 2.8: Haar Wavelet Function

This wavelet uses a process called averaging and differencing. For example, take a data sample of a string of numbers, which might represent the first row of an 8x8 pixel image or even the functional values of a discrete signal:

12	20	16	28	32	32	22	14

These numbers are grouped into pairs of two adjacent numbers, where pair one will be (12, 20), pair two will be (16, 28), and so on. First the average of the numbers in each pair is taken and the four resulting averages are placed at the beginning of a new row. Then the difference of the numbers is taken; the two numbers are subtracted and divided by two. The differences, known as the detail elements, are placed on the same row after the averages.

12	20	16	28	32	32	22	14
16	22	32	18	-4	-6	0	4
19	25	-3	7	-4	-6	0	4
22	-3	-3	7	-4	-6	0	4

Thus, the first four numbers in the second row are the averages and the last four are the detail elements. This process is repeated on the averages until there is only one average left. Detail elements are carried down from the above row and the new differences are placed in front of the old ones. Since there are eight numbers in the above sample, the process of averaging and

differencing will occur three times because $8 = 2^3$. The bottom row represents the transformed data sample. In the transformed row, there is one average and seven detail elements. This is how the process works on one-dimensional data. For two-dimensional data, such as an image matrix, the transform is performed on each row and each column of the matrix. This is equivalent to performing averaging and differencing on each row then performing the process on each row of the transpose of the row-transformed matrix (Fontenot, 2001).

2.2.1.2 The Discrete Wavelet Transform (DWT)

The discrete wavelet transform (DWT) is a linear transformation that operates on a data vector whose length is an integer power of two, transforming it into a numerically different vector of the same length. In this approach, the mother wavelet is scaled and dilated in discrete steps (Kociolek et al., 2001). For a two-dimensional digital image, Haar's discrete wavelet transform is applied to the pixel values in each row, and then in each column, thus decomposing an image into low frequency and high frequency components.

The Haar wavelet can be described as $f(x)$ where:

$$f(x) = \begin{cases} 1 & 0 \leq x < 1/2, \\ -1 & 1/2 \leq x < 1, \\ 0 & \text{otherwise.} \end{cases} \qquad (2.6)$$

The DWT scales, or decomposes an image into one low-resolution image (LL_1), which corresponds to coarse-scale coefficients, and three detail images (LH_1, HL_1 and HH_1), which represent the fine-scale coefficients, thus producing a set of four sub-band images, as in Figure 2.9(a). The process iteratively blurs the original image, eliminating fine texture details while retaining the coarse texture details, to obtain the low-resolution image; the three detailed images contain the information lost during this process. Every sub-image can be sampled by a factor of 2, hereby retaining the possibility of a complete reconstruction. This leads to a representation with an equal amount of pixels as the original image (Livens et al., 1997).

The low-resolution image can further be decomposed into the next level of low-resolution and detailed images. Therefore, depending on the number of resolution steps required l, $1+3l$ sub-band images will be produced, resulting in a multi-level decomposition as shown in Figure

2.9(b). The LL image results from a low-low-pass filter, the LH image from a low-high-pass filter, the HL image from a high-low-pass filter, and the HH image from a high-high-pass filter. In a pyramidal decomposition, only the low-resolution image (LL) is further decomposed. This allows for the analysis of texture at different scales, known as multi-resolution analysis (Mallat, 1989).

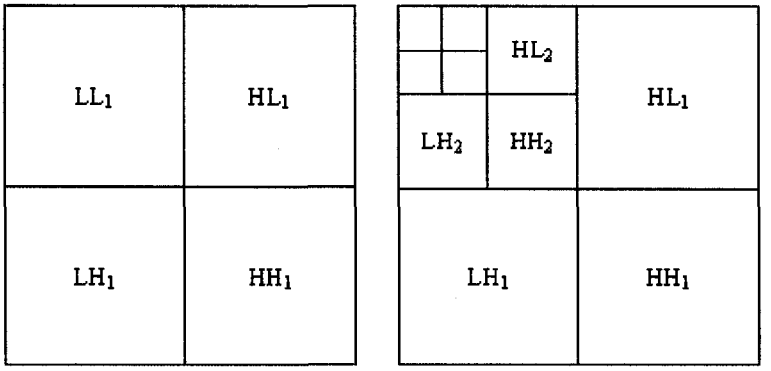

(a) One-level **(b) Multi-level**

Figure 2.9: A Pyramidal Wavelet Decomposition

Among the advantages of DWT when applied to image processing, are the similarities of the data structure with respect to the resolution, where the higher resolution images include the lower resolution images, and the possibility of decomposition at any level. This approach can be especially useful when applied to remote sensing data, such as radar and IR thermographic images, when analysis is to be carried out on coarse textures of the image using a low resolution level, or in detail on the fine textures of the image using an appropriate higher resolution level. The transform separates the fine and coarse textures, which aid in their analysis.

When the detail images are also decomposed further, we obtain the tree-structured or wavelet packet decomposition. Figure 2.10 shows the scheme for the tree-structured decomposition. It is significant due to the manner in which it connects the continuous-time multiresolution to discrete-time filters. In the figure, the signal is denoted by the sequence x[n], where n is an integer. The low-pass filter is denoted by G_0 while the high-pass filter is denoted by H_0. At each level, the high pass filter produces detail information; d[n], while the low pass filter associated with scaling function produces coarse approximations, a[n].

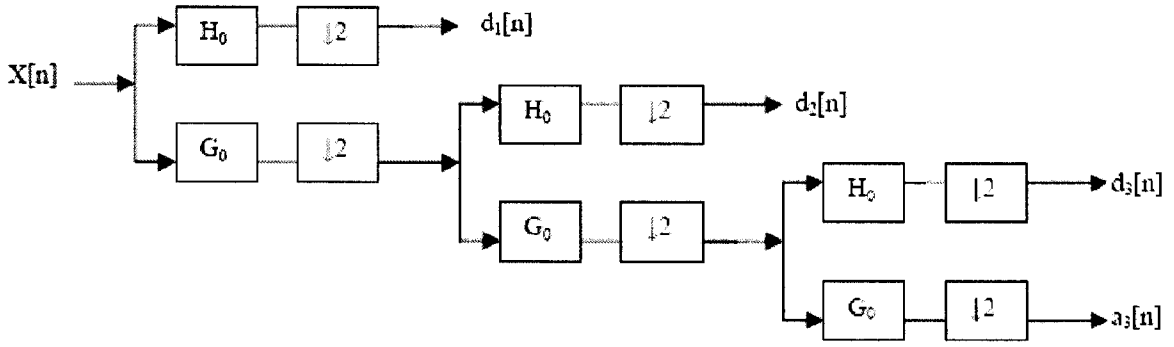

Figure 2.10: Three-level Wavelet Tree-structured Decomposition

2.2.1.3 Wavelet Reconstruction

The process, by which the discrete wavelet transform breaks down and separates signals and images into components of successively smaller resolutions, is known as decomposition or analysis. The procedure where the components are assembled back into the original signal, without loss of information, is called reconstruction, or synthesis. The mathematical manipulation that results in synthesis is called the inverse discrete wavelet transform (IDWT). Basically, the reconstruction is the reverse process of decomposition (Figure 2.11). The approximation and detail coefficients at every level are upsampled by two, passed through the low-pass and high-pass synthesis filters and then added. This process is continued until a resolution is obtained at which the texture of interest is isolated, or it can continue through the same number of levels as in the decomposition process to obtain the original signal.

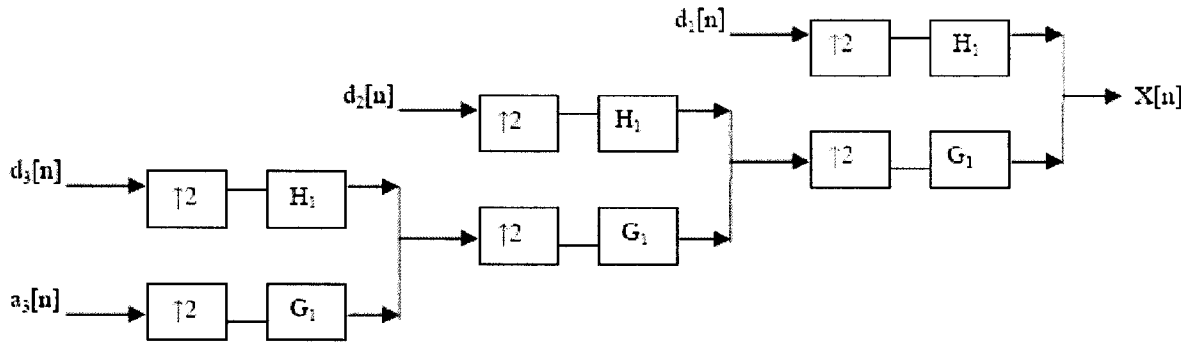

Figure 2.11: Three-level Tree Reconstruction

2.3 Spatial Image Filters

Spatial filters are area operators that create new map values as a function of values of existing neighbouring pixels. Spatial filtering is used to enhance images by applying filter functions in the image space. Filters suppress or de-emphasize certain image frequencies and pass or emphasize others. The emphasized frequencies are combined into an enhanced image. The filters usually summarize the original classified image using a moving window or kernel. According to the size of the kernel, the window scans the neighbourhood of each pixel in the classified image. Depending on the type of kernel, a value is computed for each pixel based on its neighbourhood, which is then used to create the output image.

2.3.1 Lowpass Filter

Filters that pass low frequencies are called lowpass filters. They suppress high frequencies, which correspond to fine details, such as speckle, known as salt and pepper noise in an image. Lowpass filtering reduces deviations in the image from local averages by replacing the original values with their local averages, thus smoothing the grey level values of the original image. The larger the size of the kernel employed, the more drastic the smoothing is.

2.3.2 Median Filter

Median filters are a group of filters based on ranking pixel grey-values. They smooth an image while preserving edges larger than the kernel size by replacing each centre pixel with the median value found within the neighbourhood of the filter. These filters are good at eliminating impulsive noise, such as salt and pepper noise or speckle, while preserving edge data. The usual square median filter eliminates fine vertical or horizontal lines; this can be overcome through the use of a cross-shaped mask.

2.3.3 Edge-detectors

Edge-detection is an important area of research in the field of image processing and computer vision. Edges are considered to be areas with strong intensity contrasts, causing a jump in intensity from one pixel to the next. The goal of edge-detection is to identify the points in a digital image at which the luminous intensity changes sharply. Detecting edges significantly reduces the amount of data, filtering out useless information, while preserving the important structural properties of the image.

For example, consider the detection of an edge to be one-dimensional; take a data sample of a string of numbers, which may be a single line of pixel intensities. It appears that there should be an edge between the 4th and 5th pixels in the following one-dimensional data:

5 7 6 4 152 148 149

However, a specific threshold must be selected concerning how large the intensity change must be between two neighbouring pixels in order to state that there is an edge between the two. As a result, this is one of the factors that can make detecting edges quite difficult, unless the objects in the scene are particularly simple and the illumination conditions can be easily controlled.

Based on the concept that an edge is characterized by a change in intensity over a number of pixels, edge-detection algorithms generally calculate a derivative of this intensity change. Most approaches may be grouped into two categories: gradient (first-order) and Laplacian (second-order). The gradient methods detect edges by searching for the maximum and minimum in the

first derivative of the image (Hutchinson and Chen, 2006). Gradient methods comprise such approaches as the Canny, Prewitt, Roberts, and Sobel operators. Laplacian methods look for zero-crossings in the second derivative of the image to find edges (Laws, 1980). A frequently employed Laplacian operator is the Marr-Hildreth approach.

2.3.3.1 Roberts Operator

The Roberts edge-detection algorithm (Roberts, 1965) is one of the earliest operators used in computer vision. This gradient technique works by computing the sum of the squares of the differences in intensity between diagonally adjacent pixels. This can be accomplished by convolving the image with two 2x2 kernels, which provide a simple approximation to the gradient magnitude:

+1	0
0	-1

0	+1
-1	0

Computations, though, are carried out at an interpolated point; consequently, the Roberts operator is an approximation to the continuous gradient at this interpolated point and not at an actual point. However, it is a useful technique and is still in use due to the speed of its computations.

2.3.3.2 Sobel Edge-Detector

Another gradient method of edge-detection is the Sobel algorithm (Parker, 1997; Davis, 1975). This is a discrete differentiation operator, computing an approximation of the gradient of the image intensity function. At each point in the image, the result of the Sobel operator is either the corresponding gradient vector or the norm of this vector. It uses intensity values in a 3x3 region around each image point to approximate the corresponding image gradient and integer values for the coefficients, which weight the image intensities to produce the gradient approximation. The 3x3 kernels are as follows:

1	2	1
0	0	0
-1	-2	-1

-1	0	1
-2	0	2
-1	0	1

2.3.3.3 Marr-Hildreth Algorithm

The Marr-Hildreth edge-detection method (Marr and Hildreth, 1980) is also known as the Laplacian edge-detector. This simple technique operates by convolving the image with the Laplacian of the Gaussian function, or, as a fast approximation by Difference of Gaussians. Then, zero-crossings are detected in the filtered result to obtain the edges. The Laplacian of the Gaussian operator is sometimes also referred to as the Mexican hat wavelet due to its visual shape when turned up side down.

2.3.4 Directional Filter

Other edge enhancement filters that selectively enhance image features having specific direction components are directional filters. The sum of the directional filter kernel elements is zero; the result is that areas with uniform pixel values are zeroed in the output image, while those that are variable are presented as bright edges.

2.4 Image Classification

Image classification is used to improve the qualitative visual analysis of image data with a quantitative analysis through automated identification of features in a digital image. This is desired because of the fact that a computer can analyse at the pixel level and can examine and identify as many pixels as needed, thus taking full account of the spatial and spectral details present (Schowengerdt, 1997). This type of image interpretation is considered a quantitative analysis due to its capacity to identify pixels based on their numerical properties and to provide area estimates by counting pixels (Jensen, 1996).

There are two general approaches to the classification process: supervised and unsupervised classification. Supervised classification is closely controlled by the image analyst and requires

extensive knowledge of the data and of the classes desired. The supervised artificial neural network is an example of a supervised classification technique. Unsupervised classification is more computer-automated and is dependent upon the data itself for the determination of the object classes; the analyst then identifies these classes after classification (Richards and Jia, 1999). A commonly employed unsupervised classification approach is the *K*-means clustering algorithm.

2.4.1 Artificial Neural Networks (ANNs)

Artificial neural networks are mathematical models originally designed to mimic aspects of how biological nervous systems, such as the brain, are believed to process information. These models grew out of research in Artificial Intelligence, where attempts were made to imitate the fault-tolerance and capacity to learn by modeling the low-level structure of the brain (Patterson, 1996). It is known that the human brain learns by experience, and so the neural network approach uses a non-algorithmic computing model, which is based on a process of learning from examples in order to store experiential knowledge to be used for specific tasks (Haykin, 1999).

ANNs appear to be a recent development; however, this field was established before the advent of computers. The first model of artificial neurons was developed in 1943 by the neurophysiologist Warren McCulloch and the logician Walter Pitts, based on their understanding of neurology. In 1958, Frank Rosenblatt (1958) produced considerable interest and activity in the field when he designed the Perceptron. This model had three layers, with the middle layer known as the association layer. This system was capable of learning to connect or associate a given input to a random output unit. However, it was not until the early 1980s that the field of ANNs saw some significant progress as research interest increased with the recognition of its application potential (Bishop, 1995). In recent years, ANNs have become a popular alternative to traditional statistical classification methods and have been successfully used in a variety of fields. There are about thirty different ANN models that have been developed, of which the multi-layer perceptron (MLP) is the most popular (Sarle, 1994).

2.4.1.1 The Multi-layer Perceptron (MLP)

The multi-layer perceptron network is a popular supervised ANN classification approach. The MLP (Figure 2.12) is usually composed of three layers: an input layer, a hidden layer and an output layer. In the input layer, the number of nodes corresponds to the number of input features. The number of nodes in the output layer corresponds to the number of target classes. The number of hidden nodes, however, depends on the type of data. Usually, the more there are hidden nodes, the more complex a phenomena the network can model. If not enough hidden nodes are used, the network will not be trained sufficiently.

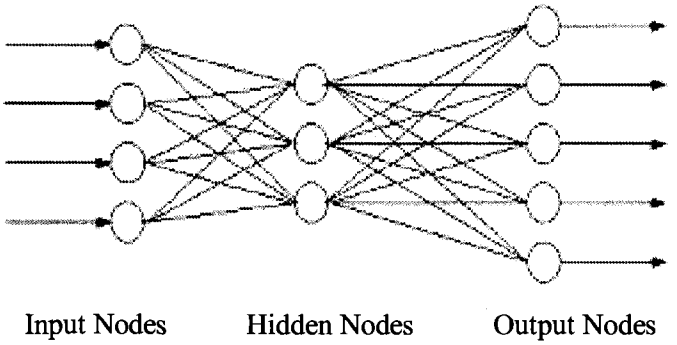

Figure 2.12: Example of an MLP Neural Network

If there are too many hidden nodes, the network will be over-trained; it will produce perfect results on training data but poor results on new data or testing data (Liu et al., 2003). As a result, the agreement or disagreement between the results of the training data and the testing data can serve as an indicator of the classification accuracy for various network set-ups (Lek and Guegan, 1999).

2.4.2 *K*-means Clustering Technique

Clustering techniques are unsupervised classification methods that are used to find natural similarities in data, in order to organize and group the data based on those similarities. Clustering approaches can be broadly divided into four groups: exclusive, overlapping, hierarchical and probabilistic techniques. The simplest of these are the exclusive clustering algorithms, which

group data in an exclusive way, so that if any data belongs to one cluster then it cannot be included in another cluster (Jain and Dubes, 1988). The *K*-means classifier is one such technique.

The *K*-means clustering algorithm is an iterative process that groups pixels into classes of interest that are defined by determining the optimal partitioning of pixels into a specified number of object classes (Figure 2.13). In general, the first step is to specify the number of classes or clusters, as well as a set of points for the centres of the clusters; these points are often chosen so that they are as far apart as possible. Then the algorithm assigns an arbitrary initial cluster vector. The second step classifies each pixel to the closest cluster. In the third step the new cluster mean vectors are calculated based on all the pixels in one cluster.

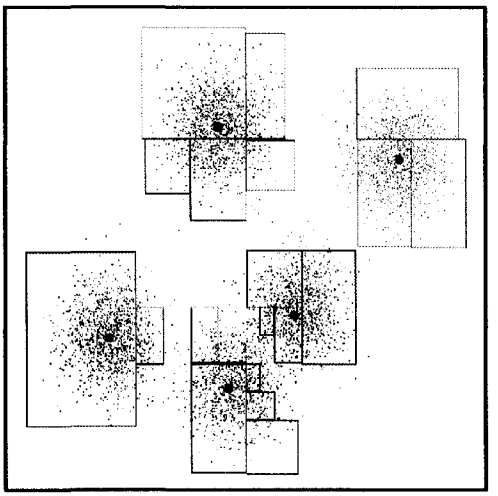

Figure 2.13: Example of *K*-means Clustering

The second and third steps are repeated until the data is classified into the predefined number of clusters and the change between the iteration is small. This change can be defined in several different ways: either by measuring the distances by which the mean cluster vectors have changed or by the percentage of pixels that have changed between iterations. The objective of the *K*-means algorithm is to minimize the variability within clusters and to maximize variability between clusters (Awcock and Thomas, 1996).

In order to accomplish this, the algorithm aims at minimizing the objective function, also referred to as the squared error function. The objective function is the sum of squares of distances between each pixel and its assigned cluster center. What this basically does is to find

the square of the Euclidian distance of each data point from the centre of its currently assigned cluster. The number derived from there is summed with all the other distances, as shown in Figure 2.14.

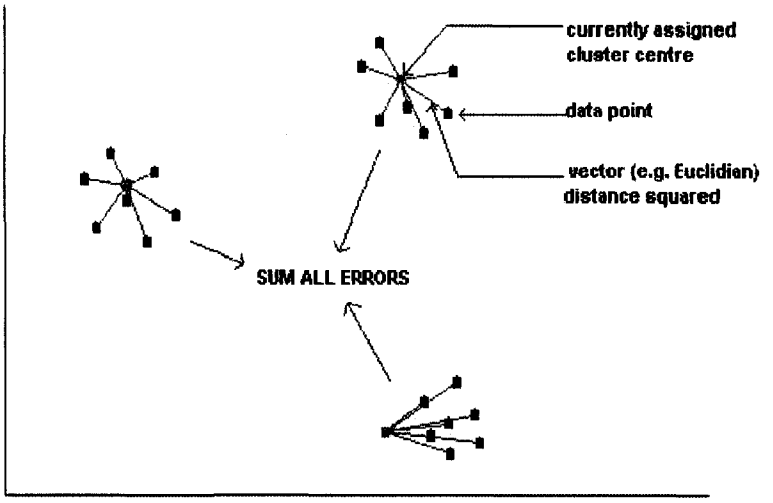

Figure 2.14: Example of *K*-means Clustering Algorithm

That sum is defined as the sum of squares, and is given by the following equation:

$$SS_{\text{distances}} = \sum_{\forall x} [x - C(x)]^2 \tag{2.7}$$

where $C(x)$ is the mean of the cluster that pixel x is assigned to. Minimizing the distances is equivalent to minimizing the Mean Squared Error (MSE). The MSE is a measure of the within cluster variability:

$$MSE = \frac{\sum_{\forall x} [x - C(x)]^2}{(N-c)b} = \frac{SS_{\text{distances}}}{(N-c)b} \tag{2.8}$$

where N is the number of pixels, c indicates the number of clusters, and b is the number of spectral bands. The main advantages of this algorithm are its simplicity and speed, which allows it to run on large datasets. Since the algorithm is extremely fast, a common method to obtaining better results is to run the algorithm several times and return the best clustering found.

2.4.3 Classification Precision: the Kappa Coefficient

The final step of the classification process is the evaluation of the precision of the results. This indicates how well the classification performed and whether or not the objectives have been achieved. One of the most common methods of expressing classification accuracy is the preparation of a classification error matrix, also known as the confusion matrix. The error matrix compares the relationship between known reference data, obtained from verification sites selected from the imagery, and the corresponding results of the classification.

Once the image is classified into different objects classes, each pixel in the verification sites is compared with the label of the class that represents it in the classified spectral space. The overall result of this process is presented in the form of a confusion matrix (Richards and Jia, 1999). From this matrix many classification precision indexes can be calculated. In a comparative study done on the different methods of evaluating the classification accuracy, it was found that the most appropriate index to provide an exact classification precision is the Kappa coefficient, because it takes account of all the elements of the confusion matrix (Fung and Ledrew, 1988).

Kappa Coefficient

$$\kappa = \frac{N\sum_{k} x_{kk} - \sum_{k} x_{k\Sigma} x_{\Sigma k}}{N^2 - \sum_{k} x_{k\Sigma} x_{\Sigma k}} \qquad (2.9)$$

where Σ is the sum over all rows in the matrix, xkk is the total of marginal rows, xk is the total of marginal columns, and N is the number of observations.

2.4.4 Post Classification

After performing the classifications, the resulting data can be manipulated in order to derive further information, to highlight certain aspects of the results or to improve the appearance of the classified image. There are various ways to further process the results, such as manually editing the classification, converting classified images into binary images, improving the classification

using auxiliary data, or filtering and smoothing the classification when there is high spectral variability in the original classification results.

In order to smooth out the classified image, kernal filters can be employed to reduce the number of spurious pixels in the image. There are many standard kernel operators, of which some are: maximum, minimum, majority, minority, mean, median, mode, standard deviation, and diversity. The majority analysis kernel operator changes spurious pixels within a large single class by selecting a kernel size; the centre pixel in the kernel is replaced with the class value of the majority of the pixels in that kernel. Larger kernel sizes produce more smoothing of the classified image.

2.5 Concrete Deterioration

There are many factors that contribute to the deterioration of concrete. Mechanical stress and fatigue, and chemical and environmental conditions are among the major causes of concrete distress. Environmental conditions, such as freeze and thaw cycles, winter de-icing, and water intrusion, in turn lead to other factors such as the alkali-aggregate reaction (AAR) and the corrosion of steel reinforcement. However, water is at the heart of most of these physical and chemical factors (Mehta et al. 1992). Moisture levels in the concrete determine the risk of corrosion attack occurring on cast-in steel and reinforcement. The amount of moisture also controls the rate of harmful mechanisms such as AAR.

When a structure is newly taken into service, there may already be damage, which can be attributed to unsatisfactory construction practices. Cracks in the concrete, which is one of the major types of deterioration, can exist even before the structure is subjected to any external loading. An excessive water-cement ratio, improper curing, and creation of high temperatures during the hardening process, may result in shrinkage, which is the direct cause of cracking. Those cracks, which exist in concrete at early stages, later expand and widen during service conditions after hardening. This deterioration is further accelerated by weathering factors, such as freeze and thaw cycles, the intrusion of water, and the corrosion of steel reinforcement, which ultimately lead to the fracture of concrete due to excessive tensile stress (Rhim, 2001). Thus,

poor construction, combined with environmental conditions, usually lead to reduced durability and service life of the concrete structure, which may manifest itself years later.

2.5.1 Alkali-Aggregate Reactions (AAR)

The most common type of concrete damage is cracking. Map-like surface cracking may indicate an adverse reaction between cementitious alkalis and aggregates. This reaction, known as the alkali-aggregate reaction (AAR) is a potentially harmful process in concrete containing reactive aggregates, and can lead to varying degrees of cracking in structures, as well as differential movement and misalignment of concrete elements and mechanical installations (Fournier and Bérubé, 2000). Structural problems related to AAR have been detected in concrete structures since the beginning of the 20th century, but it was not before the 1940s that it was first identified (Stark, 1995). Subsequently, AAR has been recognized in more than 50 countries around the world; it is likely that the problems associated with AAR exist in a larger number of countries, but concrete distress in several instances may have been attributed to other causes. AAR has been determined to be one of the most common causes of concrete deterioration in Eastern Canada (Rivard et al., 2000).

AAR is a form of chemical reaction in concrete, which occurs between alkali-reactive constituents present in the aggregates and sodium and potassium alkali hydroxides released from Portland cement, or from other sources, in the pore water of the concrete. The reaction involves two phases: the production of a hygroscopic gel, and, in the presence of moisture, the absorption of water by the gel and its expansion. If there is enough void space to accommodate the gel, such as pores and cracks, then the concrete volume remains unchanged. However, the reaction is potentially harmful when the swelling gel expands significantly, causing tensile stress and ultimately cracking in the concrete, which often results in a "map pattern" of cracks on the concrete surface (Figure 2.15). Therefore, gel secretion, swelling, and surface map-cracking in concrete are often associated with AAR development. The consequences of AAR, apart from reduced durability due to cracking, are global swelling and expansion of concrete leading to severe operational problems (Capra and Sellier, 2001).

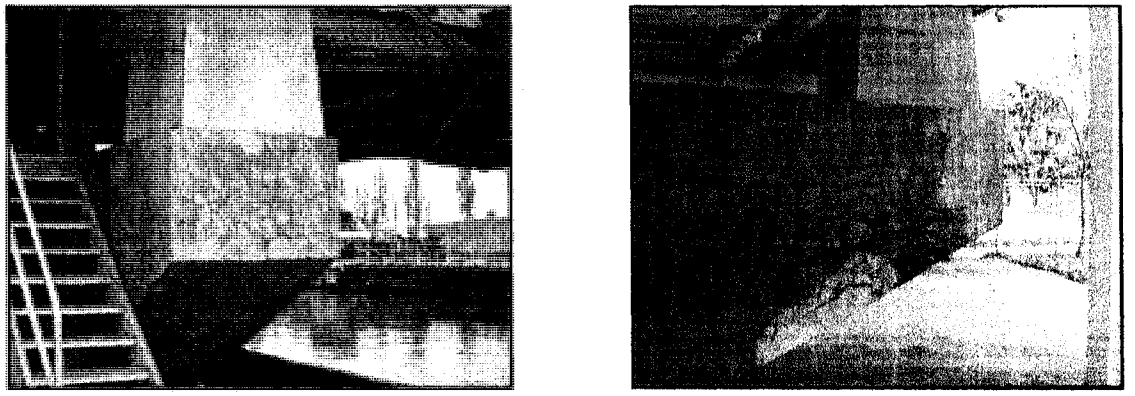

Figure 2.15: AAR-Induced Map-cracking in Components at St. Lambert Lock

Any kind of structure can be affected by AAR; however, most of the structures that are severely distressed are exposed to extreme weather, or are underground in contact with damp soil, where a sufficient amount of moisture is available for significant expansion to occur. Also, structures in direct contact with water, such as dams, locks, and bridges, are particularly susceptible to AAR. Over 104 cases of alkali-aggregate reaction in dams and spillways have been reported around the world.

AAR can cause significant damage to concrete structures, which can be costly to rectify (IRC, 2003). The swelling of the gel produced as a result of the reaction can generate excessive tensile stress in the concrete, leading to slow but progressive expansion, and internal and external cracking, which can result in a decrease in structural safety (Bakker and Postema, 2003), as well as serious operational and serviceability problems. Indications of the presence of harmful alkali-aggregate reactivity may be in the form of a complex network of micro-cracks within the affected concrete element, as well as macro-cracks at the surface that develop in a map-like pattern influenced by the presence of restraint and reinforcement (Figure 2.16). Other typical signs of AAR are closed or spalling joints, relative displacement of different portions of a structure, or fragments breaking out of the surface of the concrete, known as pop-outs.

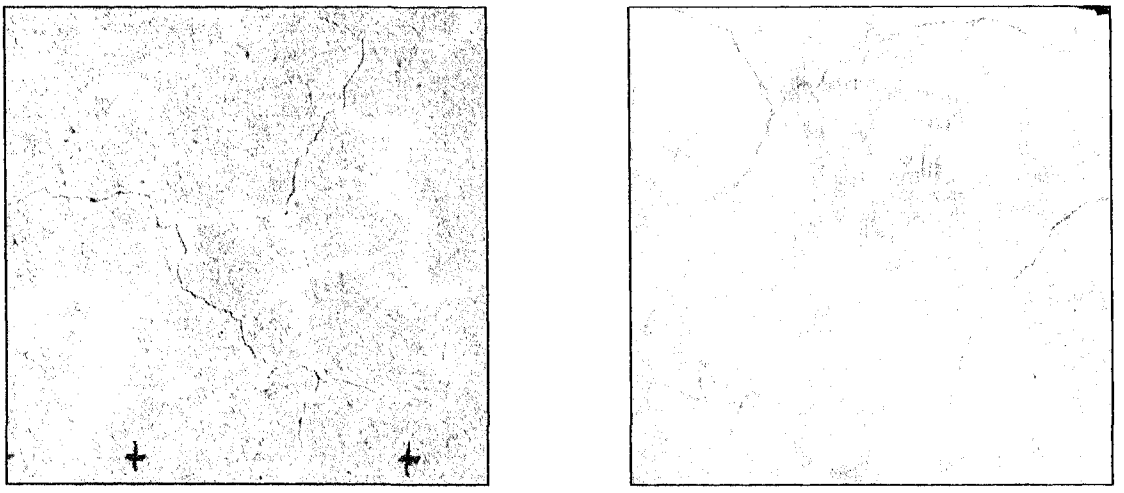

(a) CANMET Specimen **(b) GRAI Specimen**

Figure 2.16: CANMET and GRAI Specimens Exhibiting AAR cracking

Because deterioration due to alkali-aggregate reaction is a slow process, the risk of catastrophic failure is low. In fact, in Canada, much of the concrete made with reactive aggregates remains in service. However, concrete affected by the alkali-aggregate reaction can cause serviceability problems and aggravate other deterioration mechanisms, such as those that occur in frost, de-icing, or sulphate exposures. Consequently, bridges designed for 100 years of service are exhibiting concrete cracking due to AAR just seven years after construction.

2.5.2 Steel Corrosion

Corrosion of reinforcing steel in concrete is a growing international problem. Many studies have identified steel corrosion as one of the main degradation mechanisms in concrete highway bridges and parking decks, especially in maritime areas and places where de-icing salts are used during the winter season. The cost of corrosion damage caused by de-icing and sea salt on highway bridges was estimated at over $150 billion in the U.S. (Broomfield, 1997). In Canada, 50% of the estimated 70 000 bridges have an average age of between 30 and 45 years, and are in need of major rehabilitation and/or total replacement (Carter, 1999) due to corrosion distress.

The environment provided by good quality concrete to steel reinforcement is one of high alkalinity due to the presence of the hydroxides of sodium, potassium and calcium produced

during the hydration reactions. The bulk of surrounding concrete acts as a physical barrier to many of the steel's aggressors. In such an environment steel is passive and any small breaks in its protective oxide film are soon repaired. If the alkalinity of its surroundings is reduced, however, such as by neutralisation with atmospheric carbon dioxide, or by depassivating anions, such as chloride, which are able to reach the steel, then severe corrosion of the reinforcement can occur. The permeability of the concrete is important in determining the extent to which aggressive external substances can attack the steel.

Corrosion occurs when reinforcing steel that has been placed too close to the surface of the concrete, or that has been exposed by spalling, erosion, or cracking, oxidizes in the presence of moisture that is rich in salt. It is an electrochemical process that involves the transfer of electrically charged ions between two areas of the reinforcing steel surface with different potentials (anode and cathode) through the concrete pore solution, which serves as an electrolyte. The corrosion rate of the steel reinforcement depends on the ease with which the ions participating in the electrochemical process can flow. Various factors such as electrical resistivity of the concrete, electrochemical potential of the cathodic area, and the ratio of cathodic area to anodic area, control the flow of the electrically charged ions in the concrete (Ismail and Soleymani, 2002). The electrons produced during this process are conducted through the metal, while the ions that are formed are transported via the pore water.

Corrosion can damage or reduce the serviceability of concrete structures in several ways. Firstly, corrosion produces expansive products that generate tensile stress in the concrete surrounding the reinforcing steel, which may cause the concrete to crack (Figure 2.17). Secondly, corrosion products are highly porous, weak, and often form around steel reinforcement, reducing its cross-sectional area and decreasing the bond strength between the reinforcing steel and the concrete (Wang and Monteiro, 1997), which in turn can result in staining of the concrete by rust, and a decrease in the ultimate load bearing capacity and flexibility of the structure (Ismail and Soleymani, 2002). With the progress of corrosion, the corrosion product grows in size and applies increasing mechanical forces to the surrounding concrete that eventually cracks. Further corrosion causes these cracks to propagate followed by spalling and delamination of concrete cover due to the increase in volume associated with the conversion of iron to iron oxide.

Figure 2.17: Corrosion Damage in Component of Jacques-Cartier Bridge

2.5.3 Freeze-Thaw Cycles

The most destructive weathering factor in concrete deterioration is the freeze-thaw cycles that are typical of the climate in northern areas. In Canada, changing temperatures have a significant effect on the condition of road networks; each year, Canada invests $17 billion in transportation infrastructure, and it is estimated that $1.7 billion of this is spent adapting to current climate conditions (Andrey and Mills, 2003). Temperature differences and increased frequencies of freeze-thaw cycles are related to premature deterioration of pavement structures (Schmidlin et al., 1999), resulting in increased surface roughness (Haas et al., 1994), as well as a loss of pavement strength (Croney and Croney, 1999).

Deterioration of concrete from freeze-thaw actions occurs when significant saturation of the concrete causes internal tensile stress. Although any concrete infrastructure may be susceptible to freeze-thaw distress, those that are particularly affected are highways and bridge decks, airport pavements, dams, locks, and other hydraulic structures. It may be difficult to diagnose deterioration of concrete due to freeze-thaw actions because other types of deterioration mechanisms, such as AAR, often go hand in hand with freezing and thawing. However, the typical signs of freeze-thaw damage are evident in the form of scaling of the concrete surface, spalling or popping-out of large chunks of concrete, sub-parallel cracks or severe cracking on the exposed concrete surface, known as durability cracking, and internal damages in the form of

exposure of usually un-cracked aggregates, gaps around aggregates, and deterioration commonly initiating at joints and free edges where moisture is more readily available.

Concrete is critically saturated when approximately 71% of its pores, the paste, the aggregate particles, or all three, are filled with water. When water freezes to ice, it occupies 7% more volume than that of water. As ice forms in the pore system, the resulting volume expansion causes the surrounding unfrozen water to be expelled from the freezing sites. Depending on the nature of the pore system, excessive internal stresses can develop from hydraulic pressures that result due to resistance to this flow (Powers, 1975).

More recent theories consider osmotic potential to be the primary cause of excess internal stress. As pure water in the larger pores freeze, the liquid remaining in the pores becomes a more concentrated ionic solution. To maintain thermodynamic equilibrium, the less concentrated solution in the surrounding paste is drawn to the freezing sites. If adequate air void space is available, all of the freezable water will eventually diffuse to the freezing sites inside the air voids, reaching a state of equilibrium. If the air void space is inadequate, equilibrium cannot be reached and osmotic pressures sufficient to fracture the paste can result (Powers, 1975). The most widely accepted theories consider the development of internal tensile stress as a result of hydraulic pressures, osmotic pressures, or a combination of the two during freezing (U.S. Department of Transportation, 2003).

2.5.3.1 Concrete Scaling

The process of compacting and finishing concrete produces a rich layer of cement paste, mortar or concrete at the surface. Scaling occurs when portions of this surface layer break away, causing delamination of the concrete surface. The primary mechanisms of this type of concrete distress are high thermal strains, which are produced when salts from de-icing chemicals intrude into the concrete or high osmotic pressures, which are induced when relatively pure surface water attempts to equalize highly concentrated salt solutions present in the concrete during freeze-thaw cycles (Mindess and Young, 1991; Pigeon and Pleau, 1995). The layer may become detached if the stresses occurring exceed the tensile or bond strength holding the layer to the substrate. As a result, the concrete manifests flaking or peeling away of the surface layer of the concrete or mortar, causing a loss of fine aggregate; more extensive scaling can result in the loss of larger

aggregate. In severe cases, scaling can lead to deterioration that extends deep into the concrete. Successive freeze-thaw cycles during the winter seasons usually result in repeated loss of concrete surface (see Figure 2.18).

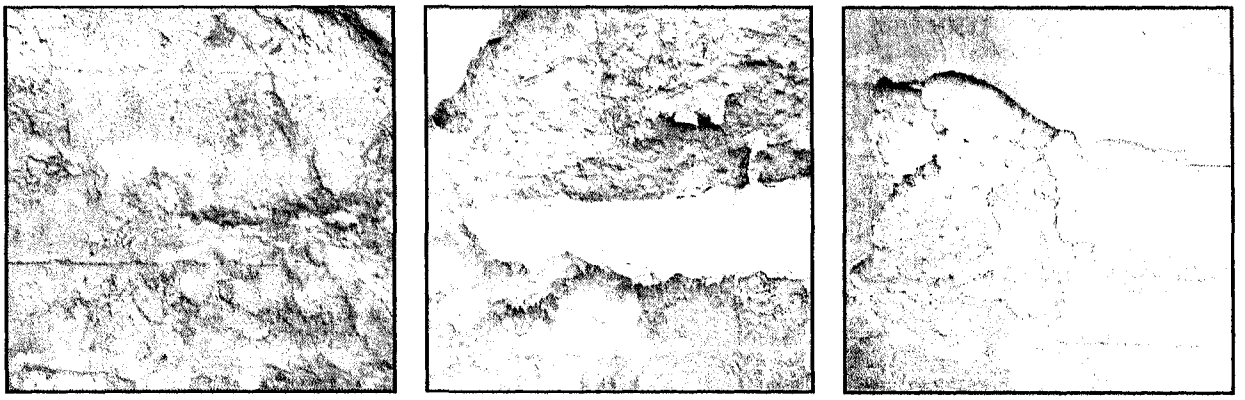

Figure 2.18: Occurrence of Scaling in Components of Train Bridge

Scaling can take place as a general condition over a large area or be isolated to locations of high water or air content near the surface. It may not even be apparent until other stresses, such as traffic and grinding action, break the detached layer into fragments, especially in the wheel paths, removing surface concrete.

2.5.3.2 Concrete Spalling

Spalling is the loss of large pieces of concrete of various sizes, and is typically caused by stress in the concrete that exceeds the design capacity, such as when expansive forces within the concrete and near the surface of the concrete act along a weak plane or create a weakened plane. Expansive forces can be caused by the stress of corrosion of reinforcing steel or imbedded metal items, where the corroded steel bars expand and exert a force on the surrounding concrete causing the concrete to bulge and crack, and ultimately lose a chunk of concrete, as seen in Figure 2.19.

Figure 2.19: Spalling Exhibited in Component of Jacques-Cartier Bridge

Internal expansion can also be caused by moisture absorbed by porous aggregates or by moisture trapped inside the matrix of the concrete by paints or sealants that do not allow moisture to migrate and escape at the surface; this moisture expands and contracts during freeze-thaw cycles. Spalling can also occur due to a condition called laitance where concrete, during placement, was mixed too wet and cement rich paste rises to the surface of the concrete thereby depriving other portions of the mix of cement-related cohesion and consolidation.

Spalling can result in the loss of a piece of the concrete pavement from the surface or along the edges of cracks and joints, and may be limited to small pieces in isolated areas or be quite deep and extensive. Corrosion of steel reinforcement can produce a large amount spalling on highway bridge decks. The spalling reduces the riding quality of the bridge and may affect the reliability of the structure. If a spall is large and causes structural damage, then repair or rehabilitation may be required in order to keep the structure in service.

2.5.3.3 Aggregate Popouts

When spalling occurs on a smaller scale, the resulting damages are known as popouts. A popout is a small volume of concrete, which has separated from the main body of the concrete leaving a roughly conical depression. Concrete popouts are generally caused by aggregate particles, near

the surface of the concrete, that absorb so much water they become critically saturated and cannot accommodate the expansion and hydraulic pressure that occurs during the freezing of water.

The stress is relieved through cracking of the particle and simultaneous bursting of the concrete between the particle and the nearest concrete surface. The offending aggregate particles are often coarse with high porosity values and medium-sized pores, between 0.1 to 5 mm, that are easily saturated. Larger pores do not normally become saturated or cause concrete distress, and water in very fine pores may not freeze readily.

Popouts usually do not exceed 50 mm diameter and 15 mm depth, consisting of the top of the aggregate and surrounding mortar that break out of the concrete surface, creating a shallow depression; examples of this can be seen in Figure 2.20. When a popout is reasonably flat at the bottom, and does not contain a fragment of the coarse aggregate, it is more likely to be an example of scaling. Popouts are typically not a structural problem, but they are unattractive and can be dangerous if they occur on walls, roads, highways and airport runways.

(a) Jacques-Cartier Bridge **(b) Terrill Bridge**

Figure 2.20: Examples of Popouts in Bridge Components

2.5.4 Erosion of Concrete Surfaces

Weathering of concrete surfaces by wind, rain, snow, or other mechanical action can cause surface loss. Temperature-related expansion and contraction of surface moisture exerts a

mechanical action and results in the gradual wearing away of the concrete surface, as in Figure 2.21. Exposed aggregates are particularly susceptible due to differences in the rates of expansion among the various constituent materials.

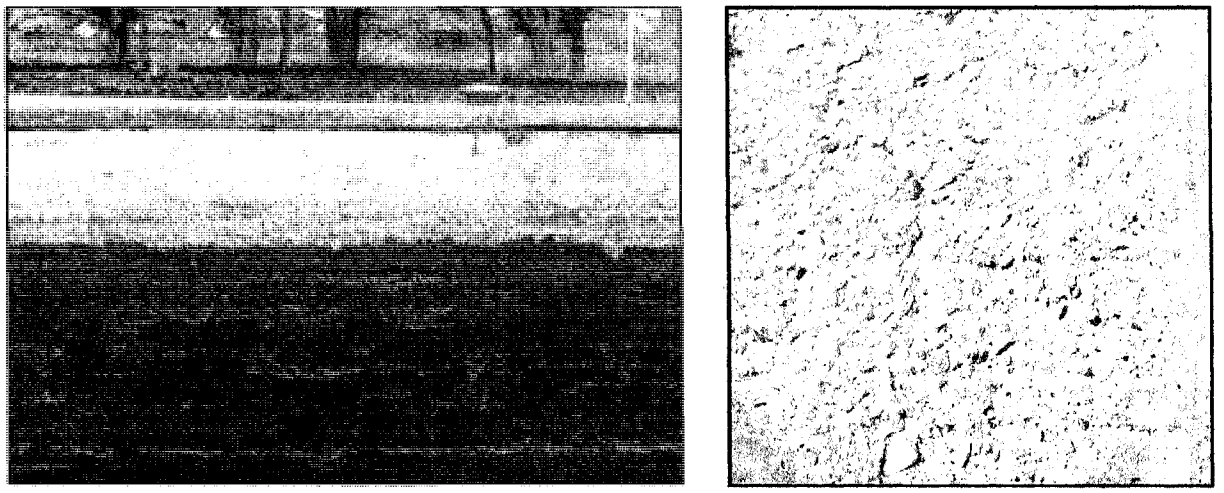

(a) St. Lambert Lock **(b) Train Bridge**

Figure 2.21: Examples of Concrete Erosion

Erosion due to abrasion results in a worn concrete surface. It is caused by the rubbing and grinding of aggregates or other debris on the concrete surface of a spillway channel or stilling basin. Cavitation is a process in which sub-atmospheric pressures, turbulent flow and impact energy are created, causing damage to the concrete. Erosion due to cavitation results in a rough pitted concrete surface; minor erosion is not a problem but severe erosion can jeopardize the structural integrity of the concrete (Ohio Department of Natural Resources Division of Water Fact Sheet, 1999).

2.5.5 Stains and Efflorescence

Stains on concrete surfaces may indicate internal problems such as corrosion or adverse chemical reactions. Corrosion usually involves reinforcing steel and the resulting stains are rust-colour. Alkali-aggregate reactions are usually seen as a white, crystallized substance, known as efflorescence. Moisture-related stains may appear as a variety of colors (see Figure 2.22).

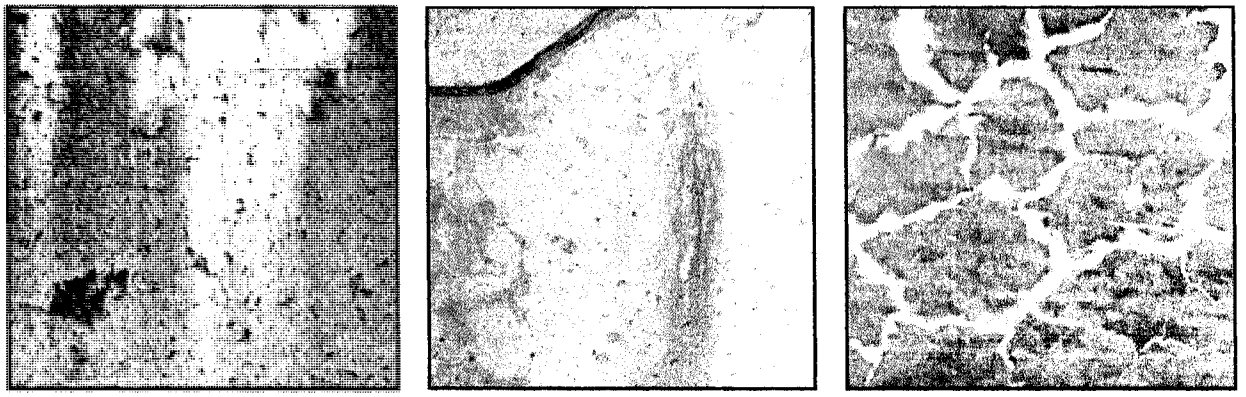

(a) Corrosion Stains **(b) Efflorescence Stains**

Figure 2.22: Examples of Stains

Efflorescence is formed by water seeping through the pores or thin cracks in the concrete. When the water evaporates, it leaves behind some minerals that have been leached from the soil, fill, or concrete. Efflorescence is typically not a structural problem. Efflorescence should be monitored because it can indicate the amount of seepage finding its way through thin cracks in the concrete and can signal areas where problems, such as inadequate drainage behind the wall or deterioration of concrete, could develop. Also, water seeping through thin cracks in the wall will make the concrete more susceptible to deterioration due to freezing and thawing of the water.

2.6 Non-Destructive Testing of Concrete

With the increasing concern about the aging and deteriorating condition of concrete infrastructures worldwide (Chong et al., 1990) accurate testing methods for evaluating the current condition of these structures are necessary in order to plan appropriate maintenance or repair procedures for the efficient allocation of resources (Scott et al., 2003). As such, trends are shifting away from the traditional destructive sampling of concrete for material analysis, towards the use of sophisticated non-destructive methods. The development of techniques, such as non-destructive testing of materials and state-of-repair assessments of concrete structures, has thus become a major subject of interest within the structural engineering community (Dérobert et al., 2002).

2.6.1 NDT Principles and Applications

Non-destructive testing (NDT) is a descriptive term used for the inspection of materials and components in such a way that allows them to be examined without changing or destroying their usefulness. For applications in concrete, they do not alter the concrete or impair the function of the structure. Although the development of NDT approaches for concrete began in the early 1930's, it has seen slow progress compared to methods such as those applied to metal, because concrete is an inherently more difficult material to test (Carino, 2003). The highly heterogeneous nature of concrete makes it very difficult to detect defects, such as voids, honeycombing, delaminations, cracks, etc., as well as to distinguish between flaws and naturally occurring inclusions. Thus, from an NDT perspective, it is still uncertain what to look for and how to see it.

Nevertheless, in recent years, there has been an increase in the use of NDT methods to detect defects and anomalies in various civil engineering structures (Clark et. al., 2003). NDT techniques used to inspect concrete and make assessments are constantly being improved and developed, particularly in an effort to maintain and rehabilitate deteriorating structures. Some NDT approaches that are currently being used in civil engineering applications are the acoustic method, seismic, ultrasonic, ground penetrating radar (GPR), and infrared (IR) thermography.

2.6.2 Concrete Imaging using NDT

2.6.2.1 Acoustic Techniques

The acoustic or stress wave NDT methods are generally based on the idea of stress (elastic) wave propagation in solids, where the presence of an internal defect interferes with the propagation of the sound waves. The presence of a flaw or anomaly can be inferred by analysing the response of the test object when it is subject to stress waves. The stress waves are usually generated by a mechanical impact on the surface of the test object, or by transmission of ultrasound waves into the test object using a transducer in contact with its surface. This produces a stress pulse that travels into the object along spherical wave fronts as compression (P) and shear (S) waves. At the same time, Rayleigh (R) waves, which are surface waves, travel away from the impact or transmission point. The P- and S-waves are reflected back by boundaries separating materials with different densities and elastic properties (internal interface) or external boundaries. The

reflected waves, or echoes, return to the surface, and cause displacements that are recorded by a receiving transducer, which is located adjacent to the point of impact or transmitting transducer (Carino, 2003).

Acoustic technology is especially well suited for sub-surface NDT applications, such as borehole imaging. Acoustic borehole scanner tools generate an image of the borehole wall by transmitting ultrasound pulses from a rotating sensor and recording the amplitude and travel time of the signals reflected at the interface between mud and formation of the borehole wall. This image is actually generated by software that takes the recorded signals and produces a three-dimensional image that resembles a real core. There are two ways of obtaining an image: using the travel time of the ultrasonic wave or the amplitude of the reflection. The data is displayed as an unrolled picture of the wall starting at 0° to 360°, at a resolution of less than 2 mm.

2.6.2.2 Infrared Thermography

Infrared (IR) thermography is a remote sensing method that is based on two principles: one is that a material with a temperature greater than absolute zero emits electromagnetic radiation, the wavelength of which depends on the temperature of the material; the other is that the presence of subsurface irregularities in a material interferes with the flow of heat due to the different rates of thermal conductivity and result in differences in surface temperature at the defective zones. The values of thermal conductivity coefficients for different materials are provided in Table 2.1 (Halliday and Resnik, 1978):

Table 2.1: Thermal Conductivity of Some Materials

Material	Thermal Conductivity (J/s·m·°C)
Steel	48
Ice	1.8
Concrete	0.8
Air	0.024

At about room temperature, the radiation is in the infrared region of the electromagnetic spectrum, between visible light and microwaves. Therefore, by measuring the surface temperature, the location of subsurface defects can be determined (Büyüköztürk, 1998).

In civil engineering, IR thermography is usually used to locate and determine the extent of voids, debonding, honeycombing, and corrosion-induced delaminations in reinforced concrete. It is a tool used in predictive maintenance and condition monitoring that can detect subsurface damage that is typically missed during visual inspections (Vavilov and Demin, 2002). Early applications of this technique were studied in the late 1970s using hand held scanners and photographic cameras to record the thermographic images. Later on, scanning was accomplished from a boom attached to a truck, and then from an airborne scanner onboard a helicopter (Clark et. al., 2003).

Measurement of the surface temperature of a test object is done during periods of relatively rapid heating or cooling to achieve the heat flow condition that is necessary to detect the differences in thermal conductivity within the material and locate the regions containing subsurface irregularities. This occurs naturally by solar heating and night-time cooling; thus the best time for infrared surveys is two to three hours after sunrise or sunset (Weil, 1995). The heat flow can also be created artificially through heating lamps, if necessary.

In general, IR thermography applications use an imaging infrared scanner, composed of an optical scanning device and a processing unit, which senses the emitted thermal radiation from the surface of the material, and produces a thermographic image of the temperature differences (Figure 8.2). This image is usually displayed on a monitor, and simultaneously recorded on videotape. A visual record of the test object can also be obtained, using a conventional video camera, for comparison with the infrared data (Weil and Rowe, 1998).

2.6.2.3 Greyscale Imagery

Greyscale images are typically composed of shades of grey, varying from black at the weakest intensity to white at the strongest, though in principle the samples could be displayed as shades of any colour, or even coded with various colours for different intensities. Greyscale images are distinct from black-and-white images, which, in the context of computer imaging, are images with only two colours, black and white; greyscale images have many shades of grey in between.

The reason for differentiating such images from any other sort of colour image is that less information needs to be provided for each pixel. In fact a grey colour is one in which the red, green and blue components all have equal intensity in RGB space, and so it is only necessary to specify a single intensity value for each pixel, as opposed to the three intensities needed to specify each pixel in a full colour image. Greyscale images intended for visual display are typically stored with 8 bits per sampled pixel, which allows 258 intensities, or shades, or levels of grey, to be recorded, usually on a non-linear scale. The accuracy provided by this format is barely sufficient to avoid visible banding artefacts, but very convenient for programming. If the greylevels are evenly spaced, however, then the difference between successive greylevels is significantly better than the greylevel resolving power of the human eye.

2.6.2.4 Colour Imagery

It is possible to construct practically all visible colours by combining the three primary colours red, green and blue, because the human eye has only three different colour receptors, each of them sensitive to one of the three colours. Different combinations in the stimulation of the receptors enable the human eye to distinguish approximately 350 000 colours. An RGB colour image is a multispectral image with one band for each colour, red, green and blue, thus producing a weighted combination of the three primary colours for each pixel.

A full 24-bit colour image contains one 8-bit value for each colour, thus being able to display 18 888 218 different colours. However, it is computationally expensive and often not necessary to use the full 24-bit image to store the colour for each pixel. Therefore, the colour for each pixel is often encoded in a single byte, resulting in an 8-bit colour image. The process of reducing the colour representation from 24-bits to 8-bits, known as colour quantization, restricts the number of possible colours to 258. However, there is normally no visible difference between a 24-colour image and the same image displayed with 8 bits.

As a result, colour images greatly increase natural vision capabilities in terms of colour perception. Since human vision is relatively poor at differentiating the brightness and colour features in the scene being viewed, the range of quantitative differentiation allowed by colour digital imaging is extremely useful for image analysis, where the additional discrimination can provide better results compared with greyscale images.

Part III

Methodology and Results

CHAPTER 3

Methodology, Study Area, and Data Descriptions

3. Introduction

In order to accomplish the objectives of this study, a methodology was developed based on the major elements of this research extending from the hypothesis and objectives formulated for this thesis, found in sections 1.4.2 and 1.4.3:

- A signal processing approach based on Haar's discrete wavelet transform;
- Statistical methods of texture analysis using first-order statistics and second-order greylevel co-occurrence matrices;
- Spatial filters and edge-detection algorithms for processing borehole acoustic imagery;
- Classification techniques using the supervised classification approach of the multilayer perceptron artificial neural network and the unsupervised classification method of *K*-means clustering.

The first step of the methodology is the signal processing phase, in which Haar's wavelet transform is applied to the images in order to decompose them and obtain the wavelet coefficients. These coefficients are then used to reconstruct the images in order to define the texture of the damage contained in the images. The statistical texture analysis phase of the methodology involves the extraction of first-order and second-order statistics from the images of the damaged concrete. First-order texture features are derived from the histogram of the images, and second-order texture features are obtained from the second-order histogram, also known as

the grey level co-occurrence matrix (GLCM). A process is then employed for selecting the most useful texture features, which are used to create texture images. The texture analysis phase is performed individually on the images, as well as in combination with the signal processing phase, in order to evaluate the contribution of the signal processing approach to the damage analysis. These two phases constitute the damage analysis process of the methodology, which is applied to all of the different types of imagery.

The first stage of the damage analysis involves the assessment of map-crack damage present in greyscale and colour imagery of the field samples. In the second stage, the damage analysis is applied to map-crack imagery from the CANMET and GRAI laboratory specimens. Greyscale, colour and thermographic imagery of the CANMET blocks and the GRAI slabs were employed. Further stages of the damage analysis deal with various other types of damage found in greyscale imagery of the field samples, such as spalling, corrosion of steel reinforcement, aggregate popouts, surface erosion, post-repair damage, and efflorescence and corrosion stains.

Another aspect of this study consists of a slightly different methodology developed for application to borehole acoustic optical imagery obtained from a concrete lock. This methodology employs the signal processing and statistical texture analysis approaches outlined above, as well as a process based on different edge-detection techniques, in order to evaluate their relative effectiveness in distinguishing crack damage from the acoustic imagery.

The classification phase, which is the final stage of the methodology, consists of employing a supervised classification approach, namely the multi-layer perceptron (MLP) artificial neural network, as well as the *K*-means unsupervised classifier. The two techniques are evaluated for their efficiency in characterizing different types of damage contained in the various images.

The phases of the above methodology, as well as the steps within each phase are presented in the methodology flow chart (Figure 3.1). Details of the methodology phases are further elaborated in different sections throughout the rest of this thesis, and presented in flow charts corresponding to each phase. The signal processing flow chart representing the steps for the wavelet transform is presented in Figure 3.12, a flow chart for the statistical texture analysis phase can be seen in Figure 3.13, and a classification flow chart is presented in Figure 3.14.

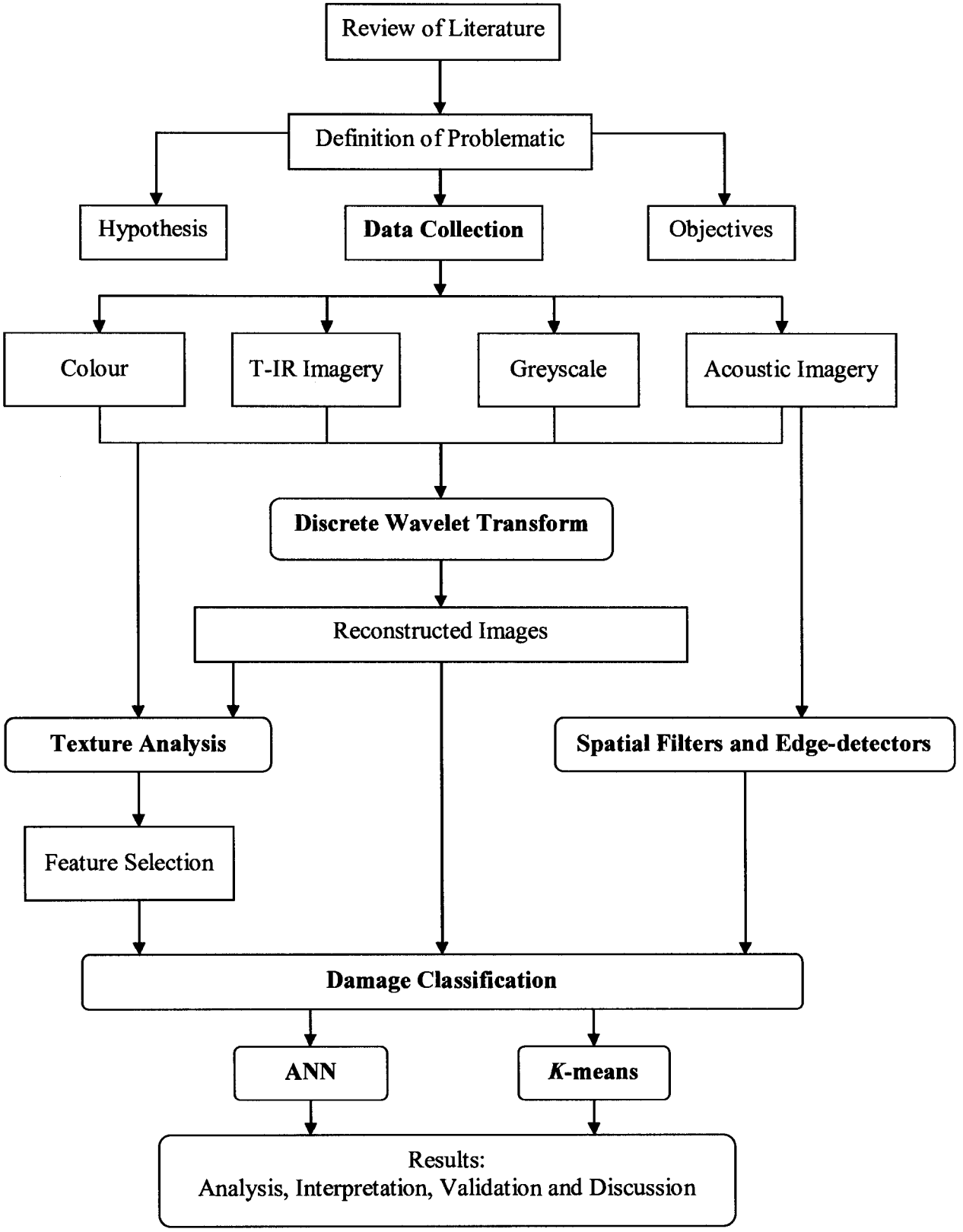

Figure 3.1: Methodology Flow Chart

3.1 Study Sites

Various concrete components from one lock and five different bridges were selected as field samples for this research. The lock is located in the city of Montréal and the bridges are situated in the city of Sherbrooke, in the southern region of Québec, Canada (Figure 3.2).

Bridge infrastructure in Montréal is subject to extreme loading, due to its port location and rapid increase in population. In Sherbrooke, although bridges may experience lighter loading, they are exposed to slightly harsher winters, with generally greater amounts of snowfall and colder temperatures. Consequently, the bridge components selected from these study areas manifest different types of concrete damage, such as cracking, steel rebar corrosion, erosion, spalling and post-repair damage, all with varying degrees of deterioration, making them ideal samples for the purposes of this study.

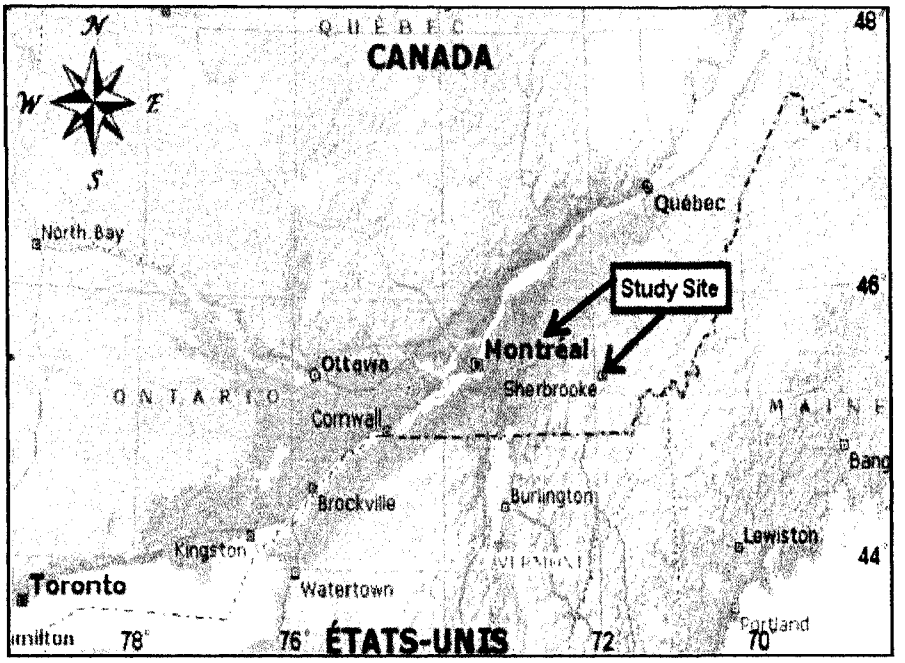

Figure 3.2: Geographic Location of Study Area

3.1.1 St. Lambert Lock

The St. Lambert Lock, which is situated in Eastern Canada, in Montréal, Québec, is one of four navigation locks built in the 1950's, that form part of the St. Lawrence Seaway, which runs along the St. Lawrence River between the port of Montréal and Lake St. François. Concrete infrastructure at the lock is regularly exposed to different factors, such as freezing and thawing cycles, watering and de-watering cycles, thermal effects, hydro-mechanical effects, ship impact, and extreme weather conditions typical of the region. These factors result in deterioration in the concrete, which range from surface cracks to steel reinforcement corrosion. Parts of the lock infrastructure are also severely affected by AAR, with various rates of concrete swelling (Gaudreault, 2000); other damage, in the form of concrete erosion, is apparent on the outer walls of the lock chamber.

The data used in this research consists of very high resolution acoustic imagery taken from two boreholes drilled in the St. Lambert Lock. The boreholes, with diameters of 3 and 4 inches, were drilled for a previous seismic tomography study and the recovered cores were tested for mechanical properties. The boreholes were not washed prior to logging and parts of the borehole wall were covered with a thin mud cake made of concrete laitance. Images of the lock are shown in Figure 3.3.

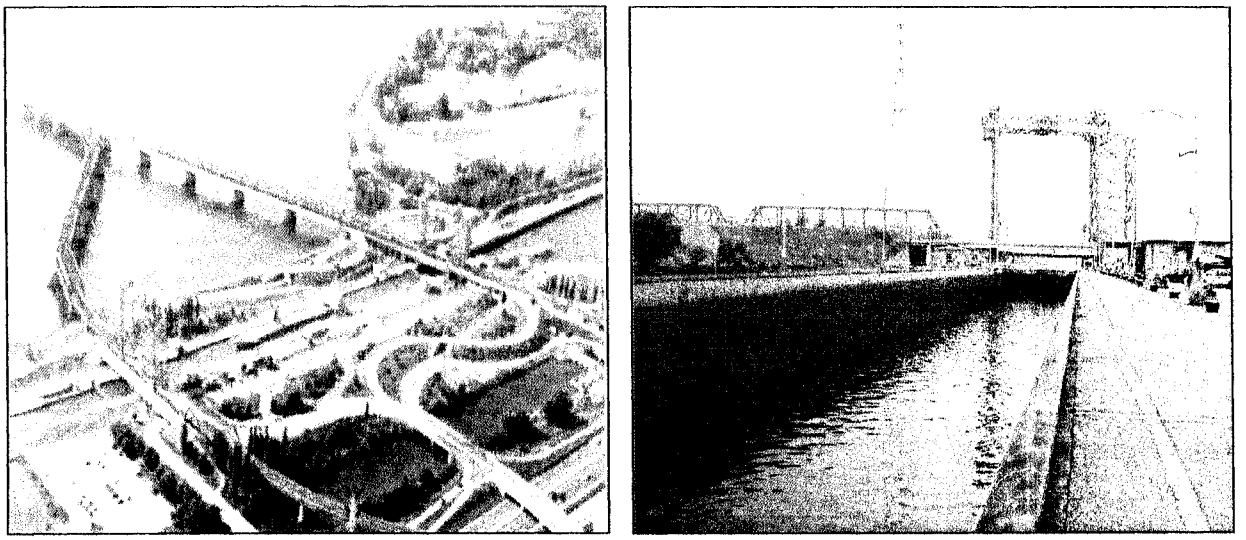

Figure 3.3: St. Lambert Lock, Montréal, Québec

3.1.2 Joffre Bridge

Some of the other components used as field samples in this study are from the Joffre Bridge, which crosses the St-François River in Downtown Sherbrooke, in the Eastern Townships of Québec. The Joffre Bridge was constructed with fully integrated fibre-optic sensors, embedded in a new composite material made of fibre-reinforced polymers created to perform in a wide range of environmental conditions and designed for normal use, such as heavy truck traffic (see Figure 3.4).

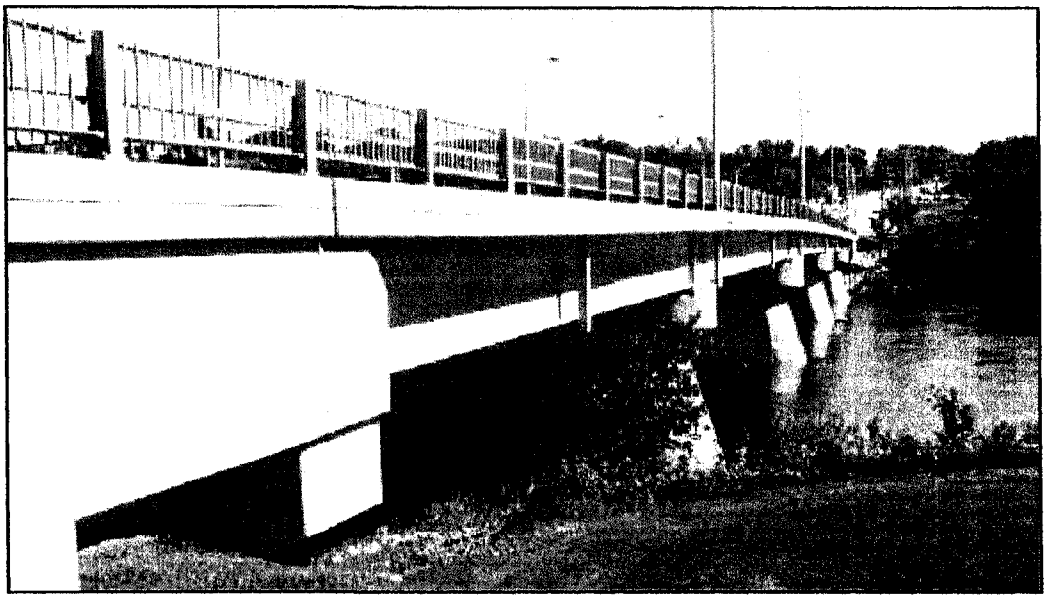

Figure 3.4: Joffre Bridge, Sherbrooke, Québec

3.1.3 Jacques-Cartier, Terrill, and Train Bridges

Components from the Jacques-Cartier Bridge, which is one of the major bridges in Sherbrooke, as well as the Terrill Bridge and two train bridges, also located in Sherbrooke, were selected as field samples. The components from these bridge infrastructure all exhibit different kinds and amounts of concrete distress: map-cracking, spalling, corrosion of reinforcement, erosion and damage due to efflorescence and corrosion stains. Figure 3.5 presents some damage due to AAR and corrosion and the resulting stains and efflorescence.

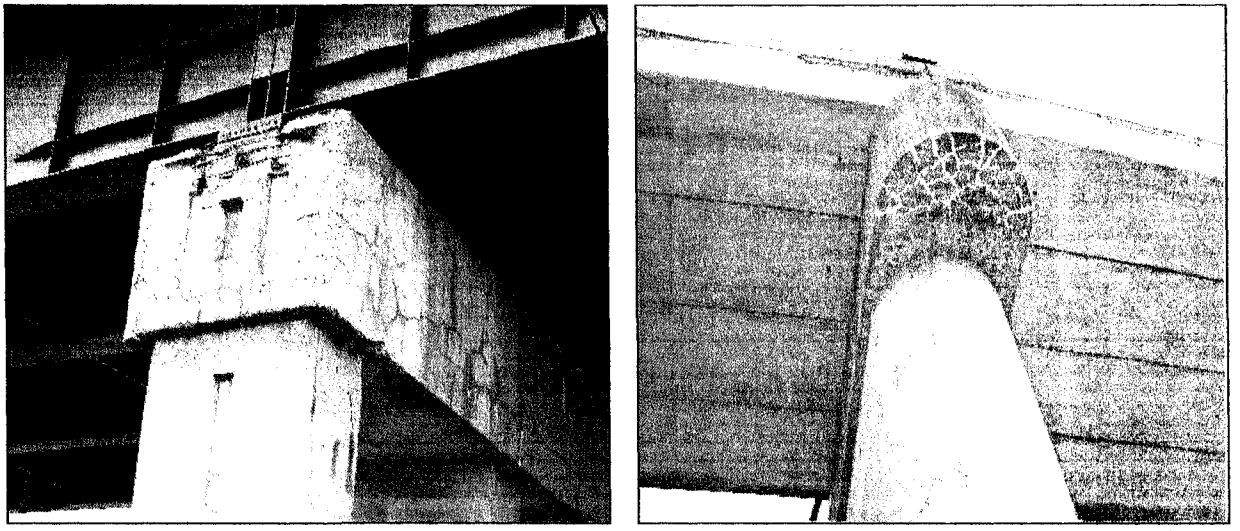

(a) Jacques-Cartier Bridge **(b) Train-bridge Support Beam**

Figure 3.5: AAR Damage in Bridge Components

3.2 Laboratory Concrete Specimens

For the purposes of this study, two sets of concrete specimens, one from the CANMET (Canada Centre for Mineral and Energy Technology) site in Ottawa, Canada, and the other from GRAI (Group for Research and Analysis in Instrumentation) at the University of Sherbrooke, Québec, Canada, were employed as laboratory samples in order to establish some correlation with and validation of results obtained from the field samples. The specimens were prepared in the laboratory with varying mixture proportions; all of them demonstrate various levels of surface cracking associated with the alkali-aggregate reaction.

3.2.1 CANMET Specimens

The set of CANMET specimens is composed of three concrete blocks, measuring 40 cm × 40 cm × 90 cm in size, which were batched in the laboratory and then left outdoors to the elements for over ten years at the CANMET site in the Ottawa region (Figure 3.6). One block, referred to in this research as C1, exhibits the lowest amount of damage. The block that has a moderate amount of concrete damage is referred to as C2, and the last block, which shows signs of the most deterioration, is referred to as C3.

Figure 3.6: Specimens at CANMET Site, Ottawa Region, Canada

3.2.2 GRAI Specimens

The GRAI specimens show concrete damage exclusively associated with AAR. They contain three concrete slabs that measure 100 cm × 100 cm × 25 cm in size (Figure 3.7). The slabs are referred to as G1, G2 and G3 in this study, in order of increasing concrete distress, where G1 has the least amount of deterioration and G3 has the most. After concrete hardening, the slabs were wrapped in damp terry cloth and stored at ambient air (20 ± 2°C) in the GRAI laboratory, at the University of Sherbrooke, Sherbrooke, Québec.

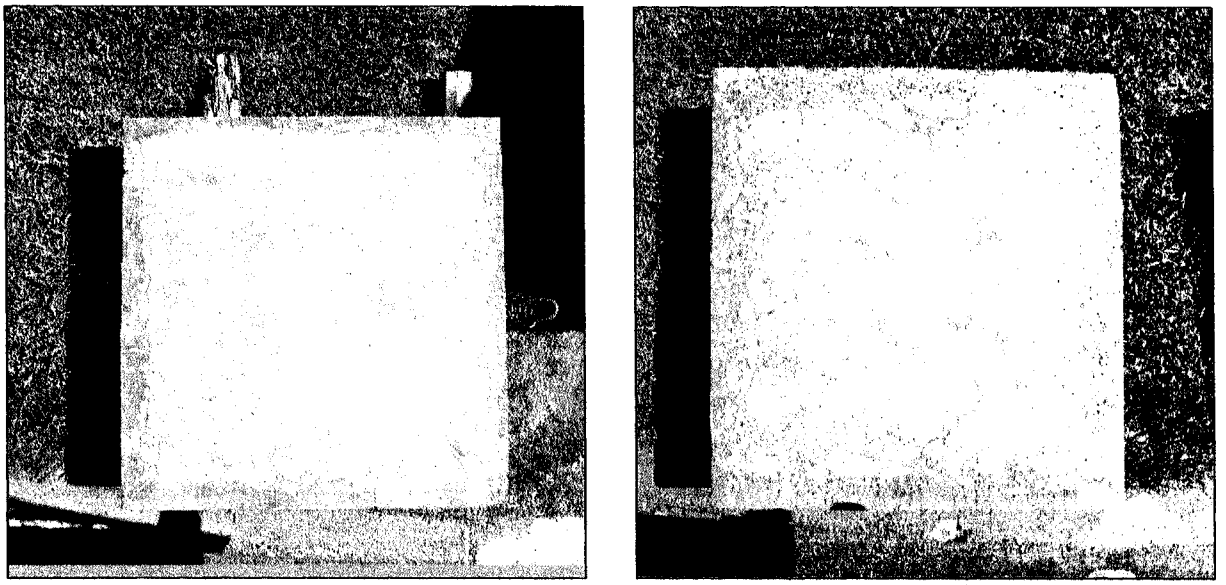

Figure 3.7: Top View of GRAI Samples at University of Sherbrooke, Québec

3.2.3 Concrete Mixture Proportions for Specimens

The CANMET specimens were prepared with the same reactive limestone as a coarse aggregate at approximately the same proportions, with the same water content; however, the total alkali content ranges from 1.99 to 5.31 kg/m³. Among the GRAI specimens, the G1 slab was made out of a non-reactive aggregate, with lower cement and water content than the G2 and G3 slabs, but with a higher total alkali content. The other two slabs were produced from a reactive limestone. Details of the mixture proportions are given in Table 3.1.

Table 3.1: Concrete Mixture Proportions

Concrete Mixtures	CANMET			GRAI		
	C1	C2	C3	G1	G2	G3
Density (kg/m³)	2303	2303	2317	2223	2326	2340
Cement content (kg/m³)	423	423	425	210	390	390
Total Na_2O_{eq} (kg/m³)	1.69	3.81	5.31	3.81	3.25	5.25
W/C	0.42	0.42	0.42	0.75	0.66	0.66

3.2.4 Test Measurements for Specimens

The amount of damage resulting from AAR is closely related to the expansion level and other indicators of concrete deterioration, such as loss of rigidity, decreasing mechanical properties, etc. (Rivard and Ballivy, 2005). Therefore, tests were carried out on the laboratory specimens in order to estimate the amount of inner damage. Expansion was measured using stainless steel studs that were fixed on the top surfaces and on the sides of the specimens. Since it is known that compression (*P*) wave velocities decrease with increasing amounts of damage (Carino, 2003), *P*-wave velocities were also measured through the Impact-echo method. These test measurements were recorded at regular intervals; the average measurements are given in Table 3.2.

Table 3.2: Average Measurements of *P*-wave Velocities and Expansion

Measurements	CANMET			GRAI		
	C1	C2	C3	G1	G2	G3
Avg. *P*-wave velocities (m.s-1)*	4909	4513	4402	3810	3590	3440
Avg. expansion (%)**	0.025	0.283	0.340	0.000	0.060	0.100
* Based on 11 measurements ** Based on side and surface measurements						

3.3 Data Acquisition and Description

3.3.1 Data Acquisition

Three types of imagery, greyscale, colour, and thermographic, were taken of the CANMET and GRAI laboratory specimens. Greyscale and colour images were obtained for all of the field samples as well. A digital camera was employed to acquire the greyscale and colour images, and the thermographic images were obtained through the use of the ThermaCAM PM595 infrared camera of FLIR Systems.

Acoustic image data from a borehole in a concrete lock was also employed in this study. Optical images of the borehole were obtained with the OBI-40 camera, and acoustic imagery was acquired using the ABI-40 Televiewer camera, developed by Mount Sopris. Basic processing was performed using the WellCAD software of Advance Logic Technology.

3.3.2 Input Image Data Description

All images of the CANMET and GRAI specimens were taken with a constant pixel resolution of 0.26 mm; however, images of the different bridge components have pixel resolutions that vary with the location of the component. All images were cropped to an image matrix of 512x512, 1024x1024 or 2048x2048 pixels, due to the needs of the wavelet transform algorithm, which requires that the image matrix be to the order of 2^n; for the purposes of this study, **n** has a value of 9, 10 or 11, depending on the image matrix.

3.3.2.1 Greyscale Images

Greyscale images of the different types of concrete deterioration, and their various levels of damage, present in the laboratory specimens and the field samples where obtained for image analysis in an effort to obtain quantitative information concerning the type and amount of damage present in the image. Figure 3.8 shows some examples of the greyscale imagery. The types of damage concerned are: map-cracks, spalling, steel corrosion, erosion, popouts, post-repair damage, and efflorescence and corrosion stains. A digital camera was employed to obtain the images; the laboratory samples have a pixel resolution of 0.26 mm.

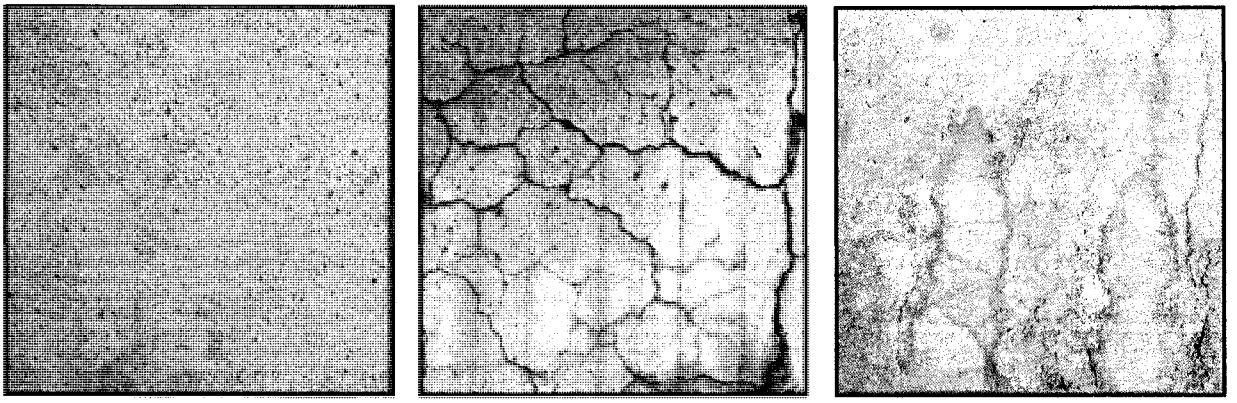

(a) No-damage **(b) Map-cracking** **(c) Post-repair Damage**

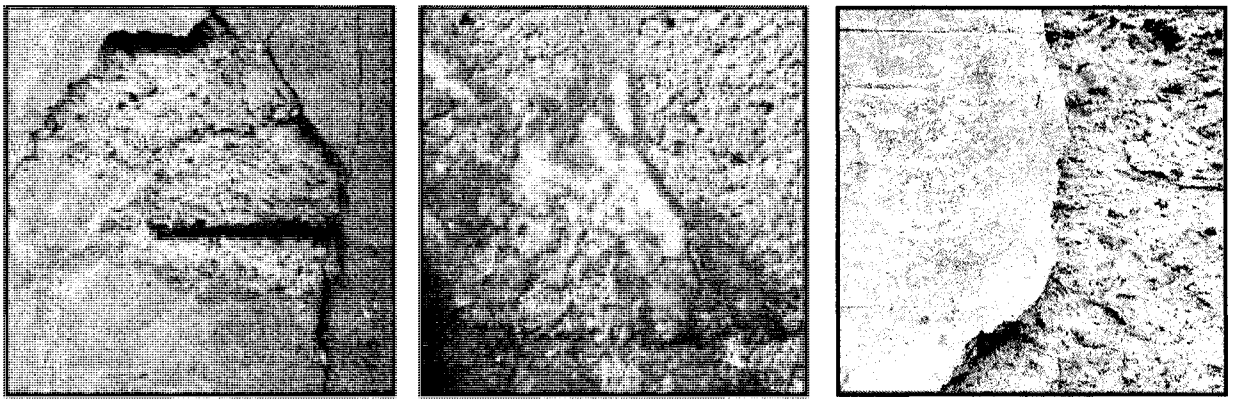

(d) Steel Corrosion **(e) Erosion** **(f) Spalling**

Figure 3.8: Examples of Greyscale Imagery of Different Types of Damage

3.3.2.2 Colour Images

Colour images portraying the same types of concrete damage as the greyscale imagery were obtained for the laboratory specimens as well as the field samples. A digital camera was also employed for these images, with the same resolution of 0.26 mm for the laboratory specimens. Figures 3.9 show the colour images of different types of damage.

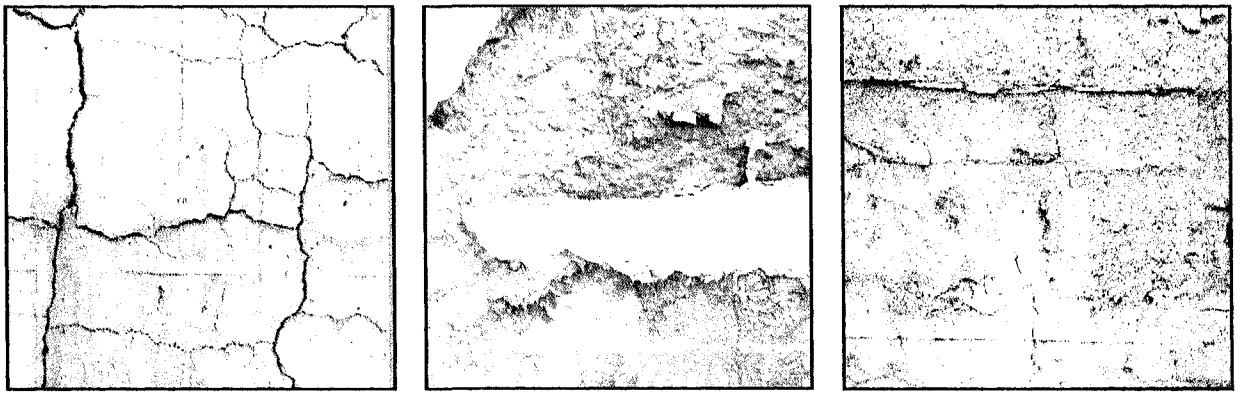

(a) Map-cracking **(b) Spalling** **(c) Erosion**

Figure 3.9: Examples of Colour Imagery of Different Types of Damage

3.3.2.3 Thermographic Images

Thermography is a technique that converts the measurement of steady or transient infrared energy, which is emitted by the target and is invisible to the human eye, into a two-dimensional pattern, or visual image, through the use of an infrared camera (Clark et al. 2003). High spatial resolution thermographic images of the laboratory specimens were obtained using the ThermaCAM PM595 of FLIR Systems. These 14-bit fully dynamic raw images have a spectral range of 9.5-13μm, and a built-in atmospheric filter with a cut-off at 9.5μm. Figure 3.10 is an example of a thermographic image taken of a GRAI specimen.

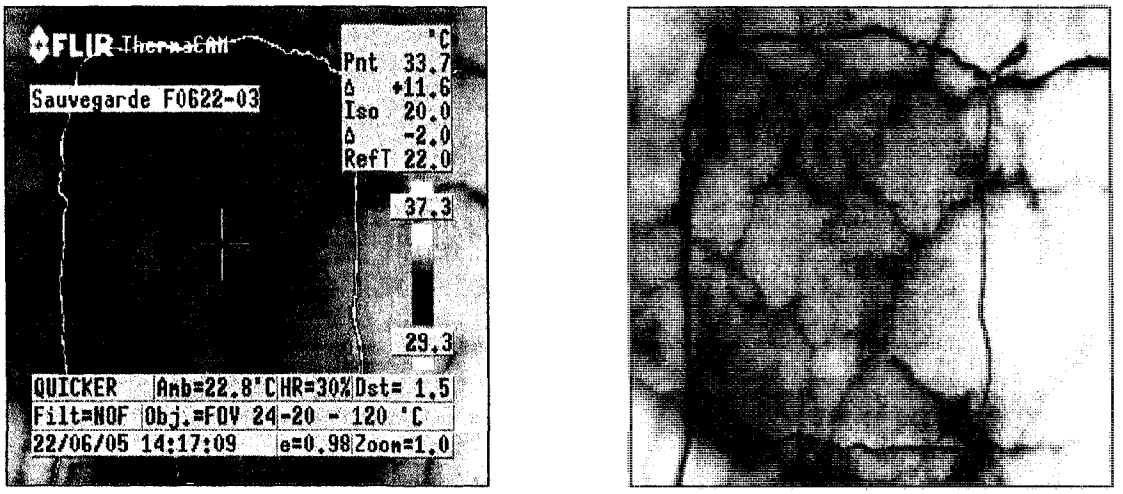

Figure 3.10: TIR Image of GRAI Specimen Exhibiting Map-cracks

3.3.2.4 Acoustic Images

Acoustic borehole scanner tools generate an image of the borehole wall by transmitting ultrasound pulses from a rotating sensor and recording the amplitude and travel time of the signals reflected at the interface between mud and formation, which is the borehole wall. The amplitude is mainly affected by the reflecting material while the travel time is affected by the distance between the probe and the borehole wall. These images are not flat; the data is displayed as an unrolled picture of the borehole wall starting at 0° to 360°. This has in influence on the measurements of some parameters, such as crack length or orientation.

Optical images of the borehole were obtained with the OBI-40 camera, and acoustic imagery was acquired using the ABI-40 Televiewer camera, developed by Mount Sopris. The up-hole mode was employed at a logging speed of 2 m/minute for a vertical sample rate of 1 sample/1.7mm. The horizontal sample rate was fixed at 252 samples/revolution. The image resolution is < 2 mm, with an acoustic calliper that can measure fractures to 0.05 mm. Some examples of images exhibiting various types of damage are shown in Figure 3.11.

Optical Image **Amplitude Image**

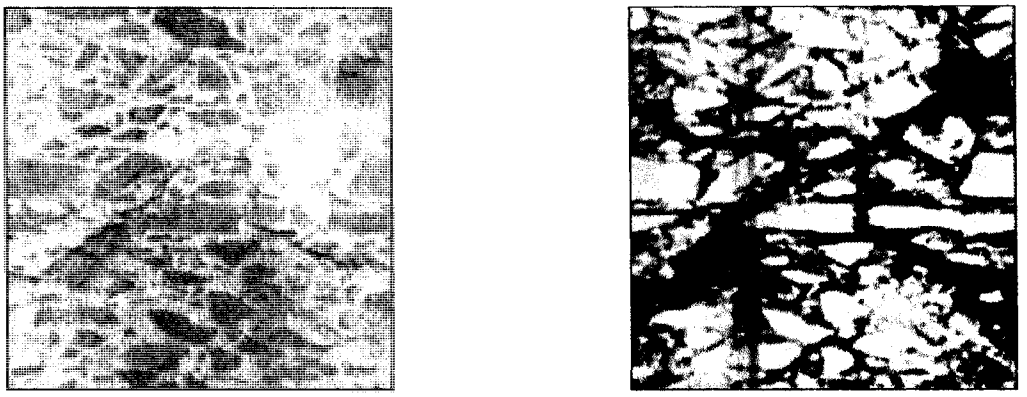

(a) Vertical Cracks

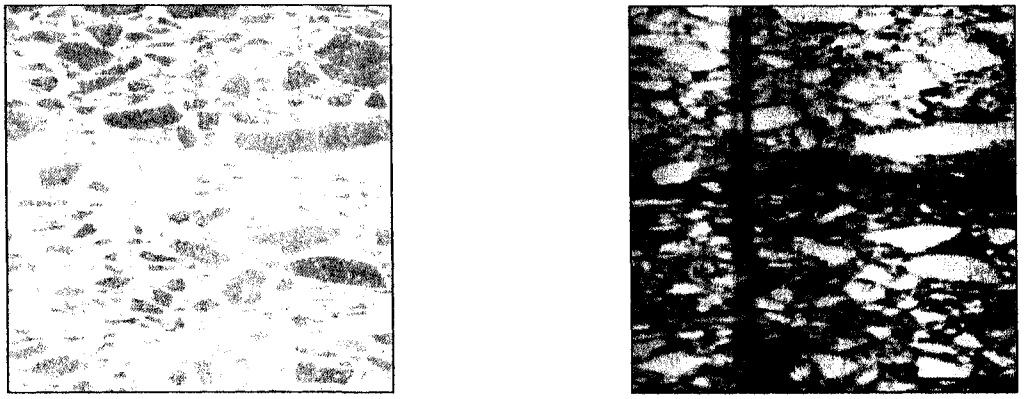

(b) Horizontal Cracks

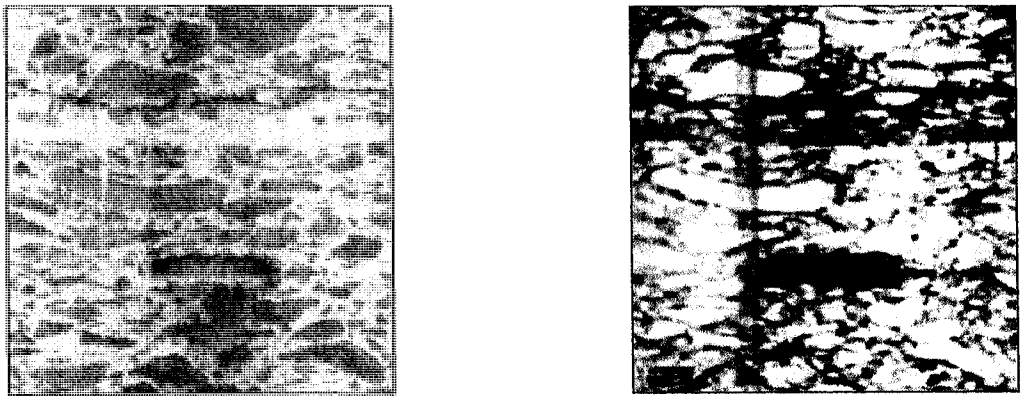

(c) Void Damage

Figure 3.11-A: Optical and Acoustic Image Samples of Damage

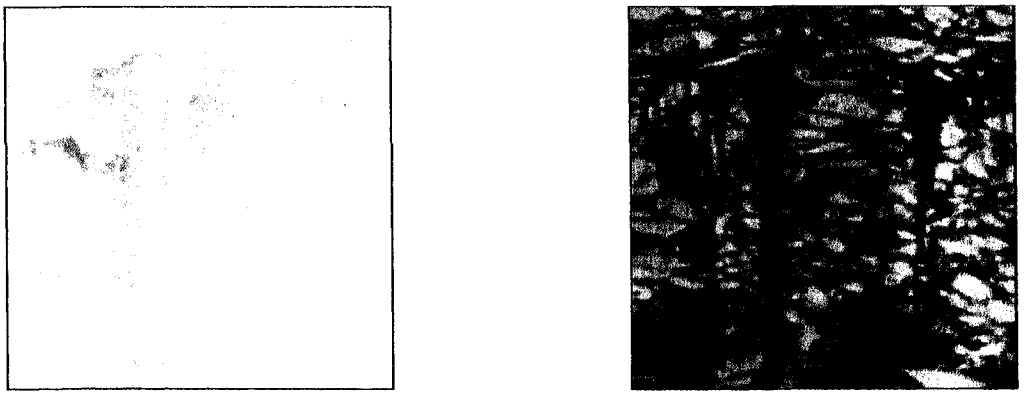

(a) Stain Damage

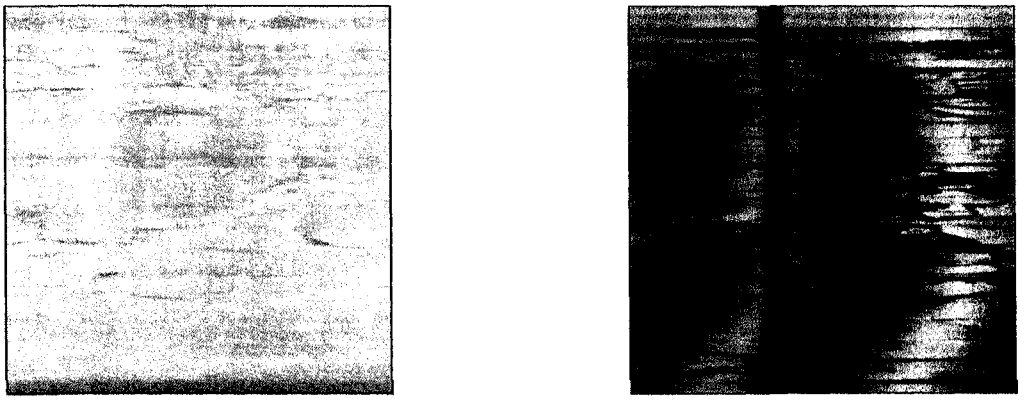

(b) Foundation Damage

Figure 3.11-B: Optical and Acoustic Image Samples of Damage (Cont'd)

3.4 Haar's Discrete Wavelet Transform

The wavelet transform allows a signal to be converted and manipulated while keeping resolution across the entire signal and still be based in time. Haar's transform is the simplest form of wavelets; it is essentially a process of averaging and differencing of values. The wavelet decomposition of a two-dimensional signal, such as an image, is obtained by performing the filtering consecutively along horizontal and vertical directions (rows and columns). In order to isolate fine variations in texture, very short-duration basis functions (high-frequency filters) are used; at the same time, very long-duration basis functions (low-frequency filters) are used for separating coarse details of texture (Masad et. al., 1999). Figure 3.12 presents a flowchart showing the different steps in the Haar wavelet transform.

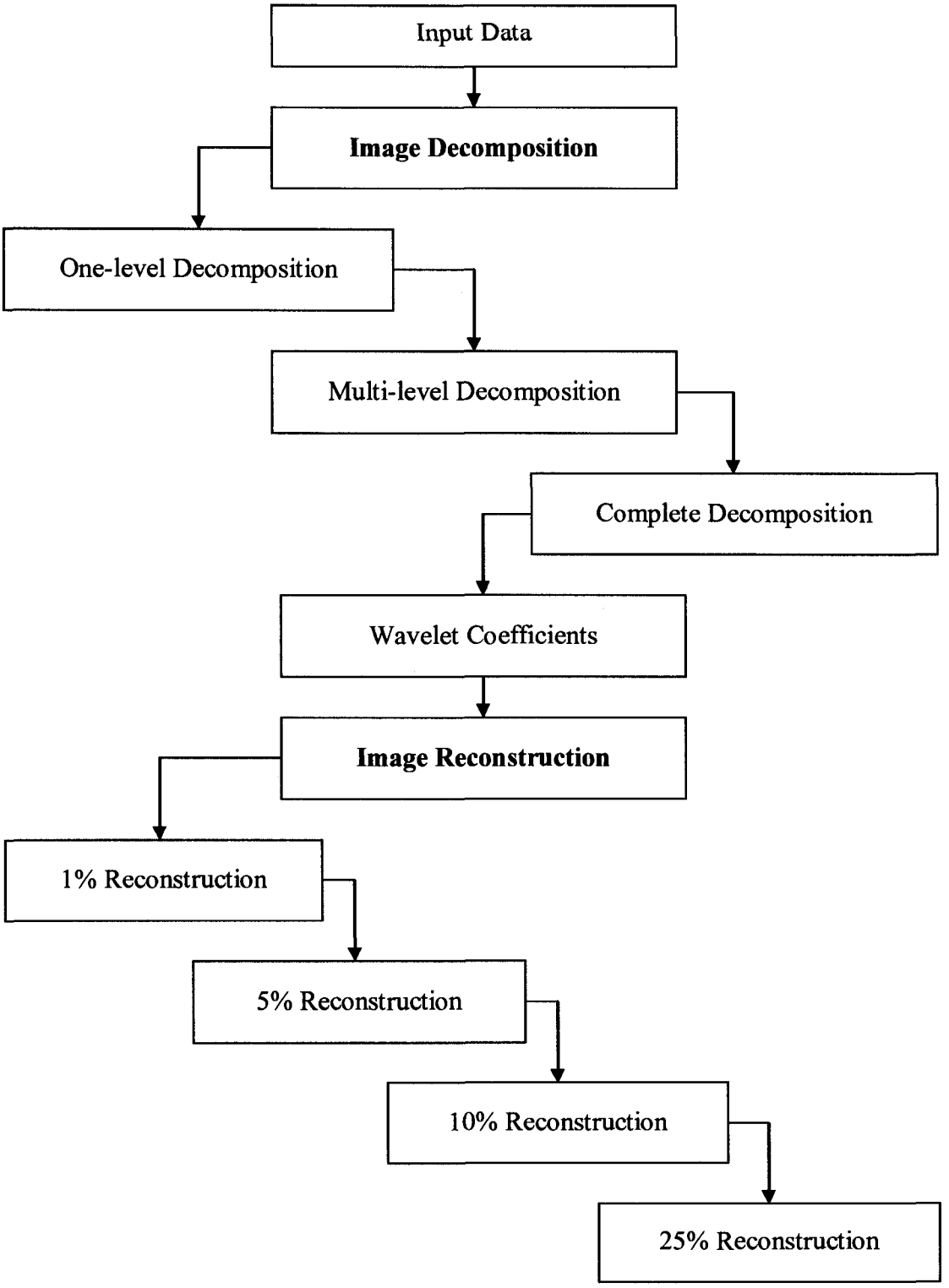

Figure 3.12: Haar Wavelet Flow Chart

3.4.1 Decomposition

The discrete wavelet transform initially decomposes an image into one approximation image and three detailed images. It filters the original image with complementary low-pass and high-pass filters in each dimension. The filtered images are down sampled at every other pixel producing four images of half the resolution of the original (Tonsmann and Tyler, 1999). In a pyramidal decomposition, the approximation image is further decomposed.

For analysis of the field data with map-crack damage, greyscale and colour imagery was employed. The first step in the analysis is the application of Haar's discrete wavelet transform on the imagery. The images were completely decomposed through Haar's wavelet transform; this resulted in the separation of coarse and fine texture details. A greyscale image sample of a bridge component with a high level of map-cracking is seen in Figure 4.1(a), with all texture information present. Figure 4.1(b) shows a one-level pyramidal decomposition of the image, resulting in four sub-band images, where the low-resolution image appears in the top left-hand corner surrounded by the three detail images. A two-level decomposition is presented in Figure 4.1(c), and Figure 4.1(d) is the full decomposition. The number of resolution steps required for the full decomposition depends on the image resolution; images with a dimension of 512x512 pixels take nine steps ($2^9 = 512$), ten steps are needed for images with a resolution of 1024x1024 pixels ($2^{10}=1024$), and eleven resolution steps are required for images with a dimension of 2048x2048 pixels ($10^{11}=2048$).

3.4.2 Reconstruction

In order to exploit the texture information isolated in the decomposed components of the image, the components are assembled to form reconstructed images, using the inverse discrete wavelet transform (IDWT). The wavelet coefficients obtained from the decomposition are upsampled and filtered. Upsampling is the process of lengthening a signal component by inserting zeros between samples. The level of upsampling can be controlled in order to produce a reconstructed image that presents the desired texture information.

After decomposition of the map-crack image sample, the resulting detail wavelet coefficients were used to produce reconstructed images for each input image; these reconstructed images

contain the coarse details, such as narrow cracks, wide cracks, and spalling damage. Images reconstructed to various levels for the same greyscale map-crack image sample shown for the decomposition step are presented in Figure 4.2. The 1% reconstruction seen in Figure 4.2(a) is produced using 99% of the wavelet coefficients, so it is almost identical to the input image. Figure 4.2(b) is the 5% reconstruction, using 95% of the coefficients; some of the fine details in the background have been removed due to the suppressed coefficients. More of the fine texture details are removed in the 10% reconstruction presented in Figure 4.2(c). For the purposes of this study, the 25% reconstructions shown in Figure 4.2(d) were employed, because at this compression most of the fine texture, also known as background noise, has been removed by the image reconstructions, while retaining the coarse details, which in this case are the cracks in the concrete surface.

3.5 Statistical Texture Analysis

Statistical texture analysis is based on the spatial distribution of grey level values in an image. First-order statistics estimate properties of individual pixel grey values and do not take into account the grey values of neighbouring pixels. Second-order statistics evaluate the grey values of two pixels occurring at a specific distance and direction from each other. Various texture features are then calculated from these statistics in order to distinguish the different classes of texture within the image.

3.5.1 First-Order Analysis

First-order statistics measure the likelihood of observing a grey value at a randomly chosen location in the image. They can be computed from the histogram of pixel intensities in the image. These depend only on the values of individual pixels, and not on the interaction or co-occurrence of neighbouring pixel values. A class of texture measures can be derived from these first-order statistics of a texture pattern.

Texture analysis rarely uses individual properties of the statistics. Instead, statistical features are derived for the extraction of textural information from the image. The following simple features are often used to characterize the first-order histogram: entropy, mean, standard deviation, third

moment, and variance. The entropy feature measures the uniformity of the histogram; when the distribution is uniform, entropy takes the maximal value, but when there is a dense cluster in the histogram, the value approaches zero. The mean reflects the average intensity of the pixel grey-levels. However, when classifying texture imagery, the images are usually normalized to have the same mean and standard deviation because these statistics are affected by the input image conditions. The third moment measures the skew of the histogram; when the histogram is symmetrical, the value is zero, and when the skew is left or right, the value is accordingly negative or positive. The variance feature measures the deviation from the mean value of the grey-levels (Tomita and Tsuji, 1990).

3.5.1.1 Window Size

In order to carry out the analysis, a moving window is employed, which refers to the size of the pixel neighbourhood around a reference pixel that represents the area of the image being analyzed. The accuracy of statistical texture analysis depends on the size of the window used. The homogeneity texture feature was randomly chosen for computing the coefficients of variation for the greyscale map-crack image, given in Figure 4.3, which shows that the coefficients stabilized around the 11x11 window for the majority of the object classes.

3.5.1.2 Selection of First-order Texture Features

In this study, the following first-order statistical information or texture features were derived from the input images, as well as from the reconstructed images produced from the wavelet coefficients obtained through the decomposition of the input images: data range, entropy, mean, skew and variance. Figure 4.4 presents these five texture features derived using an 11x11 window from the reconstructed image of the greyscale map-crack image sample shown in the wavelet transform phase.

Many of the texture features obtained from the first-order statistics are redundant and capture similar concepts. Consequently features that do not aid in texture discrimination are discarded. There exist various methods for selecting the most effective features; in this study, the features are selected through a process of visual analysis, histograms analysis, and analysis of correlation matrices. The visual analysis consists of examining the texture images individually in order to

determine which images do not provide adequate discriminatory information. After making some initial selections, the histograms of the texture features are then analysed to confirm the selections, as well as to decide if any other features should be discarded. Finally, the correlation matrix is examined for final selection of the most effective features. This process is performed for each of the different types of imagery. The histograms of the texture features derived from the reconstructed greyscale map-crack image are given in Figure 4.5, and the correlation matrix for the texture features is presented in Table 4.1.

3.5.1.3 First-order Texture Images

Once the most effective texture features are selected, they are displayed as a texture image, which are employed as the spatial data in the classification process. The texture image of the first-order texture features selected for the reconstructed greyscale map-crack image sample can be seen in Figure 4.6.

3.5.2 Grey Level Co-occurrence Matrix (GLCM)

A further improvement of the first-order statistics may be obtained through the use of the second-order statistics, which are described using the grey level co-occurrence matrix (GLCM) of the image. Texture analysis based on the method of the co-occurrence matrix employs statistical features that are derived from the matrix for the extraction of textural information from the image. These features are obtained through processes that take measured grey values to compute new values. For second-order statistics, the grey values of pixels in a window of specific size are taken and the result of the computations is written back on the central pixel; this process is repeated for all pixels in the image. The outputs of the derived features are images in which the pixel values have been changed to reflect a particular feature, or texture; therefore, the resulting feature images are also known as texture features.

A large number of texture features have been proposed; as many as fourteen different features that can be derived from these matrices are described by Haralick et al. (1973), however, only some of these are widely used. This is because many of the features are redundant, due to their high correlation. Thus they are not all useful for describing a particular texture. Some of the texture features that can be extracted from the GLCM are: contrast, correlation, dissimilarity,

energy, entropy, homogeneity, mean, second moment, standard deviation, and variance. A flowchart illustrating the steps of the GLCM texture analysis is presented in Figure 3.13.

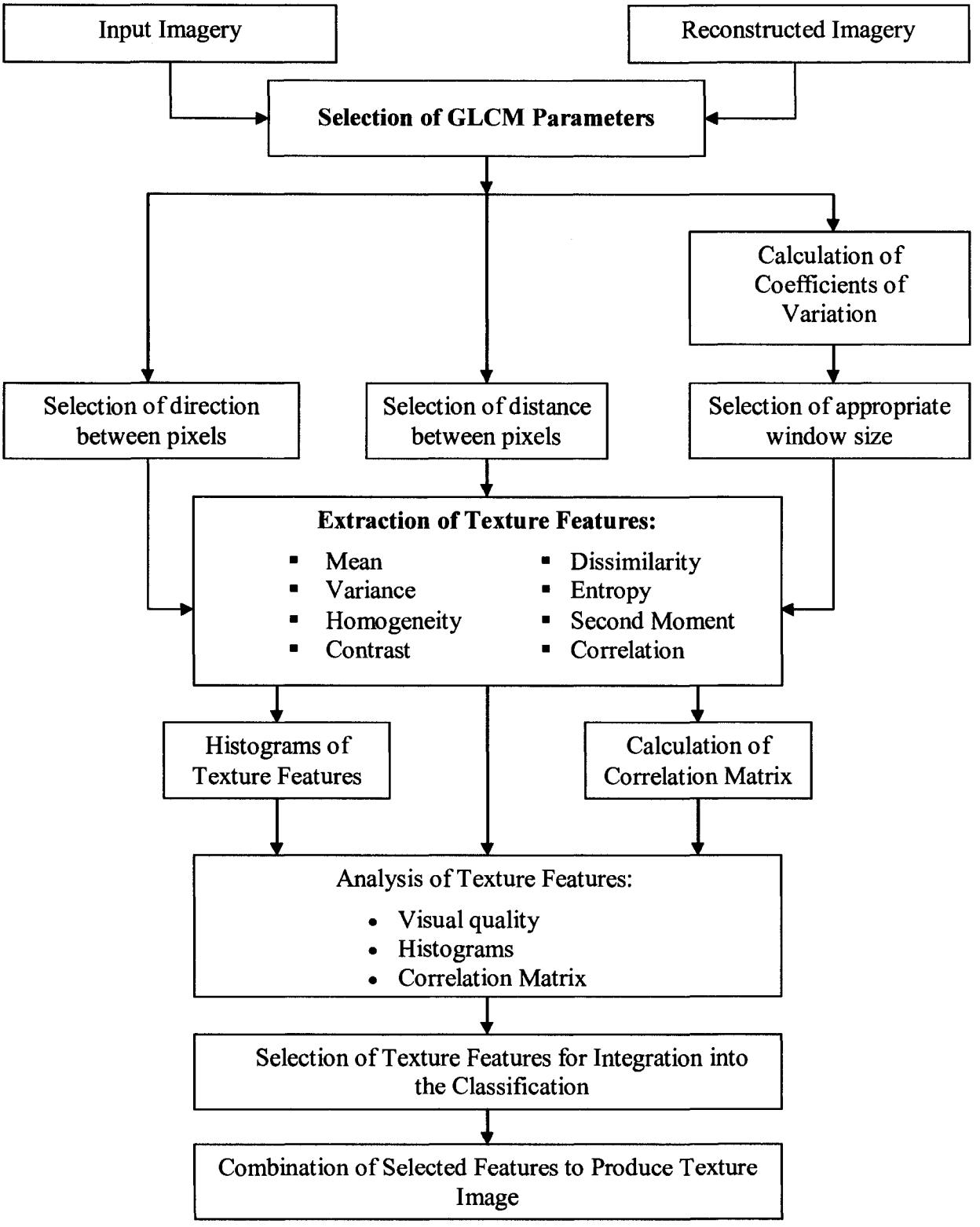

Figure 3.13: Texture Analysis Flow Chart

For the contrast feature, when a pixel has the same grey level as its neighbour, it is given a weight of 0. When a pixel differs from its neighbour's grey level by 1, there is a small contrast, and the weight is 1. If neighbouring pixels have grey levels that differ by 2, the contrast is increasing and the weight is 4. The weights continue to increase exponentially as the difference in grey levels of neighbouring pixels increases.

The correlation texture feature measures the linear dependency of grey levels on those of neighbouring pixels. It is independent of the other texture measures described here. The value 0 means the image is uncorrelated, and 1 means it is perfectly correlated.

In the dissimilarity feature, the computations are similar to that of contrast; however, the weights increase linearly. The dissimilarity and contrast features result in larger values for windows with more contrast. If weights decrease away from the diagonal, the result will be larger for windows with little contrast; conversely, homogeneity weights values by the inverse of the contrast weight, with weights decreasing exponentially away from the diagonal.

The mean of the GLCM is based on the grey level of the reference pixels, and calculates the average of the probabilities for that pixel. The variance feature is a measure of the dispersion of the values around the mean, and is similar to entropy. The standard deviation provides basically the same information as variance, but gives a different range of values.

The second moment uses the probability of pairs of pixels with the same grey level occurring as a weight for itself. High values of second moment occur when the image window is very orderly. The square root of the second moment is sometimes used as a texture measure, called energy, which is also used to measure order in the image. On the other hand, entropy is a texture measure that is used to calculate the disorderliness of the image.

3.5.2.1 GLCM Parameters

The success of the GLCM method of texture analysis is directly related to the appropriate choice concerning three parameters: the distance between pixels, the direction between pixels, and the size of the window to be used. Classification results performed using textural data are greatly

influenced by these variables; therefore, many factors need to be considered in order to make suitable selections for these.

In an image scene, there exist numerous textures with greatly varying degrees of smoothness or coarseness. An appropriate distance is usually influenced by how fine or coarse the texture of interest is. Thus, the choice of a distance between pixels depends on the texture of the object; textures that are fine generally require smaller distances, since pixels close to each other present enough variation in their grey values to characterize these textures, whereas larger distances are usually used for textures that are coarse because variations in the grey values occur in pixels farther away from each other. However, it has been found that small distances produce the best results (Karathanassi et al., 2000), since they are appropriate for textures that are fine, as well as for those that are coarse. As a result, a distance equal to 1 pixel, which is also the most commonly used, was chosen for this study.

Selecting the appropriate direction between pixels can be difficult as there are four different directions that can be used: 0° (horizontal), 45° (diagonal), 90° (vertical) and 135° (diagonal). One method consists of calculating the features of the co-occurrence matrix for the four directions and then taking their averages (Haralick, 1979). Another study has shown that certain directions can provide a better discrimination between classes than the method of taking the average of all the directions (Franklin and Peddle, 1989). However, the most common choice for the direction between pixels found in literature is 0°; consequently, this is what was used in this study by default of the image processing system employed.

The accuracy of the classification process using texture features also depends on the size of the pixel window used. This refers to the size of the pixel neighbourhood around a reference pixel that covers a certain area in the image to be analyzed at a time; after analysis of this area, the window is shifted by one pixel to the next area in the image for analysis. A 3x3 window for example, represents an area in the image that is 3 pixels x 3 pixels. If the window is too small, enough spatial information will not be extracted in order to characterize a certain object of interest. On the other hand, if the window is too large, it will either overlap onto two objects of interest and introduce the wrong spatial information (Pultz and Brown, 1987), or it will create transition limits that are too large between two types of neighbouring objects (Gong, 1990). If

the window size is too small or too large relative to the texture structure, then texture features will not accurately reflect real textural properties (Mather et al., 1998).

In order to choose an appropriate size for the window, there is a method that is based on the calculation of the coefficients of variation for each class as a function of the window size, using a given texture feature (Laur, 1989). The appropriate window size will be that for which the coefficients of variation start to stabilize for the majority of the classes, while having the lowest value. In this study, the homogeneity texture feature was randomly chosen for the calculation of the coefficients of variation for each class according to different window sizes. The coefficients of variation calculated for the greyscale map-crack image started to stabilize at the 11x11 pixel window for the majority of the classes (Figure 4.3). Table 4.14 gives the most appropriate window size selected for imagery of the other types of damage employed in this study.

3.5.2.2 Selection of Second-order Texture Features

After establishing the most effective window size and selecting the pixel distance and direction, texture features were produced for each input image, as well as for the reconstructed images. Figure 4.7 presents the eight second-order texture features extracted using an 11x11 window from the reconstructed greyscale map-crack image sample used in the first-order texture analysis step. Since it is sensible economically to ensure no more features than necessary are utilized when performing a classification, features that do not help discrimination should be discarded (Richards and Jia, 1999). Consequently, a feature selection process similar to the one used for selection of the first-order features was conducted based on visualization of the texture features, analysis of their histograms, and evaluation of the correlation matrix. Histograms of the second-order texture features for the reconstructed greyscale map-crack image are shown in Figure 4.8; Table 4.2 provides the correlation matrix for these features.

For the first step in the process of elimination, the visual quality of these texture images was analysed and three features, Contrast, Dissimilarity, and Correlation, were initially considered for discarding due to their poor quality in terms of visual information.

After displaying the histograms of all the texture images, it was confirmed that these three features, Contrast, Dissimilarity, and Correlation, were to be eliminated due to the narrow peaks

they presented. The possible elimination of another two features, Variance and Second Moment, was also considered from the histogram analysis because of the same reason.

Finally, through calculation of the correlation matrix, it was confirmed that these two features, Variance and Second Moment, as well as the first three features, Contrast, Dissimilarity and Correlation, were to be discarded due to their relatively high correlation with the other features. As a result, only three texture features, Mean, Homogeneity, and Entropy were selected for the greyscale image sample of map-crack damage taken from the field data.

3.5.2.3 Second-order Texture Images

After selecting the optimal second-order texture features, texture images are produced using the features. Figure 4.9 presents the texture image of the selected second-order texture features for the reconstructed greyscale map-crack image sample.

3.6 Spatial Filtering

Spatial filters are functions that are applied to images in order to enhance them. A window function is usually employed to perform convolutions of the image in order to yield an output image. The window function or kernel uses a square pixel neighbourhood around each pixel in order to replace its value by the average over the area centered on that pixel. The square window sizes are usually odd numbers, such as 3x3 pixels, 5x5 pixels etc., however, other values may also be employed. There are many different types of filters that produce various results; they are employed depending on the desired output.

3.6.1 Lowpass Filtering

Low pass filtering preserves the low frequency components of an image by removing the high frequency components, such as noise. These filters reduce deviations from local averages, thus smoothing the grey level values of the original image by replacing the original values with their local averages. The larger the size of the kernel employed, the more drastic the smoothing is. An output image resulting from a 5x5 kernel lowpass filter applied to the acoustic image sample can be seen in Figure 4.59 (a).

3.6.2 Median Filtering

Median filters are a group of filters based on ranking pixel grey-values. They smooth an image while preserving edges larger than the kernel size by replacing each centre pixel with the median value found within the neighbourhood of the filter. These filters are good at eliminating impulsive noise, such as salt and pepper noise or speckle, while preserving edge data. The usual square median filter eliminates fine vertical or horizontal lines; this can be overcome through the use of a cross-shaped mask. An output image from the application of a 7x7 median filter can be seen in Figure 4.59 (b).

3.6.3 Edge-detection

Edges are considered to be areas with strong intensity contrasts in an image, causing a jump in intensity from one pixel to the next. In image data of damaged concrete, these edges would characterize boundaries between areas of sound concrete and deterioration, such as cracks. Possible causes for an intensity edge are discontinuities in surface, depth, surface-reflectance, and illumination.

In order to identify edges within an image, edge-detection operators analyse the grey level of each pixel and its neighbour to determine which ones belong to areas with sharp contrast in grey-level intensity. The basic edge-detection operator is a matrix area gradient operation that is calculated by forming a matrix centered on a pixel chosen as the center of the matrix area. If the value of this matrix area is above a given threshold, then the middle pixel is classified as an edge. The slope and direction of the edge, also known as the magnitude and the orientation of the gradient vector, are usually used to establish the areas of contrast.

Most edge-detection approaches may be categorized as first- or second-order methods. First-order operators, also known as gradient methods, find edges by calculating an estimate of the gradient magnitude in the first derivative, and comparing this estimate to a fixed threshold to determine edge points (Hutchinson and Chen, 2006). Some common first-order methods consist of such approaches as the Roberts and Sobel operators. Second-order techniques, often called Laplacian operators, search for zero-crossings in the second derivative of the image to detect edges. A frequently employed second-order operators is the Marr-Hildreth approach.

3.6.4 Gradient Methods (First-order)

Edge detection based on gradient methods assumes that edges are pixels with a high gradient. A fast rate of change of intensity at some direction given by the angle of the gradient vector is observed at edge pixels. The magnitude of the gradient indicates the strength of the edge. All the gradient-based algorithms have kernel operators that calculate the strength of the slope in directions, which are orthogonal to each other, commonly vertical and horizontal. Later, the contributions of the different components of the slopes are combined to give the total value of the edge strength.

3.6.4.1 Roberts Algorithm

Since the intensity function of a digital image is only known at discrete points, derivatives of this function cannot be defined unless we assume that there is an underlying continuous intensity function, which has been sampled at the image points. With some additional assumptions, the derivative of the continuous intensity function can be computed as a function on the sampled intensity function, in this case, the digital image. It turns out that the derivatives at any particular point are functions of the intensity values at virtually all image points. However, approximations of these derivative functions can be defined at lesser or larger degrees of accuracy. The Roberts edge-detection algorithm works by computing the sum of the squares of the differences in intensity between diagonally adjacent pixels. This is accomplished by convolving the image with two 2x2 kernels, which provides a simple approximation to the gradient magnitude. The application of the Roberts algorithm on the research data is presented in Figure 4.59 (d).

3.6.4.2 Sobel Operator

The Sobel operator is an edge-detection technique used extensively in image processing. Technically, it is a discrete differentiation operator, computing an approximation of the gradient of the image intensity function. At each point in the image, the result of the Sobel operator is either the corresponding gradient vector or the norm of this vector. The algorithm calculates the gradient of the image intensity at each point, giving the direction of the largest possible increase from light to dark and the rate of change in that direction. Consequently, the results show how

abruptly or smoothly the image changes at that point, and how likely it is for that part of the image to represent an edge, as well as what the most likely orientation of that edge is.

The Sobel edge-detector uses simple 3x3 convolution kernels to create a series of gradient magnitudes; one kernel is used to detect changes in vertical contrast and another to detect horizontal contrast. This data is represented as a vector, known as the gradient vector. The vertical and horizontal gradients computed can be regarded as the x and y components of the vector, which represent the gradient magnitude and direction. Figure 4.59 (c) shows the result of applying the Sobel operator on the resampled acoustic image data.

3.6.5 Laplacian Approaches (Second-derivative)

Laplacian-based edge detectors assume that a maximum of the first derivative will occur at a zero crossing of the second derivative; thus, the edge points of an image can be detected by finding the zero crossings of the second derivative of the image intensity. To obtain both horizontal and vertical edges, the Laplacian of the image is computed, resulting in second derivatives for both the x and y directions. Since the calculation of second derivatives is very sensitive to noise, the image must be smoothed before edge detection. This can be performed in two ways: the image is first smoothed with a Gaussian mask and then filtered with the Laplacian to obtain the second derivatives, or the image is convolved with the Laplacian of the Gaussian function, which is a hybrid filter made by convolving the Gaussian smoothing filter with the Laplacian filter. As a result of the smoothing, isolated noise points and small structures are filtered out. Then, the zero crossings are detected; those pixels that have locally maximum gradient are considered as edges by the edge detector in which zero crossings of the second derivative are used. To avoid detection of insignificant edges, only the zero crossing whose corresponding first derivative is above some threshold, are selected as edge points. The edge direction is obtained using the direction in which the zero crossing occurs.

3.6.5.1 Marr-Hildreth Edge-detector

The Marr-Hildreth edge-detection method is a simple algorithm that operates by convolving the image with the Laplacian function to obtain the second derivatives for the horizontal and vertical directions. Since the calculation of second derivatives is very sensitive to noise, the image is

usually smoothed with a Gaussian mask first and then filtered with the Laplacian to obtain the second derivatives, or the image is convolved with the Laplacian of the Gaussian function, also known as the LoG operator, in one step, or as a fast approximation, by the Difference of Gaussians, often called the DoG operator. This edge-detector is sometimes also referred to as the Mexican hat operator due to the visual shape of the function when turned up-side-down. Zero-crossings are then detected in the filtered result to obtain the edges. The Marr-Hildreth method applied to the input image produces the result seen in Figure 4.59 (f).

3.6.6 Directional Filtering

Other edge enhancement filters that selectively enhance image features having specific direction components are directional filters. The sum of the directional filter kernel elements is zero; the result is that areas with uniform pixel values are zeroed in the output image, while those that are variable are presented as bright edges. The acoustic imagery contains damage with specific orientation, such as horizontal, vertical, and sub-vertical cracks. Thus, this filter was employed in order to distinguish those types of damage. Figure 4.59 (e) shows the result of a 3x3 directional filter with a 5° angle.

3.7 Classification

Classification is a method by which labels are attached to pixels according to their spectral characteristics by a computer, which is trained beforehand to recognize pixels with similar spectral properties. Typically, this process involves the analysis of digital image data and the application of statistically based decision rules for determining the object class of each pixel in an image; the pixels are then classified into their respective classes (Richards and Jia, 1999). This type of automated image interpretation is considered a quantitative analysis due to its capacity to identify pixels based on their numerical properties and to provide area estimates by counting pixels. In the process of classification, pixels are sorted into a finite number of individual object classes based on the spectral pattern present within the data for each pixel. The spectral pattern is composed of the set of brightness values, obtained in the various spectral bands for each pixel. These object classes are what the computer works with in order to perform the quantitative analysis (Richards and Jia, 1999).

Pixels are assigned to object classes through a specific set of criteria, composed of the decision rules, which are developed during the training phase of the classification. These decision rules are based on the spectral radiances observed in the data. Object classes may be associated with known features in the image or they may only represent areas that appear different to the computer. The intent of the classification process is to label all pixels in a digital image as belonging to one of several object classes; the categorized data can subsequently be used to produce summary statistics of the areas covered by each class (Jensen, 2000).

Classification of the concrete imagery is the final step in the methodology for this study. Two classifiers were employed in order to evaluate their effectiveness in distinguishing the various types of concrete deterioration in the different imagery: a supervised technique based on the multi-layer perceptron artificial neural network (ANN), and the unsupervised *K*-means approach. Figure 3.14 presents the flowchart for the ANN classifier. Different datasets were used in the classification process to determine the contribution of each type of information to the characterization of concrete damage.

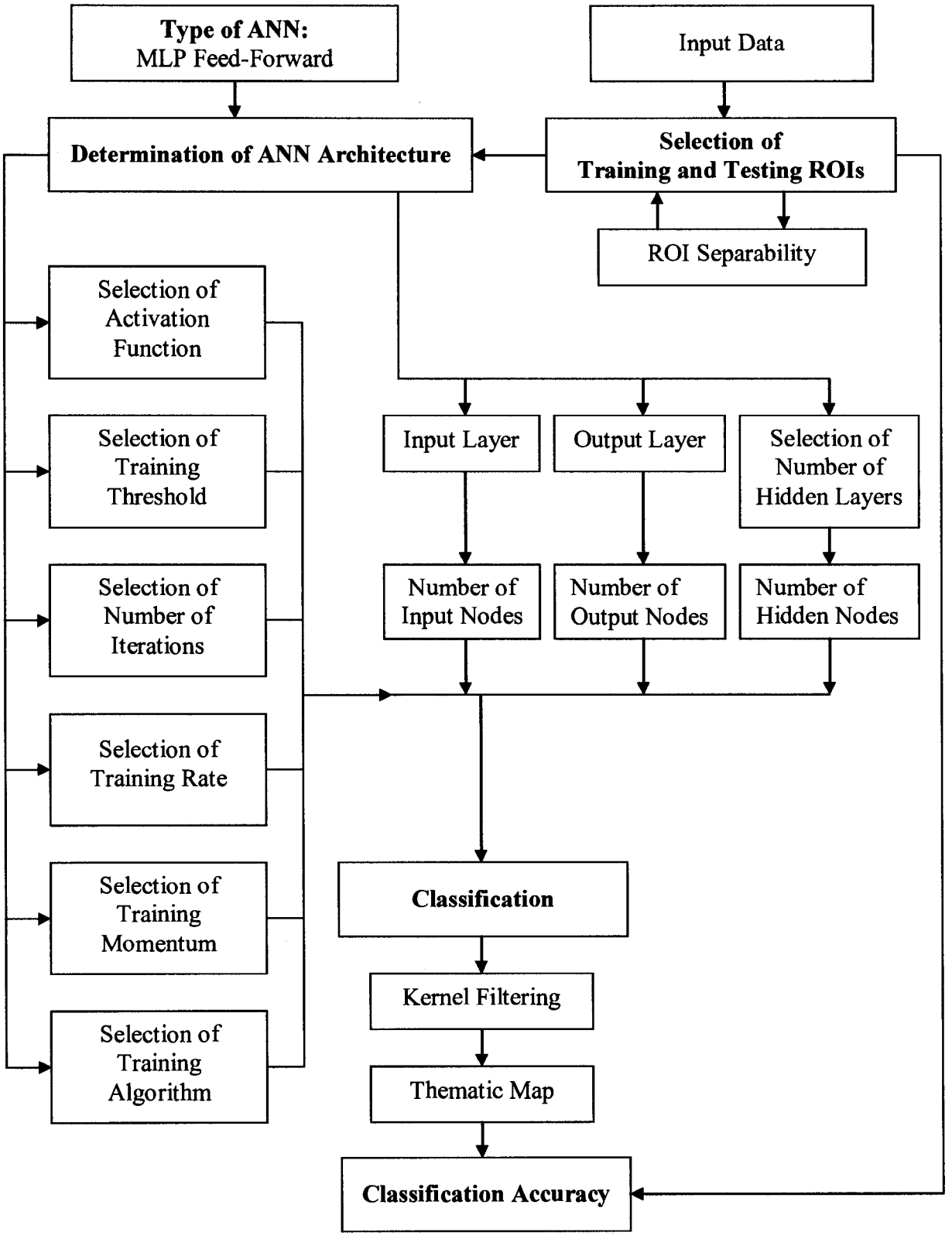

Figure 3.14: ANN Classification Flow Chart

3.7.1 The Multi-layer Perceptron (MLP)

The artificial neural network approach (ANN) has become an increasingly common alternative to traditional statistical classification methods. Among the many different kinds of supervised ANN techniques, the multi-layer perceptron (MLP) is one of the most popular methods. As such, the MLP artificial neural network was selected as the supervised classification technique used to extract the deterioration information from the concrete imagery.

MLP Architecture

The MLP normally consists of three layers: an input layer, a hidden layer and an output layer. The nodes in one layer are all connected to the nodes in the adjacent layers; however, feedback connections are not possible in the MLP. Signals travel forward from the input layer, through any hidden layers, then to the output layer. Thus, the MLP is also known as a multilayer feed-forward neural network.

Number of Input, Hidden and Output Nodes

The number of nodes used in the input layer of the ANN should correlate with the number of input features, and the number of nodes in the output layer should reflect the number of target classes. In the hidden layer, the number of hidden nodes depends on the data; generally data that does not contain too many variables will require a smaller number of hidden nodes compared to more complex data.

For classification of the various datasets in this study, a different number of input nodes were used. For the spectral datasets, the MLP network was composed of one input node to represent the unprocessed image sample. For the spatial datasets, three input nodes were used for the three selected first-order texture features, and three input nodes representing the three selected second-order texture features were employed, for a total of six input nodes. Seven input nodes representing the original image sample and the six selected texture features were used for the combined datasets. For the classifications used to evaluate the significance of the first-order texture information, three input nodes were used for the three first-order features, and for the

second-order texture information, three input nodes were employed to represent the three second-order features.

The number of output nodes used in the MLP depends on the type of damage and the number of object classes associated with it. For the images of the laboratory specimens containing map-cracking, three output nodes were used corresponding to the three object classes: wide-crack, narrow-crack and no-crack; for the field sample images, two output nodes were employed, in order to represent the two object classes of map-crack and no-crack. For most of the other types of damage two output nodes were used, one for representing the damage class and the other for representing the no-damage class. Some of the other types of damage, however, required the use of three output nodes, such as corrosion, popouts, post-repair damage, and efflorescence stains, because these images actually contained two types of damage classes along with the no-damage class. Since the data is not of a very complex nature, eight hidden nodes were employed in all of the MLP networks.

Selection of Activation Function

In the ANN, the input signal travels from the input layer to the hidden layer, where it passes through an activation function in order to compute the output from the hidden nodes. This output signal from the hidden nodes becomes the net input signal, which then travels from the hidden layer to the output nodes, where it again passes through an activation function to calculate the predicted output. There are different activation functions that can be used in an MLP network, such as logistic, Gaussian, linear, hyperbolic and threshold. When calculating the output from the hidden layers and the output layers, it is possible to use different activation functions for each layer; however, the same activation function is usually used. The most widely used activation function for the MLP network is the logistic function, which was also employed in this study.

Training Algorithm: Error Back Propagation

To minimize the error between the predicted output and the actual output of the ANN, a training algorithm is used to adjust the network's weights and thresholds during the training stage. Supervised feed-forward networks usually employ the error-back propagation approach, which was also used in this study.

Selection of Training Rate and Momentum

The training rate weights the change in the connections between the network layers. If it is too high, the training algorithm will overshoot the minimum of the error surface. If it is too low, the algorithm will take too long to reach the minimum. The training momentum is a term that tends to alter the change in the connections in the direction of the average gradient. It can prevent the learning algorithm from stopping at a local minimum instead of at a global minimum. In order to find appropriate values for the training rate and the training momentum, different values for these two can be tested for their effects on the classification accuracy. Consequently, a value of 0.2 was selected for the training rate, and 0.9 was selected for the training momentum.

Selection of Training Threshold and Number of Iterations

A value is selected for the training threshold in order to indicate when the training should stop. The training procedure usually continues until the value of the network errors is less than the training threshold. The number of training iterations indicates the number of iterations the training procedure should perform. For the training threshold, a value of 0.9 was employed and for the training iterations, a value of 1000 iterations was selected.

Training and Verification Dataset

The application of a neural network usually requires a training data set and a verification data set. In supervised training, both data sets should contain known input and output patterns. The training data set is used to train the network and must be both representative and complete. The verification data set should be independent of the training data; it is used to assess the classification accuracy of the network after training.

In order to train the MLP, regions of interest (ROIs) representing the object classes were selected from the image sample. These training ROIs consist of areas that manifest deterioration for the classes representing concrete damage, and regions of sound concrete for the no-damage classes. Verification ROIs were also created for each class from areas on the image where the training ROIs were not produced. The verification data is used to validate the training outputs of the MLP. The size of the training and verification datasets differed from image to image, as well as

with the type of damage, due to the variation of the amount of deterioration present in the images. In order to avoid poor classifications or inaccurate estimates of the elements, efforts were made to choose a sufficient number of training pixels for each class, in order to ensure adequate representation.

3.7.2 *K*-means Classifier

Clustering algorithms usually locate the centre of a class of data, which is a point that is the average of all the points in the cluster. This is determined by taking the mean of the coordinates of all the points in the clusters. To determine cluster membership, most algorithms evaluate the distance between a point and the cluster centres. Generally, the distance between two points is taken as a common metric to assess the similarity among the instances of a population. There are many different distance measures, the most popular being the Euclidean metric, which defines the distance between two points. The output from a clustering algorithm is basically a statistical description of the cluster centres with the number of components in each cluster, or an image in which the pixels in each group are assigned a symbol or colour to show that they belong to the same cluster.

The *K*-means classifier groups pixels into classes of interest by determining the optimal partitioning of pixels into a specified number of object classes. Applying the classifier usually consists of selecting the number of object classes and a set of points for the initial centre of each class. Then the classifier assigns an initial cluster vector and classifies each pixel to the closest cluster. New cluster mean vectors are calculated based on the pixels in each cluster, and then the classification is carried out again. These last two steps are repeated until the data is classified into the predefined number of clusters.

3.7.3 Results of the Classification

The results of the classification can be presented in two forms: a table that provides the classification statistics of the number of pixels in the whole image that belongs to each class, or a classified image. The classified image is also known as a thematic map, which shows the spatial distribution of the various classes present in the region of interest, in which each pixel is assigned a symbol or colour that relates it to a specific class. Thematic maps are often

represented according to a pseudo-colour table, which provides for a better visualization of the classified data.

3.7.4 Classification Accuracy

At the completion of a classification process, it is necessary to assess the accuracy of the results obtained. This provides a degree of confidence relating to the results and serves to indicate whether or not the analysis objectives have been achieved.

Accuracy is determined empirically, by selecting a sample of pixels from the classified image and checking their labels against classes determined from verification data (ground truth data). From these checks, the percentage of pixels from each class in the image labelled correctly by the classifier can be estimated, along with the proportions of pixels from each class erroneously labelled into every other class. The result of this procedure is presented in the form of a matrix, from which many classification precision indexes can be calculated. The Kappa coefficient, which is a common index used to assess classification accuracy, is the method that was adopted in this study.

3.7.5 Kernel Filtering

To smooth out the classified images, a Majority Analysis filter was applied. The Majority Analysis is used to change spurious pixels within a large single class to that class by selecting a kernel size; the centre pixel in the kernel will be replaced with the class value that the majority of the pixels in the kernel has.

It was found that the same kernel size did not produce the desired smoothing effect for all of the classified images, probably due to the variability among the different types of damage. Therefore, various kernel sizes were used for the different imagery.

3.7.6 Binary Images

In order to better represent the damage class and to further analyse surface damage, the classified images were converted into binary images. This process simplifies the image by assigning the

pixels that represent the damage in the concrete a value of 1 (black) and the background pixels a value of 0 (white). Manual or automated methods are then used to count or sum the pixels to calculate total wide-crack length, as well as average wide-crack width.

Chapter Four provides examples of classified images for the different types of concrete deterioration using the different types of imagery, along with their corresponding binary images. Tables providing the class statistic summary, which indicates the number of pixels classified into each object class, and the percentage of the image occupied by each class, are also given in Chapter Four.

CHAPTER 4

Results and Discussion

4.1 Damage Analysis of Map-crack Imagery from Field Samples

The first stage of the damage analysis of the map-crack imagery examines images obtained from field samples, which consist of deteriorated concrete components from various bridges, as described in section 3.1. All of the images exhibit different degrees of map-crack damage due to the alkali-aggregate reaction.

4.1.1 Application of Haar's Wavelet Transform

4.1.1.1 Image Decomposition

Figure 4.1 presents an example of image decomposition through the wavelet transform using a sample of a greyscale map-crack image taken from the field samples. Figure 4.1(a) is the input image, Figure 4.1(b) is the result of a one-level pyramidal decomposition of the image, Figure 4.1(c) is what the image looks like after several levels of decomposition, and Figure 4.1(d) is the fully decomposed image.

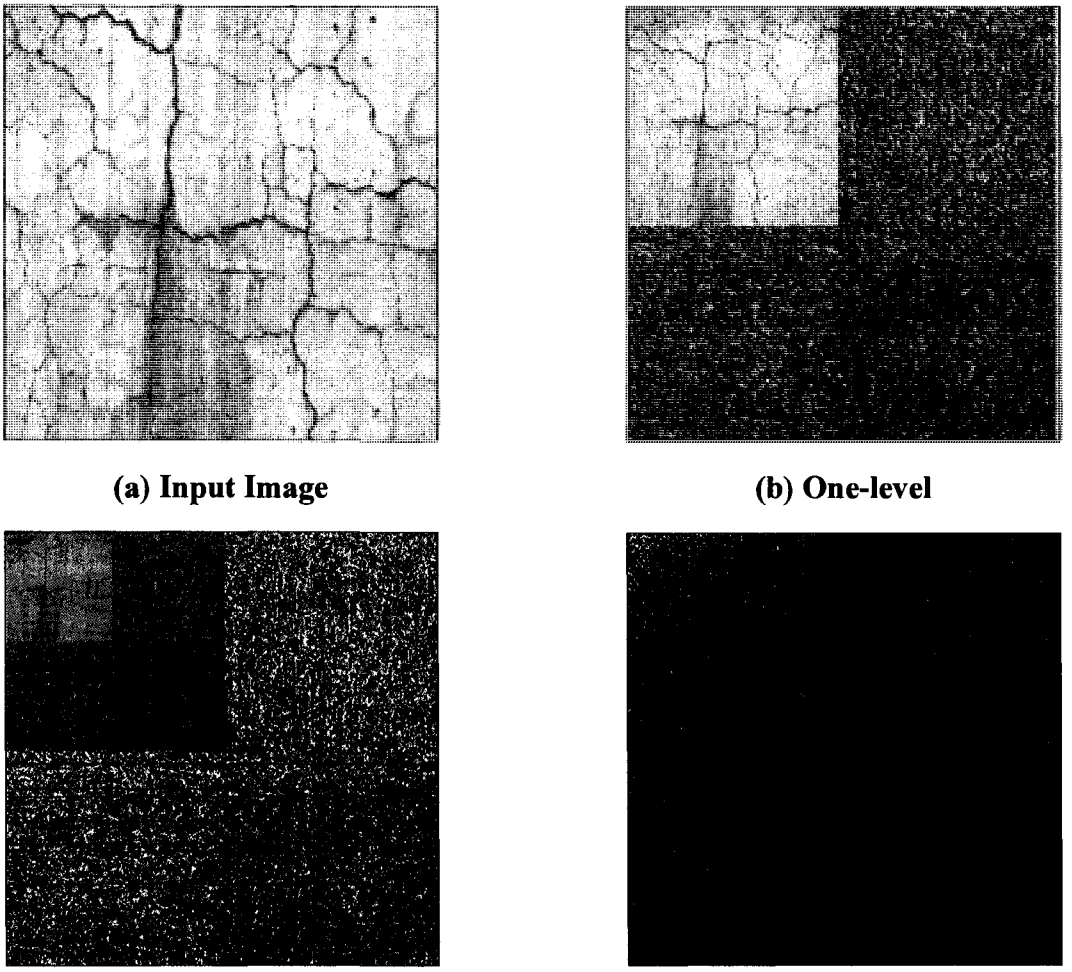

(a) Input Image **(b) One-level**

(c) Two-level **(d) Complete**

Figure 4.1: Decomposition of Greyscale Map-Crack Image

4.1.1.2 Image Reconstruction

Figure 4.2 shows an example of image reconstruction using the same greyscale map-crack image sample presented for the decomposition step. Figure 4.2(a) is the 1% reconstruction, Figure 4.2(b) is the 5% reconstruction, Figure 4.2(c) is the 10% reconstruction, and Figure 4.2(d) is the 25% reconstruction; the 25% reconstruction is the level employed for all of the reconstructed images in this study.

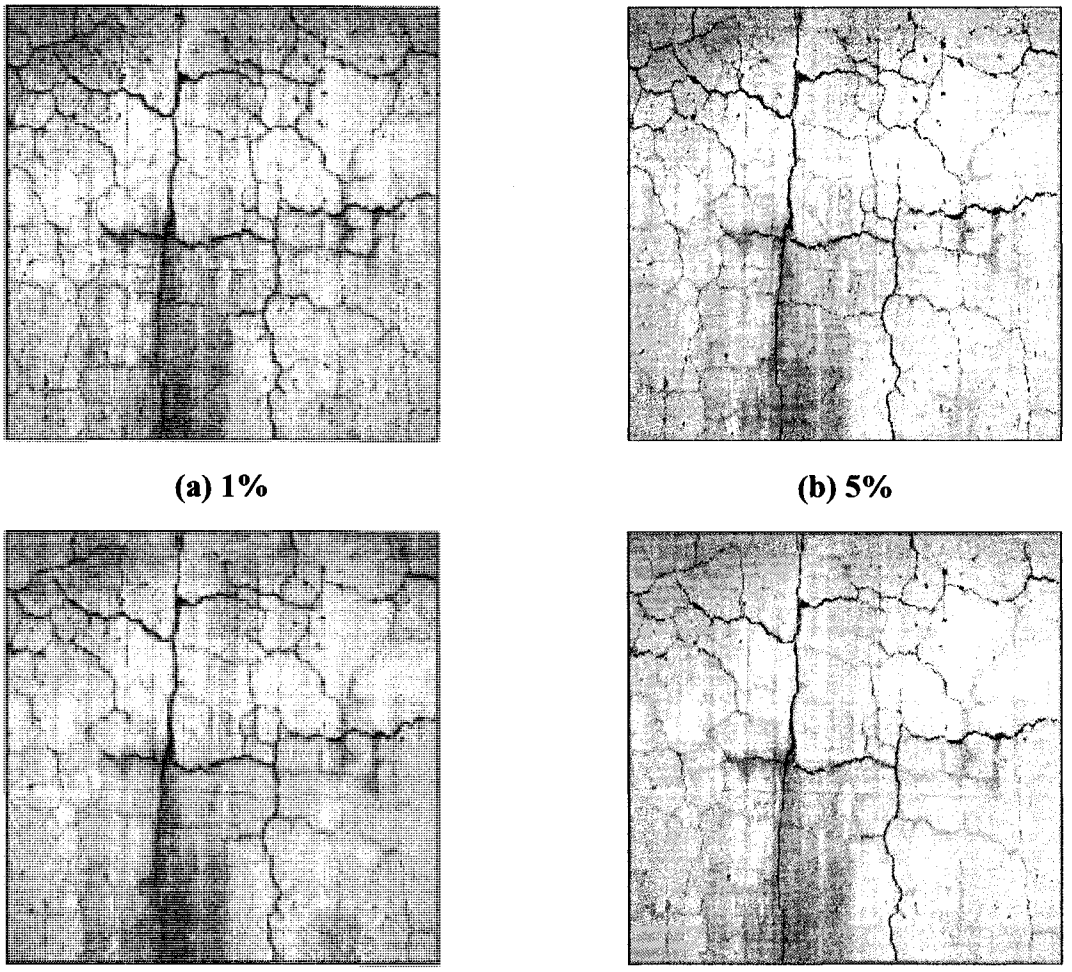

(a) 1%

(b) 5%

(c) 10%

(d) 25%

Figure 4.2: Different Levels of Reconstruction for Greyscale Map-Crack Image

4.1.2 Application of Texture Analysis

4.1.2.1 Selection of Appropriate Window

In order to determine the most appropriate window size, the homogeneity texture feature was randomly chosen for computing the coefficients of variation for each class according to different window sizes. The coefficients of variation calculated for the greyscale map-crack image are given in Figure 4.3, which shows that the coefficients stabilized around the 11x11 window for the majority of the object classes.

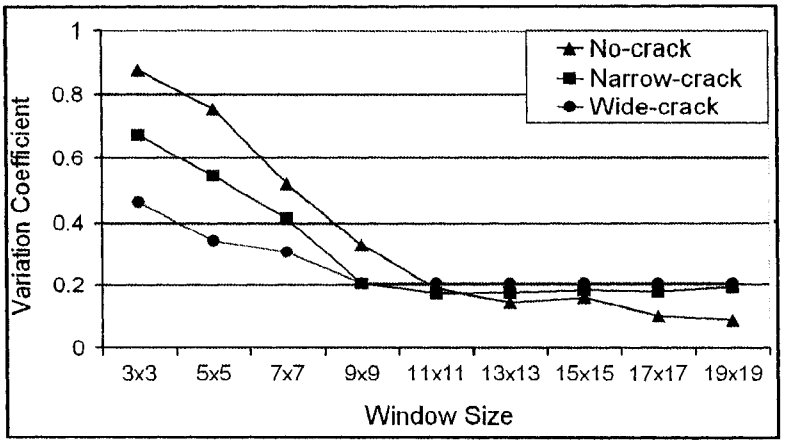

Figure 4.3: Coefficients of Variation Graph for Greyscale Map-crack Image

4.1.2.2 First-order Statistics for Greyscale Map-crack Image

First-order statistics are calculated from the histogram of an image; texture features are then extracted from these statistics. Figure 4.4 presents the five first-order texture features obtained for the reconstructed image of the greyscale map-crack image sample employed in the signal processing phase. The most effective texture features are selected through visual analysis of the texture features, histogram analysis and calculation of the correlation matrix. Figure 4.5 shows the histograms of the first-order texture features and Table 4.1 gives the correlation matrix for the features. Figure 4.6 is an example of a texture image resulting from the first-order texture features selected through the feature selection process. This texture image was produced using the mean, variance and skew texture features, which were selected for the greyscale map-crack image sample.

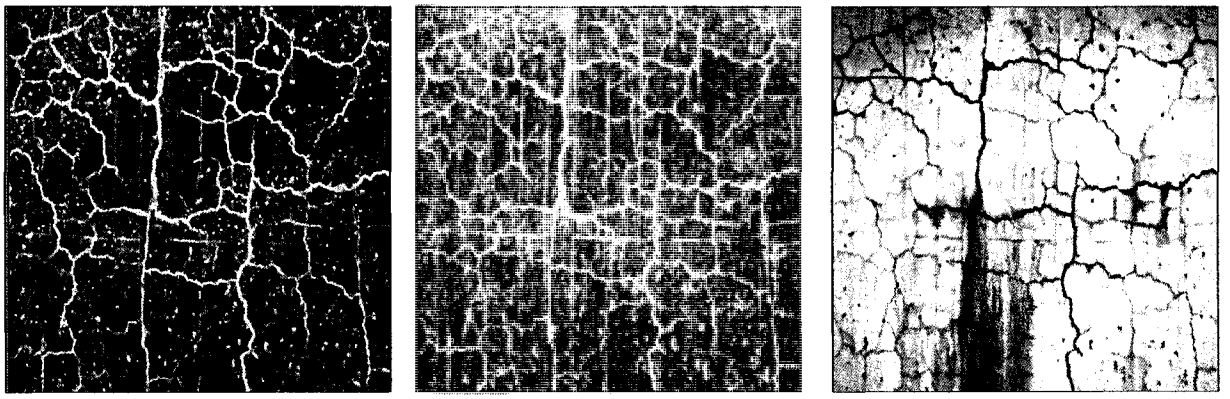

(a) Data Range (b) Entropy (c) Mean

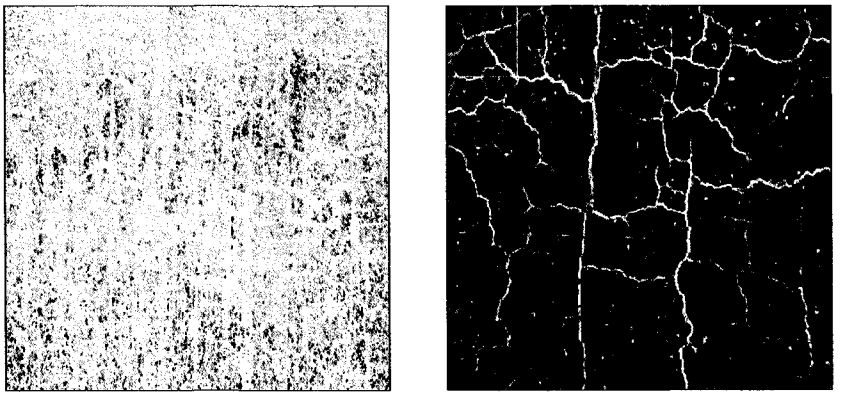

(d) Skew (e) Variance

Figure 4.4: First-order Texture Features for Greyscale Map-crack Image

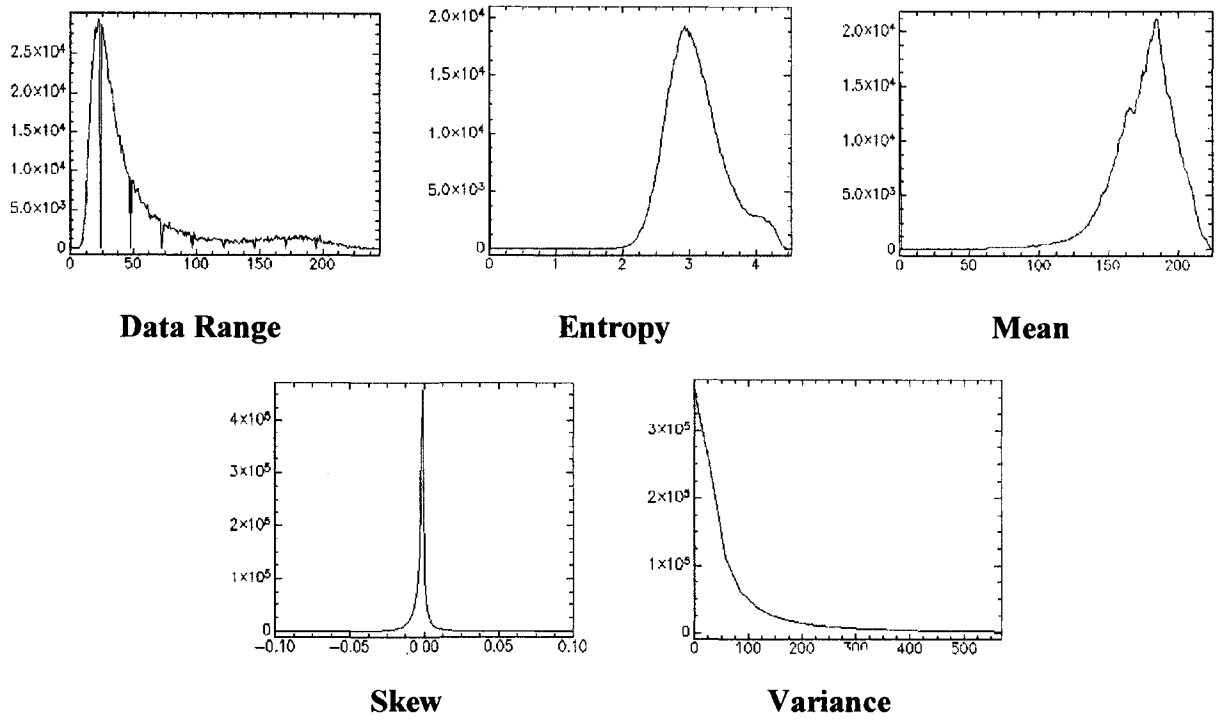

Figure 4.5: Histograms of First-order Features for Greyscale Map-crack Image

Table 4.1: Correlation Matrix of First-order Texture Features for Greyscale Map-crack Image

Features	Data Range	Mean	Variance	Entropy	Skew
Data Range	1.000	-0.229	0.812	0.669	0.100
Mean	-0.229	1.000	-0.322	0.246	-0.110
Variance	0.812	-0.322	1.000	0.499	0.077
Entropy	0.669	0.246	0.499	1.000	0.122
Skew	0.100	-0.111	0.077	0.122	1.000

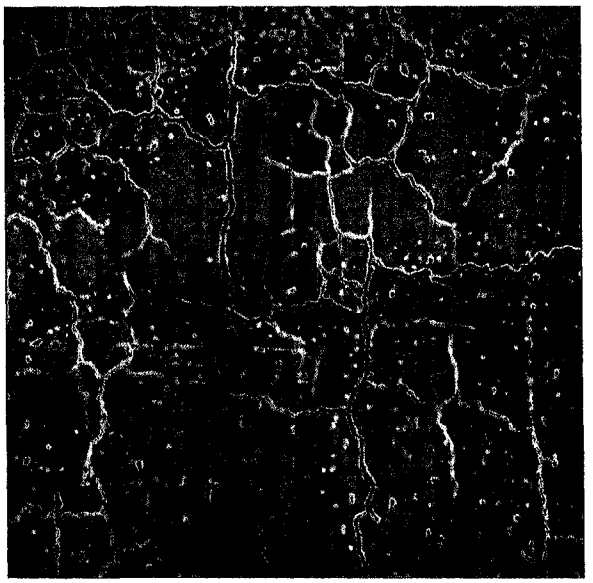

Figure 4.6: Texture Image of Selected First-order Features for Greyscale Map-crack Image: Mean, Variance, Skew

4.1.2.3 Second-order GLCM for Greyscale Map-crack Image

The GLCM was calculated for each image sample using one pixel distance, a direction of 0° between pixels, and the most appropriate window size, which in the case of the greyscale map-crack image sample employed in the signal processing phase, was an 11x11 window. Figure 4.7 shows the second-order texture features that were extracted from the GLCM for the reconstructed image of the greyscale image sample.

A feature selection process was also employed for selecting the most useful second-order texture features. Figure 4.8 presents the histograms of the eight texture features and Table 4.2 gives the correlation matrix for the features. Figure 4.9 is an example of the texture image produced using the most effective second-order texture features, selected through the feature selection process. This texture image displays the mean, homogeneity and entropy second-order texture features that were selected for the greyscale map-crack image sample.

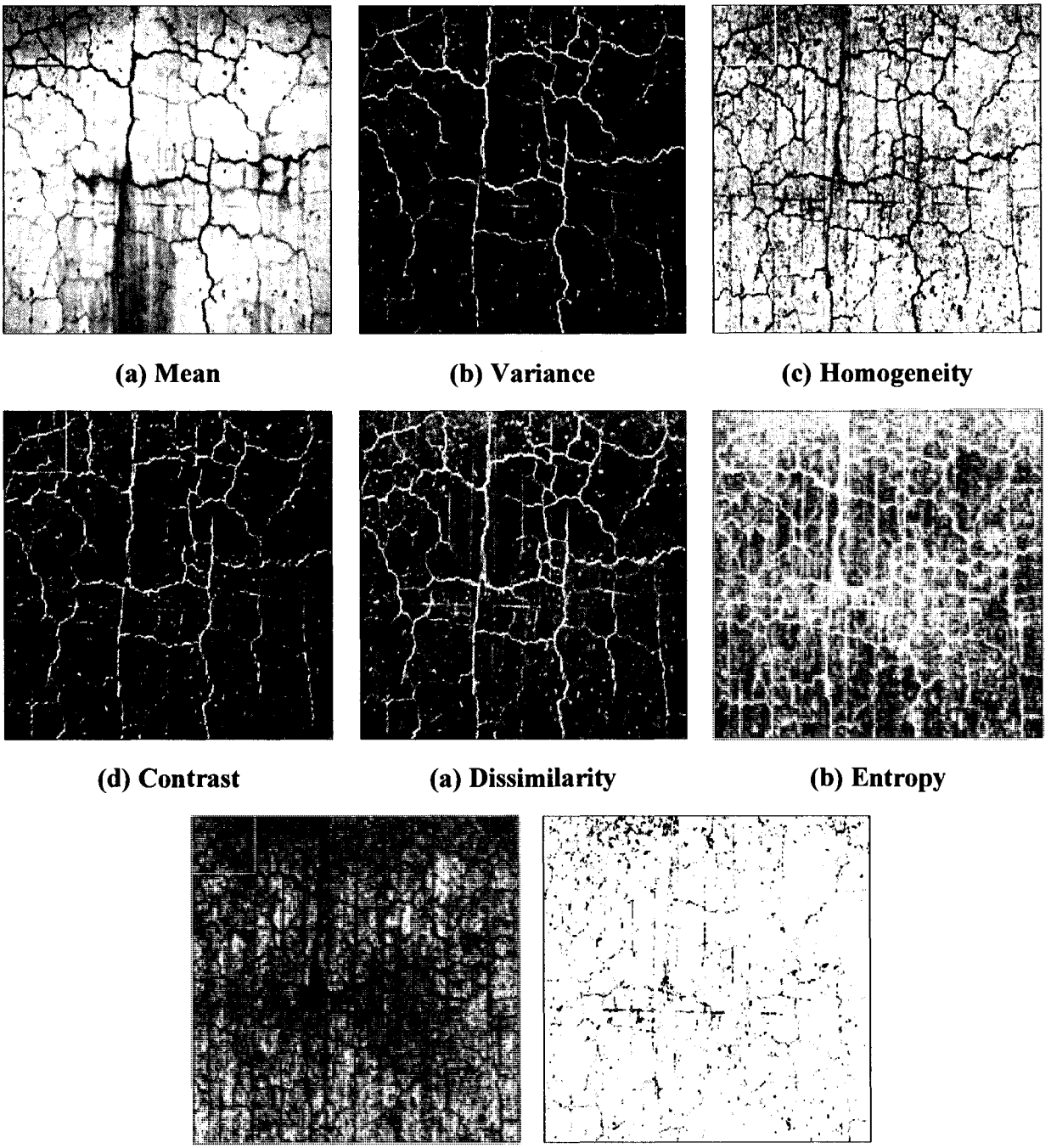

(a) Mean (b) Variance (c) Homogeneity

(d) Contrast (a) Dissimilarity (b) Entropy

(c) Second Moment (d) Correlation

Figure 4.7: Second-order Texture Features for Greyscale Map-crack Image

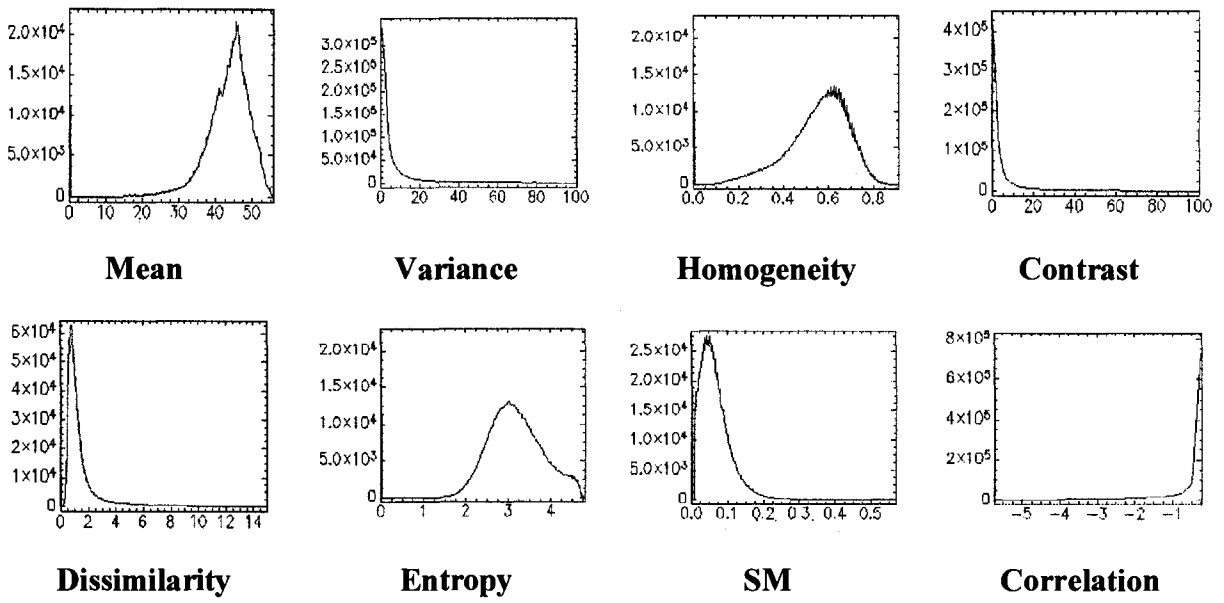

Figure 4.8: Histograms of Second-order Features for Greyscale Map-crack Image

Table 4.2: Correlation Matrix of Second-order Texture Features for Greyscale Map-crack Image

Features	Mean	Var	Homo	Cont	Diss	Ent	SM	Corr
Mean	1	-0.312	0.684	-0.240	-0.229	0.174	0.425	0.228
Var	-0.312	1	-0.515	0.833	0.857	0.500	-0.360	-0.376
Homo	0.684	-0.515	1	-0.512	-0.617	-0.324	0.797	0.450
Con	-0.240	0.833	-0.512	1	0.942	0.470	-0.338	-0.391
Diss	-0.229	0.857	-0.617	0.942	1	0.679	-0.486	-0.525
Ent	0.174	0.500	-0.324	0.470	0.679	1	-0.571	-0.454
SM	0.425	-0.360	0.797	-0.338	-0.486	-0.571	1	0.335

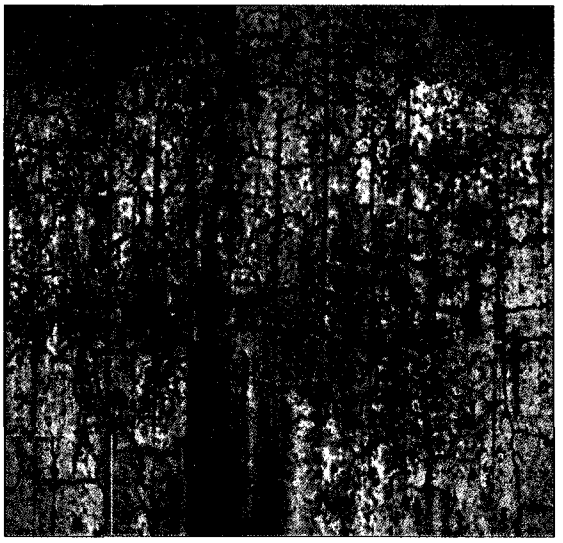

Figure 4.9: Texture Image of Selected Second-order Features for Map-crack Image: Mean, Homogeneity, Entropy

4.2 Damage Analysis of CANMET and GRAI Laboratory Specimens

The second stage of the map-crack damage analysis deals with images of laboratory specimens. The methodology described in sections 3.4 and 3.5 was applied to imagery of the CANMET blocks and GRAI slabs. Descriptions of these specimens can be found in section 3.2; these images also manifest map-crack damage typical of AAR.

4.2.1 CANMET Block Specimens

Figure 4.10 shows raw image samples of the three CANMET blocks, referred to in this study as C1, C2, and C3. The least amount of damage is displayed by C1, whereas C2 has a moderate amount of cracking, and C3 demonstrates the highest amount of map-crack damage.

In this analysis, the methodology was applied on imagery of the CANMET laboratory specimens. Haar's wavelet transform was applied on the imagery, as described in section 3.4, after which the 25% reconstructions were produced according to the steps in section 3.4.2. The texture features selected through the first-order statistical analysis, described under section 3.5.1, for the greyscale image of the C3 CANMET specimen is presented in Figure 4.11.

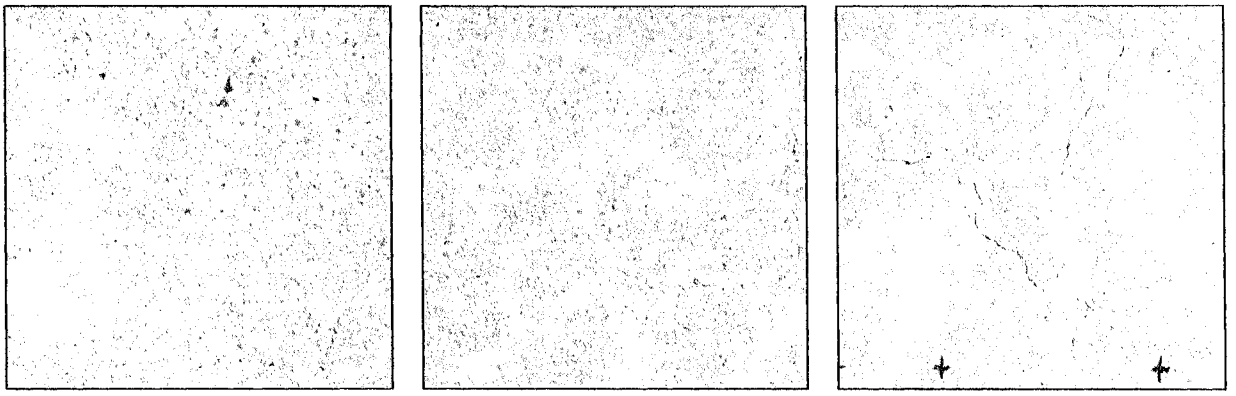

(a) C1 (b) C2 (c) C3

Figure 4.10: Image Samples of CANMET Specimens

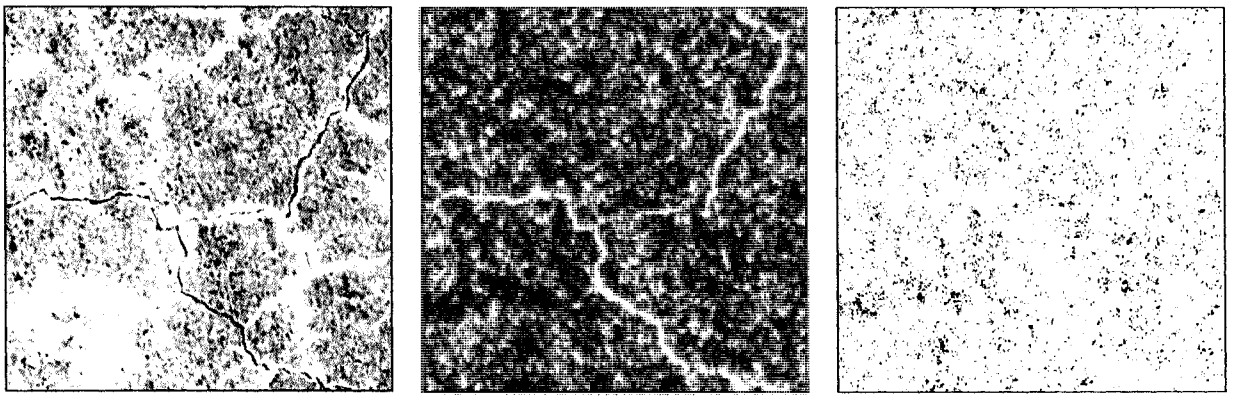

(a) Mean (b) Variance (c) Skew

Figure 4.11: Selected Texture Features from First-order Statistics for C3 Specimen

The second-order texture features selected for the same C3 image through the GLCM analysis outlined in section 3.5.2 are provided in Figure 4.12. Figure 4.13(a) is an example of the texture image obtained by selecting the most effective first-order texture features, mean, variance and skew; Figure 4.13(b) is an example of the texture image produced using the selected second-order texture features, mean, homogeneity and entropy.

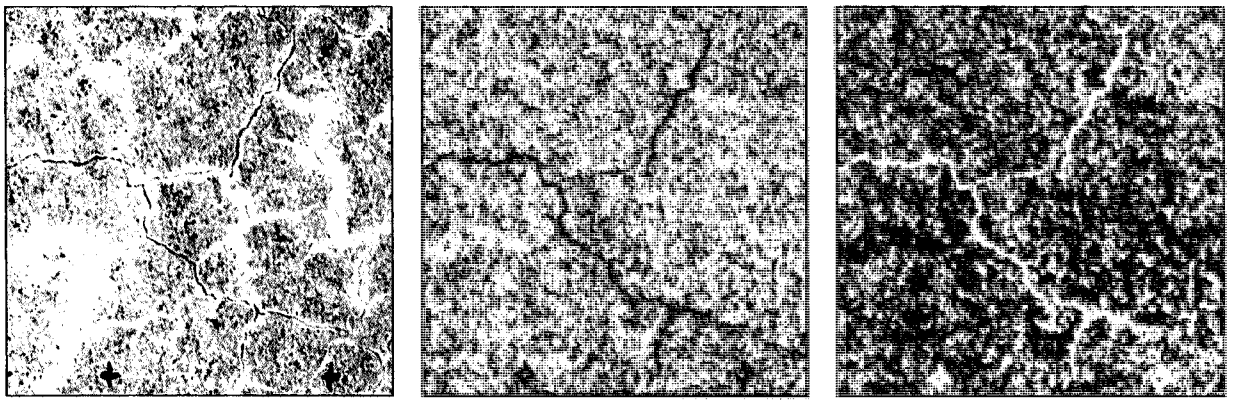

(a) Mean **(b) Homogeneity** **(c) Entropy**

Figure 4.12: Selected Texture Features from Second-order Statistics for C3 Specimen

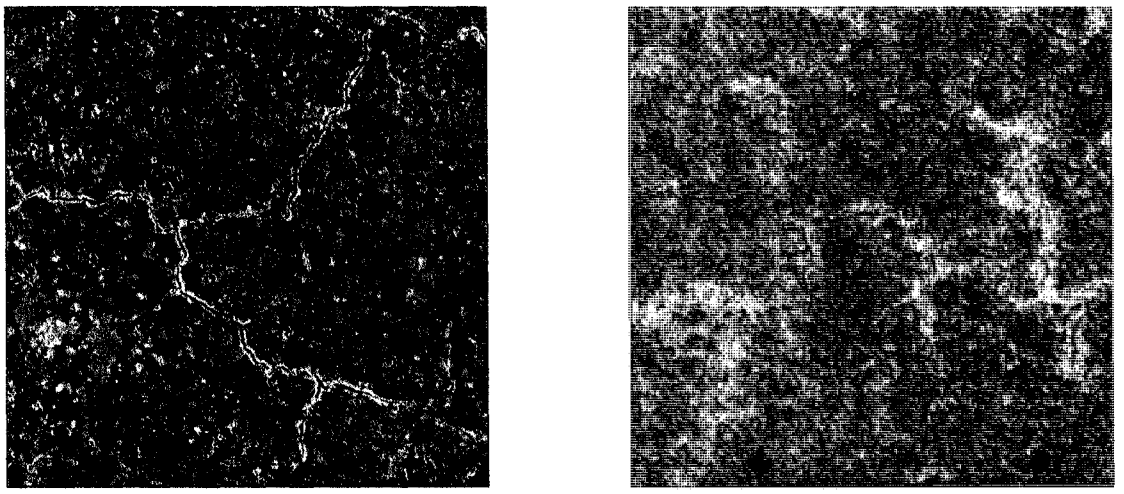

(a) First-order: Mean, Variance, Skew **(b) Second-order: Mean, Homogeneity, Entropy**

Figure 4.13: Texture Images of Selected Features for C3 Specimen

4.2.2 GRAI Slab Specimens

Figure 4.14 shows image samples of the three GRAI slabs, labelled G1, G2, and G3. As with the CANMET blocks, G1 has the least amount of damage, G2 shows a moderate amount, and G3 manifests the highest amount of crack damage.

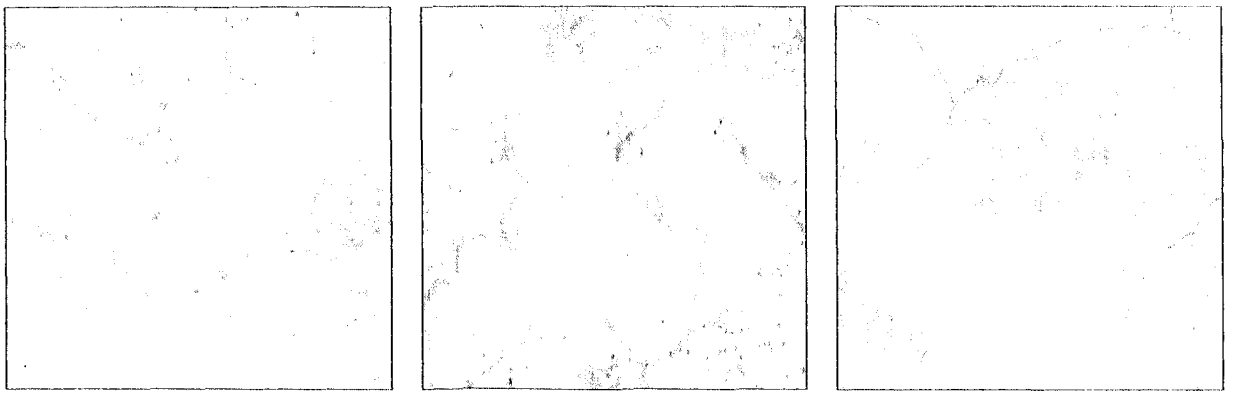

(a) G1 (b) G2 (c) G3

Figure 4.14: Image Samples of GRAI Laboratory Specimens

Haar's wavelet transform was applied on the imagery, as described in section 3.4, after which the 25% reconstructions were produced according to the steps in section 3.4.2. Texture features were then selected through the first-order statistical analysis, described under section 3.5.1. The selected first-order texture features for the reconstructed greyscale image of the G1 slab are presented in Figure 4.15, and the texture image is given in Figure 4.16. For the reconstructed greyscale image of the G2 slab, the most effective first-order texture features are provided in Figure 4.17, and the texture image of the selected features can be seen in Figure 4.18. The first-order texture features selected for the reconstructed greyscale image of the G3 specimen and the texture image of the features are given in Figure 4.19 and Figure 4.20, respectively.

For the second-order texture features, the features selected for the reconstructed greyscale image of the G2 specimen are given in Figure 4.21, and the texture image of the selected features is presented in Figure 4.22.

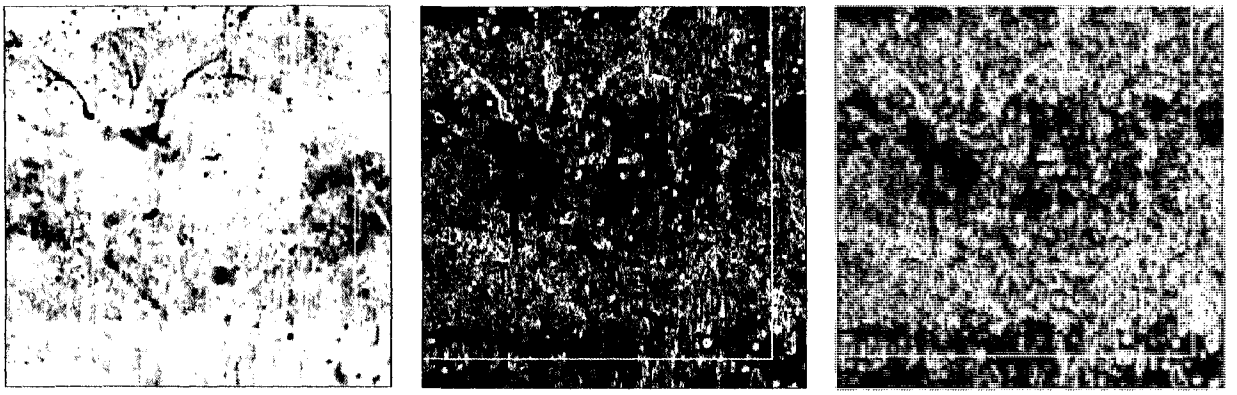

(a) Mean (b) Variance (c) Entropy

Figure 4.15: Selected First-order Texture Features for G1 Specimen

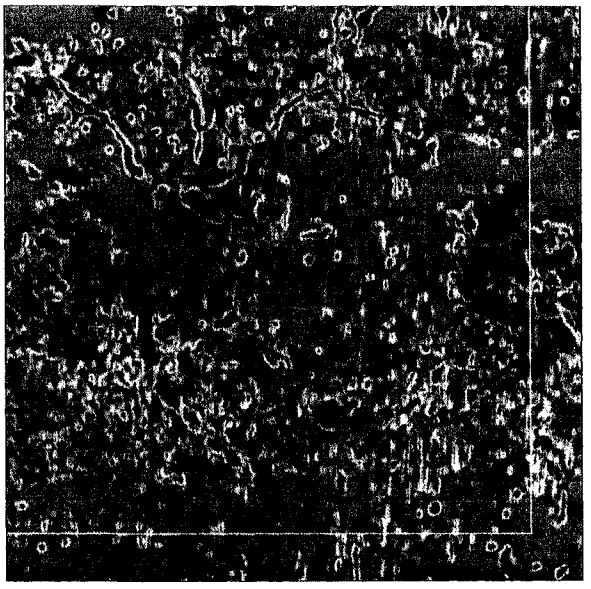

Figure 4.16: Texture Image of Selected First-order Features for G1 Specimen: Mean, Variance, Entropy

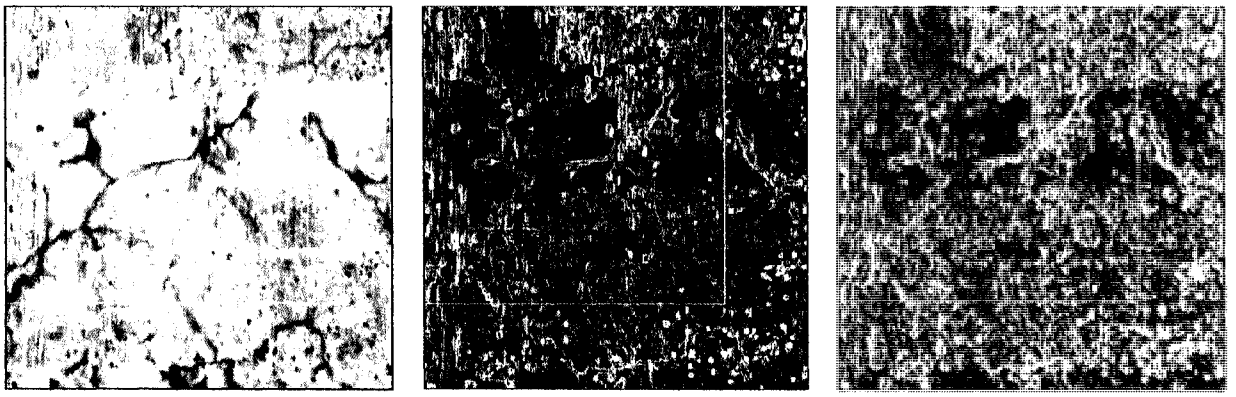

(a) Mean (b) Variance (c) Data Range

Figure 4.17: Selected First-order Texture Features for G2 specimen

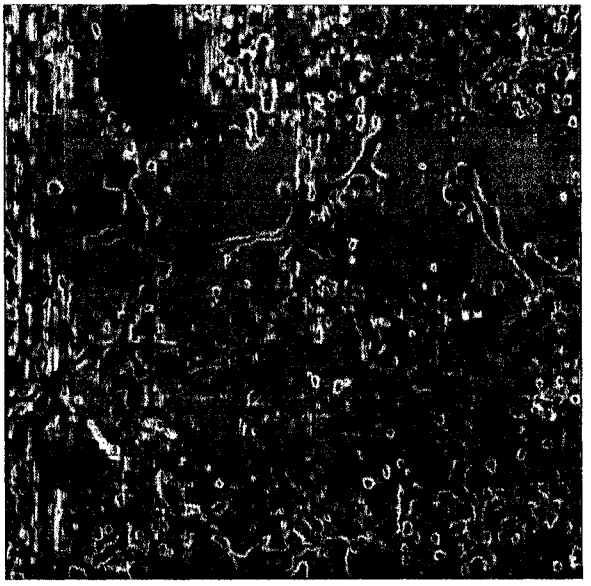

Figure 4.18: Texture Image of Selected First-order Features for G2 Specimen: Mean, Variance, Data Range

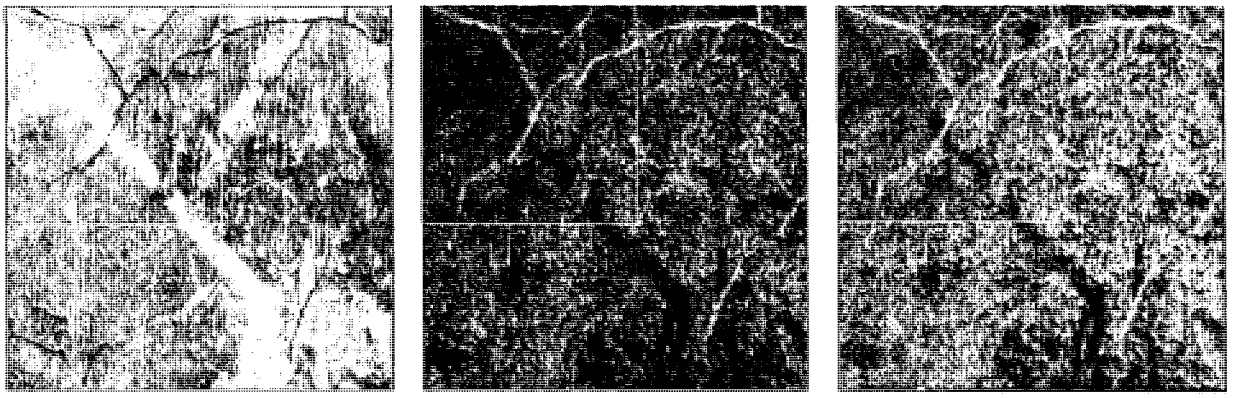

(a) Mean (b) Variance (c) Data Range

Figure 4.19: Selected First-order Texture Features for G3 Specimen

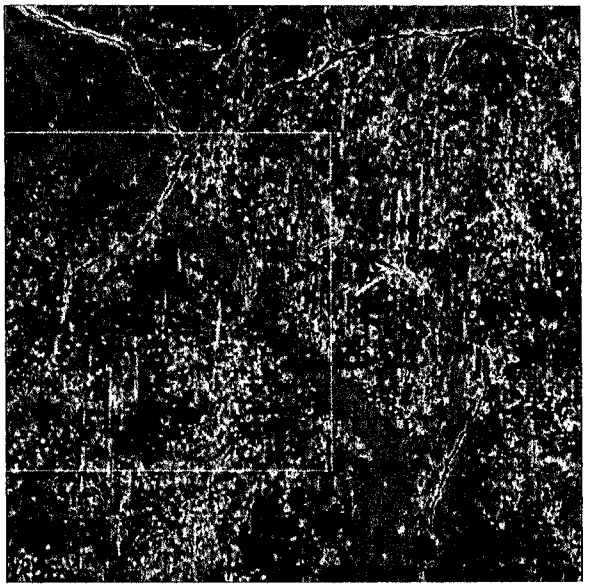

Figure 4.20: Texture Image of Selected First-order Features for G3 Specimen: Mean, Variance, Data Range

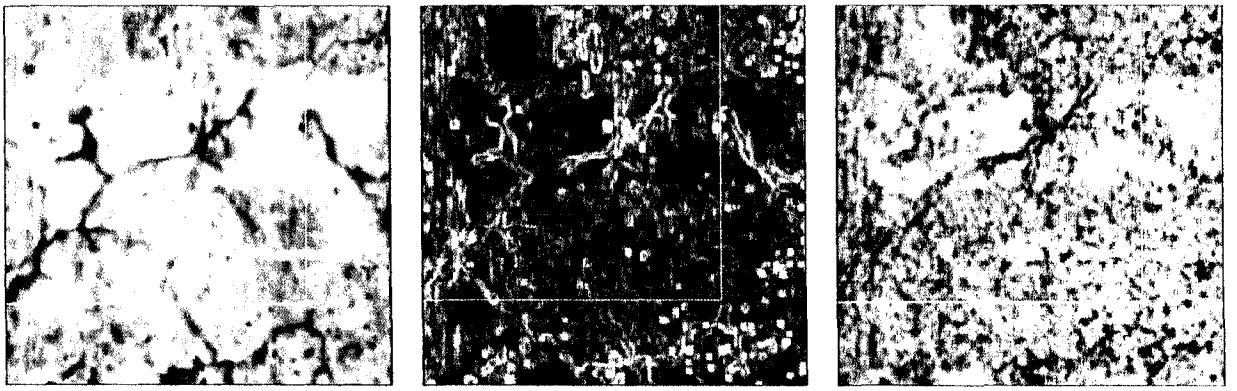

(a) Mean (b) Variance (c) Homogeneity

Figure 4.21: Selected Second-order Texture Features for G2 Specimen

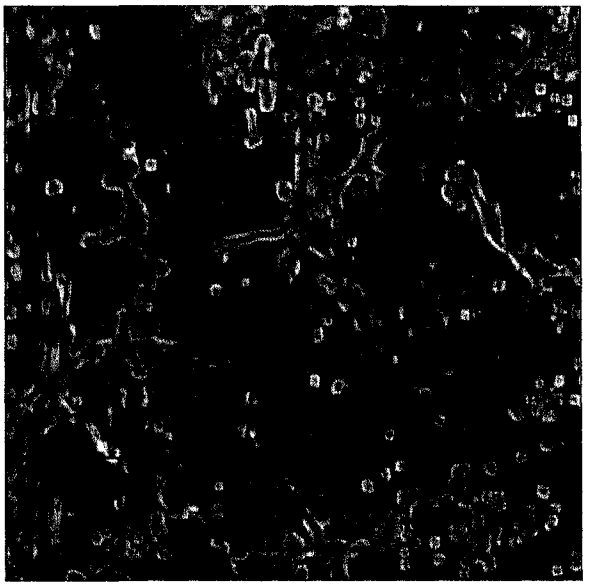

Figure 4.22: Texture Image of Selected Second-order Features for G2 Specimen: Mean Variance, Homogeneity

4.2.3 Damage Analysis of G3 GRAI Slab using Greyscale, Colour and Thermographic Imagery

Damage analysis was carried out on thermographic (TIR) and colour images of the laboratory specimens in order to determine the contribution of such imagery to the analysis of crack damage. The analysis conducted for the G3 GRAI slab is presented in this section. Figure 4.23 presents the original greyscale image with the corresponding thermographic image. The black line seen around the image is a wire that was used as a reference to set the layout of the image.

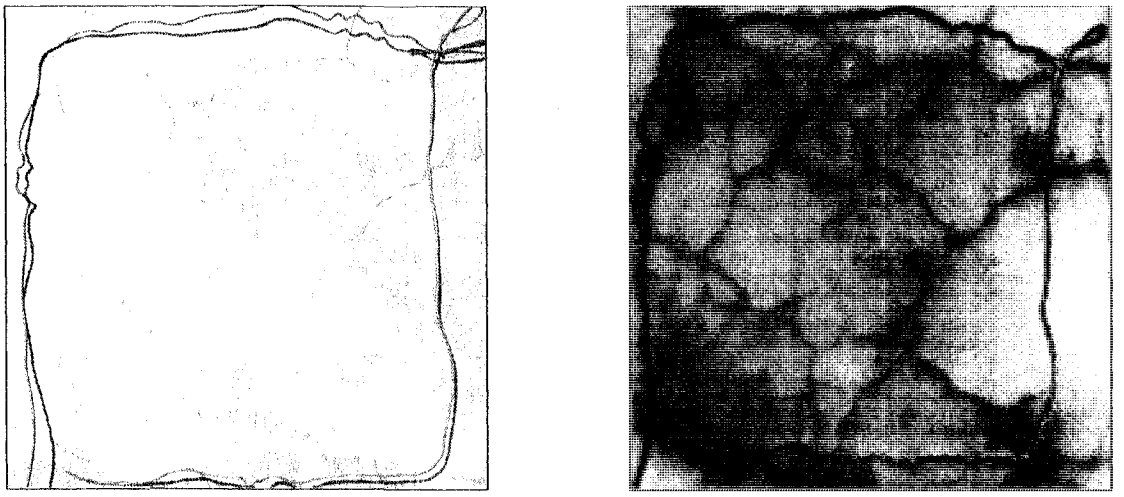

(a) Greyscale **(b) Thermographic**

Figure 4.23: Original Greyscale and TIR Images of G3 GRAI Slab

Figure 4.24 shows the resampled greyscale, thermographic, and colour images that were employed in this damage analysis. Haar's wavelet transform was applied on the imagery, as described in section 3.4, after which the reconstructions were produced according to the steps in section 3.4.2. Texture features were extracted through the first-order statistical analysis, described under section 3.5.1. The selected first-order texture features for the reconstructed greyscale G3 image, along with the texture image are shown in section 4.2.2 above, in Figures 4.19 and 4.20, respectively. The eight second-order texture features extracted through the GLCM analysis outlined in section 3.5.2 for the greyscale image of the G3 specimen are given in Figure 4.25; Figure 4.26 shows the texture image of the second-order texture features, mean, homogeneity and variance, selected for the greyscale image of the G3 specimen.

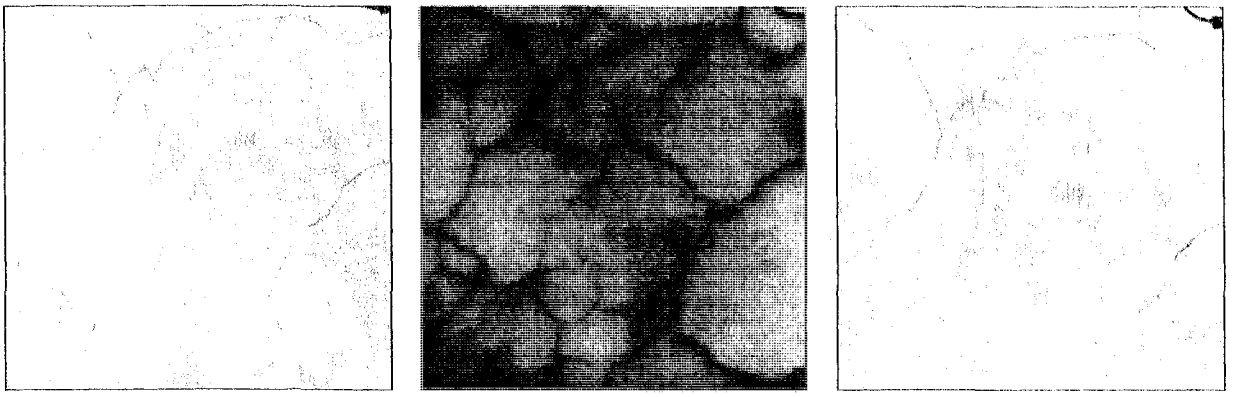

(a) Greyscale (b) Thermographic (c) Colour

Figure 4.24: Resampled Greyscale, Thermographic, and Colour Images for G3 Slab

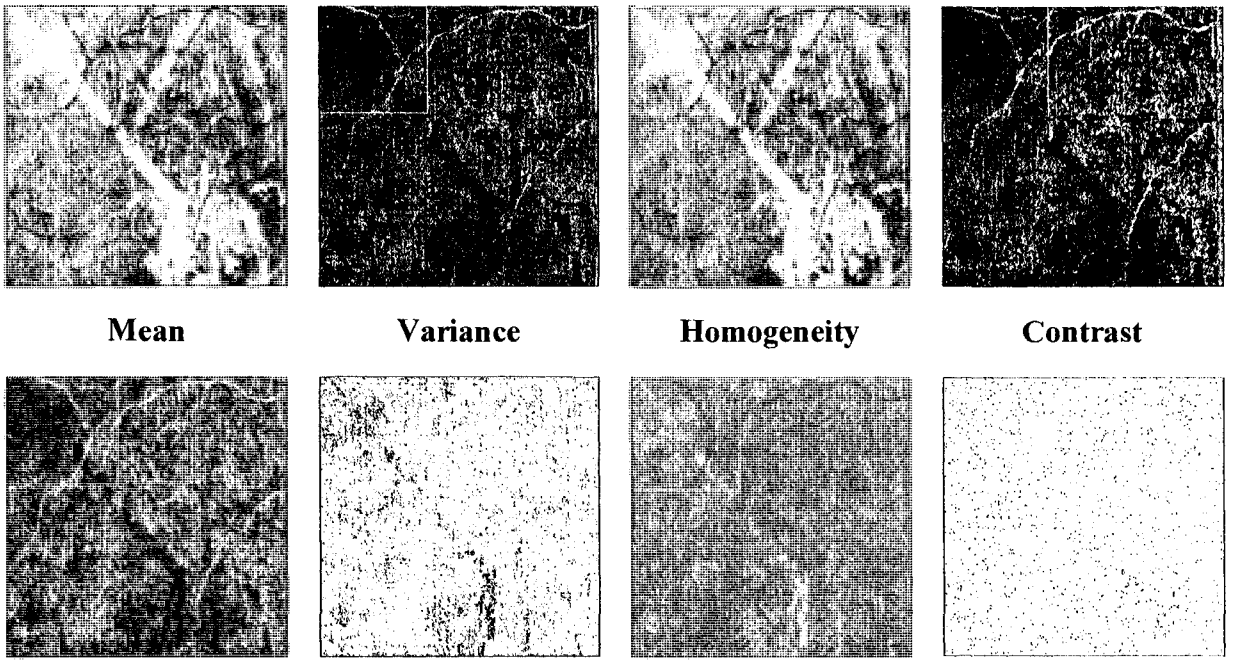

Mean Variance Homogeneity Contrast

Dissimilarity Entropy SM Correlation

Figure 4.25: Second-order Texture Features for Greyscale G3 Image

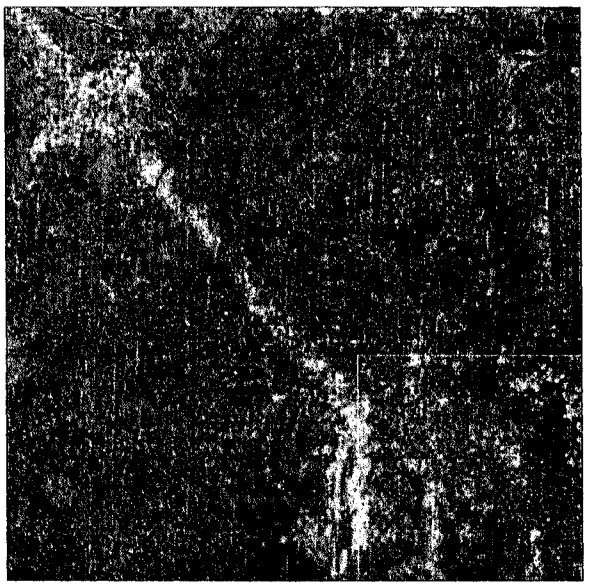

Figure 4.26: Texture Image of Selected Second-order Features for Greyscale G3 Image: Mean, Homogeneity, Variance

For the thermographic and colour imagery, the texture analysis results in three times the number of texture features as the greyscale images. This is due to the fact that these two types of imagery are encoded in three colour bands, red, green and blue, compared to grey levels used in encoding greyscale images. Consequently, the GLCM texture analysis of the thermographic and colour imagery resulted in 24 second-order texture features for each image.

Figure 4.27 displays some of the eight second-order texture features extracted from the red band of the thermographic image of the G3 specimen. Figure 4.28 presents all eight of the second-order texture features derived from the green band of the thermographic image, and Figure 4.29 shows the texture image of the selected second-order features. Some of the second-order texture features derived from the GLCM analysis for the colour image of the G3 specimen are given in Figure 4.30, and the texture image of the second-order features selected for the colour G3 image is presented in Figure 4.31.

Figure 4.29 is the texture image of the second-order features, the mean feature from the red band, the homogeneity feature from the blue band, and the correlation feature from the blue band, selected as the most effective features for the thermographic image of the G3 specimen.

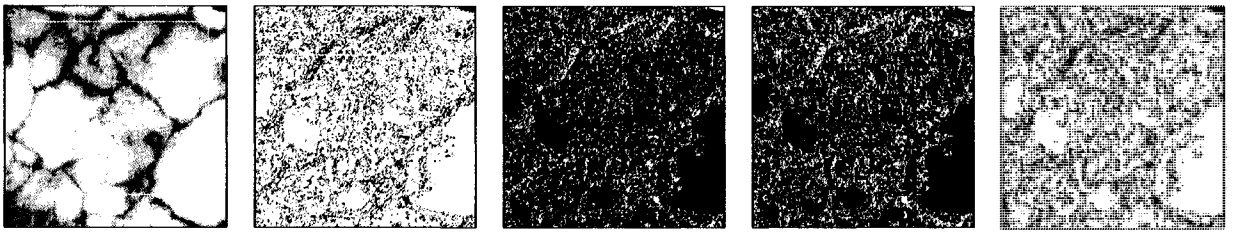

Mean Homogeneity Dissimilarity Entropy SM

Figure 4.27: Some Second-order Texture Features from Red Band of TIR G3 Image

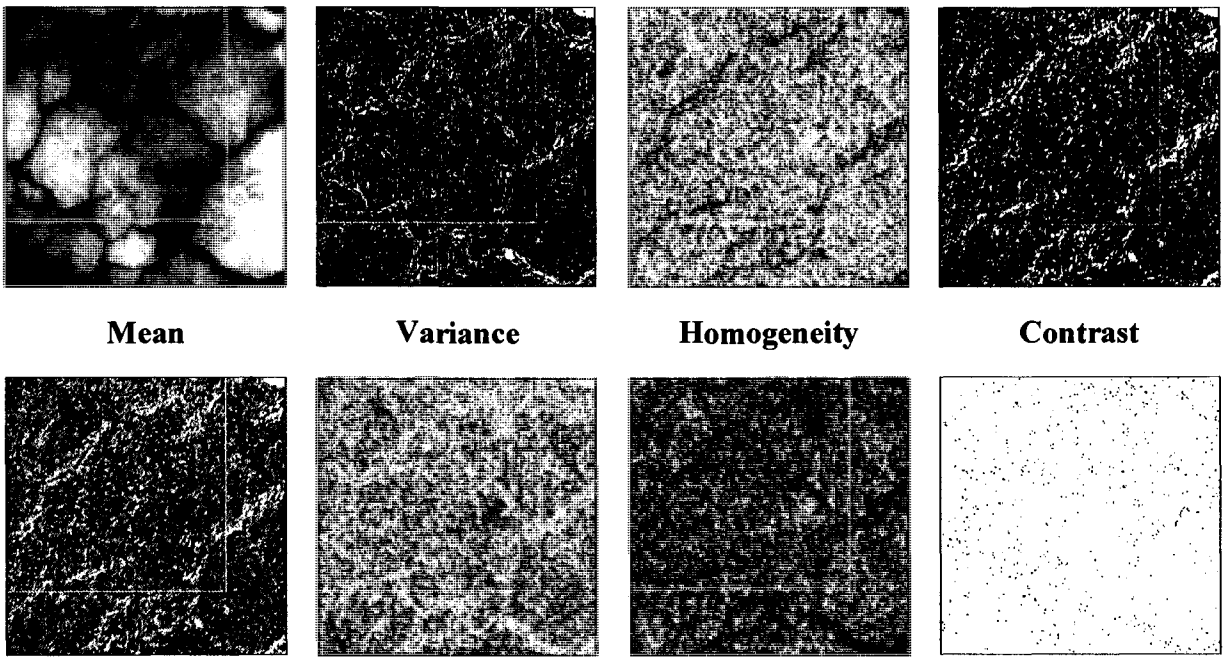

Mean Variance Homogeneity Contrast

Dissimilarity Entropy SM Correlation

Figure 4.28: Second-order Texture Features from Green Band of TIR G3 Image

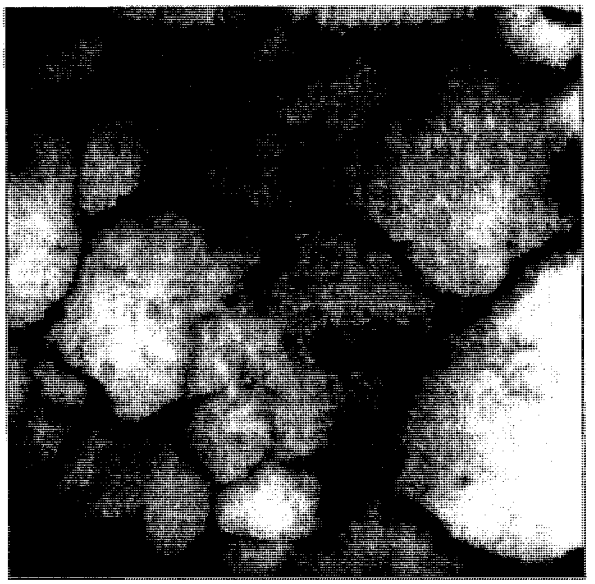

Figure 4.29: Texture Image of Selected Second-order Features for TIR G3 Image: Mean (red), Homogeneity (blue), Correlation (blue)

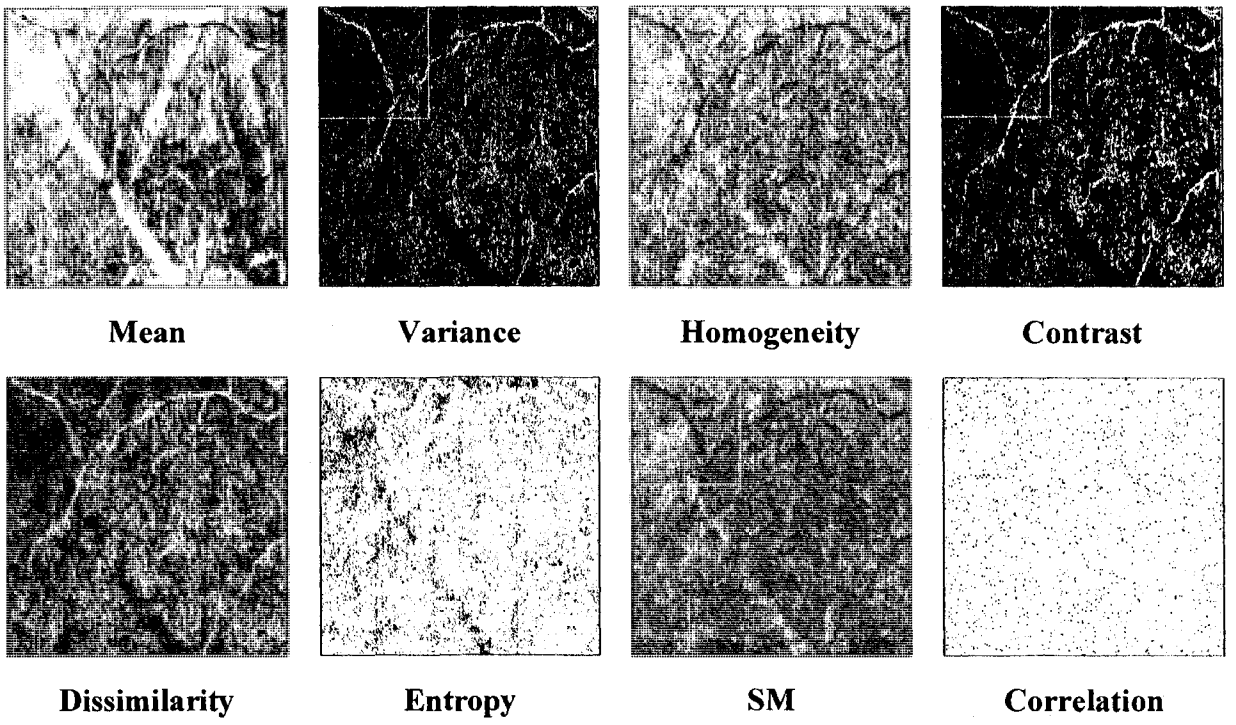

Figure 4.30: Second-order Texture Features from Green Band of Colour G3 Image

Figure 4.30 displays the eight second-order texture features derived through the GLCM analysis from the green band of the colour image for the G3 specimen. Figure 4.31 presents the texture image of the selected second-order features for the colour image: the mean feature from the red band, the homogeneity feature from the blue band, and the correlation feature from the blue band.

Figure 4.31: Texture Image of Selected Second-order Features for Colour G3 Image: Mean (red), Homogeneity (blue), Correlation (blue)

4.3 Damage Analysis of Spalling Imagery from Field Samples

Another stage of the damage analysis consists of application of the methodology outlined in sections 3.4 and 3.5 for the analysis of spalling damage from images of field samples. In this stage, greyscale images of deteriorated concrete components from various bridges were processed using Haar's discrete wavelet transform, which is explained in section 3.4. Figure 4.32 presents the decomposition of an image sample of a bridge component exhibiting spalling damage: Figure 4.32(a) is the input image, Figure 4.32(b) is a one-level pyramidal decomposition of the image, Figure 4.32(c) is the result after several levels of decomposition, and Figure 4.32(d) is the complete decomposition. The reconstruction process described in section 3.4.2 was applied to produce reconstructions using the wavelet coefficients obtained from

the decomposed imagery. Figure 4.33 displays the various reconstructions of the greyscale spalling image shown in the decomposition step. Figure 4.33(a) is the image reconstructed to 1%, Figure 4.33(b) is the 5% reconstruction, Figure 4.33(c) is the 10% reconstruction, and Figure 4.33(d) is the image reconstructed to 25%. The 25% reconstructions were employed in the subsequent analysis steps.

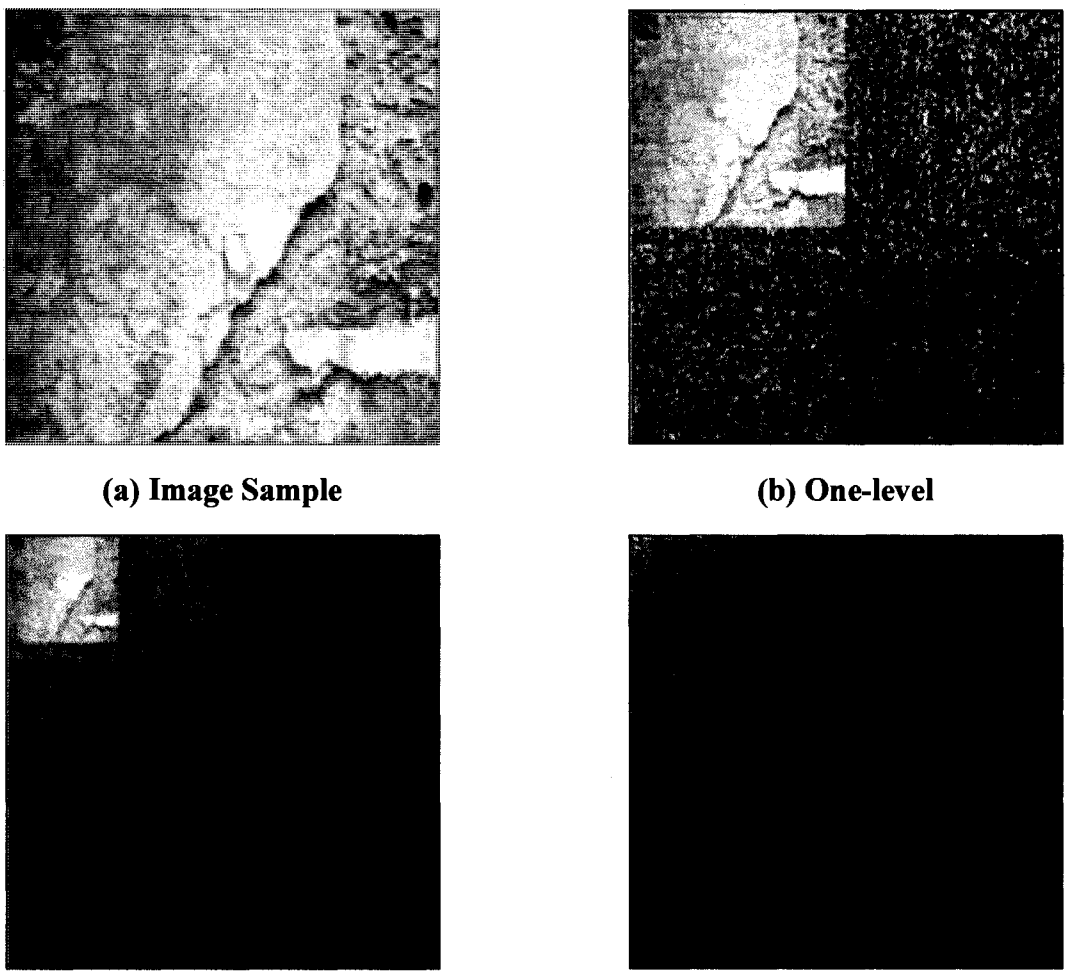

(a) Image Sample **(b) One-level**

(c) Two-level **(d) Complete**

Figure 4.32: Decomposition of Greyscale Spalling Image

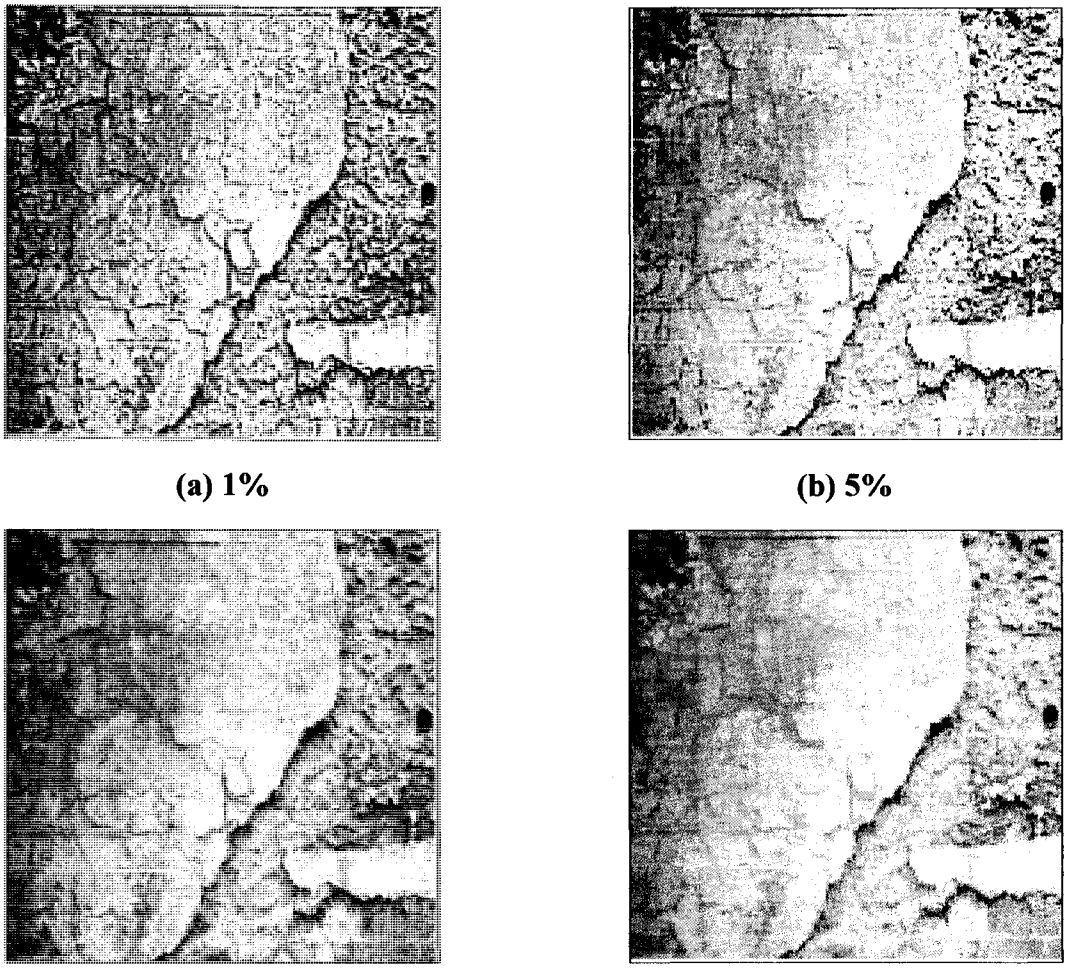

(a) 1% **(b) 5%**

(c) 10% **(d) 25%**

Figure 4.33: Different Levels of Reconstruction for Greyscale Spalling Image

The first-order and second-order statistical texture analysis processes, explained in sections 3.5.1 and 3.5.2, were applied on the spalling imagery. The coefficients of variation graph that was calculated for the GLCM analysis of the spalling image is given in Figure 4.34. The selected second-order texture features for the spalling image are presented in Figure 4.35, and the texture image of the second-order features is presented in Figure 4.36.

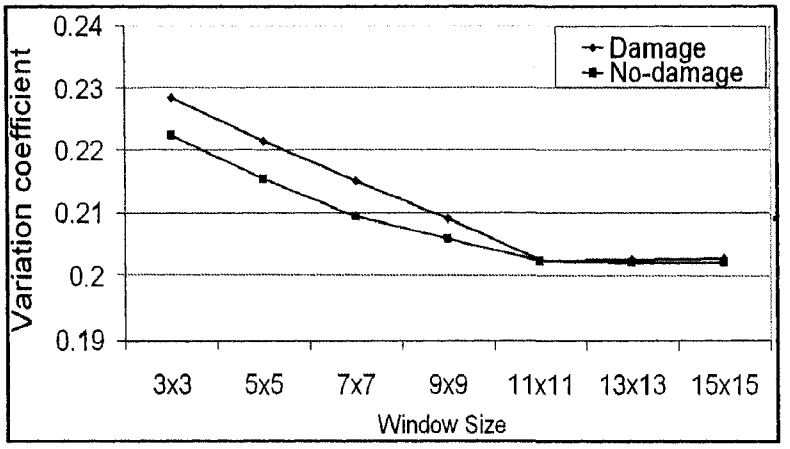

Figure 4.34: Coefficients of Variation Graph for Greyscale Spalling Image

(a) Mean **(b) Variance** **(c) Contrast**

Figure 4.35: Selected Second-order Features for Spalling Image

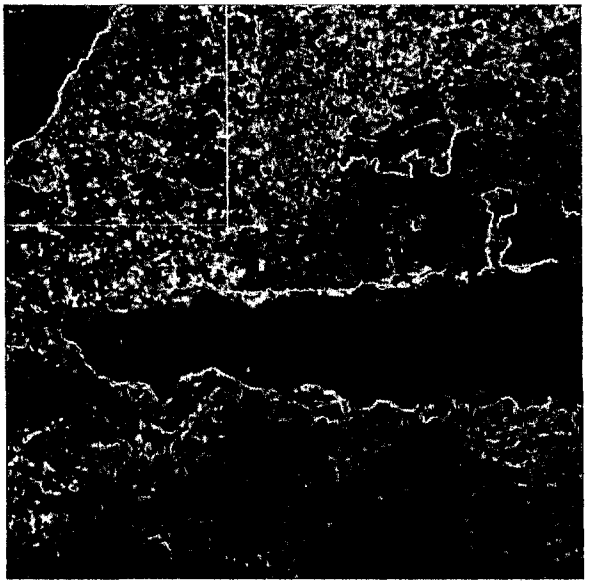

Figure 4.36: Texture Image of Selected Second-order Features for Spalling Image: Mean, Variance, Contrast

4.4 Damage Analysis of Corrosion Images from Field Samples

The damage analysis methodology explained in sections 3.4 and 3.5 was also applied for the investigation of corrosion damage in field samples. Greyscale images of bridge components exhibiting corrosion damage were resampled and decomposed using the Haar wavelet transform. The reconstructed images were further analyzed through the first- and second-order texture analysis process. Figure 4.37 provides the coefficients of variation calculated for establishing the most appropriate window size to be used in extracting the second-order texture features for a greyscale corrosion image sample. The graph for the coefficients of variation indicates that the 11x11 window is where the coefficients start to stabilize for the two classes.

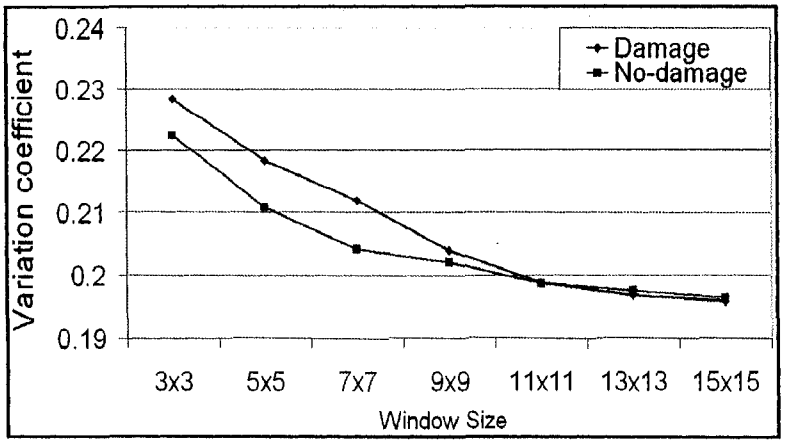

Figure 4.37: Coefficients of Variation Graph for Greyscale Corrosion Image

The following figures show the second-order texture features selected for two samples of greyscale corrosion imagery and the texture images produced from the selected features. Figure 4.38 shows the most effective texture features, mean, variance and dissimilarity, selected for greyscale corrosion image sample-1 from the eight second-order features derived through the texture analysis process; Figure 4.39 is the texture image of the second-order texture features selected for corrosion image sample-1. The texture features selected for image sample-2 of corrosion damage, mean, variance and correlation is presented in Figure 4.40, and the texture image of the texture features for corrosion image sample-2 is shown in Figure 4.41.

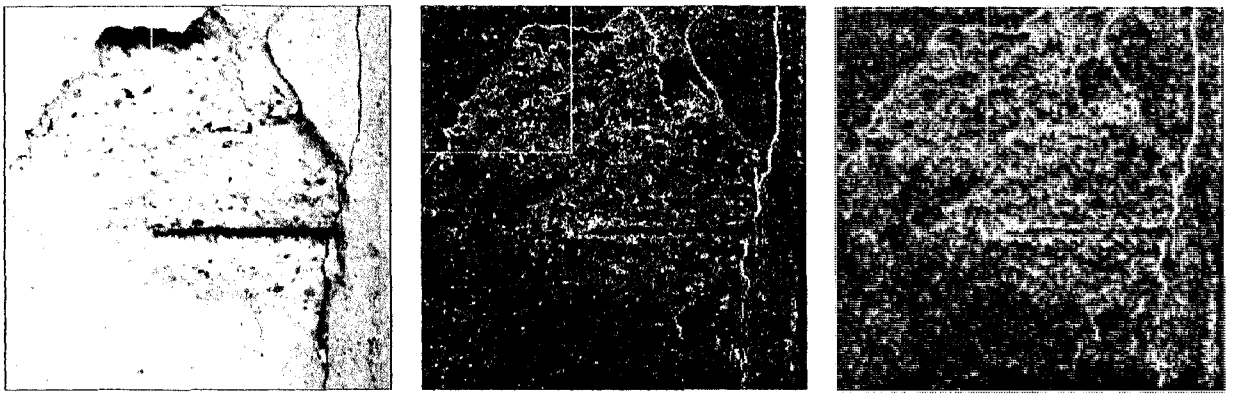

(a) Mean **(b) Variance** **(c) Dissimilarity**

Figure 4.38: Selected Second-order Texture Features for Corrosion Image-1

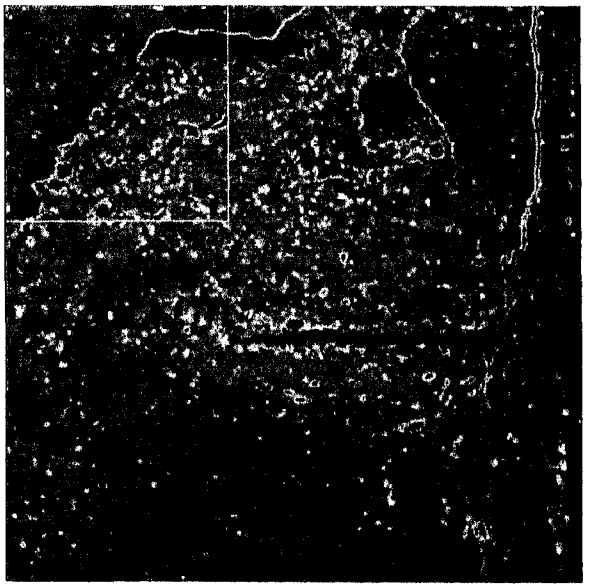

Figure 4.39: Texture Image of Selected Second-order Features for Corrosion Image Sample-1: Mean, Variance, Dissimilarity

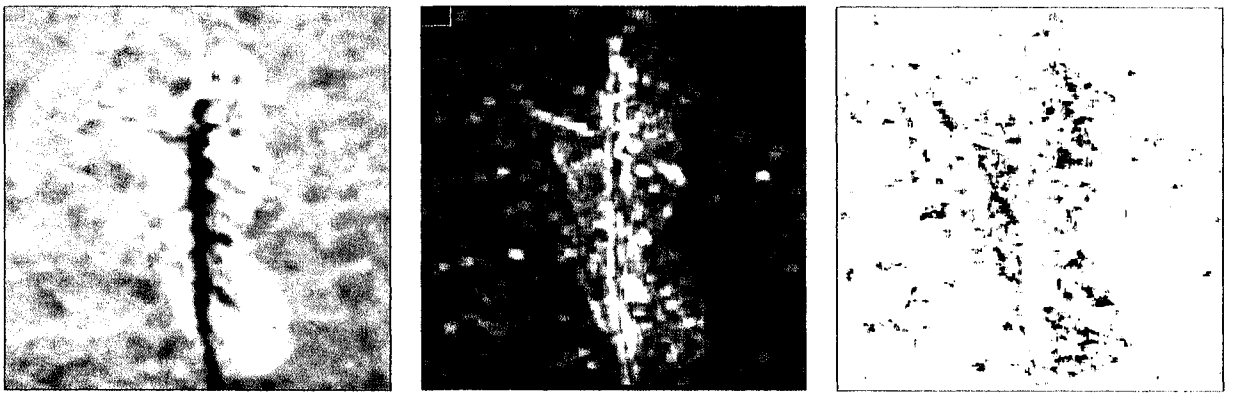

(a) Mean **(b) Variance** **(c) Correlation**

Figure 4.40: Selected Second-order Texture Features for Corrosion Image-2

Figure 4.41: Texture Image of Selected Second-order Features for Corrosion Image Sample-2: Mean, Variance, Correlation

4.5 Damage Analysis of Popouts, Erosion, Post-repair Damage, and Efflorescence and Corrosion Stains (Field Samples)

Other types of damage portrayed by the images of the deteriorated concrete bridge components were also analysed using the methodology outlined in sections 3.4 and 3.5. These include aggregate popouts, surface erosion, post-repair damage, and efflorescence and corrosion stains. Greyscale images of the different types of deterioration were resampled; the Haar wavelet transform was applied in order to obtain the reconstructed images, following which the texture analysis approach was implemented. The most effective second-order texture features selected through the texture analysis phase for image samples of the various types of damage, as well as the texture images, are presented below.

4.5.1 Popout Damage

Figure 4.42 presents the second-order texture features, mean, variance and contrast, selected from the eight texture features of the GLCM computed for a greyscale image sample of popout damage, and Figure 4.43 is the texture image.

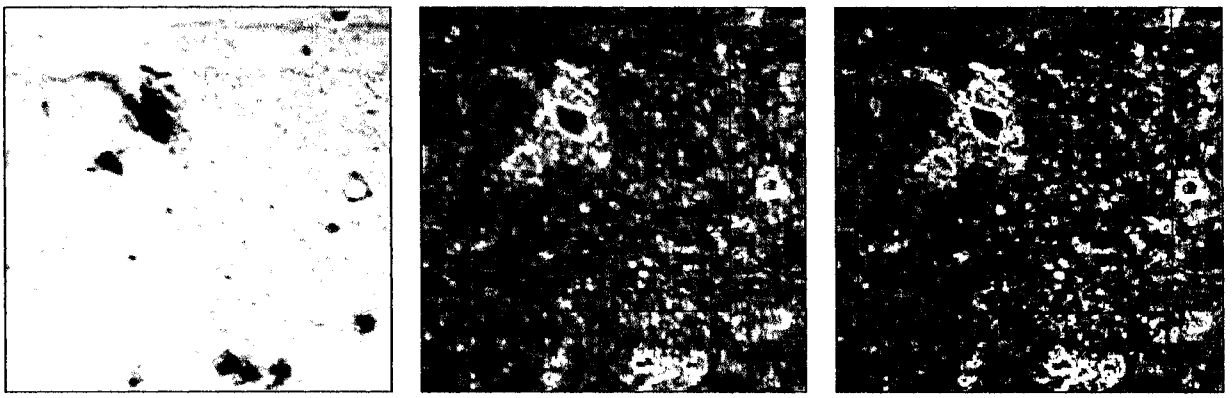

(a) Mean **(b) Variance** **(c) Contrast**

Figure 4.42: Selected Second-order Texture Features for Popout Image Sample

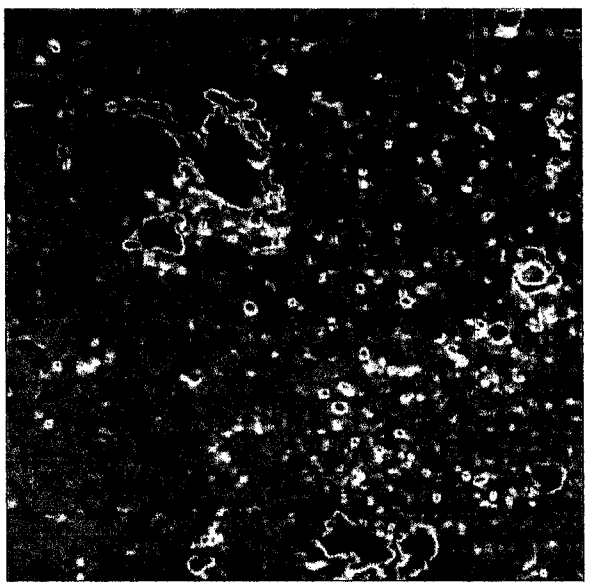

Figure 4.43: Texture Image of Selected Second-order Features for Popout Image: Mean, Variance, Contrast

4.5.2 Erosion Damage

Figure 4.44 shows the coefficients of variation calculated for determining the best window size to use in the GLCM texture analysis of greyscale imagery of erosion damage. The graph indicates that the 11x11 window is the point where the coefficients start to stabilize for the two classes. Figure 4.45 presents the second-order texture features, mean, variance and homogeneity, selected as the most effective from the eight features calculated in the texture analysis process for an image sample of erosion damage. The texture image of these selected features for the erosion image sample is given in Figure 4.46.

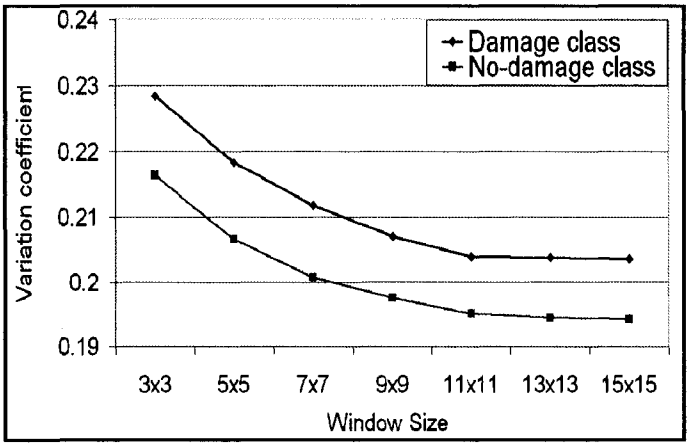

Figure 4.44: Coefficients of Variation Graph for Greyscale Erosion Image

(a) Mean (b) Variance (c) Homogeneity

Figure 4.45: Selected Second-order Texture Features for Erosion Image Sample

Figure 4.46: Texture Image of Selected Second-order Features for Erosion Image: Mean, Variance, Homogeneity

4.5.3 Post-Repair Damage

Figure 4.47 shows the second-order texture features, mean, homogeneity and second moment, selected for an image sample of post-repair damage. The texture image for the post-repair image sample is presented in Figure 4.48.

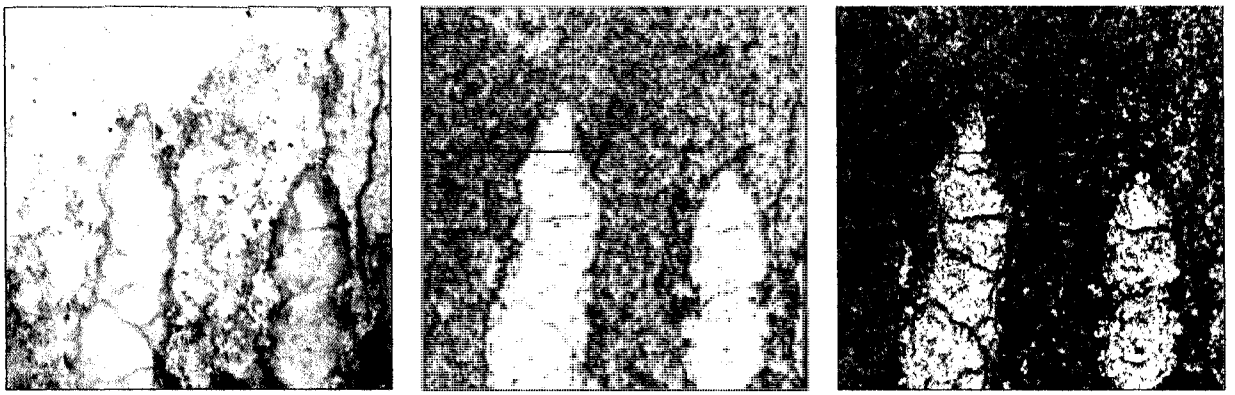

(a) Mean **(b) Homogeneity** **(c) Second Moment**

Figure 4.47: Selected Second-order Texture Features for Post-repair Image Sample

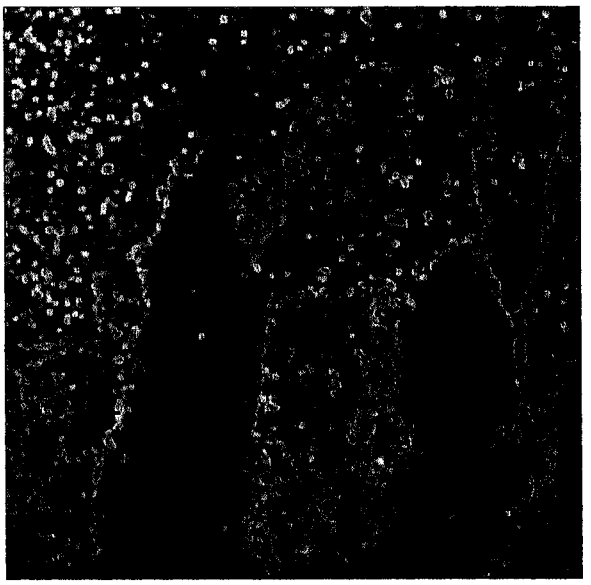

Figure 4.48: Texture Image of Selected Second-order Features for Post-repair Image Sample: Mean, Homogeneity, Second Moment

4.5.4 Efflorescence Stains

The second-order texture features, mean, variance and homogeneity, selected for an image sample of efflorescence stain are given in Figure 4.48, and the texture image for the sample is shown in Figure 4.50.

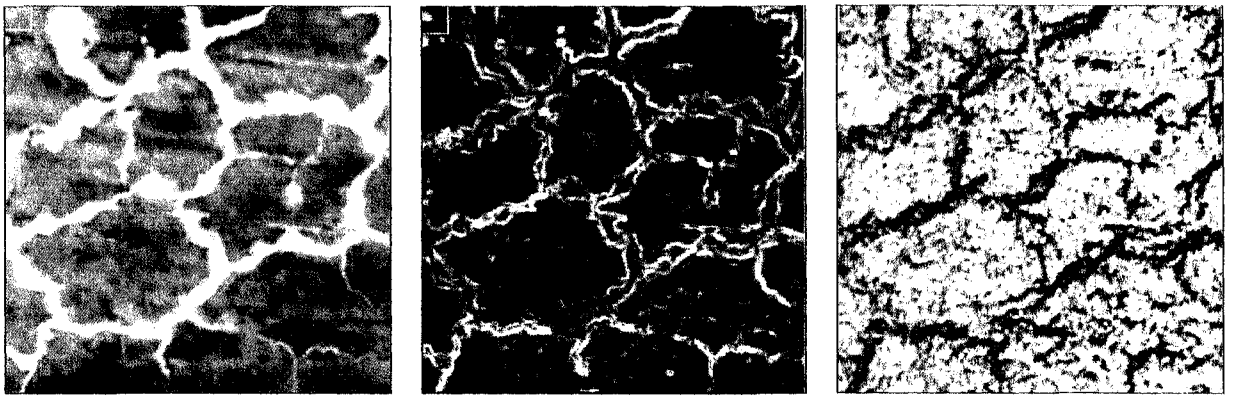

(a) Mean **(b) Variance** **(c) Homogeneity**

Figure 4.49: Selected Second-order Texture Features for Efflorescence Stain Sample

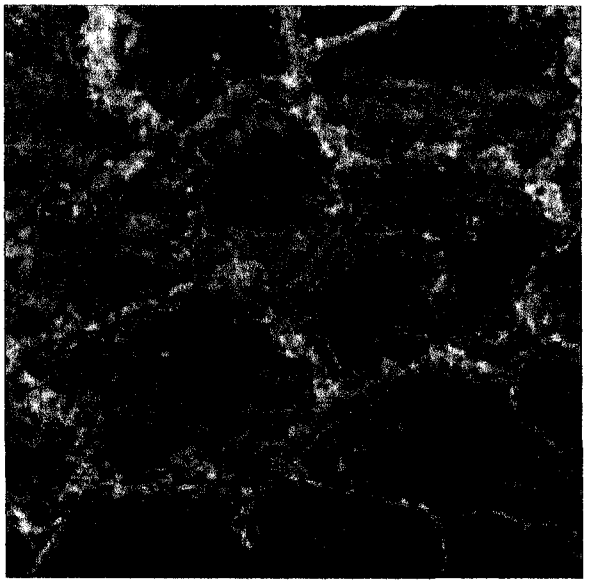

Figure 4.50: Texture Image of Selected Second-order Features for Efflorescence Stain Image Sample: Mean, Variance, Homogeneity

4.5.5 Corrosion Stains

Figure 4.51 displays the selected second-order texture features, mean, variance and homogeneity, for image sample-1 of corrosion stains. Figure 4.52 presents the texture image.

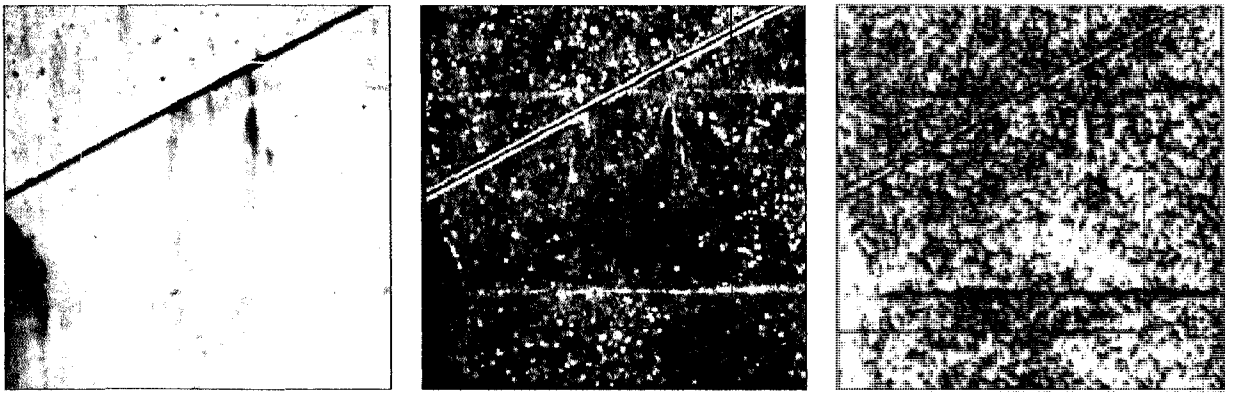

(a) Mean **(b) Variance** **(c) Homogeneity**

Figure 4.51: Selected Second-order Texture Features for Corrosion Stain Sample-1

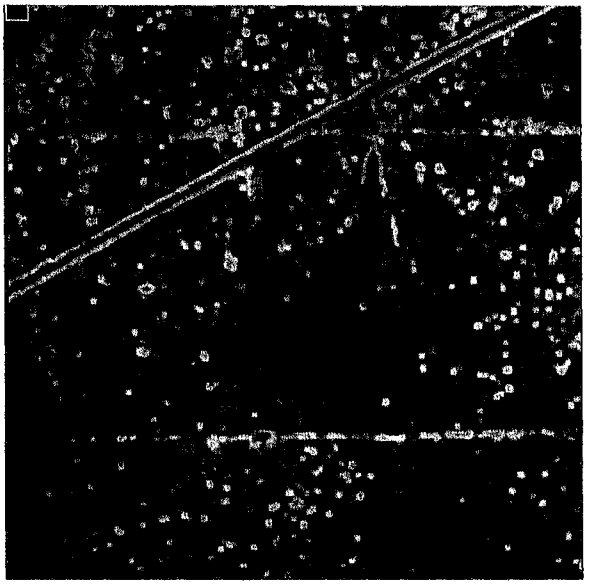

Figure 4.52: Texture Image of Selected Second-order Features for Corrosion Stain Image Sample-1: Mean, Variance, Homogeneity

The second-order texture features, mean, homogeneity, and contrast, selected for image sample-2 of corrosion stains are given in Figure 4.53, and the texture image for sample-2 is displayed in Figure 4.54.

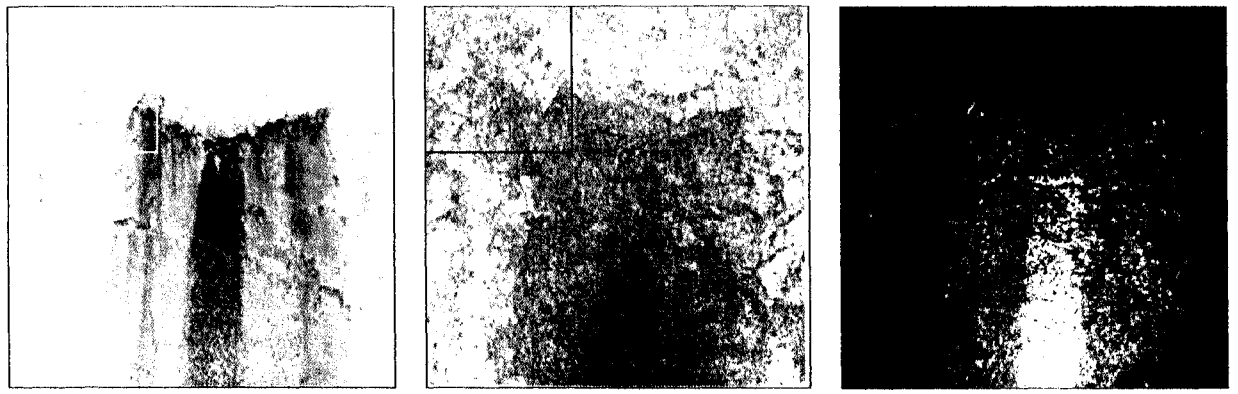

(a) Mean **(b) Homogeneity** **(c) Contrast**

Figure 4.53: Selected Second-order Texture Features for Corrosion Stain Sample-2

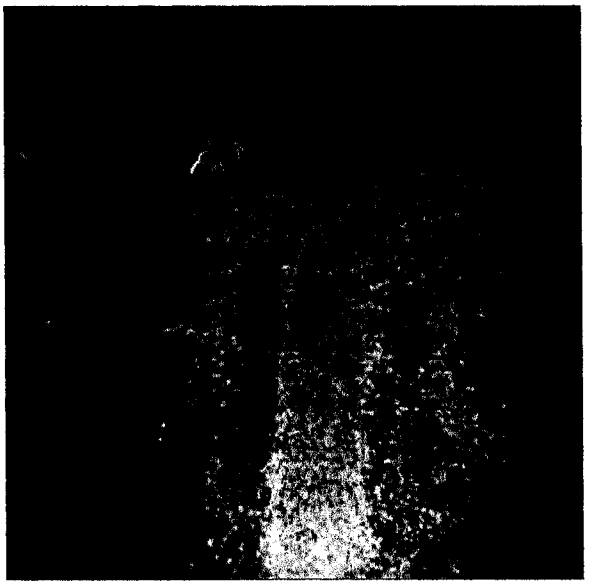

Figure 4.54: Texture Image of Selected Second-order Features for Corrosion Stain Image Sample-2: Mean, Homogeneity, Contrast

4.6 Damage Analysis of Deterioration from Acoustic Imagery

Another aspect of the damage analysis involves the study of acoustic imagery obtained from boreholes drilled in the St. Lambert Lock. Section 3.1.1 gives details of the lock, and section 3.3.2.4 provides details of the borehole acoustic imagery. Samples of the imagery are presented in Figure 3.11. The damage analysis methodology described in sections 3.4 and 3.5 was applied to the acoustic imagery; however, in this analysis, the texture phase was applied as a separate technique on the raw acoustic imagery and not on the reconstructed images. Furthermore, the spatial filtering approaches outlined in section 3.6 were also employed on the acoustic image samples.

The Haar wavelet transform was applied to the imagery in order to obtain the decompositions, as explained in section 3.4.1. Figure 4.55 shows the different stages of the decomposition of an acoustic image sample: Figure 4.55(a) presents the input acoustic image sample, different levels of decomposition are shown in Figures 4.55(b-c), and Figure 4.55(d) is the complete decomposition of the image. The image sample was then reconstructed according to the steps explained in section 3.4.2. Figure 4.56 shows the image at different levels of reconstructions.

Application of the GLCM analysis resulted in the selection of the three second-order texture features, mean, homogeneity and variance, presented in Figure 4.57; the texture image of the second-order features for the acoustic image is given in Figure 4.58.

The methodology for damage analysis in this stage also includes techniques known as spatial filters, which are employed to determine their effectiveness in detecting damage contained in acoustic imagery. Six different spatial filters are evaluated: the low-pass filter, the median filter, the Sobel edge-detector, the Roberts edge-detector, the directional edge-enhancement filter, and the Marr-Hildreth edge-detection operator. Application of the filters on the acoustic image sample resulted in the images presented in Figure 4.59.

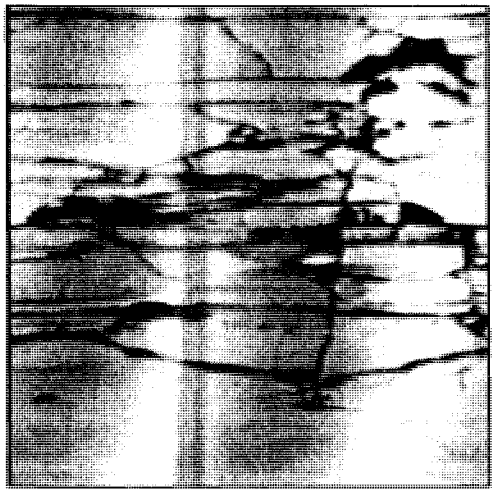

(a) Input Image

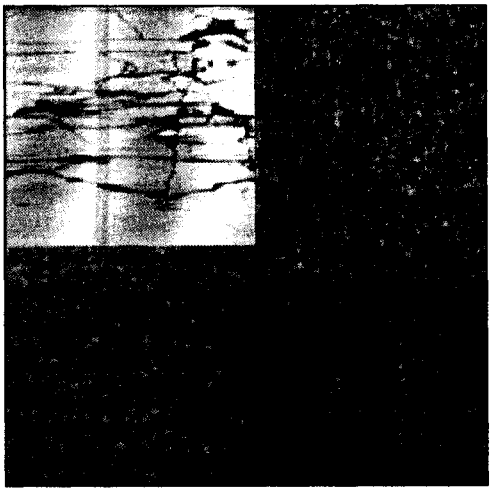

(b) One-level

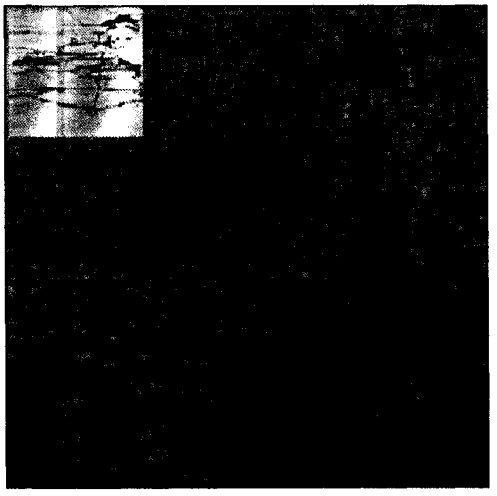

(c) Two-level

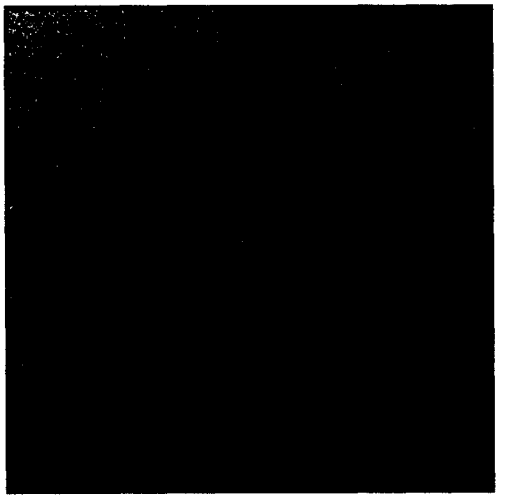

(d) Complete

Figure 4.55: Decomposition of Acoustic Image Sample

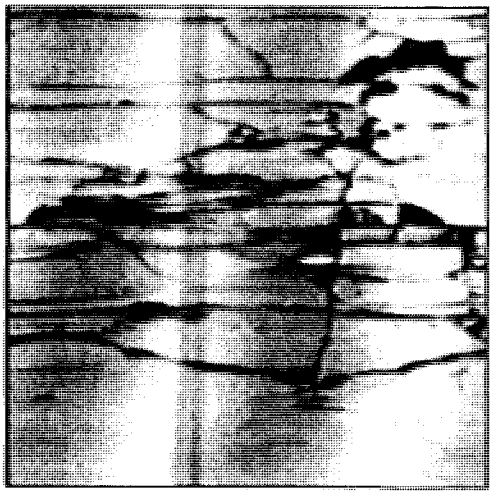

(a) 1% Reconstruction

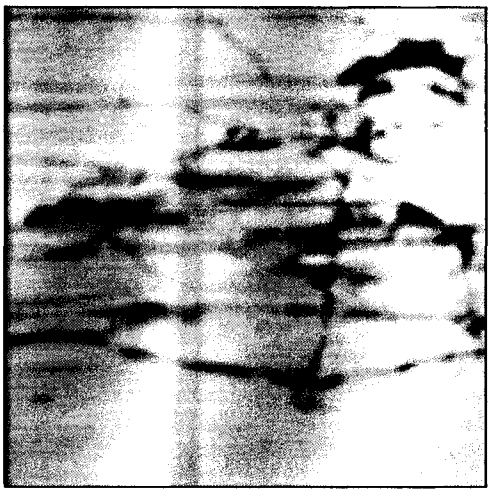

(b) 5% Reconstruction

(c) 10% Reconstruction

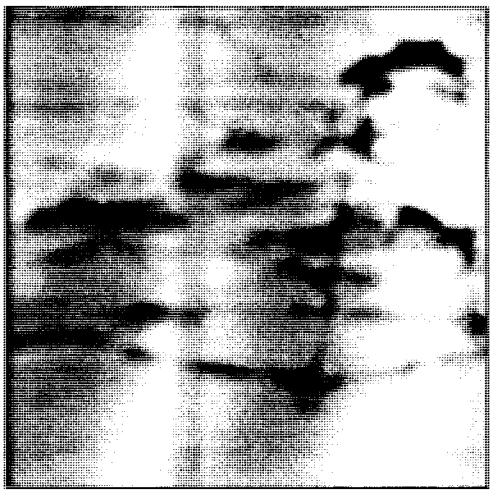

(d) 25% Reconstruction

Figure 4.56: Reconstruction of Acoustic Image Sample

(a) Mean (b) Homogeneity (c) Variance

Figure 4.57: Selected Second-order Texture Features for Acoustic Image Sample

Figure 4.58: Texture Image of Selected Second-order Features for Acoustic Image Sample: Mean, Homogeneity, Variance

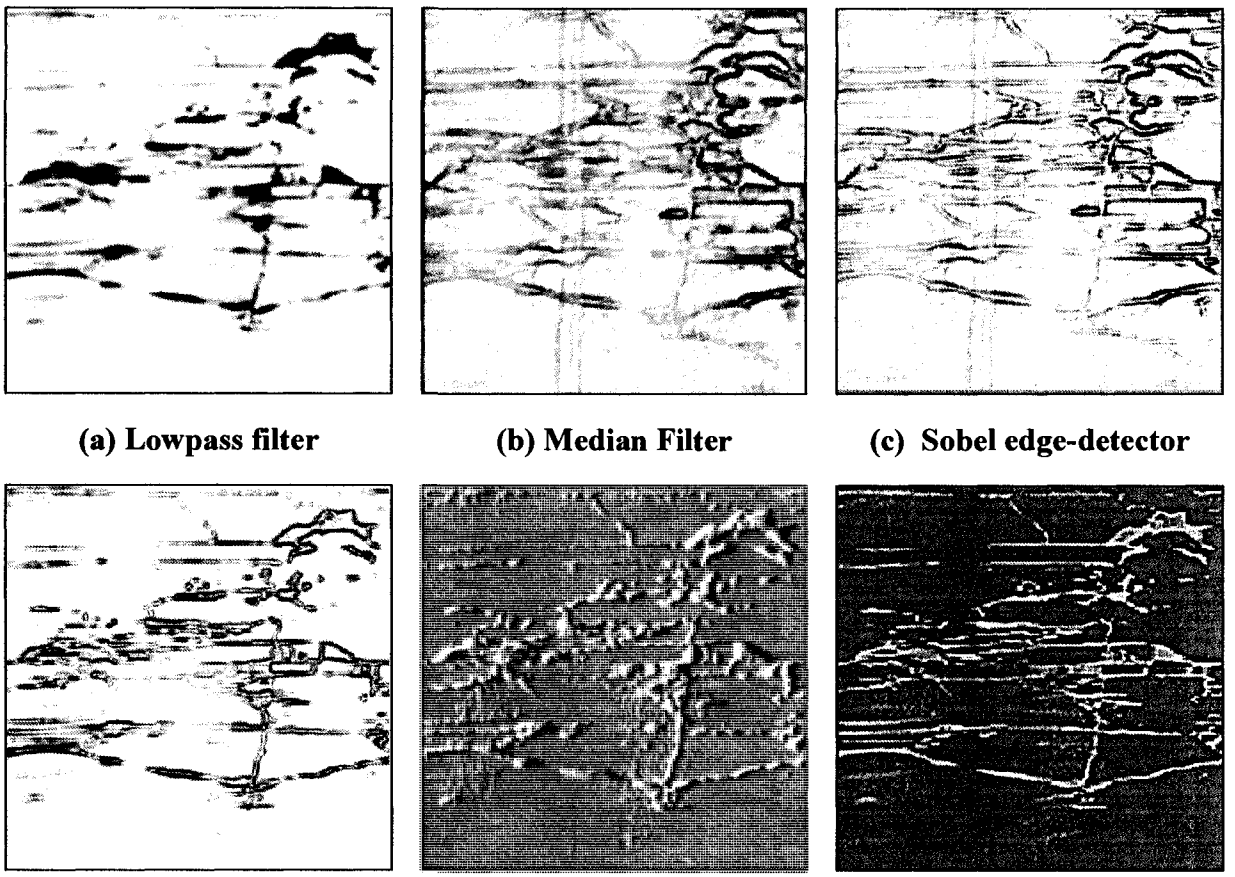

(a) Lowpass filter (b) Median Filter (c) Sobel edge-detector

(d) Roberts edge-detector (e) Directional Filter (f) Marr-Hildreth operator

Figure 4.59: Images Resulting from Application of Different Filters on Acoustic Image Sample

4.7 Classification Results

4.7.1 Map-crack Imagery from Field Samples

Figure 4.60(a) is the classified image of a greyscale map-crack image sample using the *K*-means clustering method, and Figure 4.60(b) is the classification of the same image using the ANN classifier.

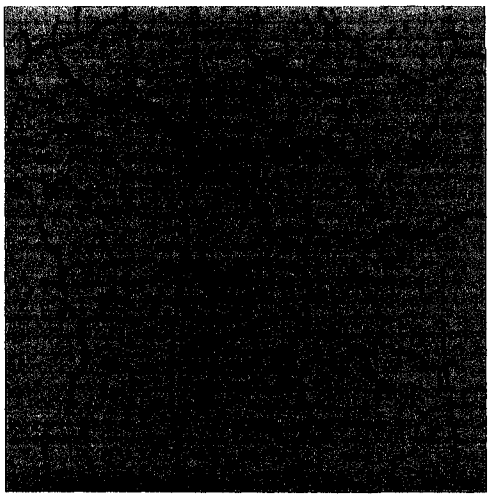

(a) *K*-means Classified Image

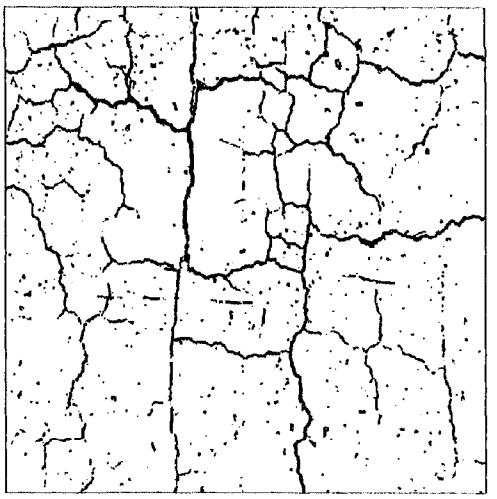

(b) *K*-means Binary Image

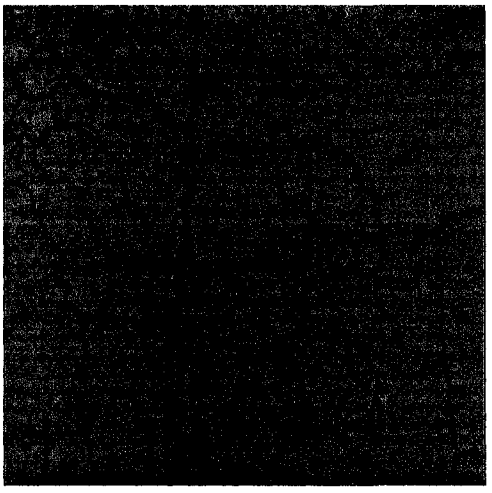

(c) ANN Classified Image

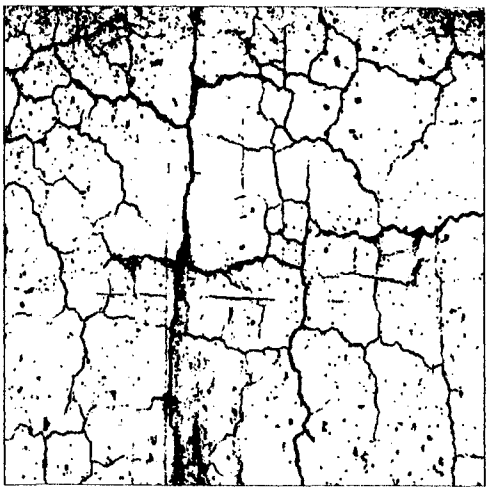

(d) ANN Binary Image

Figure 4.60: *K*-means and ANN Classifications for Greyscale Map-crack Image Sample

Table 4.3 gives the class statistics summary reports for the *K*-means and ANN classifications for the greyscale map-crack image sample.

Table 4.3: Class Statistics Summary Report for Greyscale Map-crack Image using *K*-means and ANN Classifier

***K*-means Classifier**		
Classes	**Pixels**	**Percentage (%)**
Map-crack (Blue)	338 900	8.1
No-crack (Green)	3 855 404	91.9
ANN Classifier		
Map-crack (Black)	617 402	14.7
No-crack (Green)	3 576 902	85.3
Total Number of Pixels: 4 194 304 (2048x2048)		

4.7.2 Map-crack Imagery from CANMET Laboratory Specimens

Figure 4.61 presents the ANN classifications for the greyscale imagery of the three CANMET specimens, C1, C2 and C3, as well as their corresponding binary images.

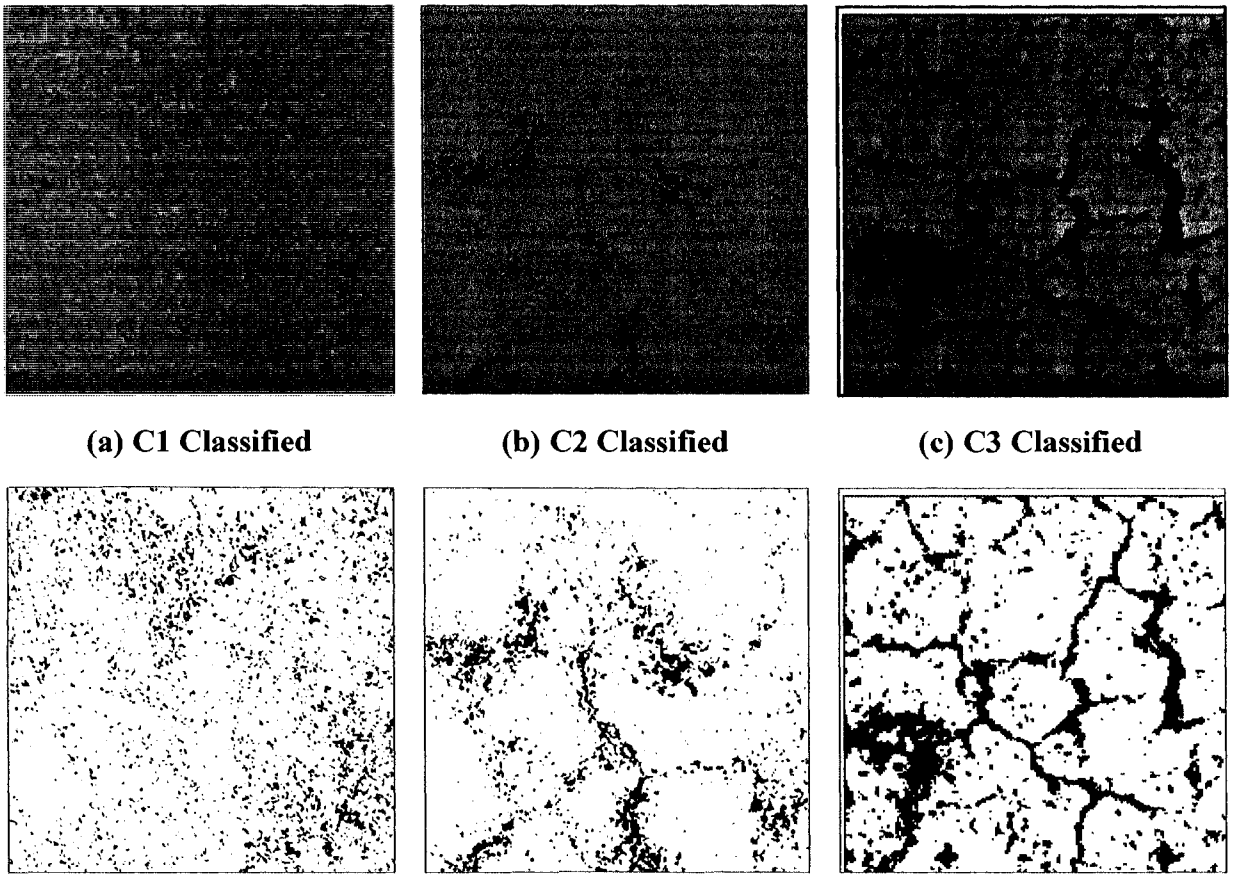

(a) C1 Classified **(b) C2 Classified** **(c) C3 Classified**

(d) C1 Binary **(e) C2 Binary** **(f) C3 Binary**

Figure 4.61: ANN Classifications for Greyscale Imagery of CANMET Specimens

Table 4.4 gives the class statistics summary for the ANN classifications of the greyscale imagery of the three CANMET blocks, C1, C2 and C3.

Table 4.4: Class Statistics Summary Report for Greyscale Imagery of CANMET Specimens using ANN Classifier

C1 Specimen		
Classes	**Pixels**	**Percentage (%)**
Wide-crack (Red)	0	0
Narrow-crack (Blue)	10 119	3.9
No-crack (Green)	252 025	96.1
Total Number of Pixels: 262 144 (512x512)		
C2 Specimen		
Wide-crack (Red)	8 939	3.4
Narrow-crack (Blue)	18 927	7.2
No-crack (Green)	234 278	89.4
Total Number of Pixels: 262 144 (512x512)		
C3 Specimen		
Wide-crack (Red)	21 548	8.2
Narrow-crack (Blue)	30 173	11.5
No-crack (Green)	210 423	80.3
Total Number of Pixels: 262 144 (512x512)		

Figure 4.62 provides the classified images for the greyscale, colour and thermographic imagery of the CANMET C3 specimen, using the ANN approach.

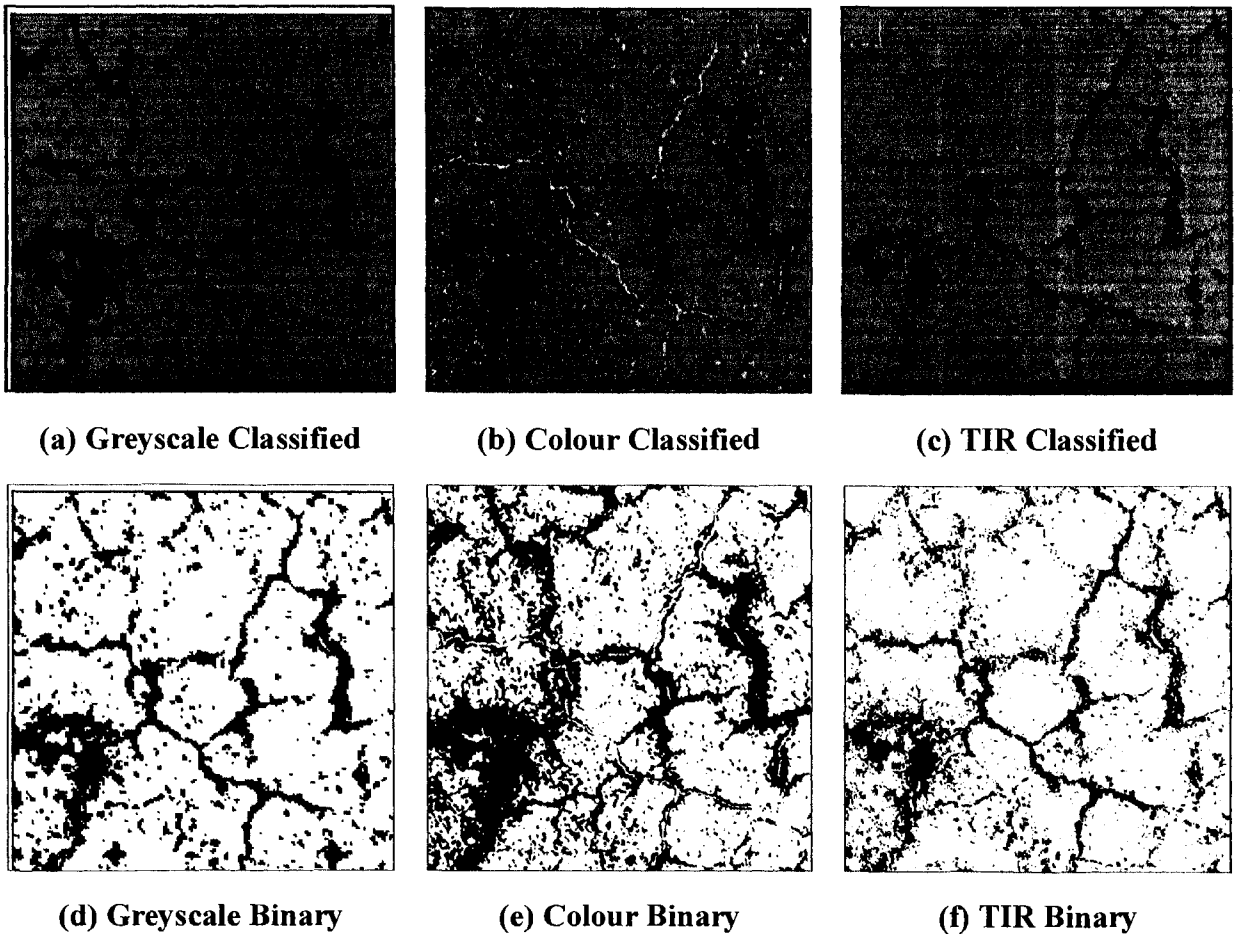

(a) Greyscale Classified **(b) Colour Classified** **(c) TIR Classified**

(d) Greyscale Binary **(e) Colour Binary** **(f) TIR Binary**

Figure 4.62: ANN Classifications for Greyscale, Colour and TIR Images of C3 Specimen

Table 4.5 gives the class statistics summary for the ANN classifications for the three types of imagery of the CANMET C3 block.

Table 4.5: Class Statistics Summary Report for Imagery of CANMET C3 Specimen using ANN Classifier

Greyscale Image		
Classes	**Pixels**	**Percentage (%)**
Wide-crack (Red)	21 548	8.2
Narrow-crack (Blue)	30 173	11.5
No-crack (Green)	210 423	80.3
Total Number of Pixels: 262 144 (512x512)		
Colour Image		
Wide-crack (Red)	26 136	9.9
Narrow-crack (Blue)	27 892	10.6
No-crack (Green)	208 116	79.5
Total Number of Pixels: 262 144 (512x512)		
Thermographic Image		
Wide-crack (Red)	24 720	9.4
Narrow-crack (Blue)	26 608	10.2
No-crack (Green)	210 816	80.4
Total Number of Pixels: 262 144 (512x512)		

4.7.3 Map-crack Imagery from GRAI Laboratory Specimens

Table 4.6 shows the class statistics summary of the ANN classifications for the greyscale imagery of the G1, G2 and G3 GRAI slabs. Figure 4.63 presents the ANN classifications for the thermographic, colour and greyscale imagery of the G3 slab. Table 4.7 provides the class statistics summary of the ANN classifications for the three types of imagery of the G3 specimen.

Table 4.6: Class Statistics Summary Report for Greyscale Imagery of GRAI Slabs using ANN Classifier

G1 Specimen		
Wide-crack (Blue)	0	0
Narrow-crack (Red)	7 157	2.7
No-crack (Green)	254 987	97.3
Total Number of Pixels: 262,144 (512 x 512)		
G2 Specimen		
Wide-crack (Red)	9 123	3.5
Narrow-crack (Blue)	5 662	2.2
No-crack (Green)	247 359	94.3
Total Number of Pixels: 262,144 (512 x 512)		
G3 Specimen		
Wide-crack (Black)	23 252	8.9
Narrow-crack (Red)	0	0
No-crack (Green)	238 892	91.1
Total Number of Pixels: 262,144 (512 x 512)		

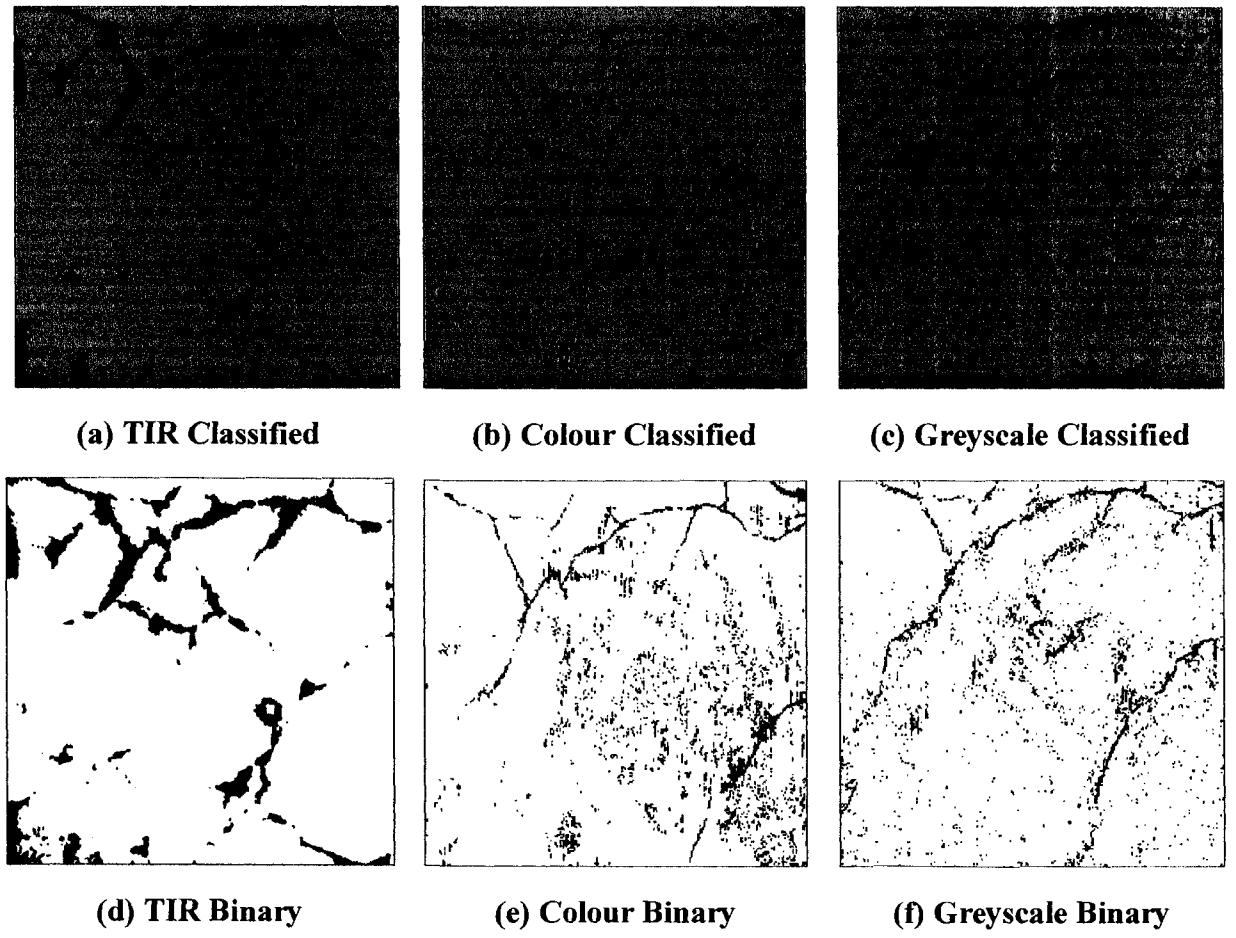

Figure 4.63: ANN Classifications for Greyscale, Colour and TIR Images of G3 Specimen

Table 4.7: Class Statistics Summary Report for Thermographic, Colour and Greyscale Images of GRAI G3 Specimen using ANN Classifier

Thermographic Image		
Classes	**Pixels**	**Percentage (%)**
Wide-crack (Red)	25 507	9.7
Narrow-crack (Blue)	0	0
No-crack (Green)	236 637	90.3
Total Number of Pixels: 262 144 (512x512)		
Colour Image		
Wide-crack (Black)	23 750	9.1
Narrow-crack (Red)	0	0
No-crack (Green)	238 394	90.9
Total Number of Pixels: 262 144 (512x512)		
Greyscale Image		
Wide-crack (Black)	23 252	8.9
Narrow-crack (Red)	0	0
No-crack (Green)	238 892	91.1
Total Number of Pixels: 262 144 (512x512)		

4.7.4 Imagery of Different Types of Damage from Field Samples

The classified images for greyscale image sample-1 of spalling damage, using the *K*-means clustering method and the ANN classifier are presented in Figure 4.64.

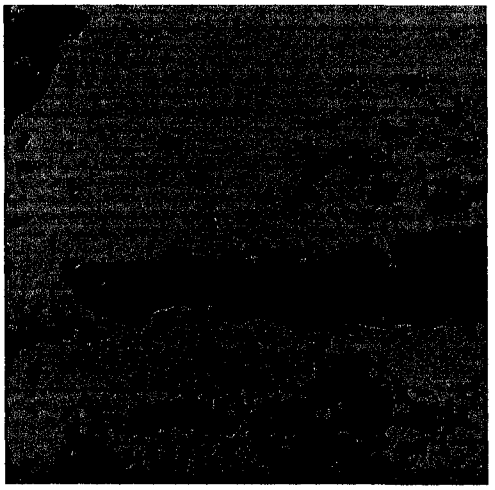

(a) *K*-Means Cluster Map

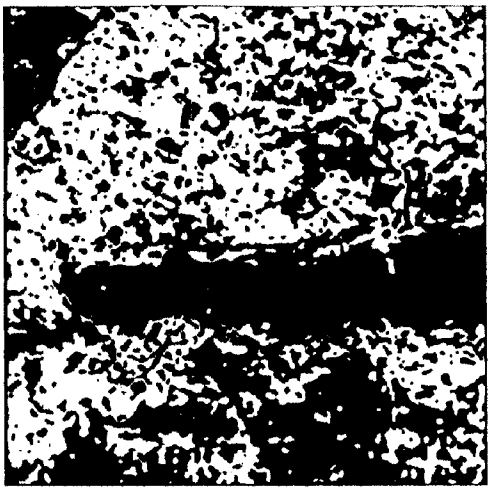

(b) *K*-Means Binary Image

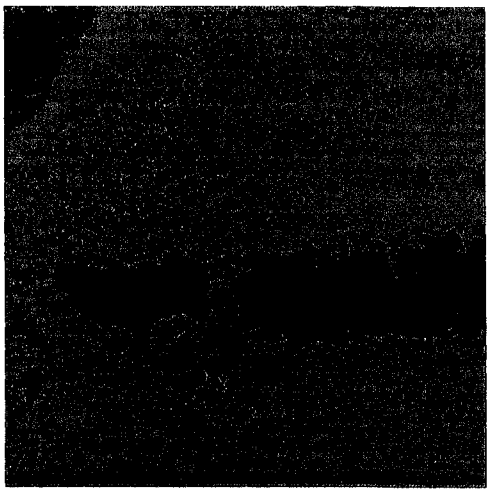

(c) ANN Classification

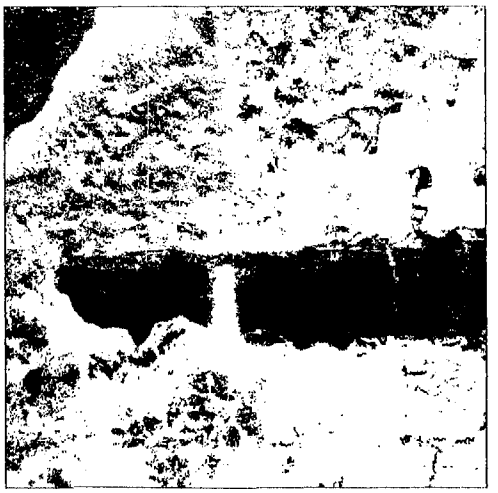

(d) ANN Binary Image

Figure 4.64: *K*-Means and ANN Classifications for Greyscale Spalling Image Sample-1

The class statistics summary reports for the *K*-means and ANN classifications for the greyscale spalling image sample-1 are given in Table 4.8.

Table 4.8: Class Statistics Summary Reports for Greyscale Spalling Image Sample-1 using *K*-means and ANN Classifiers

***K*-means**		
Classes	**Pixels**	**Percentage (%)**
Spalling (Green)	604 085	57.6
No-spalling (Red)	444 491	42.4
ANN		
Spalling (Green)	742 497	70.8
No-spalling (Red)	306 079	29.2
Total Number of Pixels: 1 048 576 (1024x1024)		

Figure 4.65 presents the *K*-means classification for greyscale image sample-2 of spalling damage, as well as the ANN classification for the same image.

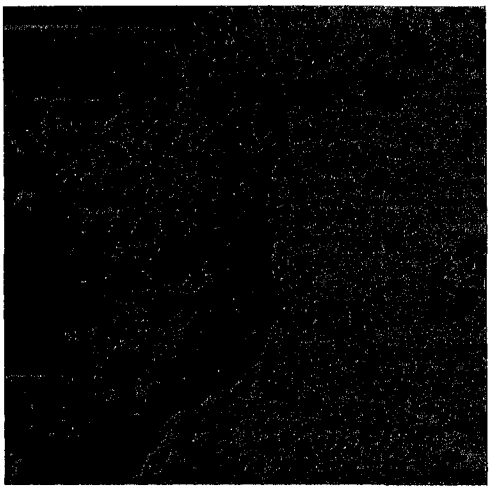

(a) *K*-Means Cluster Map

(b) *K*-Means Binary Image

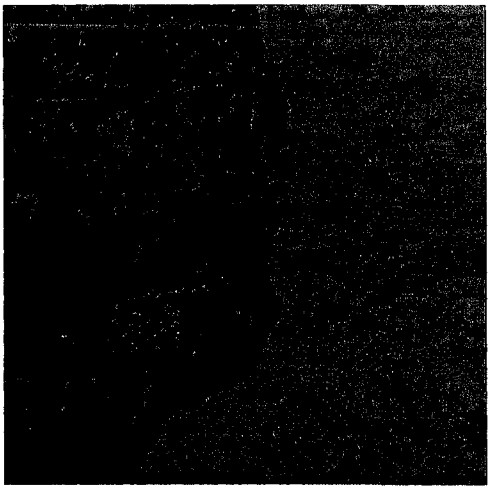

(c) ANN Classified Image

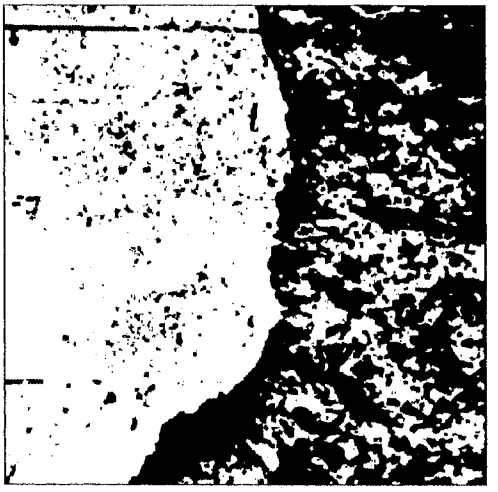

(d) ANN Binary Image

Figure 4.65: *K*-Means and ANN Classifications for Greyscale Spalling Image Sample-2

The class statistics summary reports for the *K*-means and ANN classifications for the greyscale image sample-2 of spalling damage are provided in Table 4.9.

Table 4.9: Class Statistics Summary Reports for Greyscale Spalling Image Sample-2 using *K*-means and ANN Classifiers

***K*-means**		
Classes	**Pixels**	**Percentage (%)**
Spalling (Green)	759 064	72.4
No-spalling (Red)	289 512	27.6
ANN		
Spalling (Green)	397 725	37.9
No-spalling (Red)	650 851	62.1
Total Number of Pixels: 1 048 576 (1024x1024)		

The ANN classifications for the greyscale image sample-1 and image sample-2 of corrosion damage are displayed in Figure 4.66.

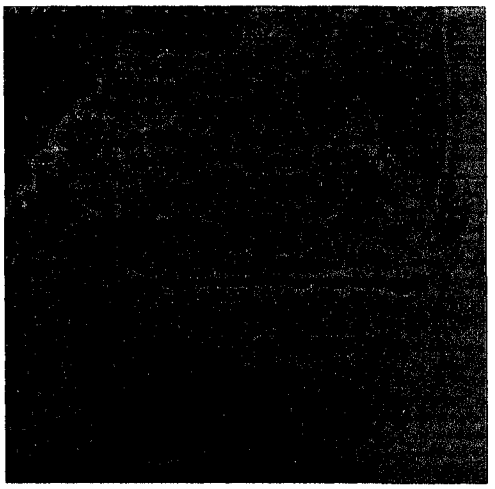

(a) Sample-1 Classified Image

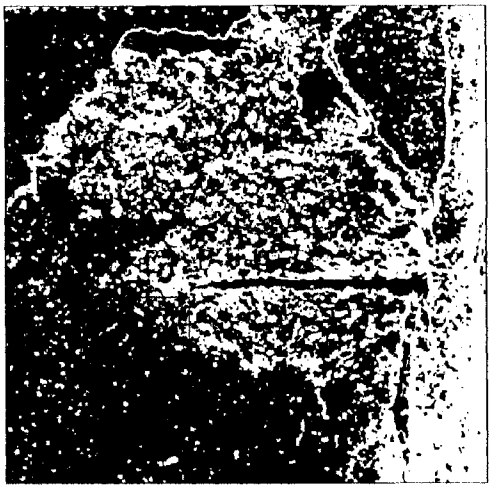

(b) Sample-1 Binary Image

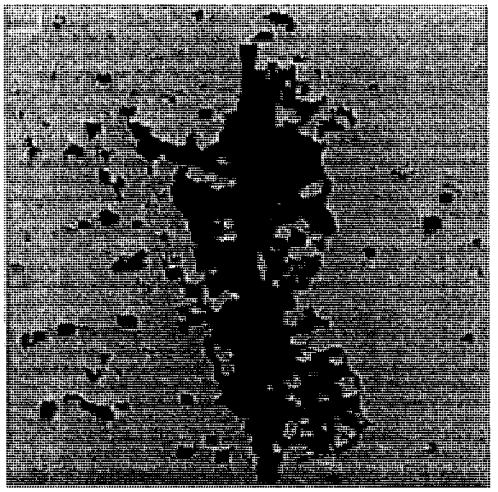

(c) Sample-2 Classified Image

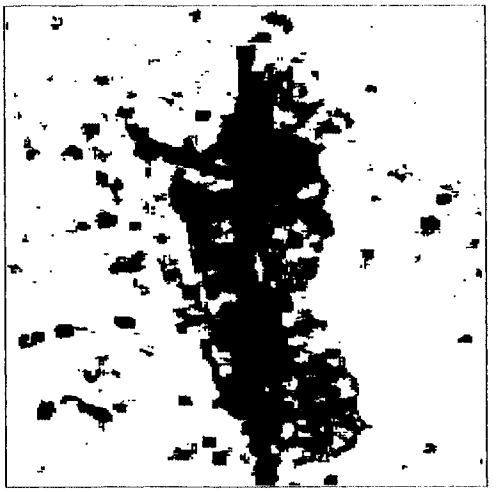

(d) Sample-2 Binary Image

Figure 4.66: ANN Classifications for Greyscale Corrosion Image Sample-1 and Sample-2

The class statistics summary reports for the ANN classifications for greyscale image sample-1 and image sample-2 of corrosion damage is given in Table 4.10.

Table 4.10: Class Statistics Summary Report for Greyscale Corrosion Image Sample-1 and Image Sample-2 using ANN Classifier

Image Sample-1		
Classes	**Pixels**	**Percentage (%)**
Corroded-steel (Red)	49 703	4.7
Spalling (Green)	400 661	38.2
No-damage (Blue)	598 212	57.1
Total Number of Pixels: 1 048 576 (1024x1024)		
Image Sample-2		
Corroded-steel (Black)	1 842	2.8
Spalling (Blue)	12 989	19.8
No-damage (Green)	50 705	77.4
Total Number of Pixels: 65 536 (256x256)		

Figure 4.67 presents the ANN classifications for greyscale image samples of popout damage, erosion damage, and post-repair damage

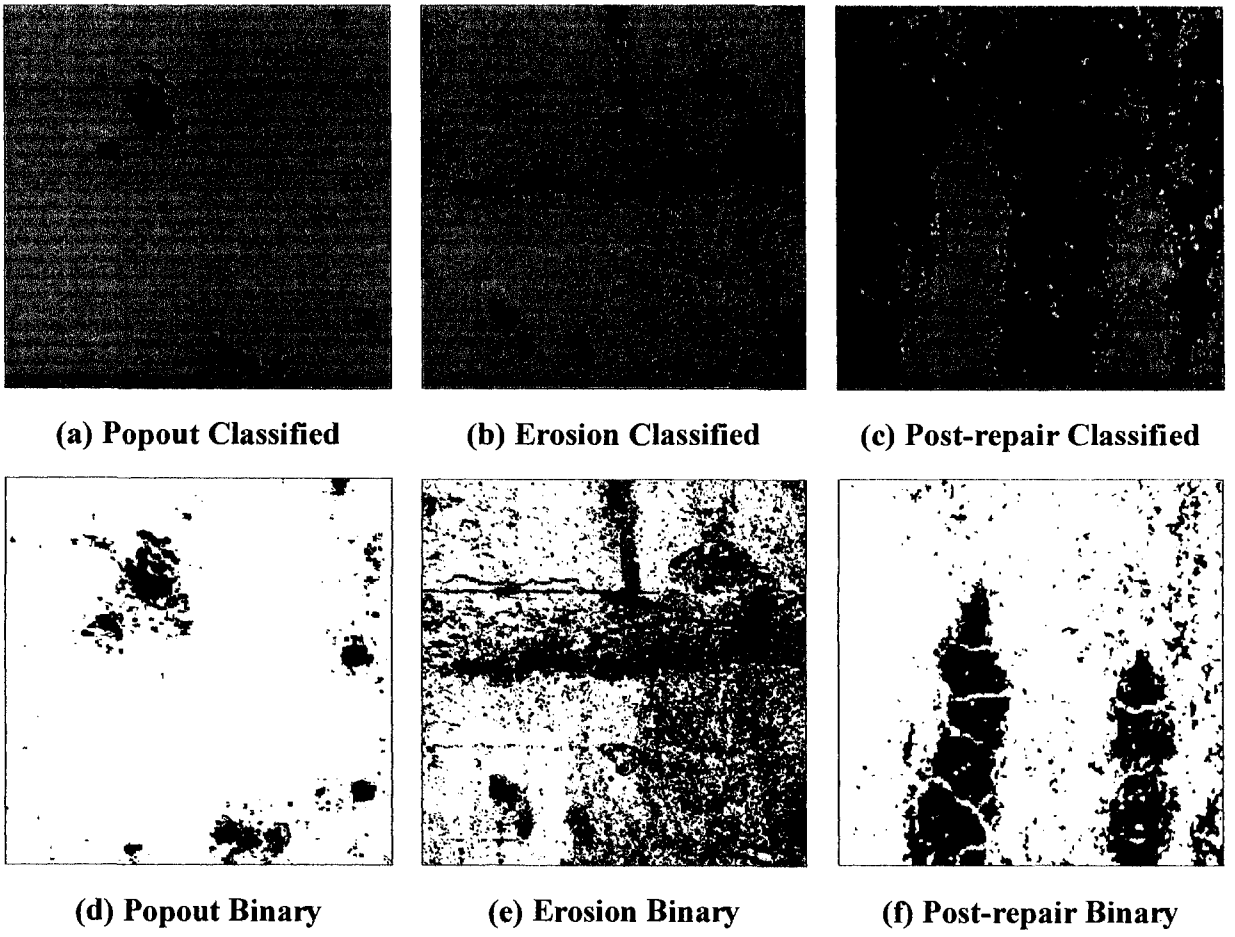

(a) Popout Classified **(b) Erosion Classified** **(c) Post-repair Classified**

(d) Popout Binary **(e) Erosion Binary** **(f) Post-repair Binary**

Figure 4.67: ANN Classifications for Greyscale Images of Different Types of Damage

Table 4.11 gives the class statistics summary reports for the ANN classifications for the image samples of the different types of damage.

Table 4.11: Class Statistics Summary Reports for Greyscale Images of Popout, Erosion and Post-repair Damage using ANN Classifier

Popout Damage		
Classes	**Pixels**	**Percentage (%)**
Popout-centre (Black)	7 471	2.9
Popout-edges (Red)	12 426	4.7
No-damage (Green)	242 247	92.4
Total Number of Pixels: 262 144 (512x512)		
Erosion Damage		
Eroded (Red)	475 319	45.3
Non-eroded (Green)	573 257	54.7
Total Number of Pixels: 1 048 576 (1024x1024)		
Post-repair Damage		
Crack (Blue)	57 986	5.5
Repaired (Green)	251 239	23.9
No-damage (Red)	739 350	70.6
Total Number of Pixels: 1 048 576 (1024x1024)		

The ANN classification for a greyscale image sample of efflorescence stain damage is provided in Figure 4.68(a); ANN classifications for greyscale image sample-1 and sample-2 of corrosion stain damage are presented in Figures 4.68(b)-(c), respectively.

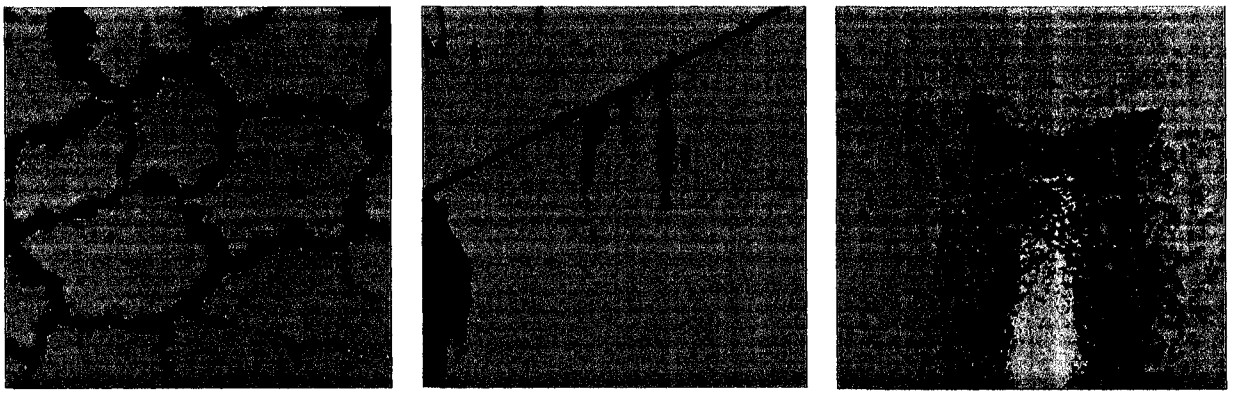

(a) Classified Efflorescence Stain | **(b) Classified Corrosion Stain Sample-1** | **(c) Classified Corrosion Stain Sample-2**

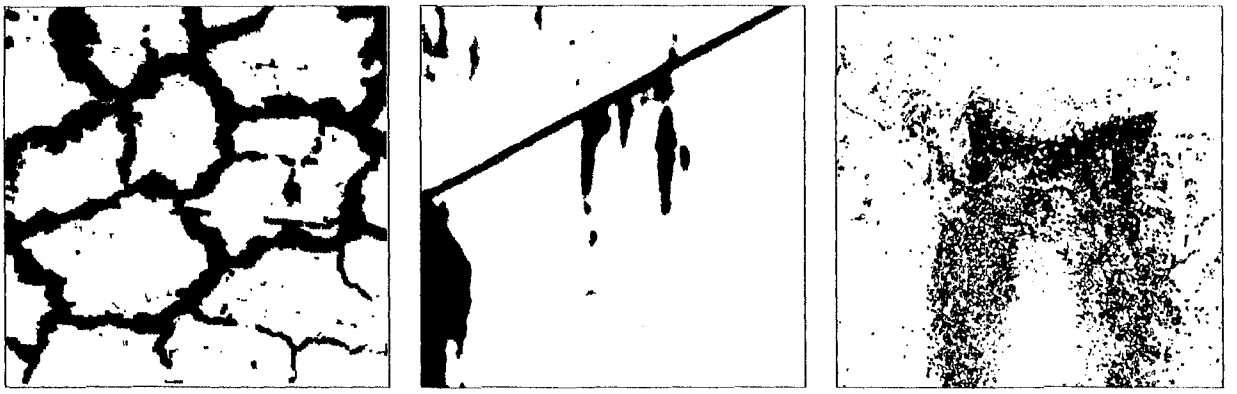

(b) Binary Efflorescence Stain | **(b) Binary Corrosion Stain Sample-1** | **(b) Binary Corrosion Stain Sample-2**

Figure 4.68: ANN Classifications for Greyscale Images of Efflorescence Stain, and Corrosion Stain Sample-1 and Sample-2

Table 4.12 gives the class statistics summary reports for the ANN classifications for the efflorescence stain damage image sample, as well as image sample-1 and sample-2 of corrosion stain damage.

Table 4.12: Class Statistics Summary Reports for Greyscale Images of Efflorescence Stain and Corrosion Stain Sample-1 and Sample-2 using ANN Classifier

Efflorescence Stain		
Classes	**Pixels**	**Percentage (%)**
Cracks (Black)	3 585	5.5
Efflorescence-Stains (Red)	14 746	22.5
No-damage (Green)	47 205	72.0
Total Number of Pixels: 65 536 (256x256)		
Corrosion Stain Sample-1		
Corrosion-Stains (Red)	29 334	11.2
No-damage (Green)	232 810	88.8
Total Number of Pixels: 262 144 (512x512)		
Corrosion Stain Sample-2		
Corrosion-Stains (Red)	390 699	37.3
No-damage (Green)	657 877	62.7
Total Number of Pixels: 1 048 576 (1024x1024)		

4.7.5 Borehole Acoustic Imagery

After application of the texture analysis, the Haar wavelet transform, as well as the various spatial filters and edge-detectors to the borehole acoustic image sample, the resulting processed images were employed as input images in order to perform the classifications. Figure 4.69 presents the *K*-means classifications of the different input images resulting from the various processing techniques. Table 4.13 provides the class statistic summaries, the individual classification accuracies for each class, the Kappa coefficients, and the overall classification accuracies obtained for the classification of each input image.

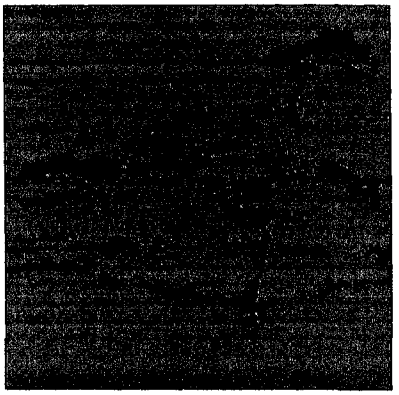

(a) Haar

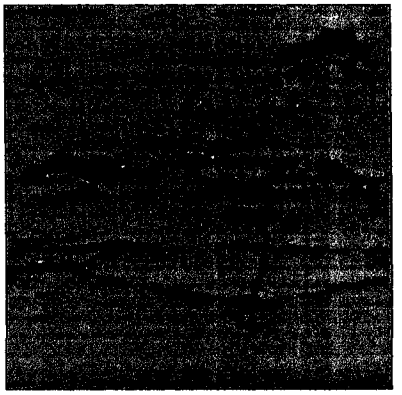

(b) Texture

(c) Lowpass

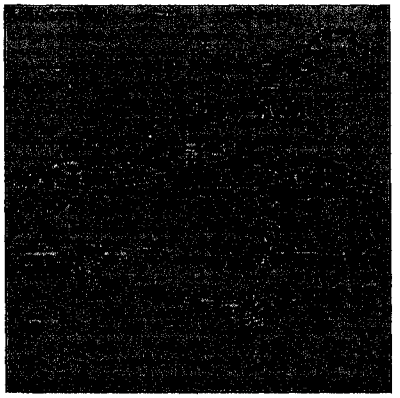

(d) Roberts

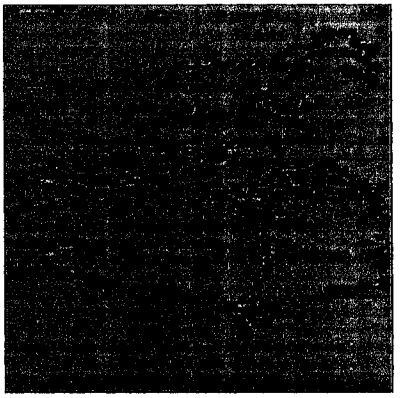

(e) Sobel

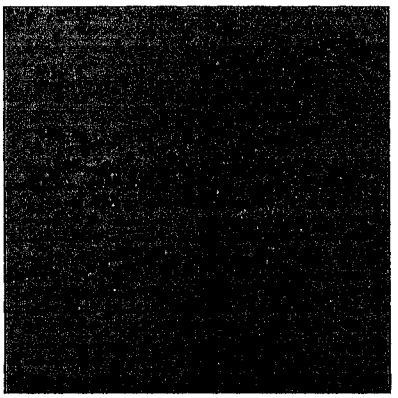

(f) Directional

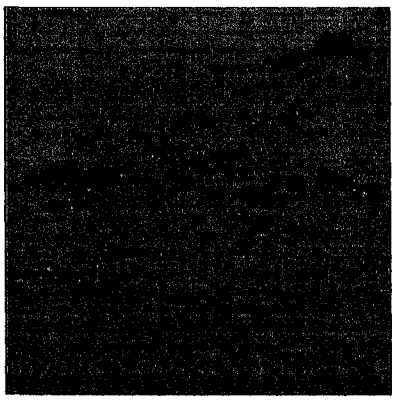

(g) Median

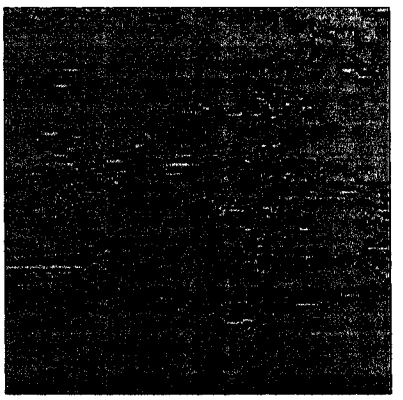

(h) Marr-Hildreth

Figure 4.69: *K*-means Classifications for Acoustic Image Sample

Table 4.13: Class Statistics, Classification Accuracies, and Kappa Coefficients for Different Input Images using *K*-means Classifier

Input Image	Classes	Pixels	Percentage (%)	Accuracy (%)	Kappa Coefficient	Overall Accuracy (%)
Texture	Damage	40 606	15.5	81.9	0.83	82.4
	No-damage	221 538	84.5	83.5		
Haar	Damage	39 558	15.1	81.3	0.82	81.7
	No-damage	222 586	84.9	82.0		
Lowpass	Damage)	38 352	14.6	79.8	0.79	80.6
	No-damage	223 792	85.4	81.9		
Roberts	Damage	47 500	18.1	74.1	0.74	75.0
	No-damage	214 644	81.9	73.6		
Sobel	Damage	45 849	17.5	74.8	0.76	76.2
	No-damage	216 295	82.5	75.7		
Directional	Damage	24 039	9.2	67.3	0.67	68.5
	No-damage	238 106	90.8	66.9		
Median	Damage	35 861	13.7	81.6	0.77	79.7
	No-damage	226 283	86.3	78.4		
Marr-Hildreth	Damage	30 618	11.7	72.6	0.70	72.1
	No-damage	231 526	88.3	70.9		
Total Number of Pixels per Image: 262 144 (512x512)						

4.8 Damage Statistics

Along with the thematic maps, the results of the classification are also described by the class statistics summary report. This report summarizes how many pixels have been classified into each object class, as well as what percentage out of the total number of pixels in the image they represent. These class statistics can be employed to derive damage quantities present in the various images. Since the results of the classification phase indicated that the combination dataset was more effective than the spatial or spectral datasets, and that the supervised ANN classifier was more efficient than the unsupervised *K*-means clustering algorithm, only the class statistics summary reports for the ANN classifications using the combination datasets produced from the greyscale imagery are employed for the purposes of damage quantification. However, in the case of the acoustic imagery, the statistics from the *K*-means classifications were used in order to quantify damage.

For the imagery of map-crack damage from field samples, Table 4.3 gives the class statistics summary of the *K*-means and ANN classifications. The ANN statistics show that the image contains 14.7% surface deterioration from map-cracks.

The class statistics of the classifications carried out for the CANMET blocks demonstrated different levels of AAR damage. The summary report for the greyscale imagery is given in Table 4.4 in section 4.7.2 above, which shows that the C1 specimen presented the least amount of surface deterioration at 3.9%, the C2 specimen had a moderate amount of narrow cracks at 7.2% and wide cracks at 3.4%, for a total of 10.6% surface deterioration, and the C3 specimen revealed a greater amount of narrow cracks at 11.5%, as well as a higher percentage of wide cracks at 8.2%, for a total surface deterioration of 19.7%. The thermographic imagery indicated 5.9% narrow-crack damage in the C1 image, 8.6% narrow-cracks and 4.1% wide-cracks for a total of 12.7% crack damage for the C2 image, and a total of 19.6% damage for the C3 image, consisting of 10.2% narrow-cracks and 9.4% wide-cracks. The colour imagery revealed 4.2% narrow-cracks for C1, 7.8% narrow-cracks and 3.9% wide-cracks for a total of 11.7% crack damage for C2, and 10.6% narrow-cracks and 9.9% wide-cracks, totalling 20.5% crack damage for C3. The differences in the amounts of damage found for the colour and greyscale imagery compared with that of the thermography may be due to pixel misclassifications, since these two types of images contain greater variations within object classes. Figure 4.70 presents a comparison of damage statistics for the three different types of imagery of the C1, C2, and C3 CANMET blocks.

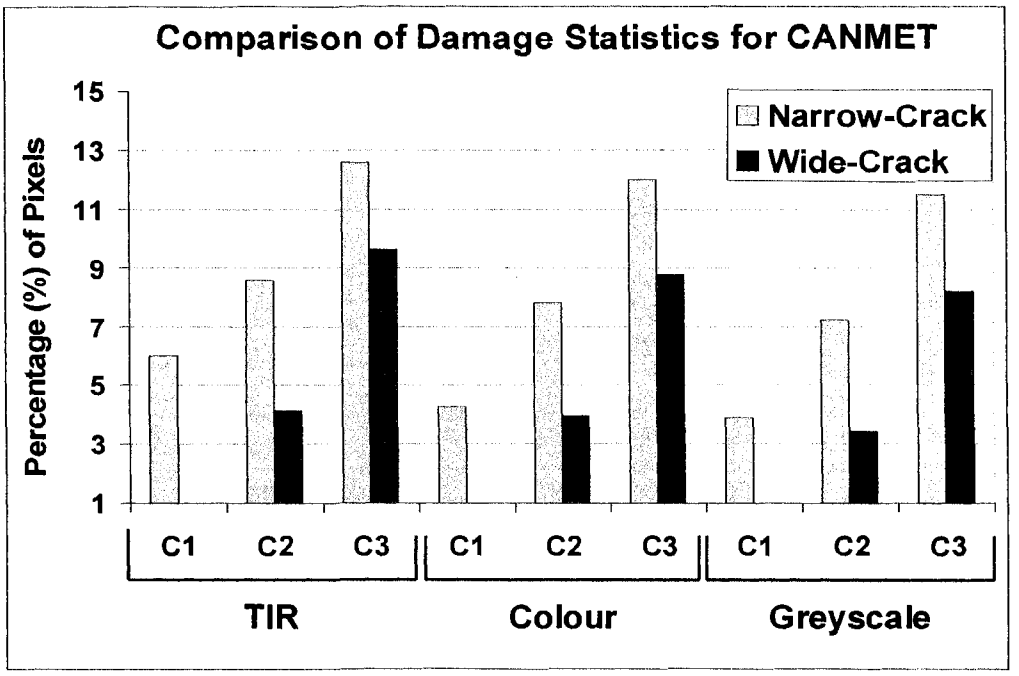

Figure 4.70: Comparison of Damage Statistics for the Three Different Types of CANMET Imagery

Table 4.6 in section 4.7.3 above shows the class statistics summary for the greyscale imagery of the GRAI slabs using the ANN classifier. These statistics also indicate different levels of deterioration due to AAR. The G1 specimen had the lowest total for surface damage at 2.7%, consisting only of narrow cracks. The G2 specimen presented a slightly higher level of surface deterioration with a total of 5.7%, composed of a moderate amount of wide cracks and narrow cracks at 3.5% and 2.2% respectively. The G3 specimen had the highest amount of surface deterioration among the three slabs, with a total of 8.9% damage consisting of wide cracks. Figure 4.71 presents a comparison of these results.

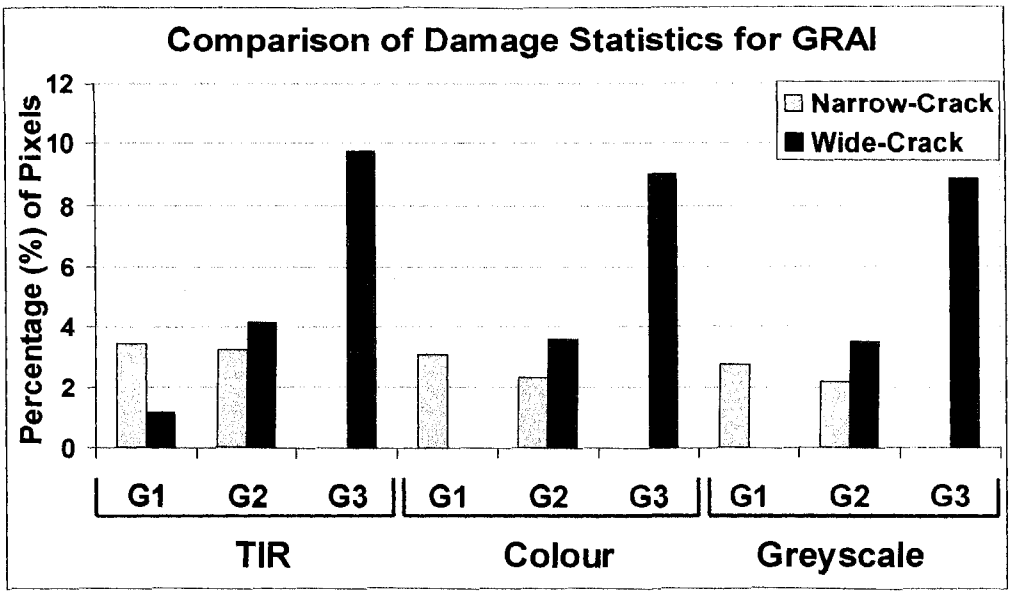

Figure 4.71: Comparison of Damage Statistics for the Three Different Types of GRAI Imagery

For the borehole acoustic imagery, the *K*-means clustering approach was employed to classify the variously processed input images. The classifications done for the acoustic image sample resulted in different amounts of damage, as presented in Table 4.13 in section 4.7.5 above. According to the percentage of pixels classified as the damage class, the texture image indicated 15.5% damage, and the Haar wavelet image presented 15.1% damage. The lowpass-filtered image resulted in 14.6% damage, the median filter indicated 13.7% damage, and the directional filter presented 9.2% damage. Among the edge-detection algorithms, the Marr-Hildreth operator showed 11.7%, the Sobel method presented 17.5%, and the Roberts approach indicated 18.1% damage. The directional and Marr-Hildreth images indicated much lower amounts of damage than the texture image because many pixels were misclassified into the no-damage class, whereas for the Sobel and Roberts images, a number of pixels were misclassified as belonging to the damage class, resulting in higher amounts of damage. Figure 4.72 provides a comparison of the different damage amounts.

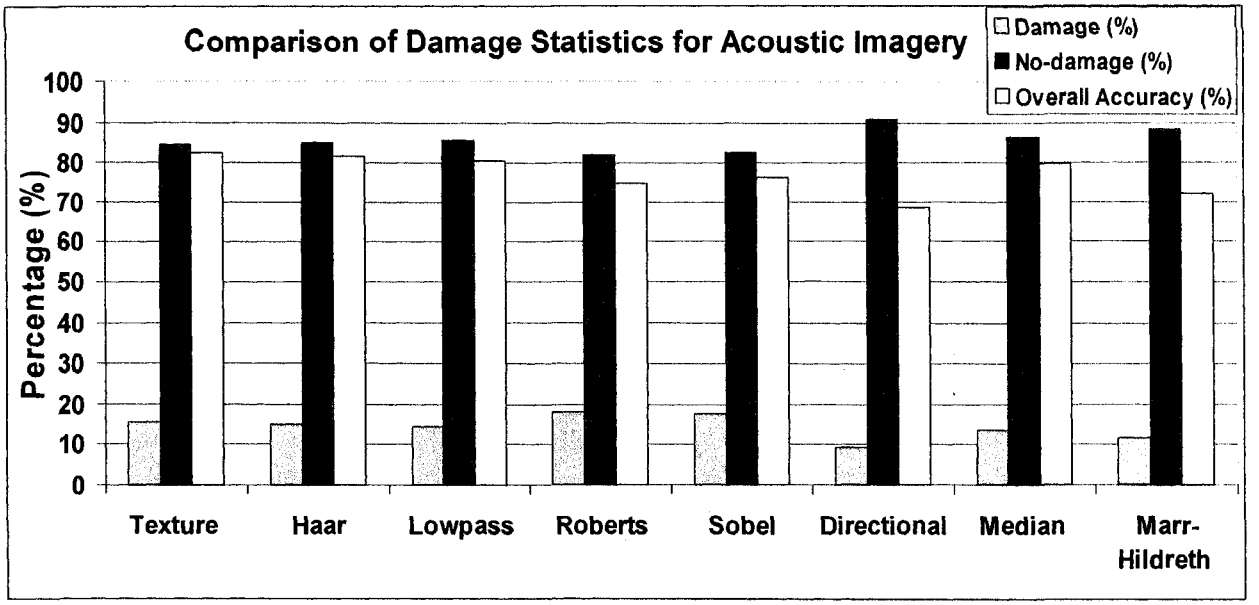

Figure 4.72: Comparison of Damage Statistics for Acoustic Imagery

4.9 Discussion of Results

4.9.1 Results of Texture Analysis Phase

Table 4.14 gives the optimum window size and texture features selected for the different types of damage described in sections 3.1, 3.2 and 3.3.

Table 4.14: Optimum Window Size and Optimum First-order and Second-order Texture Features for Each Type of Damage

Damage Type	Optimum Window Size	Optimum First-order Texture Features	Optimum Second-order Texture Features
Map-crack (Field)	11x11	Mean, Variance, Skew	Mean, Homogeneity, Entropy
Map-crack C1	7x7	Data Range, Mean, Variance	Mean, Homogeneity, Dissimilarity
Map-crack C2	9x9	Mean, Variance, Skew	Mean, Homogeneity, Entropy
Map-crack C3	11x11	Mean, Variance, Skew	Mean, Homogeneity, Entropy
Map-crack G1	7x7	Homogeneity, Mean, Variance	Mean, Homogeneity, Dissimilarity
Map-crack G2	9x9	Data Range, Mean, Variance	Mean, Variance, Homogeneity
Map-crack G3	11x11	Data Range, Mean, Variance	Mean, Variance, Homogeneity
Spalling	11x11	Entropy, Mean, Variance	Mean, Variance, Contrast
Corrosion-1	9x9	Entropy, Mean, Variance	Mean, Variance, Dissimilarity
Corrosion-2	9x9	Entropy, Mean, Variance	Mean, Variance, Correlation
Post-repair Damage	11x11	Data Range, Mean, Skew	Mean, Homogeneity, Second Moment
Erosion	11x11	Entropy, Mean, Variance	Mean, Variance, Homogeneity
Efflorescence Stain	5x5	Entropy, Mean, Variance	Mean, Variance, Homogeneity
Corrosion Stain-1	7x7	Entropy, Mean, Variance	Mean, Variance, Homogeneity
Corrosion Stain-2	7x7	Entropy, Mean, Variance	Mean, Homogeneity, Contrast
Popout Damage	5x5	Entropy, Mean, Variance	Mean, Variance, Contrast
Cracking (Acoustic)	9x9	Entropy, Mean, Variance	Mean, Variance, Homogeneity

The results of the feature selection process indicated that the same texture features are not always the best ones for a particular kind of damage; the characteristics and extent of the damage also influence the efficiency of the features. However, certain features do consistently provide better discrimination. Among the images of map-crack damage from the laboratory specimens, the C2 and C3 CANMET blocks were found to have the same set of most effective first- and second-order texture features, whereas the C1 block had a slightly different set of selected features. For the GRAI slabs, the G1 slab had a somewhat different set of effective features compared with the G2 and G3 specimens, which had the same set of texture features selected for first- and second-order features. These results reflect the varying levels of damage found in the specimens: compared with the C2 and C3 blocks, the C1 block has a much lower level of damage (see Table 4.4 in section 4.7); the same was found for the GRAI slabs, where the G1 slab has a lower amount of damage compared with the G2 and G3 slabs (see Table 4.6 in section 4.7). The imagery of map-crack damage from the field sample had the same set of selected first- and second-order texture features as the C2 and C3 CANMET blocks. This field sample was found to have a similar amount of damage as the two CANMET blocks (see Table 4.3).

The Mean and Variance first-order texture features were selected as two of the most effective features for all of the imagery exhibiting map-crack damage. This indicates that these two features are appropriate for isolating map-crack defects from first-order statistics. For the third first-order texture feature, only the G1 GRAI slab had the Entropy feature selected. This is due to the lower level of crack damage, and higher level of sound concrete found for the G1 slab, which may be an indication that the entropy feature is appropriate for distinguishing areas of the imagery that are more uniform. For the second-order features, Mean and Homogeneity were common to all of the map-crack imagery. Consequently, when employing first- or second-order statistics for texture analysis of map-crack damage, the Mean, Variance and Homogeneity texture features should provide the most effective discrimination.

For imagery of all of the other types of damage, the first-order texture features, Entropy, Mean and Variance, were consistently the same with the exception of the post-repair damage, which only had the Mean feature in common with the others. Concerning the optimum second-order texture features, the post-repair damage again had only the Mean feature in common with the other types of damage. This is due to the fact that in imagery of post-repair damage, the original

concrete and repaired concrete do not have the same texture, which makes the deterioration seem larger and more spread out than in imagery of the other types of defects. Overall, for images of these types of damage, the Entropy, Mean, Variance and Homogeneity features appear to be the most effective when employing first- or second-order statistics for texture analysis. Since Mean, Variance and Homogeneity are also the best features for map-crack damage, it can be concluded that these features would be the most efficient for detecting most types of defects in concrete imagery.

The optimum window size was found to depend very much on the size of the damage class within each image sample; consequently, larger window sizes should be used for more spread-out damage and smaller window sizes should be employed for more localized damage.

4.9.2 Results of Classification Phase

4.9.2.1 Results for Map-crack Damage in Field Samples

K-means and ANN classifications were carried out on the texture dataset of map-crack damage imagery from field samples that were processed using Haar's wavelet transform in combination with texture analysis, as well as using texture analysis alone. This was done in order to evaluate the combined approach of the wavelet transform and texture analysis. Table 4.15 gives the results of the ANN classification performed on the spatial dataset of a greyscale map-crack image sample, which was processed with and without the Haar Transform; the table provides the Kappa coefficient and overall accuracy for the image, along with the accuracies for each class.

Table 4.15: ANN Classification Accuracies for Greyscale Image of Map-crack Damage from Field Sample With and Without Haar Transform

	Texture + Haar	**Texture**
Kappa Coefficient	0.72	0.68
Overall Accuracy (%)	78.1	75.9
Classes	**Accuracy (%)**	
Map-Crack	74.8	73.2
No-Crack	76.3	74.5

The overall classification accuracy for the spatial data obtained with the Haar transform was 78.1% with a range of 74.8% to 76.3% for individual class accuracies, which is significantly higher than the overall accuracy of 75.9% and individual class accuracies between 73.2% and 74.5% acquired by the spatial data without the Haar transform.

Classifications were also carried out on the spatial dataset of map-crack imagery, for which the texture data was produced using a combination of first-order and second-order statistics, as well as using second-order statistics alone. This was done in order to evaluate the effectiveness of combining the first- and second-order statistics. Table 4.16 provides the ANN classification results for an image sample of map-crack damage.

Table 4.16: ANN Classification Accuracies for Greyscale Image of Map-crack Damage from Field Sample With and Without First-order Data

	First-order + Second-order	**Second-order**
Kappa Coefficient	0.72	0.69
Overall Accuracy (%)	78.1	76.3
Classes	**Accuracy (%)**	
Map-Crack	74.8	72.9
No-Crack	76.3	75.1

The combination of first- and second-order texture information provided a higher overall classification accuracy compared to the second-order data alone, at 78.1% and 76.3% respectively. Class accuracies were also higher for the combined dataset at a range of 74.8% to 76.3% compared to a range of 72.9% to 75.1% for the second-order data.

The results of the *K*-means and ANN classifications done for a greyscale image sample of map-crack damage processed with the Haar transform are presented in Table 4.17 and Table 4.18 respectively, which show the Kappa coefficients and overall accuracies for the three datasets, spectral, spatial, and combined, as well as the classification accuracies obtained for each class.

For the *K*-means classifications, the overall accuracy for the spectral dataset was 76.2%, the spatial dataset had an overall classification accuracy of 73.7%, and the combined dataset had an overall accuracy that was somewhat higher than that of the other two datasets, at 78.3%.

Classification accuracies for the individual damage classes ranged from 77.8% to 78.9% for the spectral dataset, 74.8% to 76.3% for the spatial dataset, and 79.4% to 81.7% for the combined dataset.

The ANN classifications resulted in an overall accuracy of 79.6% for the spectral dataset, the spatial dataset had an overall accuracy of 78.1%, and the combined dataset had an overall accuracy that was once again relatively higher, at 83.2%. Individual class accuracies ranged from 83.1% to 84.8% for the spectral dataset, 81.8% to 82.7% for the spatial dataset, and 85.3% to 86.5% for the combined dataset.

Table 4.17: *K*-means Classification Accuracies for Greyscale Image of Map-crack Damage from Field Sample

	Spectral Dataset	**Spatial Dataset**	**Combined Dataset**
Kappa Coefficient	0.71	0.69	0.75
Overall Accuracy (%)	76.2	73.7	78.3
Classes	**Accuracy (%)**		
Map-Crack	77.8	74.8	79.4
No-Crack	78.9	76.3	81.7

Table 4.18: ANN Classification Accuracies for Greyscale Image of Map-crack Damage from Field Sample

	Spectral Dataset	**Spatial Dataset**	**Combined Dataset**
Kappa Coefficient	0.76	0.72	0.81
Overall Accuracy (%)	79.6	78.1	83.2
Classes	**Accuracy (%)**		
Map-Crack	83.1	81.8	86.5
No-Crack	84.8	82.7	85.3

These classifications for map-crack damage in field data indicate that the classifications performed on images, which have been processed with texture analysis in combination with the Haar transform, provided better classification accuracies compared with classifications performed on imagery processed without the Haar transform.

In terms of texture information, the combination of first- and second-order spatial data resulted in higher classification accuracies than classifications done with only second-order texture information. The results also indicate that the spectral dataset is more effective than the spatial dataset, which consistently had lower overall classification accuracies, as well as accuracies for each damage class. This may be due to the fact that in general, texture features are highly correlated and do not provide enough information to distinguish more homogeneous areas in an image. The combined dataset, however, provided comparatively higher classification accuracies, both overall and on an individual basis, than the purely spectral and spatial datasets.

Between the two types of classifications carried out on the map-crack field data, the ANN approach produced higher overall classification accuracies with a range of 78.1% to 83.2%, compared with the *K*-means classifier, which had overall classification accuracies between 73.7% and 79.3%.

4.9.2.2 Results for Map-crack Damage in CANMET Blocks

Results of the *K*-means classifications done for the three CANMET blocks using the thermographic, colour and greyscale imagery in the spatial, spectral and combination datasets are presented in Table 4.19. This table provides the Kappa coefficients and overall accuracies for each specimen, C1, C2 and C3, along with the classification accuracies for each class. The spatial data for these classifications was obtained through texture analysis in combination with the Haar transform.

The overall accuracies obtained through the *K*-means classifications for the CANMET specimens using the spectral dataset ranged from 78.9% to 81.2%. The spatial dataset had overall classification accuracies between 70.3% and 73.4%. For the combination dataset, the overall accuracies ranged from 80.7% to 83.1%. Classification accuracies for the individual classes were between 79.5% and 83.3% for the spectral dataset, between 72.3% and 78.6% for the spatial

dataset, and between 82.9% and 87.6% for the combination dataset. In terms of imagery, the overall *K*-means classification accuracies obtained for the three types of CANMET imagery differed slightly with respect to each other. The thermographic imagery had overall accuracies between 71.5% and 83.1%. For the colour imagery, the overall accuracies ranged from 70.8% to 82.6%. The greyscale imagery had an overall classification accuracy range of 69.7% to 81.8%.

Table 4.19: *K*-means Classification Accuracies for CANMET Specimens

Spectral Dataset									
CANMET Blocks	**Thermographic**			**Colour**			**Greyscale**		
	C1	**C2**	**C3**	**C1**	**C2**	**C3**	**C1**	**C2**	**C3**
Kappa Coefficient	0.75	0.76	0.73	0.75	0.72	0.75	0.73	0.74	0.72
Overall Accuracy (%)	80.8	81.2	79.7	80.3	79.1	79.5	81.0	78.9	79.3
Classes	**Accuracy (%)**								
Wide Crack	82.3	81.5	81.9	82.8	80.5	80.7	79.5	81.8	80.6
Narrow Crack	81.7	83.1	82.5	81.4	82.2	81.0	80.9	82.1	79.7
No Crack	82.6	82.0	83.3	80.8	81.6	82.7	81.3	79.8	81.2
Spatial Dataset									
Kappa Coefficient	0.71	0.70	0.71	0.68	0.69	0.70	0.68	0.67	0.69
Overall Accuracy (%)	72.7	71.5	73.4	70.8	73.1	72.5	69.7	70.3	71.6
Classes	**Accuracy (%)**								
Wide Crack	77.4	75.8	78.6	76.4	74.5	76.1	74.0	72.8	73.3
Narrow Crack	76.8	74.3	75.9	74.7	75.2	73.8	73.7	73.9	72.9
No Crack	74.9	75.0	74.8	75.6	73.4	75.1	72.3	74.2	72.5
Combined Dataset									
Kappa Coefficient	0.80	0.81	0.79	0.81	0.78	0.80	0.79	0.77	0.78
Overall Accuracy (%)	83.1	82.8	82.2	81.7	82.6	81.4	81.8	80.7	80.9
Classes	**Accuracy (%)**								
Wide Crack	87.2	85.5	84.3	86.7	83.9	84.4	84.8	83.6	82.9
Narrow Crack	85.2	84.7	86.1	84.1	86.0	85.6	83.7	84.6	83.4
No Crack	84.9	86.3	87.6	85.0	84.2	85.7	84.0	85.1	83.1

Table 4.20 presents the results of the ANN classifications for each of the three CANMET blocks, C1, C2 and C3, providing the classification accuracies obtained for each class, as well as the Kappa coefficients and overall accuracies for the three types of imagery, thermographic, colour and greyscale, employed in the spectral, spatial, and combined datasets.

Table 4.20: ANN Classification Accuracies for CANMET Specimens

Spectral Dataset									
CANMET Blocks	**Thermographic**			**Colour**			**Greyscale**		
	C1	**C2**	**C3**	**C1**	**C2**	**C3**	**C1**	**C2**	**C3**
Kappa Coefficient	0.81	0.78	0.79	0.78	0.80	0.76	0.77	0.79	0.78
Overall Accuracy (%)	83.9	84.2	82.7	83.5	82.4	81.3	82.6	80.6	83.1
Classes	**Accuracy (%)**								
Wide Crack	84.6	85.2	84.4	83.9	83.3	82.7	82.9	82.0	83.0
Narrow Crack	85.0	83.8	83.6	84.0	82.1	83.4	81.5	83.2	81.7
No Crack	84.9	84.1	82.3	82.6	83.5	81.9	83.1	82.5	81.2
Spatial Dataset									
Kappa Coefficient	0.73	0.73	0.74	0.69	0.71	0.74	0.74	0.73	0.76
Overall Accuracy (%)	74.5	73.1	76.3	71.4	75.2	74.1	72.3	76.5	75.4
Classes	**Accuracy (%)**								
Wide Crack	81.3	79.9	83.5	78.6	78.1	78.4	76.8	78.1	78.4
Narrow Crack	79.7	78.6	81.5	77.7	73.9	77.5	76.3	72.9	77.5
No Crack	82.4	76.7	80.6	75.3	74.6	74.2	73.6	71.4	74.2
Combined Dataset									
Kappa Coefficient	0.85	0.84	0.84	0.86	0.83	0.86	0.83	0.84	0.85
Overall Accuracy (%)	88.7	86.2	87.5	85.6	88.1	86.9	85.5	87.6	84.8
Classes	**Accuracy (%)**								
Wide Crack	89.2	86.4	87.9	86.9	88.4	87.5	86.3	85.7	84.1
Narrow Crack	87.6	89.9	89.7	85.3	87.8	84.9	85.1	84.6	85.9
No Crack	88.9	87.3	89.0	87.0	86.7	85.8	84.2	86.6	84.2

The overall ANN classification accuracies obtained for the CANMET blocks using the spectral dataset were between 80.6% and 84.2%. For the spatial dataset, the overall accuracies ranged from 71.4% to 76.5%. The combined dataset, on the other hand, had overall classification accuracies ranging from 84.8% to 88.7%. For the individual classes, the classification accuracies ranged from 81.2% to 85.2% for the spectral dataset, 71.4% to 83.5% for the spatial dataset, and 84.1% to 89.9% for the combined dataset.

Overall classification accuracies for the different types of CANMET imagery using the ANN classifier varied somewhat, with a range of 73.1% to 88.7% for the thermography, 71.4% to 88.1% for the colour imagery, and 72.3% to 87.6% for the greyscale imagery.

As with the classifications of map-crack imagery from the field samples, these classifications performed with map-crack imagery of the CANMET laboratory specimens also indicate that the combination dataset is more effective in characterizing the damage than the spatial or spectral datasets, obtaining higher overall classification accuracies, as well as higher accuracies for the individual damage classes, than the other two datasets.

Another finding similar with that of the classifications for the map-crack field data is that the ANN classifier performed better than the *K*-means approach, with overall classification accuracies ranging between 71.4% and 88.7%, compared with an overall classification accuracy range of 69.7% to 83.1% for the *K*-means classifier.

4.9.2.3 Results for Map-crack Damage in GRAI Slabs

Results of the *K*-means classifications done for the three GRAI specimens using the thermographic, colour and greyscale imagery in the spatial, spectral and combination datasets are presented in Table 4.21. This table provides the Kappa coefficients and overall accuracies for each specimen, along with the classification accuracies for each class. The spatial data employed in these classifications was obtained through texture analysis with the Haar transform.

The *K*-means classifications for the GRAI slabs produced overall classification accuracies that ranged between 75.7% and 79.4% for the spectral dataset. For the spatial dataset, the overall accuracies ranged from 71.5% to 73.9%. The combined dataset had overall classification

accuracies ranging from 80.4% to 82.8%. Classification accuracies for individual damage classes ranged between 75.3% and 79.5% for the spectral dataset, between 70.5% and 75.3% for the spatial dataset, and between 80.3% and 83.7% for the combined dataset. For the different types of GRAI imagery, the overall classification accuracies obtained using the *K*-means classifier ranged from 72.3% to 82.8% for the thermographic imagery, 72.7% to 81.9% for the colour imagery, and 71.5% to 82.1% for the greyscale imagery.

Table 4.21: *K*-means Classification Accuracies for GRAI Specimens

Spectral Dataset									
GRAI Slabs	**Thermographic**			**Visual Colour**			**Greyscale**		
	G1	**G2**	**G3**	**G1**	**G2**	**G3**	**G1**	**G2**	**G3**
Kappa Coefficient	0.76	0.74	0.75	0.73	0.75	0.74	0.73	0.72	0.75
Overall Accuracy (%)	77.8	78.2	79.4	75.7	77.9	76.6	76.3	75.9	76.5
Classes	**Accuracy (%)**								
Wide Crack	78.7	77.5	78.3	77.7	76.8	78.1	76.9	77.4	75.8
Narrow Crack	76.4	78.4	77.9	76.2	78.5	75.7	77.2	76.3	75.3
No Crack	78.6	79.1	79.5	78.2	77.8	76.5	78.0	75.6	77.1
Spatial Dataset									
Kappa Coefficient	0.73	0.72	0.71	0.71	0.70	0.72	0.70	0.71	0.71
Overall Accuracy (%)	72.3	73.2	73.9	72.8	73.1	72.7	71.5	72.0	72.6
Classes	**Accuracy (%)**								
Wide Crack	73.9	75.3	74.6	72.4	73.7	74.2	70.8	71.5	72.1
Narrow Crack	72.8	73.6	71.7	72.9	70.6	72.2	71.6	70.5	71.2
No Crack	73.3	72.4	75.0	71.3	74.6	73.1	72.7	70.9	71.8
Combined Dataset									
Kappa Coefficient	0.78	0.80	0.81	0.79	0.77	0.80	0.78	0.77	0.79
Overall Accuracy (%)	80.9	82.8	81.7	81.3	80.7	81.9	80.4	81.2	82.1
Classes	**Accuracy (%)**								
Wide Crack	83.7	82.2	80.8	82.5	81.4	83.0	81.8	82.0	80.5
Narrow Crack	82.6	81.9	81.6	81.7	80.1	82.6	80.3	82.6	81.5
No Crack	80.3	83.5	82.1	82.7	80.6	81.3	82.9	81.1	82.8

Table 4.22 presents the results of the ANN classifications for each of the three GRAI blocks, providing the classification accuracies obtained for each class, as well as the Kappa coefficients and overall accuracies for the GRAI specimens, using the thermographic, colour and greyscale imagery in the three datasets.

Table 4.22: ANN Classification Accuracies for GRAI Specimens

Spectral Dataset									
GRAI Slabs	**Thermographic**			**Visual Colour**			**Greyscale**		
	G1	**G2**	**G3**	**G1**	**G2**	**G3**	**G1**	**G2**	**G3**
Kappa Coefficient	0.79	0.79	0.80	0.78	0.76	0.79	0.77	0.75	0.78
Overall Accuracy (%)	82.4	80.8	83.1	81.7	79.8	78.6	81.5	80.4	77.4
Classes	**Accuracy (%)**								
Wide Crack	82.6	83.8	82.9	83.0	82.3	81.7	80.6	81.8	81.4
Narrow Crack	81.9	82.7	83.2	80.9	81.6	80.4	81.3	79.9	80.2
No Crack	83.4	82.1	84.2	82.5	83.3	81.5	82.5	81.0	79.7
Spatial Dataset									
Kappa Coefficient	0.75	0.74	0.76	0.72	0.74	0.74	0.73	0.72	0.74
Overall Accuracy (%)	75.6	76.9	74.2	73.9	72.6	73.0	71.9	74.3	75.3
Classes	**Accuracy (%)**								
Wide Crack	76.7	78.1	80.0	73.4	76.1	78.9	73.2	77.1	75.7
Narrow Crack	74.7	75.2	73.8	74.1	72.9	73.4	73.7	72.9	73.6
No Crack	76.6	74.9	79.1	72.6	76.4	78.2	73.9	71.4	77.0
Combined Dataset									
Kappa Coefficient	0.81	0.84	0.85	0.83	0.84	0.82	0.83	0.80	0.82
Overall Accuracy (%)	85.9	82.9	84.7	84.9	82.2	85.1	83.2	84.5	83.6
Classes	**Accuracy (%)**								
Wide Crack	86.6	84.3	82.4	83.2	86.0	84.5	83.7	85.1	84.0
Narrow Crack	85.4	83.9	86.9	84.7	82.2	86.3	82.0	82.6	84.3
No Crack	82.8	87.4	88.2	85.9	83.8	85.2	84.7	83.1	85.8

The overall classification accuracies obtained for the GRAI slabs using the ANN classifier on the spectral dataset ranged from 77.4% to 83.1%. The overall accuracies for the spatial dataset were between 71.9% and 76.9%. For the combined dataset, the overall classification accuracies ranged from 82.2% to 88.7%. The classification accuracies for the individual classes were between 79.7% and 84.2% for the spectral dataset, between 71.4% and 80.0% for the spatial dataset, and between 82.0% and 88.2% for the combined dataset.

Application of the ANN classifier on the different types of GRAI imagery produced overall classification accuracies that ranged from 73.1% to 88.7% for the thermography, from 71.4% to 88.1% for the colour imagery, and from 72.3% to 87.6% for the greyscale imagery.

Once again, the results of the classifications performed with imagery of the GRAI laboratory specimens indicate the efficiency of the combined dataset over the spatial or spectral datasets; overall classification accuracies, and accuracies for the individual damage classes, were relatively higher for the combined dataset compared with the other two datasets.

These classifications also demonstrate that the ANN classifications produced higher overall classification accuracies than the *K*-means classifier, with accuracies ranging between 71.9% and 85.9%, compared with an accuracy range of 71.5% to 82.8% for the *K*-means approach.

4.9.2.4 Discussion of Map-Crack Classification Results

The results of the classifications done for the field samples and laboratory specimens exhibiting map-crack damage show the importance of signal processing to the spatial data acquired through texture analysis. The wavelet transform effectively separated the coarse texture information, which consists of the defects in the concrete, from the finer textures in the imagery, improving the extraction of these deterioration features in the texture analysis process. Also, better classifications produced by the combination of first- and second-order texture information demonstrate the value of the different statistics to the spatial data. Since first-order statistics provide information concerning individual pixels and second-order statistics present information about pairs of pixels, it was expected that the combination of this information would produce better classifications, although the process of extracting and selecting both first- and second-

order texture features requires slightly more computational time than working with second-order statistics alone.

Improved classification accuracies resulting from the combined dataset for the map-crack imagery indicate the significant contribution of texture information to the characterization of concrete damage. The additional information provided by the spatial data improved the characterization of the heterogeneous areas in the image. These results are similar to those found by Shaban and Dikshit (2001) who conducted an in-depth study on the use of texture features to improve the classification of remote sensing imagery of urban areas. Furthermore, the ANN classifier appears to be more efficient than the *K*-means clustering technique, achieving higher overall classification accuracies for all the image samples.

Among the different types of imagery, the thermography produced overall classification accuracies that were slightly higher than the colour and greyscale imagery. Although the thermographic images do not have the same resolution as the optical imagery, this does not affect the results of the classifications, because each image is processed separately with the wavelet transform and the texture analysis according to the individual image properties.

4.9.2.5 Results for Spalling, Corrosion, Popouts, Erosion, Post-repair Damage, and Efflorescence and Corrosion Stains

Since the discussion for map-crack damage found that the combined approach of texture analysis and the wavelet transform, as well as classifications involving both first- and second-order textural data along with the spectral-spatial dataset provided improved results, discussions for imagery of concrete damage exhibiting spalling, corrosion, popouts, erosion, post-repair damage, and efflorescence and corrosion stains focus on results obtained using these techniques. The results of the classifications for the other types of concrete damage are provided in Table 4.23. This table shows the Kappa coefficient and overall classification accuracy for each type of damage, as well as the classification accuracy for each damage class, based on the ANN classifications using the greyscale image samples and the combined spatial-spectral dataset, since these were found to be the most effective in the map-crack damage classifications.

Table 4.23: Overall ANN Classification Accuracies and Kappa Coefficients for Different Types of Damage and Accuracies for Each Class

Damage Type	Classes	Accuracy (%)	Kappa Coefficient	Overall Accuracy
Spalling	Spalling	83.2	0.82	83.4
	No-spalling	84.7		
Corrosion	Corroded-steel	83.8	0.81	84.7
	Spalling	82.5		
	No-damage	83.2		
Popouts	Popout-centre	85.1	0.84	85.5
	Popout-edges	81.9		
	No-damage	84.3		
Erosion	Eroded	78.4	0.78	77.6
	Non-eroded	79.1		
Post-repair Damage	Crack	75.9	0.75	76.8
	Repaired	76.5		
	No-damage	77.1		
Efflorescence Stains	Cracks	79.4	0.79	82.1
	Stains	77.9		
	No-damage	81.7		
Corrosion Stains	Stains	77.3	0.76	78.6
	No-damage	78.0		

4.9.2.6 Results for Acoustic Imagery

For the borehole acoustic imagery, classifications were carried out on the Haar transformed image, on the texture image, as well as on the output images resulting from the application of the various spatial filters and edge-detectors. The overall classification accuracies, the Kappa coefficients, and the individual classification accuracies for each class obtained through the ANN classifier are presented in Table 4.13 in section 4.7.5 above.

Results of the classification indicate that among the different image processing techniques, the GLCM texture analysis method produced the highest overall classification accuracy at 82.4%.

The next most effective approach was the Haar wavelet transform, with an overall accuracy of 81.7%. Among the spatial filters, the lowpass filter provided an overall accuracy that was slightly lower than that of the Haar transform, at 80.6%. The median filter produced better classification accuracies than the remaining techniques, with an overall accuracy of 79.7%. The Sobel and Roberts edge-detection algorithms obtained overall accuracies of 76.2% and 75.0%, respectively, which were somewhat higher than the 72.1% overall accuracy of the Marr-Hildreth edge-detector. The directional filter was the least effective technique, with an overall classification accuracy of 68.5%.

The four techniques of GLCM, Haar transform, lowpass filter and median filter produced better results than the other four approaches; this is probably due to the fact that the acoustic image had very little background noise, which resulted in distinct textural classes for the GLCM method and good separation of texture details through the Haar transform. Since the lowpass filter and the median filter essentially smooth an image and reduce noise, they were quite efficient in defining the crack damage. The low amount of noise in the acoustic image also resulted in relatively higher overall accuracies for the Roberts and Sobel operators compared with the directional filter; however, the Marr-Hildreth algorithm was expected to produce better results among the edge-detectors. Applying the Laplacian without the Gaussian filtering may increase the effectiveness of this technique with acoustic imagery.

4.10 Cracking Quantification

In order to further analyse surface damage, the classified images were converted into binary images. This process simplifies the image by assigning the pixels that represent damage a value of 1 (black) and the background pixels a value of 0 (white). Manual or automated methods are then used to count or sum the pixels to calculate total crack length, as well as average crack width.

In order to quantify the total length of cracks from the imagery of the laboratory specimens, the number of pixels along the length of each branch of the cracks was summed and the total multiplied by the pixel resolution of 0.26 mm. For the CANMET blocks, a total length of 237 mm of wide cracks was calculated for the C3 specimen, for the C2 specimen, the total length was

found to be 98 mm, and for the C1 specimen, the total length was 0 mm. Among the GRAI slabs, the total length of wide cracks was calculated to be 0 mm, 39 mm and 107 mm for the G1, G2 and G3 specimens, respectively. The average crack width was determined by measuring the width at several points along the cracks. Figure 4.73 is an example of this analysis applied on the classification of the CANMET C3 specimen; Figure 4.73(a) shows the crack damage with examples of crack segments. Figure 4.73(b) provides examples of crack width measurements for the specimen; each square represents one pixel at a resolution of 0.26 mm. As a result, the average width of cracks in the CANMET blocks was found to be 1.6 mm in the C3 specimen, 0.8 mm in the C2 specimen, and 0 mm for the C1 specimen. For the GRAI slabs, the average crack widths were 0 mm for G1, 0.3 mm for G2 and 0.8 mm for the G3 specimen.

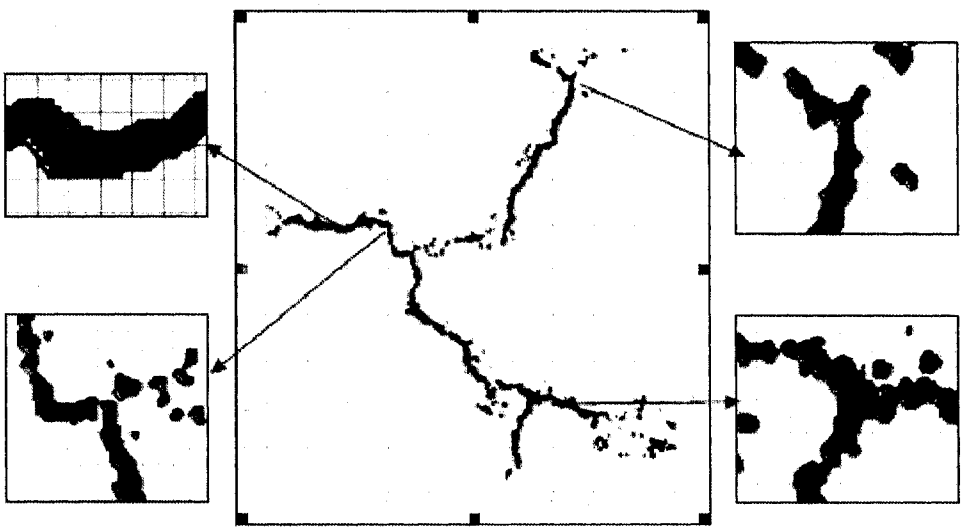

(a) Examples of crack segments

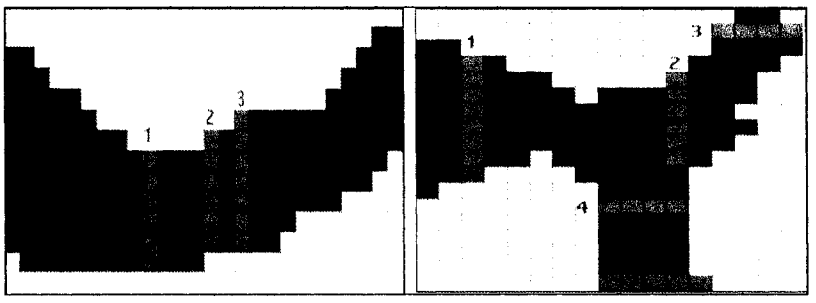

(b) Examples of crack width measurements

Figure 4.73: Crack Width Measurements for CANMET-C3; Pixel Resolution 0.26 mm

These findings are supported by concrete mixture data and test measurements recorded for the CANMET and GRAI specimens. The concrete mixture data found in Table 3.1 show that among the CANMET blocks, the C3 sample was prepared with the highest alkali content, and the C1 sample with the lowest. This corresponds well with the higher percentage of damage found in the C3 sample and the lowest percentage found for the C1 sample. The highest values for the total length of wide cracks as well as for the average width of cracks found for the C3 sample also relate well to its having the lowest average for the *P*-wave velocity tests, provided in Table 3.2, indicating the presence of the most deterioration.

As for the GRAI slabs, the absence of wide cracks in the G1 specimen, which had a value of 0 mm for the average width of cracks, as well as for the total length of cracks, is corroborated by its having the lowest expansion level, indicating very little damage. A higher level of expansion was measured on the G2 specimen, with the G3 specimen having the highest measurement for expansion level among the slabs. Figure 4.74 presents a comparison of the total amount of crack damage and expansion levels among the three CANMET blocks and the three GRAI slabs. Figure 4.75 is a comparison of the total crack length and expansion levels for all the specimens.

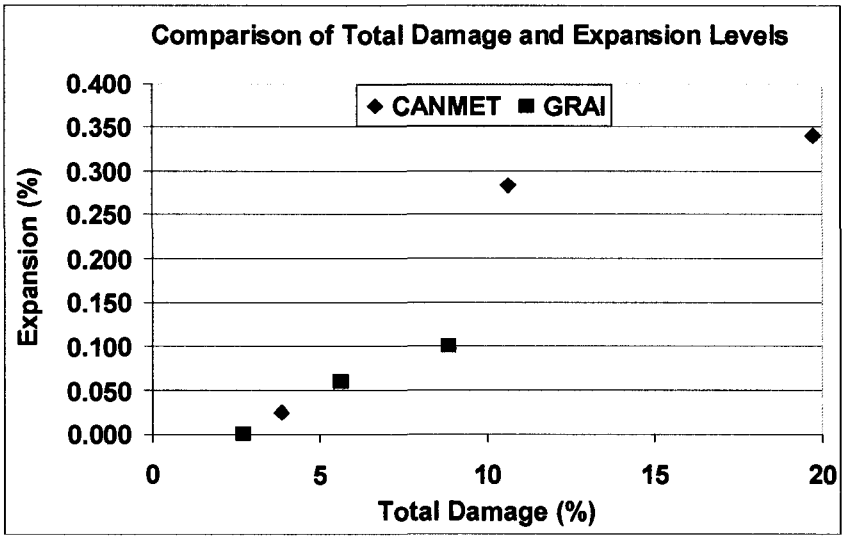

Figure 4.74: Comparison of Total Crack Damage and Expansion Levels

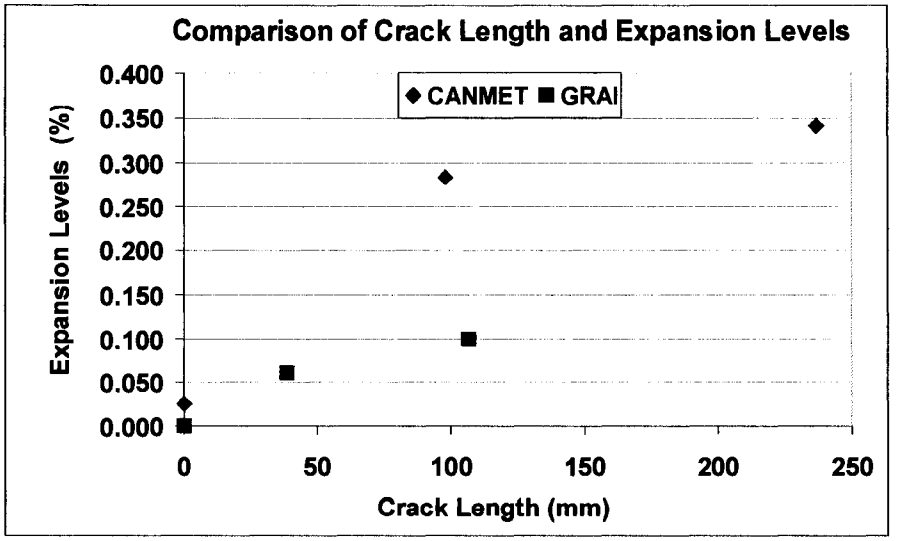

Figure 4.75: Comparison of Crack Length and Expansion Levels

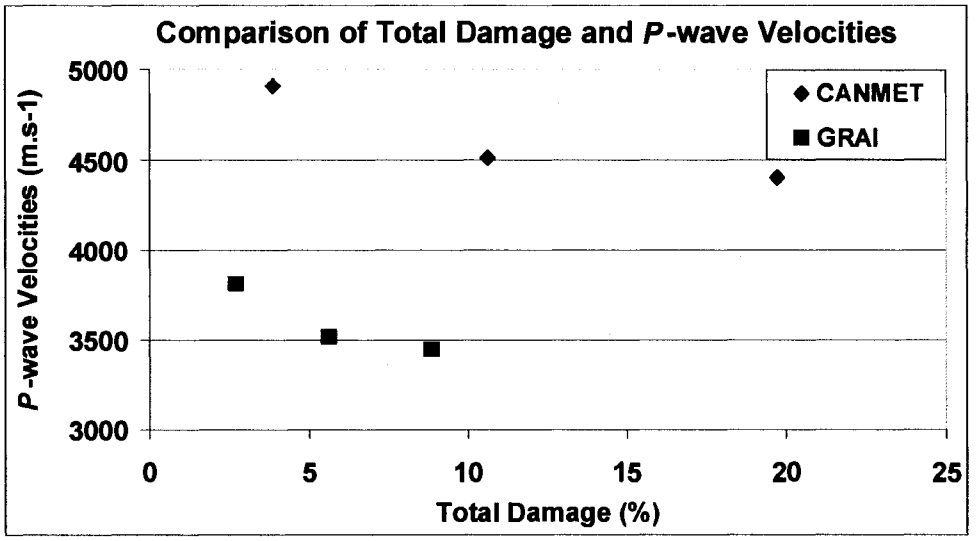

Figure 4.76: Comparison of Total Crack Damage and *P*-wave Velocities

This process was also conducted for the imagery of the field samples. Figure 4.76 shows the binary image of the classification for the train bridge component along with zoomed areas indicating the different ranges of crack widths: R1 is from 0.10 mm to 0.15 mm, R2 is between 0.15 mm and 0.20 mm, R3 is from 0.20 mm to 0.30 mm, and R4 is above 0.30 mm.

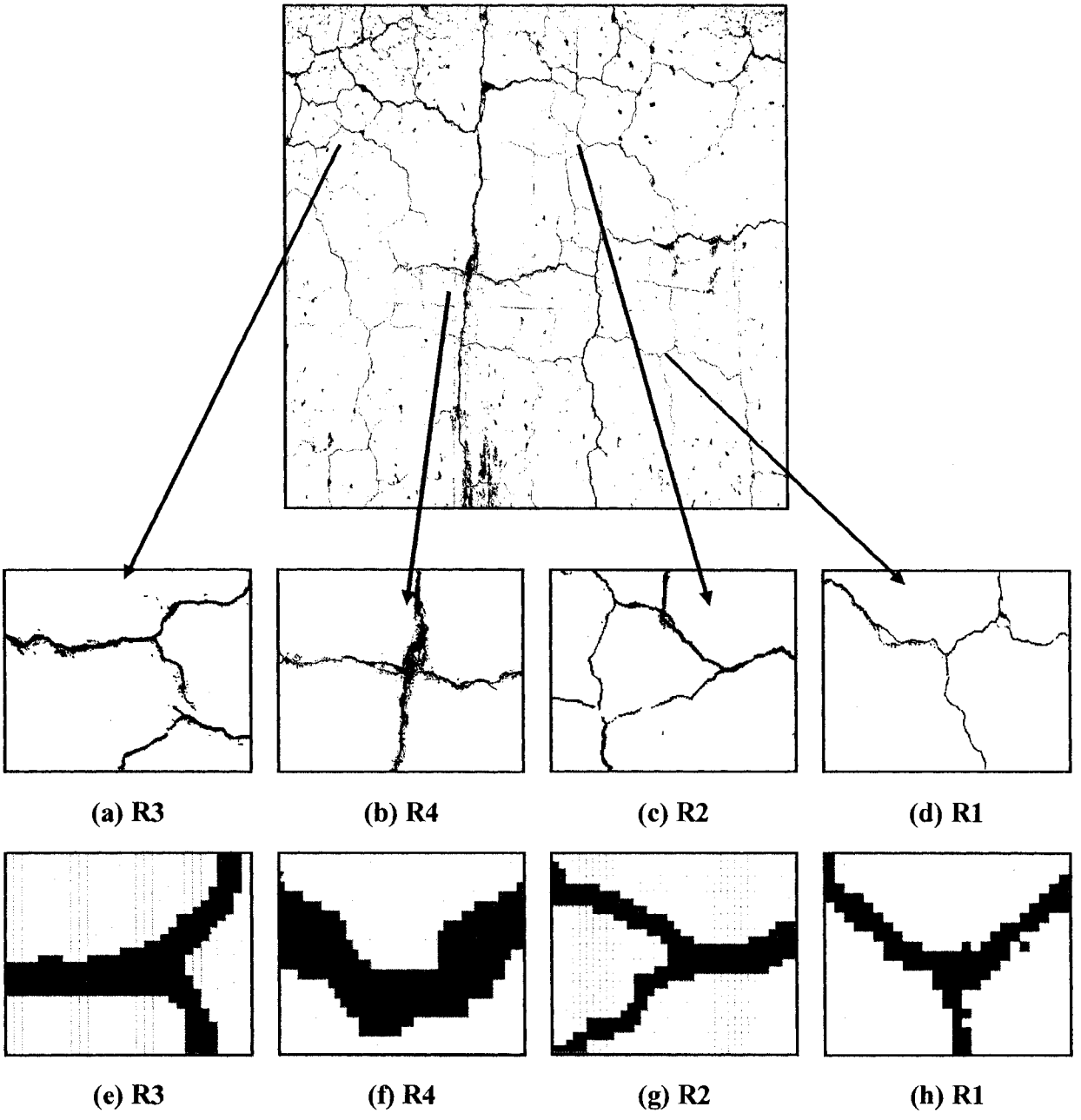

Figure 4.77: Crack-width Ranges from Binary Image of Train Bridge Component; (a)-(d) Zoomed to 1x and (e)-(h) Zoomed to 20x with a Grid of 1 Pixel per Square

CHAPTER 5

Conclusions and Recommendations

5.1 Conclusions

The main goal of this thesis was to improve image processing methods through hybridization in order to extract quantitative information concerning concrete damage from images obtained through different NDT approaches. It was hypothesised that statistical texture analysis would provide a good basis that could be improved upon through hybridization with the wavelet transform, through the combination of first- and second-order statistics, and through the addition of spectral data.

The results of this research confirm the major hypothesis of this thesis, that statistical texture analysis is quite an efficient method for the discrimination of different types of deterioration, such as cracks, spalling, corrosion, popouts, erosion, post-repair damage, as well as efflorescence and corrosion stains, from optical and thermographic concrete imagery. The experiments demonstrate that the combined transform and statistical-based approach of Haar's discrete wavelet and GLCM texture analysis was more effective in reducing the amount of background noise and unwanted texture information usually present in concrete imagery compared with only the GLCM approach. This affirms the hypothesis that through this hybrid technique, the detection of deterioration from concrete imagery can be improved.

Classifications conducted with the different statistics indicate that the combination of first-order and second-order statistics allow for the extraction of more representative texture features to characterize different types of concrete damage than the second-order statistics alone. It was also found that the spectral data contributed significantly to the classifications of the different damage

classes, as revealed by the experiments conducted with the three datasets, in which the combined dataset of spectral and spatial information produced the highest classification accuracies. These results verify the hypotheses that both first- and second-order texture features, as well as a combination of spectral and spatial data can provide better discrimination of concrete damage.

Selection of the optimum texture features for images of the different types of damage indicated that certain features work best for defects with similar characteristics. The same first- and second-order texture features were found to be most effective for images of map-crack damage with similar amounts of deterioration; images that had very little crack damage had a different set of optimum features. For imagery of the other types of concrete damage, the same first-order features were established as the most efficient, except for the post-repair damage. The optimum second-order statistics were mostly the same for all of the other damage types, except for the post repair damage. The characteristics for this damage were quite different than the other types, resulting in different optimum first- and second-order texture features. However, it was found that some texture features are generally effective for most types of concrete damage.

Results of the classifications show that the supervised ANN classifier produced classification accuracies that were higher compared with the unsupervised *K*-means clustering algorithm. However, application of the ANN requires more computational time due to the selection of training and verification ROIs.

In terms of imagery, the thermographic classifications produced higher accuracies than the colour and greyscale classifications. This is partly due to the fact that thermographic images contain less variability within the concrete imagery, and at the same time increase the visibility of deterioration that may be otherwise imperceptible, even in colour or greyscale imagery. However, using thermography or even colour imagery in texture applications is computationally costly and results in a large number of features. There are also some limitations involved in acquiring thermographic imagery: the thermographic camera is still somewhat expensive and image quality is highly influenced by weather conditions. Consequently, due to the dimensionality of the thermographic imagery and the limitations in acquiring them, the use of greyscale imagery appears to be quite acceptable, since classification accuracies resulting from these images are only slightly lower than those of thermographic imagery.

Application of the spatial filters and edge-detection techniques on the borehole acoustic imagery indicated that the lowpass filter outperformed the other methods, along with the median filter, which produced classification accuracies slightly lower than the lowpass filter. Among the edge-detectors, the gradient approaches worked best; the Sobel operator produced higher classification results compared to the Roberts algorithm. The Laplacian edge-detector and the directional filter had lower classification accuracies than all other methods. However, the texture analysis approach and the wavelet transform produced classification results that were significantly higher than any of the spatial filters and edge-detection operators, with the texture analysis method being the most effective of all the techniques. As a result, it was concluded that the texture analysis approach is comparatively more effective for detecting concrete damage.

Quantification of the amount of surface deterioration present in the image samples was effectively performed using class statistics summaries from the classifications. Further damage quantities were obtained for the map-crack imagery after conversion of the thematic maps into binary images, such as total crack length and average crack width, by using pixel summations. The damage quantities obtained for the CANMET and GRAI laboratory specimens demonstrated good correlation with test measurements done for the specimens. For this type of analysis, high resolution imagery is desirable in order to obtain accurate damage estimates; consequently, close-up images of the concrete surface would be more appropriate. For a flexible image acquisition system, greyscale or colour imaging should be considered, since these can be acquired even from a distance and are less dependant on weather conditions compared with IR thermography. As a result, this type of quantitative information obtained through NDT imaging can improve the quality of concrete condition information used for making decisions concerning maintenance and repairs.

5.2 Recommendations

The image processing methods outlined in this research for analysing NDT imagery appear to be quite efficient in providing cost- and time-effective quantitative evaluations of concrete damage from optical imagery; these approaches allow assessments to be carried out more often, and can be used to supplement visual inspections.

The quantitative analysis resulting from these approaches can also be used for the development of an automated system for damage assessment to determine the different levels of deterioration from concrete imagery. An automated system would facilitate the analysis and classification of a large volume of image data. Consequently, the parameters that were found to be most appropriate through this research could be used to develop a model for image analysis; such a model would employ the specific level of reconstruction for the wavelet transform, the first- and second-order texture features found to be globally appropriate for the texture analysis, and a combination of first- and second-order statistics and a combination of spectral and spatial data for the classifications.

There are some factors that require further study, however, in order to make the system more automated. One factor is a window size that would be appropriate for imagery of concrete damage in general, since this was not established through this research. It would be interesting to see if any window size can be used that would be acceptable for damage that is spread out as well as localized in the imagery. Another factor is the type of classifier to be employed. Although this research found that the supervised ANN classifier produced better classification accuracies compared with the unsupervised *K*-means clustering algorithm, it required significant analyst input. An effective classification method that functions with less analyst intervention would be desirable, such as an unsupervised neural network that does not require the analyst to select the ROIs for training. A third factor that requires more study is the type of imagery. This image analysis model would be based on the use of greyscale NDT imagery, since this research found limitations concerning computation time and dimensionality for thermographic and colour imagery. However, studies can be conducted in order to determine which bands of RGB are more suitable for these two types of images in an effort to reduce the number of features that need to be computed, and results compared with those of greyscale imagery to see if there is any significant difference.

Other topics for future studies can also be considered. One topic concerns the application of the statistical analysis. This research dealt with only first- and second-order statistics; higher-order statistics were not commonly employed with remote-sensing imagery previously due to the computational costs involved when working with large image dimensions. Since concrete imagery has relatively much smaller image dimensions, and computer efficiency has steadily

increased, the use of third-and higher-order statistics for the texture analysis of concrete imagery can also be further experimented. Another subject is the development of a standard set-up for data acquisition, which would control the resolution and uniformity of large-scale data. Additional studies can comprise the development of a model for incorporating concrete image data from various NDT imaging techniques, such as optical images, which present image data of the surface, infrared thermography and acoustics, which are used for subsurface conditions, and ground penetrating radar, which is employed to obtain below-surface information of a structure.

Furthermore, the image analysis model employed in this research has the potential to be developed as a component for automated damage assessment, which can be incorporated into a structural health monitoring system for concrete infrastructure. Automation of the system would allow for the assessment of a large volume of data, which could be used to establish a database of monitoring imagery, inspection results, etc. Since the imaging and inspection data can be stored in a digital format, image and data retrieval using metadata and content-based methods can be employed in order to compare the damage characteristics with previous inspection results and information. Data concerning a particular structure can be put together to form a three-dimensional representation of the condition using GIS techniques. This can aid in monitoring the condition of a structure; a history of inspection results can thus be examined and compared in order to quantitatively establish changes that occur with time.

References

Abdel-Qader, I., Abudayyeh, O., and Kelly, M. (2003) Analysis of edge-detection techniques for crack identification in bridges. Journal of Computing in Civil Engineering, vol. 17, no. 4, pp. 255 – 263.

Abudayyeh, O., Al Bataineh, M., and Abdel-Qader, I. (2004) An imaging data model for concrete bridge inspection. Advances in Engineering Software, vol. 35, pp. 474 – 480.

Ahearn, S.C. (1988) Combining Laplacian images of different spatial frequencies (scales): implications for remote sensing analysis. IEEE Transactions on Geosciences and Remote Sensing, vol. 26, pp. 826 – 831.

Andrey J. and Mills, B. (2003) Climate change and the Canadian transport system: vulnerabilities and adaptations. Weather and Transportation in Canada, (J. Andrey, and C. Knapper, eds.), Department of Geography Publication Series Monograph no. 55, University of Waterloo, Waterloo, Ontario.

Awcock, G.W. and Thomas, R. (1996) Applied Image Processing. McGraw-Hill, New York.

Bakker, J. and Postema, F. (2003) Monitoring of concrete structures on ASR: a "smart structure" project. International Symposium on Non-Destructive Testing in Civil Engineering, Berlin, Germany.

Bishop, C.M. (1995) Neural Networks for Pattern Recognition. 2nd edition, Clarendon Press, Oxford, New York.

Brodatz P. (1966) Textures: A Photographic Album for Artists and Designers. Dover Publications, New York.

Broomfield, J.P. (1997) Corrosion of Steel in Concrete: Understanding, Investigation and Repair. E. & F.N. Spon Ltd., London, UK.

Büyüköztürk, O. (1998) Imaging of concrete structures. NDT&E International, vol. 31, no. 4, pp. 233 – 243.

Capra, B. and Sellier, A. (2001) Mechanical modeling of alkali-aggregate reaction in concrete structures. Proceedings of the Conference on Fracture Mechanics of Concrete Structures, France, pp. 183 – 190.

Carino, N. (2003) Non-destructive test methods to evaluate concrete structures. Proceedings of the 6th CANMET/ACI International Conference on Durability of Concrete, Thessaloniki, Greece.

Carter, P. (1999) A national agenda for technological research and development in road and inter-modal transportation. Transportation Association of Canada, Ottawa, Ontario.

Chen, C.H. (1998) Pattern recognition in non-destructive evaluation of materials. Handbook of Pattern Recognition and Computer Vision, 2nd edition, (C.H. Chen, L.F. Pau and P.S.P. Wang, eds.), World Scientific Publishing Co., Singapore, pp. 455 – 471.

Chong, K.P., Scalzi, J.B., and Dillon, O.W. (1990) Overview of non-destructive testing evaluation projects and initiatives at NSF. Journal of Intelligent Materials, Systems & Structures, vol. 1, pp. 422 – 431.

Clark, M.R., McCann, D.M., and Forde, M.C. (2003) Application of infrared thermography to the non-destructive testing of concrete and masonry bridges. NDT&E International, vol. 36, pp. 265 – 275.

Coggins, J.M. (1982) A framework for texture analysis based on spatial filtering. PhD Thesis, Computer Science Department, Michigan State University, Michigan, USA.

Croney, D. and Croney, P. (1999) Design and Performance of Road Pavements. 3rd edition, McGraw-Hill, Toronto.

Daugman, J.G. (1990) An information-theoretic view of analog representation in striate cortex. Comp. Neuroscience, pp. 403 – 424.

Davis, L. (1975) A survey of edge detection techniques. Computer Vision, Graphics, and Image Processing, vol. 4, no. 3, pp. 248 – 270.

Dérobert, X., Aubagnac, C., and Abraham, O. (2002) Comparison of NDT techniques on a post-tensioned beam before its autopsy. NDT&E International, vol. 35, pp. 541 – 548.

Fontenot, M. (2001) A wavelet introduction. Consortium for Computing in Small Colleges, South Central Conference, JCSC vol. 17, no.3, pp. 290 – 296.

Fournier, B. and Bérubé, M.A. (2000) Alkali-aggregate reaction in concrete: a review of basic concepts and engineering implications. Canadian Journal of Civil Engineering, vol. 27, pp. 167 – 191.

Franklin, S.E. and Peddle, D.R. (1989) Spectral texture for improved class discrimination in complex terrain. International Journal of Remote Sensing, vol. 10, no. 8, pp. 1437 – 1443.

Fung, T. and Ledrew, E. (1988) The determination of optimal threshold levels for change detection using various accuracy indices. Photogrammetric Engineering and Remote Sensing, vol. 54, no. 10, pp. 1449 – 1454.

Gaudreault, M. (2000) The St. Lawrence Seaway (Québec, Canada): a case study in the management of structures affected by alkali-aggregate reaction. Proceedings of the 11th International Conference on AAR in Concrete, Québec City, Canada, pp. 1293 – 1302.

Gong, P. (1990) Improving accuracies in land use classification with high spatial resolution satellite: a contextual classification approach. PhD Thesis, University of Waterloo, Waterloo, Ontario, Canada.

Haar, A. (1910) Zur theorie der orthogonalen funktionen-systeme. Math. Ann., vol. 69, pp. 331 – 371.

Haas, R., Hudson, W.R., and Zaniewski, J. (1994) Modern Pavement Management. Krieger Publishing Co., Malabar, Florida.

Halliday, D. and Resnick, R. (1978) Physics. 3rd edition, John Wiley & Sons, New York.

Haralick, R.M. (1979) Statistical and structural approaches to texture. Proceedings of the IEEE, vol. 67, no. 5, pp. 786 – 804.

Haralick, R.M., Shanmugan, K. and Dinstein, I. (1973) Textural features for image classification. IEEE Transactions on Systems, Man, and Cybernetics, vol. 8, pp. 610 – 621.

Hay, G.J. and Niemann, K.O. (1996) Visualizing 3D texture: a three dimensional structural approach to model forest texture. Canadian Journal of Remote Sensing, vol. 20, pp. 90 – 101.

Haykin, S. (1999) Neural Networks. 2nd Edition, Prentice-Hall, New Jersey.

He, D-C. and Wang, L. (1991) Texture features based on texture spectrum. Pattern Recognition, vol. 24, no. 5, pp. 391 – 399.

Hsiao, C.H. (2004) Haar wavelet approach to linear stiff systems. Mathematics and Computers in Simulation, vol. 64. pp. 561 – 567.

Hutchinson, T.C. and Chen, Z.Q. (2006) Improved image analysis for evaluating concrete damage. Technical Notes, Journal of Computing in Civil Engineering, vol. 20, no. 3, pp. 210 – 216.

Institute for Research in Construction (2003) http://irc.nrc-cnrc.gc.ca/uir/structures/index.html

Ismail, M.E. and Soleymani, H.R. (2002) Monitoring corrosion rate for ordinary Portland concrete (OPC) and high-performance concrete (HPC) specimens subjected to chloride attack. Canadian Journal of Civil engineering, vol. 29, pp. 863 – 874.

Jain, A.K. and Bhattacharjee, S. (1992) Texture segmentation using Gabor filters for automatic document processing. Machine Vision and Applications, vol. 5, pp. 169 – 184.

Jain, A.K. and Dubes, R.C. (1988) Algorithms for Clustering Data. Prentice Hall, Englewood Cliffs, New Jersey.

Jawerth, B. and Sweldens, W. (1994) An overview of wavelet based multiresolution analyses. SIAM Review, vol. 36, no. 3, pp. 377 – 412.

Jensen, J.R. (1996) Introductory Digital Image Processing. 2nd edition, Prentice-Hall, New Jersey.

Jensen, J.R. (2000) Remote Sensing of the Environment: An Earth Resource Perspective. Prentice-Hall, New Jersey.

Julesz, B. (1962) Visual pattern discrimination. IRE Transactions on Information Theory, vol. 8, pp. 84 – 92.

Julesz, B., Gilbert, E.N., Shepp, L.A., and Frisch, H.L. (1973) Inability of Humans to discriminate between visual textures that agree in second-order statistics – revisited. Perception, vol. 2, pp. 391 – 405.

Karathanassi, V., Iossifidis, C.H., and Rokos, D. (2000) A texture-based classification method for classifying built areas according to their density. International Journal of Remote Sensing, vol. 21, no. 9, pp. 1807 – 1823.

Kociolek, M., Materka, A., Strzelecki, M., and Szczypinski, P. (2001) Discrete wavelet transform-derived features for digital image texture analysis. Proceedings of the International Conference on Signals and Electronic Systems, Lodz, Poland, pp. 163 – 168.

Laur, H. (1989) Analyse d'images radar en télédétection: discriminateurs radiométriques et texturaux. Thèse de doctorat, no. 403, Université Paul Sabatier, Toulouse, France.

Laws, K.I. (1980) Textured image segmentation. PhD Thesis, University of Southern California, California, USA.

Lek, S. and Guegan, J.F. (1999) Artificial neural networks as a tool in ecological modeling: an introduction. Ecological Modeling, vol. 120, pp. 65 – 73.

Li, J., Tan, J., and Shatadal, P. (2001) Classification of tough and tender beef by image texture analysis. Meat Sciences, vol. 57, pp. 341 – 346.

Liu, C., Zhang, L., Davis, C.J., Solomon, D.S., Brann, T.B., and Caldwell, L.E. (2003) Comparison of neural networks and statistical methods in classification of ecological habitats using FIA data. Forest Science, vol. 49, no. 4, pp. 619 – 631.

Livens, S., Scheunders, P., Van de Wouwer, G., and Van Dyck, D. (1997) Wavelets for Texture Analysis, http://www.ruca.ua.ac.be/VisionLab/WTA.html

Livens, S., Scheunders, P., Van de Wouwer, G., Van Dyck, D., Smets, H., Winkelmans, J., and Bogaerts, W. (1996) A texture analysis approach to corrosion image classification. Microscopy, Microanalysis, & Microstructures, vol. 7, no. 2, pp. 143 – 152.

Mallat, S.G. (1989) A theory for multiresolution signal decomposition: the wavelet representation. IEEE Transactions on Pattern Analysis and Machine Intelligence, vol. 11, pp. 674 – 693.

Marr, D. and Hildreth, E. (1980) Theory of edge-detection. Proceedings of the Royal Society London, vol. 207, pp. 187 – 217.

Masad, E., Muhunthan, B., Shashidhar, N., and Harman, T. (1999) Internal structure characterization of asphalt concrete using image analysis. ASCE Journal of Computing in Civil Engineering, vol. 13, no. 2, pp. 88 – 95.

Mather, P.M., Tso, B., and Koch, M. (1998) An evaluation of the Landsat TM spectral data and SAR-derived textural information for lithological discrimination in the Red Sea Hills, Sudan. International Journal of Remote Sensing, vol. 19, no. 4, pp. 587 – 604.

Mehta, P.K., Schiessl, P., and Raupach, M. (1992) Performance and durability of concrete systems. Proceedings of the 9th International Congress on the Chemistry of Cement, New Delhi, India, vol.1, pp. 597 – 659.

Mindess, S. and Young, J.F. (1981) Concrete. Prentice-Hall, Englewood Cliffs, New Jersey.

Ohio Department of Natural Resources Division of Water Fact Sheet (1999) Dam safety: problems with concrete materials. Fact Sheet 99-56, Ohio.

Parker, J.R. (1997) Algorithms for Image Processing and Computer Vision. John Wiley & Sons, New York.

Patterson, D. (1996) Artificial Neural Network. Prentice-Hall, Singapore.

Perkins, C. and Fricke, T. (2000) Wavelets. Report for Department of Electrical Engineering, University of California, Berkeley, California.

Pickett, R.M. (1970) Visual analysis of texture in the detection and recognition of objects. Picture Processing and Psycho-pictorics (B.C. Lipkin and A. Rosenfeld, eds.), Academic Press, New York, pp. 298 – 308.

Pigeon, M. and Pleau, R. (1995) Durability of Concrete in Cold Climates. E&FN Spon, London, UK.

Powers, T.C. (1975) Freezing effects in concrete. Durability of Concrete, SP-47, American Concrete Institute, Detroit, Michigan, pp. 1 – 12.

Pultz, T.J. and Brown, R.J. (1987) SAR image classification of agricultural targets using first- and second-order statistics. Canadian Journal of Remote Sensing, vol. 13, no. 2, pp. 85 – 91.

Rhim, H.C. (2001) Condition monitoring of deteriorating concrete dams using radar. Cement and Concrete Research, vol. 31, pp. 363 – 373.

Richards, J.A. and Jia, X. (1999) Remote Sensing Digital Image Analysis: An Introduction. 3rd edition, Springer-Verlag, New York.

Rivard, P. and Ballivy, G. (2005) Assessment of the expansion related to alkali-silica reaction by the damage rating index method. Construction and Building Materials, vol. 19, no. 2, pp. 83 – 90.

Rivard, P., Fournier, B., and Ballivy, G. (2000) Quantitative petrographic techniques for concrete damage due to ASR: experimental and application. Cement, Concrete and Aggregates, CCAGDP, vol. 22, no. 1, pp. 63 – 72.

Roberts, L. (1965) Machine perception of three-dimensional solids. Optical and Electro-Optical Information Processing, (J. Tippett, ed.), MIT Press, Cambridge, Massachusetts, pp. 159 – 197.

Rosenblatt, F. (1958) The perceptron: A probabilistic model for information storage and organization in the brain. Psych. Rev., vol. 65, pp. 386 – 408.

Sali, E. and Wolfson, H. (1992) Texture classification in aerial photographs and satellite data. International Journal of Remote Sensing, vol. 13, no. 18, pp. 3395 – 3408.

Sarle, W.S. (1994) Neural networks and statistical methods. Proceeding of the 19th SAS Users Group International Conference, SAS Institute, Cary, North Carolina.

Scheunders, P., Livens, S., Van de Wouwer, G., Vautrot, P., and Van Dyck, D. (1997) Wavelet-based texture analysis, International Journal of Computer Science and Information Management.

Schmidlin, T.W., Dethier, R.E., and Eggleston, K.L. (1999) Freeze-thaw days in the North-eastern United States. J Climate Appl Meteor, vol. 26, no. 1, pp. 142 – 155.

Schowengerdt, R.A. (1997) Remote Sensing: Models and Methods for Image Processing. 2nd edition, Academic Press, San Diego.

Scott, M., Rezaizadeh, A., Delahaza, A., Santos, C.G., Moore, M., Graybeal, B., and Washer, G. (2003) A comparison of non-destructive evaluation methods for bridge deck assessment. NDT&E International, vol. 36, pp. 245 – 255.

Shaban, M.A. and Dikshit, O. (2001) Improvement of classification in urban areas by the use of textural features: the case study of Lucknow city, Uttar Pradesh. International Journal of Remote Sensing, vol. 22, no. 4, pp. 565 – 593.

Smith, S.W. (1998) The Scientist and Engineer's Guide to Digital Signal Processing. California Technical Publishing, San Diego, California.

Stark, D. (1995) Alkali-aggregate reaction and its effects on concrete. Proceeding of the Second International Conference on Alkali-Aggregate Reaction in Hydroelectric Plants and Dams, USCOLD, Chattanooga, Tennessee, pp. 9 – 18.

Strömberg, J.O. (1981) A modified franklin system and higher-order spline systems on $\mathbf{R}^n$ as unconditional bases for hardy spaces. Conference on Harmonic Analysis in Honour of Antoni Zygmund, vol. II, pp. 475 – 494.

Tomita, F. and Tsuji, S. (1990) Computer Analysis of Visual Textures. Kluwer Academic Publishers, London.

Tonsmann, G. and Tyler, J.M. (1999) Estimation of oceanic surface velocity fields using wavelets. Proceedings of SPIE Conference on Wavelet Application VI, Orlando, Florida, vol. 3723, pp. 122 – 129.

Tuceryan, M. and Jain, A.K. (1998) Texture analysis. Handbook of Pattern Recognition and Computer Vision, 2nd edition, (C.H. Chen, L.F. Pau and P.S.P. Wang, eds.), World Scientific Publishing Co., pp. 207 – 248.

U.S. Department of Transportation, Federal Highway Administration, (2003) National Technical Information Service, Springfield, VA 22616, NTIS publication no. PB255322.

Van de Wouwer, G. (1998) Wavelets for multiscale texture analysis. PhD Thesis, Antwerpen University, Netherlands.

Vavilov, V. and Demin, V. (2002) Infrared thermographic inspection of operating smokestacks. Infrared Physics & Technology, vol. 43, pp. 229 – 232.

Wang, K. and Monteiro, P.J. (1997) Corrosion products of reinforcing steel and effects on the concrete deterioration. Proceeding of the 3rd CANMET/ACI International conference on Performance of Concrete in a Marine Environment, St. Andrews by the Sea, New Brunswick, pp. 83 – 97.

Washer, G.A. (1998) Developments for the non-destructive evaluation of highway bridges in the USA. NDT & E International, vol. 31, no. 4, pp. 245 – 249.

Weil, G.J. (1995) Non-destructive testing of bridge, highway and airport pavements. International Symposium on Non-destructive Testing in Civil Engineering (NDT-CE), Berlin, vol.1, pp. 467 – 474.

Weil, G.J. and Rowe, T.J. (1998) Non-destructive testing and repair of the concrete roof shell at the Seattle Kingdom. NDT&E International, vol. 31, no. 6, pp. 389 – 400.

Zhu, C. and Yang, X. (1998) Study of remote sensing image texture analysis and classification using wavelet. International Journal of Remote Sensing, vol. 19, no. 16, pp. 3197 – 3203.

Zizzari , A., Seiffert, U., Michaelis, B., Gademann, G., and Swiderski, S. (2001) Detection of tumor in digital images of the brain. Proceedings of the IASTED International conference on Signal Processing, Pattern Recognition & Applications, Rhodes, Greece, pp. 132 – 137.

APPENDICES

PAPERS PUBLISHED FROM THIS THESIS

Damage classification of concrete structures based on grey level co-occurrence matrix using Haar's discrete wavelet transform

Shahid Kabir and Patrice Rivard

Département de génie civil

Université de Sherbrooke, Sherbrooke, Québec, Canada J1K 2R1

Computers and Concrete, Vol.4, no. 3 (2007) 243-257

Neural-network-based damage classification of bridge infrastructure using texture analysis

Shahid Kabir, Patrice Rivard and Gérard Ballivy

Département de génie civil

Université de Sherbrooke, Sherbrooke, Québec, Canada J1K 2R1

Can. J. Civ. Eng. 35 : 258-267 (2008)